Study of Persistent and Flaring Gamma-Ray Emission from Active Galactic Nuclei with the MAGIC Telescopes and Prospects for Future Open Data Formats in Gamma-Ray Astronomy

DISSERTATION

zur Erlangung des akademischen Grades
doctor rerum naturalium
(Dr. rer. nat.)
im Fach: Physik
Spezialisierung: Experimentalphysik

eingereicht an der
Mathematisch-Naturwissenschaftlichen Fakultät
der Humboldt-Universität zu Berlin

von

Cosimo Nigro

Präsident der Humboldt-Universität zu Berlin:
Prof. Dr.-Ing. Dr. Sabine Kunst

Dekan der Mathematisch-Naturwissenschaftlichen Fakultät:
Prof. Dr. Elmar Kulke

Gutachter: 1. Prof. Dr. Elisa Bernardini
2. Dr. Gernot Maier
3. Prof. Dr. Alberto Franceschini

Tag der mündlichen Prüfung: 23 September 2019

Ai miei genitori Rocco e Lucia,
a mio fratello Diego.

Abstract

Powered by the accretion of matter to a supermassive black hole residing at their centre, active galaxies constitute the most powerful and persistent sources of radiation in the universe. A tenth of these sources shows collimated relativistic outflows of plasma commonly referred to as jets. Their electromagnetic emission can extend in some cases in the gamma-ray domain. The aim of this work is to characterise the mechanisms and the sites beyond this highly-energetic emission.

To accomplish this task we employ observations of two jetted active galaxies at hundreds of GeV conducted with the MAGIC imaging atmospheric Cherenkov telescopes. We support the physical interpretation with observations at lower energies ($100\,\mathrm{MeV} - 100\,\mathrm{GeV}$) by the *Fermi* Gamma-ray Space Telescope and with multi-wavelength data sets collected from instruments observing the sky at lower frequencies.

We examine two peculiar jetted active galaxies: PKS 1510-089 and NGC 1275. They belong to classes of sources relatively rare to detect by imaging Cherenkov telescopes. PKS 1510-089, having the peak of its highest-energy continuum in the $\mathrm{MeV} - \mathrm{GeV}$ regime, manifests very low fluxes at hundreds of GeV and is normally observable in this energy regime only during flaring states. The MAGIC telescopes, monitoring the source since 2012, detect a significant emission over tens of observation hours in what appears to be a low but persistent gamma-ray state. NGC 1275 detection is instead hampered by a jet that, contrarily to most of the active galaxies detected in gamma-rays, is misaligned with the line of sight of the observer. Despite the consequent poor Doppler boost of its intrinsic luminosity, the source has shown in the period between September 2016 and February 2017 a major outburst in its gamma-ray activity: MAGIC recorded the source highest gamma-ray luminosity, variability of the order of few hours and for the first time emission of TeV photons.

The broad band emission of jetted active galaxies is commonly modelled with the radiative processes of a population of particles accelerated in a blob of plasma streaming along the jet. The persistent gamma-ray emission of PKS 1510-089 conforms to this scenario as it can be described with the inverse Compton scattering of electrons accelerated in the jet over the photon fields generated by the accretion of matter to the central black hole. It appears though that the luminous, energetic and fast gamma-ray outburst observed for NGC 1275 cannot be accommodated easily within the same jet-dominated scenario. One could therefore consider that in such an extreme flaring state the acceleration of particles and their successive radiation has an origin close to the event horizon of the black hole residing at the centre of the galaxy.

From both the sources studied it is evident that the combination of data from different instruments critically drives the physical interpretation. Instruments for gamma-ray astronomy, inheriting their technologies and analysis principles from particle-physics experiments, deliver data products that are remarkably different from those produced by the rest of the astronomical community. Additionally each experiment owns a different analysis software and data structure. Moving towards accessible and interoperable data becomes a compelling issue for gamma-ray astronomers as they prepare for the next generation instrument, the Cherenkov Telescope Array, that will be operated as an observatory open to the entire astronomical community.

This thesis presents the technical endeavour to produce high-level data for Cherenkov telescopes, and more generally for gamma-ray instruments, in a format that allows for multi-instrument analyses and fosters accessibility of data and reproducibility of results.

An example of a future gamma-ray astronomy analysis that pursues this approach is provided by combining uniformed high-level data from a gamma-ray satellite and four Cherenkov telescopes to obtain the spectrum of the Crab nebula. The novel approach we propose performs the data analysis and disseminates the results making use only of open-source assets.

We make the case that once the data standardisation is finalised then open-source analysis tools can develop to comply with such a uniformed format and reproducible scientific results arise as a natural consequence of this effort.

Zusammenfassung

Angetrieben durch die Akkretion von Materie in ein super massives Schwarzes Loch in ihrem Zentrum, stellen aktive Galaxien die stärksten und beständigsten Strahlungsquellen im Universum dar. Ein Zehntel dieser Quellen weist gebündelte relativistische Plasmaausbrüche auf, sogenannte Jets. Ihre elektromagnetische Emission kann sich bis in den Gammastrahlenbereich ausbreiten. Das Ziel dieser Arbeit ist, diese Mechanismen und die Orte jenseits der hoch energetischen Emission zu charakterisieren.

Dafür werden die Observationen von zwei Aktiven Galaxien im Bereich von hunderten von GeV verwendet, welche mit den Cherenkov Teleskopen MAGIC aufgenommen wurden. Die physikalische Interpretation wird mit Observationsdaten bei niedrigeren Energien (100 MeV − 100 GeV) des *Fermi* Gamma-Ray Space Teleskops und mit weiteren Daten von Instrumenten, die den Himmel bei niedrigeren Frequenzen observieren, unterstützt.

Wir untersuchen zwei besondere Aktive Galaxien mit Jet: PKS 1510-089 und NGC 1275. Sie gehören zu einer Galaxienklasse, welche mit Cherenkov Teleskopen relativ selten detektiert werden kann. PKS 1510-089 erreicht sein Maximum bei den höchsten Energien im MeV−GeV Bereich, zeigt sehr niedrige Flüsse im Bereich von hunderten GeV und ist dort normalerweise nur während starker Flussausbrüche, sogenannten Flares, messbar. Die MAGIC Teleskope, welche die Quelle seit 2012 immer wieder beobachten, detektieren eine signifikante Emission über dutzende von Observationsstunden, was auf schwache aber kontinuierliche Gammastrahlung aus dieser Quelle hinweist. Die Detektion von NGC 1275 wird stattdessen durch die Ausrichtung des Jets erschwert, welcher, anders als bei den meisten im Gammastrahlenbereich detektierten Aktiven Galaxien, nicht in Richtung des Beobachters zeigt. Trotz des resultierenden schwachen Doppler-Boost, zeigte die Quelle in der Periode von September 2016 bis Februar 2017 einen großen Ausbruch im Gammerstrahlenbereich: MAGIC zeichnete die bisher höchste Luminosität der Quelle auf, sowie eine Variabilität in der Grössenordnung von wenigen Stunden und die erstmalige Emission von TeV Photonen.

Die Bandbreite der Emission von Aktiven Galaxien wird normalerweise mit Strahlungsprozessen von Teilchenpopulationen modelliert, welche in Plasmaansammlungen, die sich entlang des Jetstroms bewegen, beschleunigt werden. Die konstante Gammaemission von PKS 1510-089 ist konform mit dem Szenario, welches diese mit inverser Compton-Streuung von in den Photonfeldern im Jet beschleunigten Elektronen erklärt. Die luminöse, energetische uns kurzzeitige Gammastrahlenausbruch der Quelle NGC 1275 kann jedoch nicht mit dem selben Jet dominierten Szenario vereinbart werden. Daher kann angenommen werden, dass die Beschleunigung von Teilchen und dessen sukzessiver Strahlung in einem solch extremen Flarezustand ihren Ursprung in der Nähe des Ereignishorizonts des schwarzen Lochs im Galaxienzentrum hat.

Für die beiden hier studierten Quellen ist die Kombination der Daten verschiedener Instrumente bei der physikalischen Interpretation maßgeblich. Instrumente der Gammaastronomie, welche ihre Technologien und Analyseprinzipien von Experimenten der Teilchenphysik übernommen haben, liefern Daten, welche sich auffallend von denen der restlichen experimentellen Astronomie unterscheiden. Des Weiteren besitzt jedes Experiment sowohl seine eigene Analyse als auch eine individuelle Datenstruktur. Die Entwicklung hin zu zugänglichen und interoperablen Daten wird für die Gammastrahlenastronomen bei

der Vorbereitung auf das Instrument der nächsten Generation, dem Cherenkov Teleskop Array, das als ein der gesamten astronomischen Gemeinschaft offen stehendes Observatorium betrieben werden soll, zu einem zwingenden Thema.

Diese Dissertation zeigt die Produktion von Cherenkov Teleskop Daten, und generell Daten der Gammastrahleninstrumente, in einem einheitlichen Format, welches die Multiinstrumentanalyse erlaubt und sowohl den Zugang zu den Daten als auch die Reproduzierbarkeit von Ergebnissen erlaubt.

Ein Beispiel zukünftiger Gammaastronomieanalysen, wie in diesem Ansatz angestrebt, wird durch die Kombination von vereinheitlichten Daten eines Gammasatelliten und vier Cherenkov Teleskopen bereitgestellt, um das Spektrum des Krebsnebels zu erhalten. Mit dem hier vorgeschlagenen, neuen Ansatz wird die Analyse mit ausschließlich open-source Daten durchgeführt und dessen Ergebnisse veröffentlicht.

Wir legen die Grundlage, dass nach Abschluss der Datenstandardisierung Open-Source-Analysewerkzeuge entwickelt werden können, um einem so einheitlichen Format gerecht zu werden, und reproduzierbare wissenschaftliche Ergebnisse als natürliche Folge entstehen.

Contents

1 | Introduction

> [Astrophysics] is closely allied on the one hand to astronomy, of which it may properly be classed as a branch, and on the other hand to chemistry and physics; but it assumes wide privileges, and it is ready to draw material which it can use with profit from any source, however distant. It seeks to ascertain the nature of the heavenly body, rather than their position or motion in space - *what* they are, rather than *where* they are; and for my own convenience I shall use the terms astrophysics and astronomy to denote the sciences of which these aims are respectively characteristics.
>
> Keeler (1897)

James E. Keeler addressed with such words the term *astrophysics* in one of the first issues of the *Astrophysical Journal*, of which he was one of the co-founder. Astrophysics is born when the spectrograph is first accosted to a telescope by Fraunhofer (1823) who employed the objective prisms he himself produced to observe Venus, Sirius and other bright heavenly bodies. The realisation that the celestial bodies are constituted (produce the same spectral lines) of the terrestrial elements poses the basis for a new science whose objective is to infer from the properties of radiation the nature of the celestial sources producing it.

Two centuries after Fraunhofer observations, 120 years after Keeler's paper, the spectrograph that astrophysicists nowadays possess has extended to cover almost 20 orders of magnitude in frequency. Such a modern spectrograph, that we may call *multi-wavelength astrophysics*, is constituted by very diverse instruments. Arrays of radio antennas and optical telescopes at ground sides with infrared, ultraviolet and X-ray satellites (circumventing atmosphere absorption in such frequency bands). This thesis is concerned with the highest-energy end of the modern spectrograph: gamma-ray astronomy at hundreds of GeV ($\nu \sim 10^{25}$ Hz). Chapter 2 introduces this astronomical branch presenting the imaging atmospheric Cherenkov technique and the instrument used for the investigations in this thesis, the MAGIC telescopes. The detection of cosmic gamma rays calls for the usage of technologies that are typical of particle-physics experiments. This heritage has impeded the full integration of this discipline among the other branches of modern astronomy, especially from the point of view of its data products. In Chapter 3, that constitutes along with Chapter 2 the technical part of this thesis, we attempt to overcome this historical data division by standardising high-level gamma-ray data to a format that has marked a 40-years standard in astronomy at all wavelengths: the Flexible Image Transport System. Such conversion aims not only

at making gamma-ray data interoperable but also at fostering their usage and investigation by members of the larger astronomical community. This represents a critical issue for the next generation of imaging Cherenkov telescopes, represented by the Cherenkov Telescope Array, that will be operated as an open observatory, sharing its observational time, data and software with the astronomical community.

Decades before the construction of instruments for gamma-ray astronomy, particle detectors were already used to study the cosmic radiation constituted of charged nuclei continuously impinging on Earth discovered by Hess (1912). In the era that saw the dawning of the accelerator technology[I], the cosmic rays (CRs) constituted the only viable source of high-energy particles. As a matter of fact both the positron (Anderson, 1933) and the muon (Neddermeyer and Anderson, 1938) were discovered among the products of their interactions in Earth atmosphere. The CR spectrum is today characterised over 12 orders of magnitude in energy and almost 30 orders of magnitude in flux. Measurements from space-based and ground-based detectors of the CR differential flux (i.e. the flux in $\mathrm{cm}^{-2}\,\mathrm{s}^{-1}$ per energy bin) versus total particle energy are represented with red points against red axes in Figure 1.1. The overall spectrum can be remarkably described by a power-law of the energy ($E^{-\Gamma}$), with two transition points: the *knee* at $\approx 3 \times 10^6$ GeV, where the spectral index steepens from 2.7 to 3.1 and the *ankle* at $\approx 10^{10}$ GeV, where it flattens again. The overall CR composition is dominated by protons ($\approx 80\%$) and He nuclei ($\approx 15\%$), with nuclei as heavy as Nickel observed. Electrons and positrons, also detected, contribute to 1% of the total CR particles[II].

Phenomena like the CR spectrum bring particle physics and astrophysics on a common ground, *astroparticle physics*, questing them after the mechanisms and sites of cosmic particle acceleration. Regarding the mechanisms, as we shall see in Chapter 4, it is understood that a power-law energy distribution of particles constitutes the paramount signature of acceleration due to random scattering in the magnetic field dragged by relativistic shocks perturbing the plasma of astrophysical sources. Sites of acceleration have not been pinpointed yet, still important insights can be derived from a simple criterion obtained by Hillas (1984), who expresses the maximum energy at which a CR can be accelerated by an astrophysical source as

$$E_{\mathrm{max}} = Z \frac{U}{c} \left(\frac{B}{\mu\mathrm{G}} \right) \left(\frac{R}{\mathrm{kpc}} \right) \ \mathrm{EeV}, \tag{1.1}$$

where Z is the CR charge in electron charge units, U the velocity of the scattering magnetic centres causing the acceleration, c the speed of light in vacuum, B the magnetic field tangled with the source and R the size over which acceleration takes palace, measured in pc[III]. Supernova remnants (leftovers of massive star exploded in our galactic neighbourhood) are characterised by shocks with $U/c \approx 10^{-2}$, magnetic fields of $B = 4\,\mu\mathrm{G}$ and maximum sizes of 5 pc. They can therefore accelerate CRs up to hundreds of TeV, i.e. up to the knee region. Expanding the search for cosmic accelerators outside the Milky Way, we observe that a small percentage ($\sim 10\%$) of the known active galaxies (i.e. galaxies with a core outshining in power and energy the typical emission of common galaxies, see Chapter 4) shows distinctive jetted relativistic outflows of plasma. These jets present shocks with $U/c \to 1$, for which tangled magnetic fields of few G

[I] The largest cyclotron built in Berkeley before the 1960s could accelerate deuterons to 16 MeV (Lawrence et al., 1939).
[II] For a to date, thorough, overview on CRs, the interested reader is referred to Chapters 2 to 7 of Spurio 2018.
[III] $1\,\mathrm{pc} = 3.09 \times 10^{18}$ cm.

and transverse sections of $\sim 0.1\,\mathrm{pc}$ are derived. They can accelerate protons to $10^2\,\mathrm{EeV} = 10^{20}\,\mathrm{eV}$, i.e. above the ankle[IV]. Being active galaxies powered by supermassive black holes, acceleration of particles might become feasible also in their immediate vicinity, in the electric fields generated by the rotation of the magnetic field lines attached to the accreting material (see Chapter 6). The transition in spectral index of the CR spectrum can be interpreted as due to acceleration in different source classes.

Confirming the galactic production of CRs, the *Fermi*-LAT collaboration has detected the signature of neutral pion decay (product of $p-p$ interactions) in gamma rays produced by supernovae remnants (Ackermann et al., 2013). Substantiating instead the broader hypothesis that acceleration of hadrons occurs in astrophysical source, the IceCube Collaboration (2013) detected a diffuse extraterrestrial flux of neutrinos at energies between $\sim 10-10^3\,\mathrm{TeV}$. Astrophysical neutrinos are the product of the interactions of hadrons (dominating the CR composition) with the environments in which they are accelerated (see Section 4.5.6). Contrary to charged CRs that are deflected by extragalactic magnetic fields in their path to Earth, astrophysical neutrinos travel undeflected and hence can be used for astronomy, tracing back to the astrophysical sites of their production.

The objective of this work is to characterise the mechanisms and the regions beyond the gamma-ray emission of the jetted active galaxies we pointed at as the accelerators of the highest-energy CRs. For this purpose we examine two sources observed at hundreds of GeV with the MAGIC telescopes: PKS 1510-089 and NGC 1275. The physical discussion, primarily driven by the MAGIC results, tries to model the entire broad-band electromagnetic spectrum. The latter is built employing observations in GeV energies gathered by the *Fermi* Gamma-ray Space Telescope and by several instruments at lower frequencies (X-ray down to radio for PKS 1510-089, optical for NGC 1275).

If we were to consider the entire electromagnetic spectrum of a jetted active galaxy and we were to plot it with the same representation of the CR spectrum, i.e. differential flux versus energy, then a remarkably similar trend would arise. The black and gray points illustrate in Figure 1.1 that the differential fluxes of the Markarian 421 (black) and Markarian 501 (gray) active galaxies cover 30 orders of magnitude in flux (as the CR spectrum) and 20 orders of magnitude in energy (against the 10 of the CRs). The overall spectrum can be as well broken down in several power laws with a major break in spectral index occurring at $\sim$ MeV energies. Such break, as we shall see in Section 4.5, separates two continuum emission dominated by different radiative processes (rather than accelerations dominated by different sources as in the CR spectrum). Power-law electromagnetic spectra can be ascribed to the radiative processes of power-law particle distributions (as the one observed in CRs) accelerated in the jets of the galaxy. Thus the direct detection of CRs does not constitute the only path to study the acceleration of particles in astrophysical environments: the observation of broadband electromagnetic spectra, manifestation of the interactions of these particles with their environments, provides further insights to the study of their acceleration.

One of the most commonly adopted scenarios to describe the broad-band emission of jetted galaxies is introduced in Chapter 4. The so-called *leptonic* models we consider in this work account for the

[IV] The role of other astrophysical sources in particle acceleration is not commented upon in this short introduction, we focus on supernova remnants since a signature of proton acceleration has been observed in gamma rays (see text) and on active galaxies as they constitute the topic of this thesis.

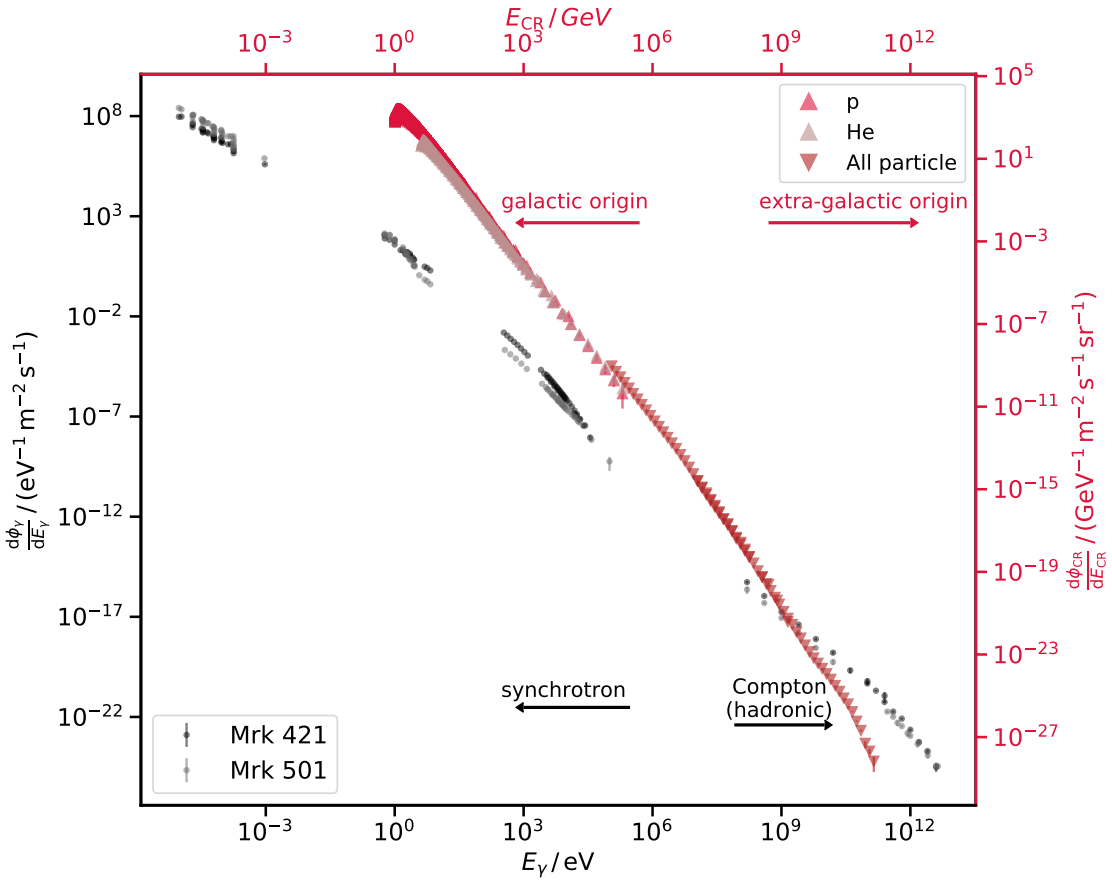

Figure 1.1: Differential flux versus total energy representation of the CRs spectrum and of the electromagnetic spectrum of two active galaxies. The CR data are represented with red markers. Upwards triangle are the p (light red) and He (pink) spectra collected by space-based instruments (PAMELA, CREAM, AMS), fetched through the Database of Charged Cosmic Rays (Maurin et al., 2014). Downward triangles represent all-particle flux spectra measured by Tibet-III (Amenomori et al., 2008), KASCADE-Grande (Apel et al., 2012) and Auger (Fenu et al., 2017). The axes referring to this spectral points are highlighted in red. The black points and black axes represent the electromagnetic spectrum of the active galaxies Markarian 421 (Abdo et al., 2011a) and Markarian 501 (Abdo et al., 2011b). Both the spectra are characterised by a remarkable change in spectral slope at 3×10^6 GeV for CRs and in soft the MeV regime for the electromagnetic spectrum of the Markarians. In the first case the break marks the separation between the contribution of two different source classes, in the second case between two different radiative processes or regions of the galaxy generating the high-energy emission.

low-energy continuum emission (radio to X-ray) with the synchrotron radiation of electrons accelerated in the blob while the high-energy continuum emission (X-ray to gamma-rays) is reproduced with the inverse Compton of the same electrons on photon fields internal or external to the jet. A particular class of models, not included in this thesis, and labelled as *hadronic*, describes instead the highest-energy emission as due to the products of proton interaction with the jet or galactic environment and are in addition able to predict the neutrino emission expected from these sources.

The first source studied in this work is PKS 1510-089. Chapter 5 presents the observations of this source gathered by the MAGIC telescopes since 2012. Using the flux densely sampled in time by the *Fermi* satellite we identify a state of low gamma-ray emission. The latter is simultaneous to a total of ≈ 80 hours of MAGIC observations over which the source shows a significant signal. After building the multi-wavelength spectrum we conclude that the highest-energy continuum emission can be modelled with the inverse Compton of the jet electrons on photon fields external to the jet, produced by the accretion of the black hole at the centre of the galaxy. While active galaxies are generally detected in gamma rays over outbursts of their activity, in this case the acceleration ad radiation processes appear to produce a persistent emission that can be detected up to hundreds of GeV. This baseline scenario, attributing the entire broad-band electromagnetic spectrum to a region in the jet, seems to be challenged by the extreme outburst observed by MAGIC for the source NGC 1275 in the period between September 2016 and February 2017, presented in Chapter 6. We use the aforementioned jet-dominated model to derive that the short time variability (and the consequent small emitting region), the unprecedented flux level and the emission of TeV photons are difficult to accommodate at once with the same electron population accelerated in a single blob in the jet. Compton-produced TeV gamma rays and synchrotron-produced optical photons should consistently absorb each other via $\gamma\gamma$ pair production in the small emitting region inferred from the data. Additionally gamma-ray and optical fluxes, if due to the radiative processes of the same particle population, should manifest a certain extent of correlation that we do not observe comparing data sets in these energy bands. We hence suggest that electrons and positrons might accelerate and radiate before the jet formation, in the immediate vicinity of the Black Hole, in the magnetosphere formed by the magnetic field lines transported by the disk dragged and forced to rotate with the central black hole.

The outlook in Chapter 7 summarises the main results of this work and prospects the advantages that the usage of uniformed high-level data could bring to the current generation of Cherenkov telescopes, besides those anticipated for the forthcoming Cherenkov Telescope Array. Especially for science cases like PKS 1510-089 and NGC 1275, i.e. sources not bright *per se* in the energy range accessible by Cherenkov telescopes, the combination of data (particularly the archival ones) might be critical to detect such sources and to characterise their spectral features and temporal evolution.

The author's contribution to each result presented here is stated by an epigraph at the beginning of each section or chapter. Chapter 2 and Chapter 4 are oriented towards a general overview but contains sections with original work highlighted by an epigraph at their beginning. Chapter 3, 5 and 6 present published material and the contributions of the author and of his collaborators are stated in the opening epigraph.

2 | VHE Gamma-ray Astronomy, Detection and Analysis Principles

Electron-positron pair production in the electric field of an atomic nucleus dominates the interaction with matter of photons of energies $E_\gamma > 30\,\mathrm{MeV}$. Telescopes for gamma-ray astronomy at the highest energies are designed to exploit this process and the particular realisation of the detection technique flags different branches of the discipline. High Energy (HE, $100\,\mathrm{MeV} < E_\gamma < 100\,\mathrm{GeV}$) gamma-ray astronomy relies on direct detection via space-borne instruments: pair-conversion telescopes. The $e^\pm$ conversion is realised in a tracking detector[I] reconstructing the primary photon direction through the trails of the charged pairs. The tracker is coupled to a calorimeter estimating the primary photon energy via containment of its charged products. The whole system is enclosed by scintillator detectors rejecting charged cosmic particles. In the Very High Energy (VHE, $100\,\mathrm{GeV} < E_\gamma < 100\,\mathrm{TeV}$) regime, the steeply falling flux of astrophysical sources (Figure 1.1) does not allow the collection areas realisable for space-borne instrument ($\sim \mathrm{m}^2$) to accumulate significant statistics within their limited ($\sim$ years) lifetime. VHEs become the domain of ground based instrument such as Imaging Atmospheric Cherenkov Telescopes (IACT) with collection areas of $\sim 10^5\,\mathrm{m}^2$. Their detection technique is indirect: pair production of cosmic gamma rays with atmospheric nuclei initiates a particle cascade whose charged component polarises the atmospheric molecules that in turn emit nano-second flashes of ultraviolet (UV) light through the Cherenkov effect. Cherenkov photons are collected by large optical reflectors ($\sim 10\,\mathrm{meters}$) and focused onto a camera of photomutiplier tubes (PMTs) with nano-second read-out electronics. Sampling the developement of the particle cascade through its Cherenkov light allows the reconstruction of the primary photon direction while the intensity of the light emitted, hence the total charge developed by the PMTs, represents a proxy for the primary energy.

This chapter provides a brief introduction to the air showers generated by cosmic particles and their Cherenkov emission. It illustrates the VHE detection and analysis techniques through the example of the Florian Goebel Major Atmospheric Gamma-ray Imaging Cherenkov (MAGIC) experiment in which this thesis work has been conducted. Further IACT facilities are described in the context of Chapter 3. In describing the analysis principles, emphasis is given on the contributions within the scope of the technical work of this thesis, namely the realisation of a prototypical open format for the instrument data, whose application follows in Chapter 3, and the computation of the sensitivity of the instrument.

2.1 Extensive Air Showers

The interaction of relativistic charged cosmic particles (protons and ionised nuclei, electrons and positrons) or cosmic gamma rays with nuclei in Earth's atmosphere initiates a cascade of processes producing further particles and radiation. Particle multiplication ceases when a critical energy, dependent on the nature of the interaction fostering the cascade, is reached and the components of the cascade starts to be absorbed by the atmosphere. The global phenomenon is usually referred to as Extensive Air Showers (EAS). Depending on the primary particle, EAS are differentiated in *hadronic*, when triggered by protons or

[I] The tracking detector was a spark chamber in the early era of SAS-2, COS-B and the Energetic Gamma Ray Experiment Telescope (EGRET), and changed to a tracker / converter system (high-Z material interleaved by silicon strip detectors) in the most recent years of the Astrorivelatore Gamma ad Immagini LEggero (AGILE) and the Large Area telescope on board the Fermi satellite (*Fermi*-LAT).

heavier nuclei, or *electromagnetic* (EM), when triggered by gamma rays or electrons (from now on, if not specified, we will refer to both electrons and positrons with the term *electrons*).

To set up a mathematical description of the problem we consider that the cascade development is governed by the competing processes of interaction and decay of particles. Given a target material of mass and number density $\rho\,(\mathrm{g\,cm^{-3}})$ and $n\,(\mathrm{cm^{-3}})$, respectively, the *interaction length* for a process with cross section σ is introduced as $\lambda = \rho\,/\,(n\sigma) = Am_p\,/\,\sigma$. The last equality is obtained for a material composed of nuclei with mass number A and nucleon mass equivalent to the proton mass m_p. λ is measured in mass thickness units $(\mathrm{g\,cm^{-2}})$. The *decay length* is expressed as $d = \rho\gamma c\tau'$, with γ Lorentz factor of the particle and τ' the decay time in the particle rest frame. In EAS theory the penetration of the cascade in the atmosphere is conventionally also described in mass thickness units. To comply with this, the *vertical atmospheric depth* X, representing the atmospheric density integrated in altitude from the observation level h, is introduced

$$X = \int_h^\infty \mathrm{d}z\ \rho(z). \tag{2.1}$$

The development of showers in the atmopshere is described by a set of coupled differential equations, dubbed as *cascade* or *transport* equations, following the notation of Gaisser et al. (2016)

$$\frac{\mathrm{d}N_i(E_i, X)}{\mathrm{d}X} = -\left(\frac{1}{\lambda_i} + \frac{1}{d_i}\right) N_i(E_i, X) + \sum_j \int \frac{F_{ji}(E_i, E_j)}{E_i} \frac{N_j(E_j, X)}{\lambda_j} \mathrm{d}E_j. \tag{2.2}$$

Here N_i is the number of particle of species i, function of the energy E_i and of the vertical depth X; λ_i and d_i are the interaction and decay lengths, respectively. F_{ji} represents the inclusive cross section for a particle j with energy E_j and interaction length λ_j to interact with an atmospheric nucleus and produce a particle of species i with energy E_i. The first term on the left-hand side of Eq. 2.2 is an absorption term accounting for particles of species i lost to decay and further interaction. The second addend is a source term reckoning how many particles of species i are produced in the decay of different parent particles j (hence the $\sum_j$) and coupling the differential equation for the species i to the others.

A first instance of Eq. 2.2, coupling photons and electrons was introduced by Carlson and Oppenheimer (1937). The thorough study of the EM case is contained in the seminal work of Rossi and Greisen (1941), forking the problem in Eq. 2.2, labelled as *Approximation A*, to account also for collision losses of electrons, in the so called *Approximation B*. The solution of Eq. 2.2 is beyond the scope of this dissertation and can be addressed by Chapters 5, 15 and 16 of Gaisser et al. (2016) and the original work of Rossi and Greisen (1941). The purpose of the following EAS discussion will be to highlight, with the simplest model possible, the striking differences between EM and hadronic air showers that constitute, respectively, the signal and the background events of IACTs.

2.1.1 Isothermal Barotropic Atmospheric Model

A model of the atmosphere, an integral part of an IACT detector, is required before describing the air showers and their Cherenkov emission. The phenomenon of the EAS is generally limited to Earth's troposphere, the lowest atmospheric layer. Reaching up from 6 to 20 km in altitude (poles to equator)

and containing 75 % of the total atmosphere mass, the troposphere is characterised by a negative gradient of temperature with height $\approx -7\,\mathrm{K}\,/\,\mathrm{km}$ (cfr. Figure. 3 in NASA 1976) and can be assumed isothermal in a first approximation: $T(h) = \text{const}$. The equation of state for the ideal gas reads

$$\rho = \frac{MP}{k_B T}, \tag{2.3}$$

where M is the mean molecular mass, P is the pressure, k_B the Boltzmann constant and T the temperature. The state equation, given the isothermal assumption, has density dependent only on the pressure and it is labeled as barotropic. The pressure P at a given altitude is given by the amount of atmospheric mass weighting above h; an increase in altitude $\mathrm{d}h$ will therefore cause a decrease of pressure $\mathrm{d}P = -\rho g \mathrm{d}h$, when plugged into Eq. 2.3 gives the differential equation

$$\frac{\mathrm{d}P}{P} = -\frac{\mathrm{d}h}{\frac{k_B T}{Mg}}. \tag{2.4}$$

Using $T = T_0$, temperature at Earth surface, we can introduce the *scale height*

$$h_0 = \frac{k_B T_0}{Mg}, \tag{2.5}$$

and solve 2.4 obtaining for P (and for ρ, given the proportionality in 2.3)

$$P(h) = P_0 \exp(-h/h_0), \quad \rho(h) = \rho_0 \exp(-h/h_0). \tag{2.6}$$

P_0 and ρ_0 are the pressure and density values at ground level. Integrating $\rho(h)$ in Eq. 2.6 according to Eq. 2.1 returns an exponential scale with h_0 also for the vertical depth

$$X = \int_h^\infty \rho_0 \exp(-z/h_0)\mathrm{d}z = \rho_0 h_0 \left[-\exp(-z/h_0)\right]_h^\infty = X_0 \exp(-h/h_0), \tag{2.7}$$

where $X_0 = \rho_0 h_0$. All numerical values for the quantities in Eq. 2.3-2.7 are given in Table 2.1, the physical constants in Table A.1. X ranges from 0 at the atmosphere top, to $X(h = 0) = X_0$ at ground level. X_0 represents the total mass thickness a particle has to pass trough to reach the ground.

quantity	definition	value
M	mean molecular mass of dry air	$4.808 \times 10^{-23}\,\mathrm{g}$
T_0	temperature at ground level	$2.8815 \times 10^{2}\,\mathrm{K}$
P_0	pressure at ground level	$1.01325 \times 10^{5}\,\mathrm{Pa}$
ρ_0	density at ground level	$1.2250 \times 10^{-3}\,\mathrm{g\,cm^{-3}}$
h_0	scale height	$8.44\,\mathrm{km}$
X_0	vertical depth at ground level	$1033.60\,\mathrm{g\,cm^{-2}}$

Table 2.1: Numerical values for the isothermal-barotropic model, Eq. 2.3-2.7. Values from M to ρ_0 are taken from the U.S. standard atmosphere model (NASA, 1976). h_0 and X_0 are computed using Eq. 2.5 and 2.7 from the other values.

2.1.2 Air Showers as n-ary Trees

An iterative scheme representing the EAS as a simple binary tree was introduced by Carlson and Oppenheimer (1937) to get an order-of-magnitude estimate of the particle content for an EM shower. It is today commonly referred to as Heitler model (Heitler, 1944) and its extension to the hadronic case is due to Matthews (2005). We will describe the general n-ary tree (or Heitler-Matthews) model as it derives salient features of the showers without solving the system of differential equations in Eq. 2.2. The basic assumptions (**A.1**-**A.3**, valid both for the EM and the hadronic case) are:

A.1 the atmosphere is divided in layers of constant mass thickness $x = \ln 2\, \lambda_i$ where λ_i is a characteristic interaction length related to the particle leading the development of the shower;

A.2 the shower is represented as an n-ary tree: after the atmospheric layer k is traversed each branch of the tree (representing a particle) splits into n daughter branches (or particles), each carrying a fraction n of the mother particle energy $E_k = E_{k-1}/n$. If E_0 is the energy of the primary starting the cascade, at the stage k each daughter particle will carry an energy E_0/n^k;

A.3 the development of the shower ceases at the layer $k_{\max}$, where the energy in the individual particles ($n^{k_{\max}}$, at this stage) becomes equals to a critical energy E_i^c below which further multiplication is not possible

$$\frac{E_0}{n^{k_{\max}}} = E_i^c \Rightarrow k_{\max} = \frac{\ln(E_0/E_i^c)}{\ln n}. \tag{2.8}$$

Using these assumptions it is possible to derive two essential shower features (**F.1**-**F.2**), confirmed by MC simulations. If E_0 is the energy of the primary:

F.1 E_0 is linear in the total number of particle in the shower;

F.2 the vertical depth where the EM component (photons and electrons) reaches its maximum size, labelled as $X_{\max}$, is logarithmically proportional to E_0.

The n-ary tree model does not provide information for the shower after the maximum development is reached.

Electromagnetic Case: Binary Tree

In the EM case (shower initiated by a photon or electron) the shower can be represented as a binary tree: $n = 2$. After each atmospheric layer is traversed the particle number is doubled: a photon will create an $e^{\pm}$ pair while an electron will traverse the layer radiating a bremsstrahlung photon. The binary tree development is sketched in Figure 2.1a. In this simplified model we assume equal the radiation lengths for the two processes (neglecting the factor $\lambda_{\text{pair}} = 9/7\, \lambda_{\text{brems}}$ relating them, cf. Section 2.7.3 in Leo 1994). The thickness of the atmospheric layer in **A.1** is $\ln 2\, \lambda_e$, with $\lambda_e = \lambda_{\text{pair}} = \lambda_{\text{brems}} = 37\,\text{g}\,\text{cm}^{-2}$ in air. In the regime dominated by radiative losses, the energy of an electron degrades exponentially: $E(X) = E_0 \exp(-X/\lambda_{\text{brems}})$; hence, the factor $\ln 2$ in the atmospheric layer thickness (**A.1**) is chosen to halve the energy of the electrons at each layer $E(X = \ln 2\, \lambda_{\text{brems}}) = E_0/2$. Similarly, after pair production,

each member of the $e^{\pm}$ pair carries also half of photon energy. Henceforth we can reasonably assume that after each splitting (due to bremsstrahlung or pair production indistinctly) each daughter particle (electrons or photons indistinctly) will carry half of the mother particle energy, $E_k = E_{k-1}/2$ (as per **A.2**). The multiplication ceases when the electrons energy reaches the critical value $E_e^{\rm c} = 85\,\text{MeV}$, below which energy losses via ionisations dominates over the ones via bremsstrahlung. When the EM multiplication ceases the maximum particle content is reached: $N_{\max} = 2^{k_{\max}}$, with $k_{\max} = \ln(E_0/E_e^{\rm c})/\ln 2$, directly from Eq. 2.8. The total energy content of an EM shower can be formulated as

$$E_0 = N_{\max} E_e^{\rm c}. \tag{2.9}$$

And the linear dependence in **F.1** is derived. Labelling as $X_{\max}$ the vertical depth at which the number of photons and electrons of a shower reaches its maximum, one obtains

$$X_{\max}^{\gamma} = k_{\max} \ln 2\, \lambda_e = \lambda_e \ln\left(\frac{E_0}{E_e^{\rm c}}\right), \tag{2.10}$$

deriving in this way the second shower feature, **F.2**. The superscript γ indicates this is the height of maximum content for an EM shower. The binary-tree model overestimates the number of electrons: $N_e = 2/3\,N$ (with N total number of particle). Since multiple bremsstrahlung photons are radiated at each multiplicative stage and many electrons undergo collision losses and abandon the shower, a corrective factor $g = 10$ as in Matthews (2005) has to be applied

$$N_e = \frac{1}{g} N_{\max} = \frac{1}{g}\frac{E_0}{E_e^{\rm c}}. \tag{2.11}$$

Hadronic Case

In case of showers initiated by hadrons the cascade development is driven by pions produced in strong interactions. We adopt for the thickness of the atmospheric layers in **A.1** an interaction length approximately constant for strongly interacting particles (i.e. for protons and pions indistinctly) that we will refer to as λ_π. The multiplicity of the shower splitting in this case is the number of hadrons produced in each strong interaction: $n_{\rm h}$. A sketch of a n-ary tree initiated by a proton is given in Figure 2.1b. After the first interaction, $k = 1$, the proton produces n_h hadrons. For this simplified model only pion production is assumed in strong interactions, with the following proportion: $n_{\rm ch} = 2/3\,n_h$ charged and $1/3\,n_h = 1/2\,n_{\rm ch}$ neutral. Each $\pi^{\pm}$ will further produce n_h pions after traversing another atmospheric layer, $k = 2$, while π^0 will immediately ($\tau_{\pi_0} \sim 10^{-18}\,\text{s}$) decay in two photons, starting two EM cascades. The critical energy for which the cascade growth stops is $E_\pi^{\rm c}$, reached when the decay length for charged pions (dependent on their Lorentz factor γ, cfr. Section 2.1) becomes smaller than the thickness of the atmospheric layers: $d_{\pi^\pm} < \ln 2\,\lambda_\pi$. The numerical values we will use: $\lambda_\pi = 120\,\text{g}\,\text{cm}^{-2}$, $n_{\rm ch} = 10$ and $E_\pi^{\rm c} = 20\,\text{GeV}$, are obtained in Matthews (2005) and are tuned to represent CR air showers in the knee region, $E_0 = 10^{14} - 10^{17}\,\text{eV}$. At the layer $k_{\max}$ all the charged pions decay in flight into muons before traversing another layer and interacting again. The fraction of the primary energy devolved to hadronic

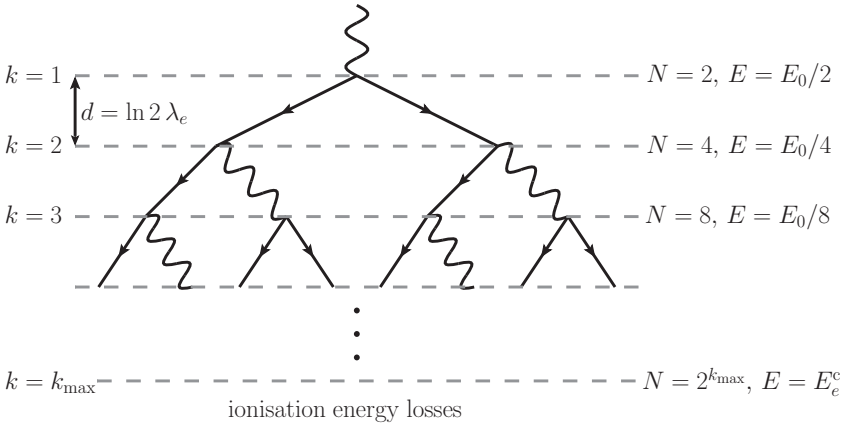

(a) EM air shower initiated by a photon as a binary tree process. After traversing a layer of mass thickness $\ln 2\,\lambda_e$, $k = 1$, a photon produces an $e^{\pm}$ pair. After traversing another atmospheric layer, $k = 2$, the secondary electrons radiate bremsstrahlung photon and the total number of particles is doubled, $N = 4$. The binary splitting continues until the layer $k = k_{\max}$ where the energy in the individual particle equals the critical energy E_e^{c}, below which ionisation energy losses becomes dominant. Further radiation of bremsstrahlung photons is suppressed and the cascading stops.

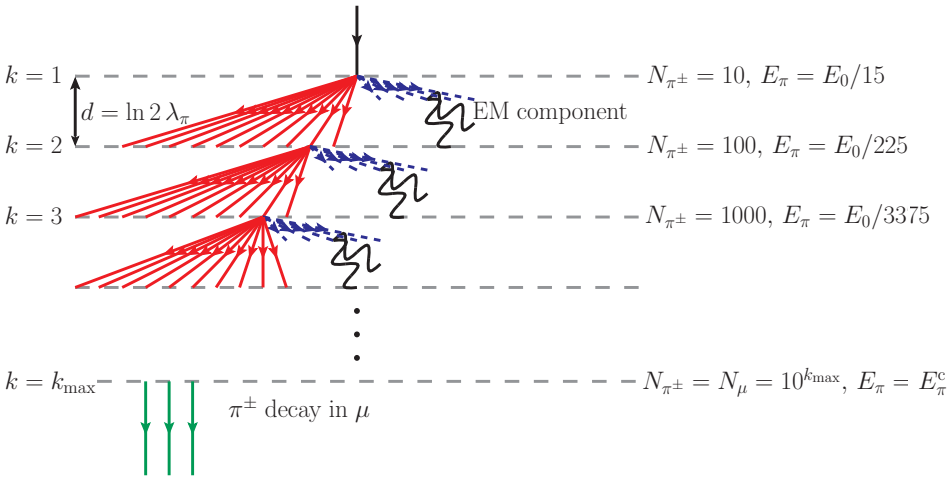

(b) Hadronic air shower initiated by a proton as a n-ary tree process. After traversing a layer of mass thickness $\ln 2\,\lambda_\pi$, $k = 1$, a proton produces n_{h} hadrons: $n_{ch} = 10$ charged pions (in red) and $n_{ch}/2 = 5$ neutral pions (in blue). After traversing another atmospheric layer, $k = 2$, the secondary $\pi^\pm$ generate $3/2\,n_{\mathrm{ch}} = 15$ more hadrons, while the π_0 immediately decay and start two EM cascades each. The multiplication ceases at the layer $k_{\max}$ where the energy of the individual hadrons reaches the critical energy E_π^{c} at which the decay length $d_{\pi^\pm}$ is smaller than the atmospheric layer thickness. Pions decay into muons and no further pion production via strong interactions is possible. A muon component (in green) replaces the charged pion and the shower fades out.

Figure 2.1: Schematic view of EAS as n-ary tree processes.

processes can be expressed as $N_{\pi^\pm} E_\pi^c = N_\mu E_\pi^c$. On the other hand, identifying with $N_{\max}$ the total number of $e^\pm$ and γ in the shower, the fraction of primary energy devolved to EM processes is $N_{\max} E_e^c$. We can write the energy conservation for the hadronic EAS, similar to Eq. 2.9, as

$$E_0 = N_{\max} E_e^c + N_\mu E_\pi^c = g E_e^c \left(N_e + \frac{E_\pi^c}{g E_e^c} N_\mu \right) \approx 0.85\,\text{GeV}\,(N_e + 24\,N_\mu). \tag{2.12}$$

In the hadronic case the primary energy is a linear combination of the number of muons and electrons in the shower. **F.1** is derived again and a direct estimate of the primary energy can be obtained by a particle detector able to measure the μ and $e^\pm$ produced by an EAS. A peculiar feature of the hadronic case is the presence of a muon component. The total number of μ can be estimated from Eq. 2.8

$$\ln N_\mu = \ln N_{\pi^\pm} = \ln \left((n_{\text{ch}})^{k_{\max}} \right) = \frac{\ln (n_{\text{ch}})}{\ln \left(\frac{3}{2} n_{\text{ch}} \right)} \ln \left(\frac{E_0}{E_\pi^c} \right) \Rightarrow N_\mu = \left(\frac{E_0}{E_\pi^c} \right)^\beta, \tag{2.13}$$

with $\beta = \ln(n_{\text{ch}}) / \ln(3/2\, n_{\text{ch}})$. The EM cascading component starts immediately after the first interaction, as shown in Figure 2.1b. The vertical depth at which the EM component of the shower reaches its maximum can be computed considering an EM shower that starts after the first layer ($\ln 2\, \lambda_\pi$), with energy $E_0/(3n_{\text{ch}})$

$$X_{\max}^p = \ln 2\, \lambda_\pi + \ln \left(\frac{E_0}{3 n_{\text{ch}} E_e^c} \right) \lambda_e, \tag{2.14}$$

where the superscript p indicates this time the shower has been started by a proton. **F.2** is derived again.

2.1.3 Longitudinal Development, EM Case

Despite remarkably obtaining the main shower features (particle content and height of the EM component maximum), the Heitler model has a very simplistic description of the longitudinal development (along the shower axis): a simple geometric progression (or power-law) growth. In the EM case Greisen (1956) derived a parametrisation for the number of electrons as a function of the atmospheric depth, based on the solutions of Eq. 2.2 under *Approximation B*

$$N_e^\gamma(X) = \frac{0.31}{\sqrt{\ln(E_0/E_e^c)}} \exp \left[\left(1 - \frac{3}{2} s \right) \frac{X}{\lambda_e} \right] \tag{2.15}$$

introducing the parameter *shower age*, s[II], often defined as

$$s = \frac{3X}{X + 2X_{\max}^\gamma}. \tag{2.16}$$

The Greisen parametrisation is plotted in Figure 2.2 for gamma-ray primaries within the VHE regime. Showers of the same age sit at the same point of their relative development, e.g. $s = 0$ at the beginning

[II] The concept of age introduced in the literature the concept of *universality* since numerous simulations have resulted in shower features parametrisable as a function of s, independently of the primary energy or of the composition (Nerling et al., 2006). Lipari (2009) mathematically clarifies the age definition, elegantly reconnecting to the work of Rossi and Greisen (1941).

of the shower, $s = 1$ at its maximum, $s > 1$ after multiplication has ceased. The loci of constant s are connected by golden lines in Figure 2.2. The figure also shows how the Heitler model, despite failing to reproduce the longitudinal development, correctly predicts the position of the shower maximum and reasonably approximate the maximum N_e. Ground based gamma-ray observatories are typically located at altitude of $\sim 2\,\mathrm{km}$, well below the maximum of the showers initiated by TeV gamma rays, seemingly occurring around 8 km.

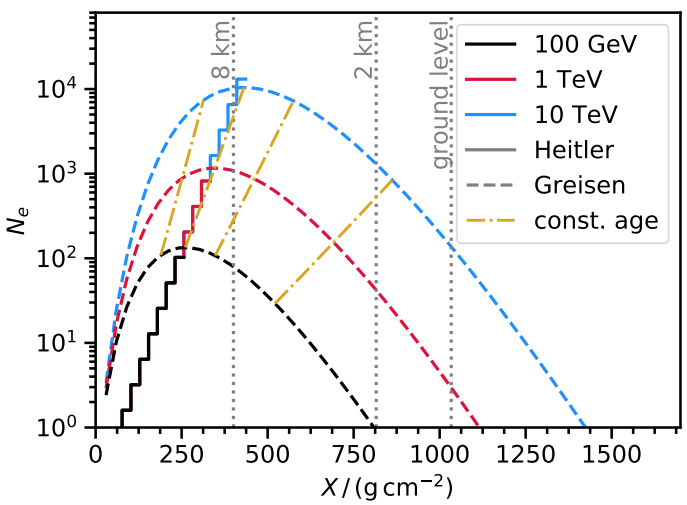

Figure 2.2: Greisen parametrisation for EM air showers with $E = 100\,\mathrm{GeV}, 1\,\mathrm{TeV}, 10\,\mathrm{TeV}$ (dashed lines). The Loci of constant age $s = 0.8, 1.0, 1.2, 1.5$ are connected by dot-dashed golden lines. The simple power-law growth 2^k of the Heitler model, corrected by the factor g in Eq. 2.11, is displayed with the solid line steps: despite oversimplifying the longitudinal development, it returns correctly the shower maximum position and approximately the total electron content. The conversion between vertical atmospheric depths and altitudes are obtained with Eq. 2.7.

2.1.4 Differences between Gamma-Ray and Hadronic Air Showers

After having collected some quantitative informations on the shower features and development, in this section we draw some qualitative differences commenting on EAS simulations. EAS are nowadays studied via Monte Carlo (MC) methods, with programs able to follow the path of the particles in the atmosphere accounting not only for interactions, decay and energy losses but also for secondary effect such as particle deflection in Earth's geomagnetic field. The COsmic Ray SImulations for KAscade[III] (CORSIKA), originally created for the KASCADE CR experiment (Heck et al., 1998), is nowadays vastly used in several astroparticle disciplines. We will use Figure 2.3, representing simulations from de Naurois and Mazin (2015) of showers initiated by sub-TeV gamma rays and protons, and the results of Section 2.1.2 to infer the main differences between the EM and hadronic cases:

D.1 *lateral spread.* The transverse momentum characterising hadronic interactions ($p_\mathrm{T} \sim 400\,\mathrm{MeV}$, Gaisser et al. 2016) results in a major lateral spread of the order of $\sim$ km for the hadronic case. EM cascades are spread only by Coulomb scattering of electrons and are contained within a Moliere radius (Leo, 1994) of $r_1 = 9.3\,\mathrm{g\,cm^{-2}}$, corresponding to 80 m at sea level and 200 m, at shower maximum;

[III] https://www.ikp.kit.edu/corsika/70.php

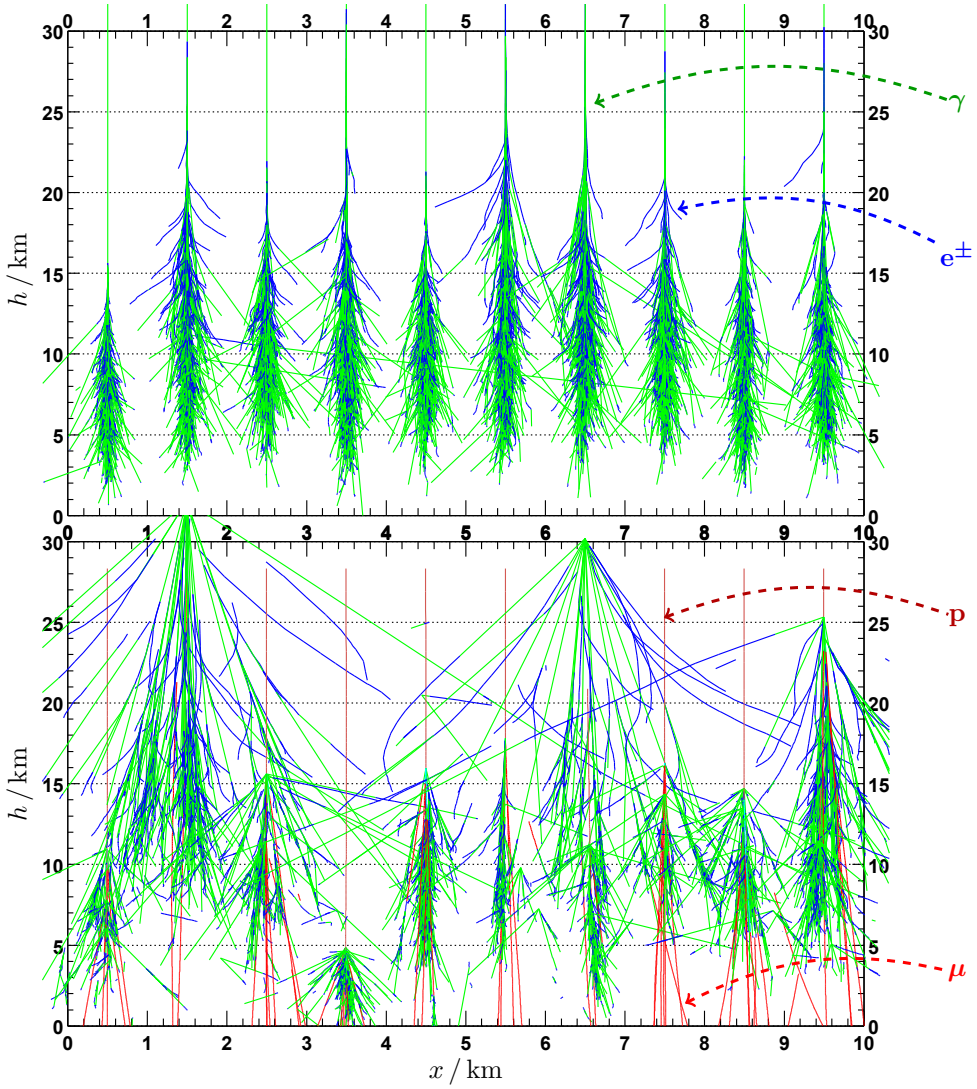

Figure 2.3: MC simulations of air showers from de Naurois and Mazin (2015). The upper panel displays 10 realisations of an air shower triggered by a gamma-ray of 300 GeV. Green lines track the path of photons, blue lines that of electrons. The bottom panel displays 10 realisations of hadronic air showers for a primary of 300 GeV energy. Dark red lines track protons path in the atmosphere and light red lines that of muons. While the proton EAS developement fluctuates from a realisation to the other, EM air showers are in comparison remarkably uniform and contained in a cylinder of height 20 km and radius $200 - 300$ m.

D.2 *penetration.* Hadronic air showers develop deeper in the atmosphere. This can be ascribed to the fact that $\lambda_\pi > \lambda_e$, i.e. a larger mass thickness have to be traversed for an hadronic interaction to happen. Other than few fluctuations, we can see in the bottom panel of Figure 2.3 that most of the proton initiated showers start below 15 km;

D.3 *muon content.* In the simple Heitler-Matthews model we have assumed that there is no muon production in EM showers and we derived Eq. 2.13 to predict the number of muons in the hadronic case. The cross-section for the $\gamma \to 2\mu$ production (Braibant et al., 2012) is low but non zero for TeV photons. Hillas (1996) quotes a factor 30 lower μ content in the EM case;

D.4 *shower to shower fluctuations.* Hadronic showers are composed by several EM sub-showers generated by π_0. Their development is less homogenous and fluctuates from a case to the other.

After discussing Cherenkov radiation in the next section, we will recall **D.1**-**D.4** to underline differences in Cherenkov emission from hadronic and EM showers and to introduce an efficient method of signal / background discrimination through their images.

2.2 Atmospheric Cherenkov Radiation

A charged particle moving through a dieletric medium induces a transient polarisation on the medium molecules. The wavelets of the EM dipole transitions generated by the molecules returning to their initial state can interfere constructively if the particle has a velocity $v = \beta c$, higher than the phase velocity of light in the medium c/n, with n index of refraction. A wavefront subtending an angle θ_c is formed under the coherence requirement

$$\cos\theta_c = \frac{c/n}{v} = \frac{1}{\beta n}. \tag{2.17}$$

The conical wavefront generated by such an effect, named after Čerenkov (1937) (adapted in English to Cherenkov), is displayed in Figure 2.4. From Eq. 2.17 we can immediately derive: the threshold velocity to have Cherenkov emission: $\beta_{\text{th}} = 1/n$; the maximum aperture angle of the cone $\theta_{c,\,\max} = \arccos(1/n)$. The refraction index is a function of the atmospheric variables, most noticeably of the pressure. Holding the isothermal barotropic atmosphere hypothesis introduced in Section 2.1.1, Boley (1964) expresses the index of refraction as

$$n = 1 + \eta; \quad \eta \ll 1, \tag{2.18}$$

and give an exponential scale with h_0 also to η

$$\eta(h) = 0.00029 \exp(-h/h_0). \tag{2.19}$$

At ground level $n = 1.00029$, and $\theta_{c,\,\max} = 1.3°$. The threshold Lorentz factor to emit Cherenkov radiation at ground level is $\gamma_{\text{th}} \approx 42$, corresponding to: an electron of ≈ 21 MeV, a muon of ≈ 4.4 GeV and a proton of ≈ 39 GeV. The energy $\mathrm{d}E$ radiated via Cherenkov effect per unit path $\mathrm{d}l$ (Jackson, 1999),

can be expressed in cgs units (erg / cm) as

$$\frac{\mathrm{d}E}{\mathrm{d}l} = \left(\frac{ze}{c}\right)^2 \int_{\beta^2 n^2(\omega)>1} \left(1 - \frac{1}{\beta^2 n^2(\omega)}\right) \omega \mathrm{d}\omega, \tag{2.20}$$

where ze is the particle charge expressed in multiples z of the elementary charge e.Eq. 2.20 formulates the spectral distribution of the Cherenkov radiation in terms of the angular frequency ω. Since $\frac{\mathrm{d}^2E}{\mathrm{d}\hbar\mathrm{d}\omega} \propto \omega$, it follows that $\frac{\mathrm{d}^2E}{\mathrm{d}\hbar\mathrm{d}\lambda} \propto \lambda^{-3}$ and the number of photons emitted per unit path, per unit wavelenght $\mathrm{d}\lambda$ will be $\frac{\mathrm{d}^2N_{\mathrm{ph}}}{\mathrm{d}l\mathrm{d}\lambda} \propto \lambda^{-2}$. Considering n constant over the visible spectrum ($\lambda_1 = 400\,\mathrm{nm}$, $\lambda_2 = 700\,\mathrm{nm}$), we can obtain the number of Cherenkov photons radiated by an electron ($z = 1$) per unit path as

$$\frac{\mathrm{d}N_{\mathrm{ph}}}{\mathrm{d}l} = 2\pi\alpha \left(1 - \frac{1}{\beta^2 n^2}\right) \int_{\lambda_1}^{\lambda_2} \frac{1}{\lambda^2} \mathrm{d}\lambda = 2\pi\alpha \sin^2\theta_{\mathrm{c}} \left(\frac{1}{\lambda_1} - \frac{1}{\lambda_2}\right), \tag{2.21}$$

where $\alpha = e^2/(\hbar c)$ is the fine-structure constant and $\hbar$ the Planck constant divided by 2π. Considering a maximum emission angle of $\theta_{\mathrm{c,\,max}} = 1.3°$, we obtain $\mathrm{d}N_{\mathrm{ph}}/\mathrm{d}l = 0.3$ photons cm^{-1} or $\approx 10^4$ photons / radiation length. Both Boley (1964) and Greisen (1960) estimates that $\sim 4\times 10^5$ Cherenkov photons are produced by an electron reaching ground level. If we were to compute $\mathrm{d}E/\mathrm{d}l$ from Eq. 2.20 we would obtain an energy loss of 0.7 eV/cm (Boley, 1964), negligible compared to the electron energy losses by ionisation (Tanabashi et al., 2018) and therefore not affecting the shower development. Given the λ^{-2} dependency of $\frac{\mathrm{d}^2N_{\mathrm{ph}}}{\mathrm{d}l\mathrm{d}\lambda}$, the Cherenkov spectrum will peak at lower frequencies. Scattering on air molecules and particulate matters (referred ot as aerosol) in Earth's atmosphere, and absorption by Ozone, will cause a peak in the spectrum at $\lambda = 330\,\mathrm{nm}$ at an altitude around 2000 m (cf. Figure 3.9 in Wagner 2006).

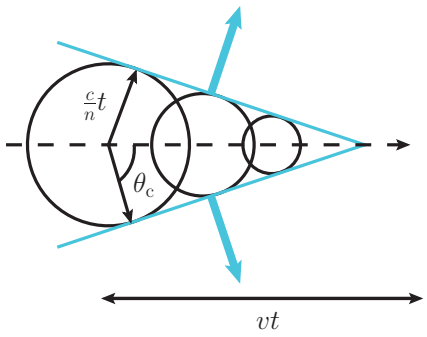

Figure 2.4: A relativistic particle (dashed path) with velocity higher than the phase velocity of light in the medium, $v = \beta c > c/n$, induces polarisation that in turns generates dipole transition EM waves (black circles) interfering constructively to form a wavefront at angle θ_{c} (indicated in light blue). Adapted from Leo (1994).

2.2.1 Cherenkov Radiation from Air Showers

The total number of Cherenkov photons produced by an EAS can be written as (Grieder, 2010)

$$Q = \int_{E_{\mathrm{th}}}^{E_0} \mathrm{d}E \int_0^{X_0} \mathrm{d}X\; N_e(X, E; E_0)\, \frac{\mathrm{d}N_{\mathrm{ph}}}{\mathrm{d}X}, \tag{2.22}$$

where $E_{\rm th}$ is the energy threshold for Cherenkov emission, $N_e(X, E; E_0)$ is the number of electrons as a function of the energy and the vertical depth and $\mathrm{d}N_{\rm ph}/\mathrm{d}X$ is the number of photons emitted per radiation length. An approximate estimate can be obtained fixing $\mathrm{d}N_{\rm ph}/\mathrm{d}X$ to the value of $\approx 10^4$ photons / radiation length (value at ground level) and simplifying the integration in energy considering that both Greisen (1960) and Grieder (2010) report that, averaged over the whole shower, 40% of the electrons have energy greater than $E_{\rm th}$. Eq. 2.22 simplifies to

$$Q \approx 4000 \int_0^{X_0} N_e(X)\mathrm{d}X, \tag{2.23}$$

where the integral represents the total electron content of the shower. Remembering that for the Heitler model the latter is proportional to E_0 (cf. Eq. 2.11, **F.1**), we have thus found in Eq. 2.23 a *calorimetric relation*: the total Cherenkov flux of an air shower is proportional to its electron content, that is in turn linear in the primary energy.

Hillas (1996) ascribes the Cherenkov light at detector level to three shower components in case of a TeV gamma ray primary:

- 25% of the light is produced by particles above 10 km. The refraction index increase at lower altitudes and so does the opening angle $\theta_{\rm c}$. A focused annulus (or ring) of light, with radius 120 m, is formed at the the detector level. The effect is sketched in Figure 2.5: blue lines represents the Cherenkov cone opening in case of a single particle. For light emitted at lower heights, given the proximity of the ground, the higher opening angle does not add up to the annulus but touches the ground close to the shower axis;

- 50% of the emission, due to the shower core near its maximum, is contained in a cylinder of radius 21 m and height 4 km, with centre at 8 km (shower maximum). This area, sketched as a light blue filled rectangle in Figure 2.5, approximates an ideal calorimeter because the light it contains gives the beast measure of the energy. If we were to observe such a cylinder form an observatory at 2 km altitude (hence 6 km below the maximum) the lateral spread of the light would be seen under an angle of 0.2°. In case of a proton initiated air shower the major lateral spread discussed in **D.1** will result in a larger light-cylinder of 71 m radius (contour dashed in red in Figure 2.5), that will be seen under an angle of 0.75° at the observatory;

- the remaining 25% comes from individual particles radiating below 6 km. Measuring the intensity of the light these particle will produce local isolated peaks near the shower axis.

The bottom part of Figure 2.5 also outlines the flux of Cherenkov photons (green lines) in a detector, as a function of the distance from the shower axis. In absence of scattering all the particles would travel perpendicularly to the ground and a sharp increase of the flux due to the annulus would appear at 120 m (dashed green line). Accounting for particle scattering the intensity transition will be smoother but nonetheless the annulus would be recognisable through a shoulder in the flux at 120 m. Within 100 m the photon density is almost flat hence the calorimetric response is still linear and measurement of the

primary energy is reliable. The plateau will be lost in case of a penetrating shower either due to a proton or to a very energetic, $\sim 100\,\mathrm{TeV}$, gamma ray primary.

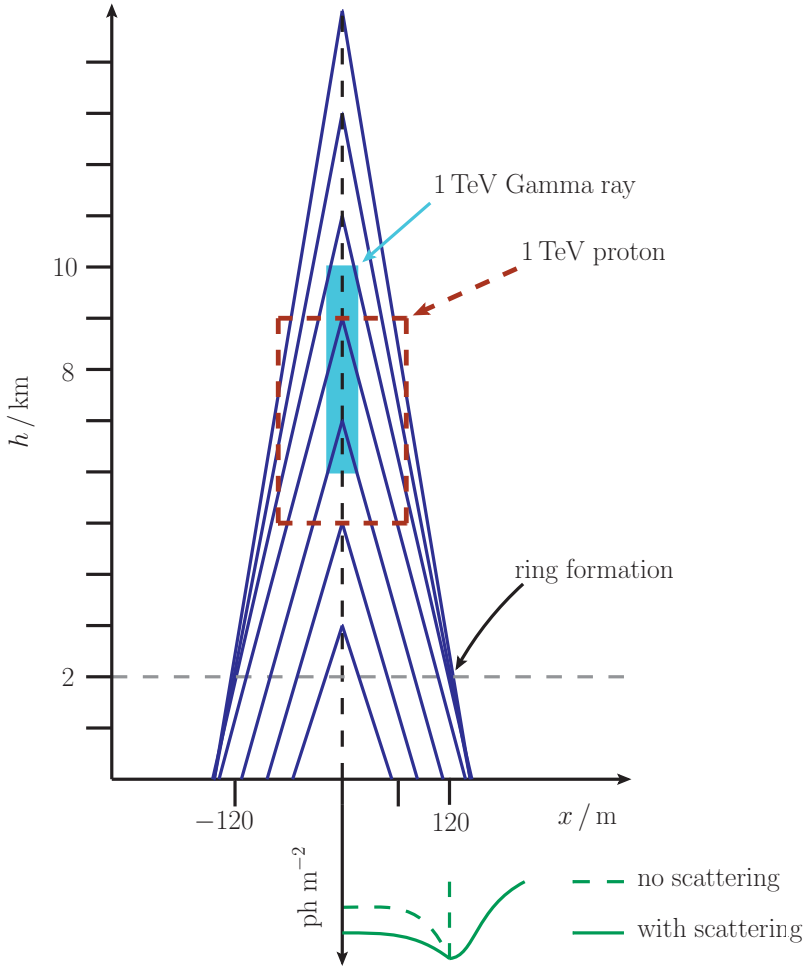

Figure 2.5: Hillas (1996) schematisation of an air shower Cherenkov emission. For particles with $h > 10\,\mathrm{km}$ the increase of n and θ_c results in an annulus formed at ground, containing 25% of the total light. 50% of the emission come from a cylinder depicted with a full light blue box in case of a gamma ray primary and as a red dashed rectangle in case of a proton primary. The graph at the bottom of the plot shows the Cherenkov photon flux (photons per square meter, shown as a green line) as a function of the distance from the shower axis in a detector at 2 km altitude. If all the particles were to travel perpendicularly without scattering the annulus would produce a sharp rise after which the intensity would drop to zero (dashed green line). In real showers the scattering smooths the distribution without washing away the annulus contribution that appears as a flat peak, or a shoulder, at 120 m (solid green line). Adapted from Hillas (1996)

2.2.2 The Imaging Technique

The first-generation of Cherenkov atmospheric detectors represented essentially a single building unit of a modern imaging telescope. Galbraith and Jelley (1953), the first to detect light pulses associated with CRs, used a single PMT placed with the cathode at the focal point of a parabolic mirror with a diameter of 25 cm. Geiger counters surrounds the optical detector, to ensure the coincidence between the Cherenkov flashes and the charged component of the EAS. This simple setup was repeated in a small array by the group of Chudakov et al. (1960) with meter-sized mirrors, following the suggestion of Cocconi (1960) to search for point sources of gamma-ray showers in the isotropic CR showers background. Later in Chudakov et al. (1964) the same group reported about the monitoring of the rate of showers while selected radio sources (radio galaxies and supernovae) crossed the small 1° field of view (FoV) of the array:

no statistically significant excess of flashes around the supposed sources were found. The construction of a prototypical second-generation Cherenkov telescope was completed in 1968 at Mt. Hopkins in Arizona, at the Fred Lawrence Whipple observatory. Multiple hexagonal mirrors with spherical curvatures and adjustable position were arranged in a reflector of 10 m diameter. The number of PMTs sitting in the focal point was upgraded to two, few years after construction: one measuring the rates of showers while tracking a candidate source, the other, few degrees apart, measuring the background to be subtracted. The technique at this stage found mere hints of signal from the Crab nebula (Weekes et al., 1972; Fazio et al., 1972)[IV]. In Turver and Weekes (1981) a project of a camera with 37 PMTs was presented, envisioning that a pixelised camera could produce a discretised image of an air shower development through its Cherenkov light. The camera was realised and mounted in the focal point of the Whipple 10 m telescope. Hillas (1985) later elaborated a robust method to interpret the main features of such images to reject those produced by CR air showers, leading the Whipple 10 m group to the firm detection of the Crab nebula in Weekes et al. (1989).

Hillas Image Parametrisation

The distinguishable features of EM and hadronic air showers highlighted in Section 2.1.4 results in two different light patterns over a pixelised camera. Cherenkov light from EM showers results in regular elliptic shapes (cf. Figure 9 of Turver and Weekes 1981 and Section 4.8 of Rieke 1969) with minor axis of $\sim 0.2°$ (as explained in Section 2.2.1), the orientation and the symmetry depending on the relative geometry between the shower axis and the optical axis of the detector, as shown in Figure 2.6. A shower with an axis of development matching the optical axis of the telescope produces a circular light pattern in the centre of the camera (label 1 in Figure 2.6). A shower with axis parallel but shifted from the optical one illuminates an elliptical pattern with the ellipse major axis pointing to the source position (label 2 in Figure 2.6)[V]. A shower with axis not parallel and shifted from the optical one will produce an ellipse whose major axis does not intercept the camera centre (label 3 in Figure 2.6). Light patterns of hadronic air showers generally do not exhibit regular shapes (label 0 in Figure 2.6). The larger lateral spread, stated in **D.1**, induces trigger patterns as large as 1° (Section 2.2.1) composed of overlapping patches of light generated by the EM sub-showers, described in **D.4**, with additional pixels triggered by the Cherenkov emission of the muon component, described in **D.3**. Once the uniform illumination due to the night sky background (NSB) has been subtracted from the camera, the total shower information is reduced to charge and coordinates of a cluster of triggered pixels. Hillas (1985) combines them in few geometrical quantities representing an ellipse[VI], shown in Figure 2.7. *Length* and *width* represent the root mean square (RMS) spread of the light in direction parallel and perpendicular to the cluster major axis, respectively. The *centroid* (labelled C in Figure 2.7) is the centre of gravity (CoG) of the signals in the PMTs associated with the image; its *distance* from the centre of the field of view (or the source position

[IV] Vladimirsky et al. (1973) found in the same years hint of signal from Cygnus X-3 although using a first-generation detector.

[V] This ellipse is not always symmetric: labelling the distance at ground level between the optical axis and the shower axis as *impact*, a larger impact results in a light distribution skewed towards the camera centre (cf. Figure 10 of Turver and Weekes 1981).

[VI] For their exact calculation the interested reader is referred to section 6.1 of De Naurois (2012).

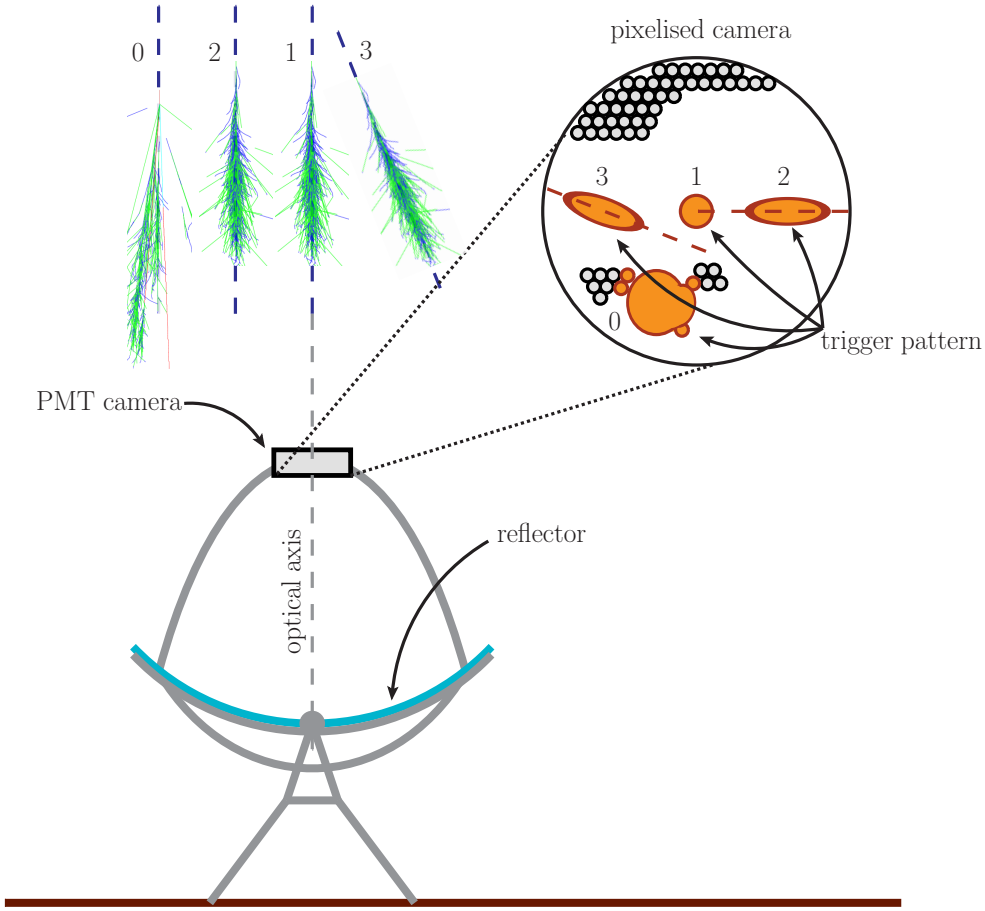

Figure 2.6: Schematisation of the imaging technique. A Cherenkov telescope essential components are a large reflector and a camera, sitting in its focal plane, assembled with several PMTs pixels. Cherenkov light from gamma-ray initiated showers induce regular elliptic light patterns (highlighted in orange) on the camera. If the axis of the shower development (dashed blue line) is aligned with the optical axis (1) a round light spot illuminates the camera. A shower with an axis parallel with the optical one (2) produces an elliptical shape whose major axis (dashed red line in the camera view) intercepts the camera centre. A misaligned shower axis (3) results in the major axis of the ellipse not intercepting the camera centre. A hadronic air shower (0) produces an irregular light pattern due to the different EM sub-showers and the Cherenkov light of the muons that trigger some of the pixels.

in the camera, S) is a measure of the *impact* parameter. *miss* and α, the perpendicular distance from S and the orientation of the main axis, respectively, are expected to be very small for real gamma-ray events coming from the source (the shower axis points back to the source position). A small *azwidth*, the RMS spread of the light in the direction orthogonal to the distance, incorporates the desiderata of a narrow image pointing to the source. The Whipple 10 m group in Weekes et al. (1989) achieved a 98% CR rejection efficiency using only a cut in azwidth (employing only images contained in the internal pixels). We will refer to image *size* to indicate the total charge content (in phe) of the cluster of pixels associated with the image.

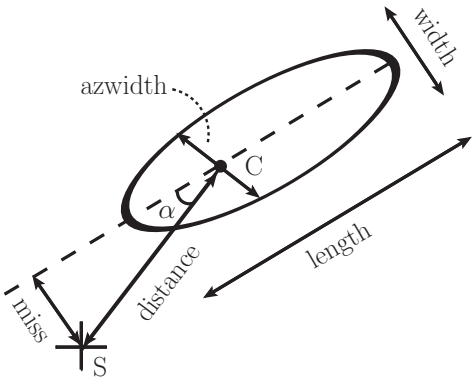

Figure 2.7: Hillas geometric parametrisation of Cherenkov images. Comparing the triggered PMTs pattern to an ellipse length and width are its major and minor axis, respectively. Given the centre of gravity of the image (C), small impact parameters results in small distances from the source position S. Gamma-ray showers pointing to the source are expected to have images with small angular (α) or orthogonal (miss) distances with respect ot the soruce position in the camera S. The spread of the light in the direction orthogonal to the distance, the azwidth, conjugate the information on the lateral developement and the axis orientation of a shower.

2.3 The Major Atmospheric Imaging Gamma-ray Cherenkov

2.3.1 History

The historical review of Hillas (2013) marks the birth of the third generation of Cherenkov instruments with the construction of the first stereoscopic system by the High-Energy-Gamma-Ray Astronomy (HEGRA, Pühlhofer et al. 2003) collaboration at the Observatorio del Roque de los Muchachos (ORM), 2200 m of altitude, on the Canary Island of La Palma. By 1998 the array of 5 telescopes with reflectors of 3.3 m diameter and 271 pixels cameras was completed. A stereoscopic system allows an improved direction reconstruction (the gamma ray direction can be obtained simply crossing the major axes of individual images), energy estimation and background rejection. Characteristic of a stereoscopic system is the suppression of the muon *local* triggers. An arc of a Cherenkov annulus generated by a muon can mimic a low energy event. Difficultly, though, the same ring can trigger two telescopes as far as 100 m apart. Therefore a trigger between more telescopes can cancel this background. As the original Whipple 10 m established the imaging technique, the HEGRA detectors[VII] realised the stereoscopic concept. The array was decommissioned in 2002, when the construction of its successor, the MAGIC telescope, started at the same site. Aiming at expanding the IACT energy reach (at the time starting at hundreds of GeV) down to the tens of GeV, MAGIC-I (M1 from now on, on the left in Figure 2.8) started operations in 2004

[VII] For HEGRA's main achievements the interested reader is referred to Hillas (2013) review.

(Baixeras et al., 2004). A pioneering instrument, MAGIC-I combined the largest reflector of the era, 17 m of diameter[VIII], with a light-weight structure of carbon fibre and aluminium (the structure supporting the reflector is assembled without any welding) allowing a fast movement of 180° in less than 20 s. One of the target science-case of MAGIC are Gamma-Ray Bursts (GRBs), where a fast re-pointing is essential in catching a gamma-ray emission that typically lasts few seconds. After 15 years of operation, such design proved to be successful as MAGIC detected the first GRB in VHE (Mirzoyan, 2019). Stereoscopic observations started in summer 2009 with the operation of a second telescope, upgraded clone of the first one, MAGIC-II (M2 from now on, on the centre of Figure 2.8). Stereoscopic performances using the Crab Nebula are assessed in Aleksić et al. (2012a). The last upgrade of the telescope, dated 2012, uniformed the outdated camera and readout system of M1 to the newer of M2. The current performance of the upgraded telescopes are reported in Aleksić et al. (2016a) and Aleksić et al. (2016b).

Figure 2.8: View of the MAGIC telescopes at the ORM. MAGIC-I on the left, MAGIC-II on the centre and the MAGIC data acquisition building with the orange roof, named counting house, on the right. The dome on top of the white tower attached to the counting house contains the MAGIC LIght Detection And Ranging system to measure the atmospheric transmission. The Gran Telescopio Canarias[IX]stands out in the background. Photo from https://magicold.mpp.mpg.de/gallery/index.html.

[VIII]The record was overcome in 2012 with the first light of the 28 m diameter H.E.S.S.-II telescope.
[IX]http://www.gtc.iac.es/

2.3.2 Hardware Components

In the following section we briefly examine the main hardware components of the actual MAGIC telescopes configuration, after the 2012 upgrade. Readers interested in a more detailed hardware description as well as in pre-upgrade specifics are referred to Aleksić et al. (2016a) and to Section 3.2 of Giavitto (2012) and Section 2.2 of López-Coto (2015).

Reflector

The tessellated *reflector* surface of both telescopes approximates a paraboloid, an isochronous surface. Therefore the arrival times of photons on the dish are conserved in the camera plane (residing in the focal point) and a smaller time window can be used to integrate the signal. The focal length f equals the dish diameter D, $f = D = 17\,\mathrm{m}$, and 247 squared tiles of $1\,\mathrm{m}^2$ compose the global reflector surface. Each tile is made of an aluminium alloy (AlMgSi), has a spherical surface curvature varying around 35 m and has a nominal Point Spread Function[X] (PSF) smaller than 10 mm. The different mirror solutions for M1 and M2 mirrors are given in Bastieri et al. (2005) and Bastieri et al. (2008), respectively. An active mirror control system (Biland et al., 2008) corrects the collective focus acting on the individual mirror position through step motors, counteracting the deformation of the light-weight support structure of the reflector (weighting only ~ 5.5 tons) during the telescope movement. The reflector is suspended by two lateral steel towers connected to a mount that allows azimuthal movement rotating over a circular rail.

Cameras

The PMTs and their electronics are enclosed by cylindrical aluminium containers of 1.46 m diameter and 0.81 m height. The total camera mass of 850 kg is sustained by an aluminium arc, stabilised by steel cables tied to the dish frame, holding the camera in the focal point of the reflector; the structure of the arc continues behind the reflector and is connected to another motor allowing for altitude movement. Each camera contains 1039 PMT pixels of 2.54 cm diameter, with 6 dynodes and quantum efficiency of 32% in the blue band. The high voltages (HVs) of the PMTs are set to obtain a moderate gain of 3×10^4. The PMT cathodes are coupled to light concentrators (Winston cones) with hexagonal outer windows and embedded in the dodecagonal arrangement shown in Figure 2.9; the Winston cones face a plexiglas window insulating the camera electronics from the outside and protected by closable lids. To achieve light-weight design and fast movement the trigger and the readout are separated from the PMTs electronics and are installed in a data acquisition (DAQ) building, named Counting House (CH, on the right of Figure 2.8). The analog signal of each PMT, after passing through a low-noise pre-amplifier, is converted into an optical signal by a vertical cavity surface emitting laser and travels, through 162 m optical fibre cables, to the CH.

[X] The optical PSF is defined as the 39% containment radius of the light spot generated by a point-like source in the focal point. The PSF of the single mirrors and of the global reflector is measured through star images acquired with a dedicated Charge-Coupled Device (CCD) camera located in the centre of the reflector.

Trigger and Data Acquisition

In the CH receiver boards (receivers) equipped with photodiodes convert back the optical signal from the individual PMTs to an electrical one that is split in a readout analog branch and in a digital trigger branch. The lowest level trigger, level 0 trigger (L0), is applied by the receivers: a digital 1 is issued if the amplitude of the pixel signal is above a (programmable) discriminator threshold (DT) for a (programmable) minimum time. The L0 rate is $\sim 800\,\mathrm{kHz}$ with the DT typically set to $\sim 5\,\mathrm{phe}$. Cherenkov flashes trigger small regions of pixels in a few ns time window; the next level trigger, dubbed L1, searches for n Next Neighbour (NN) pixels with a L0 signal, within a gate of $8 - 9\,\mathrm{ns}$. For stereo observations a 3NN multiplicity is used (i.e. a pixel above threshold has to be in contact with at least two others). L1 operates on 19 overlapping cells of 37 PMTs each, highlighted in light blue in Figure 2.9, at a typical rate of $\sim 15\,\mathrm{kHz}$. A logical OR of all the 19 macrocells of each telescope is sent to the stereoscopic trigger, dubbed level 3 (L3). The latter searches for a coincidence between these two signals after having stretched them to 100 ns width and delayed them according to the respective telescope pointing (the distance between the focal planes changes with the pointing and so does the arrival times of the shower photons to each telescope). L3 activates the individual telescope readout at a rate of $250 - 350\,\mathrm{Hz}$.

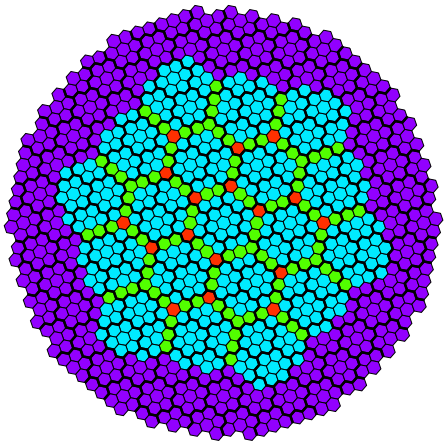

Figure 2.9: The 1039 PMTs in the MAGIC cameras are arranged, through the hexagonal window of their light collectors, in a dodecagonal shape. The level 1 trigger, searching for compact groups of pixels with amplitude above threshold in a few ns time window, operates in 19 overlapping macrocells of 37 pixels each, higlighted in light blue. Pixels belonging to two macrocells are filled in green, pixels belonging to three macrocells in red. Figure from Aleksić et al. (2016a).

The core of the MAGIC readout system is the Domino Ring Sampler chip version 4 (DRS4, specifics can be found in Sitarek et al. 2013 and Bitossi et al. 2016). The DRS4 is an analogue memory realised via a ring buffer of 1024 switching capacitors. The sampling frequency is tuned at 1.64 GSample/s, in the event of a trigger, the capacitors value are digitised at a lower speed by a 14-bit analogue to digital converter (ADC).[XI] The chip allows to select only a small Region of Interest (RoI) of 50 capacitors to be digitised (i.e. a sampling window of 30 ns), thus reducing the dead time to $26\,\mu\mathrm{s}$. The readout is organised in 12 boards per telescope, each hosting 4 mezzanines with 3 DRS4 chips each. The 8 input channels per chip grant 1152 readable channels, covering all the pixels. A dedicated DAQ computer per each telescope administrates, through a multi-thread `C++` program, the reading, on-line analysis and storage of the data

[XI] A pedestal run with closed lids and HV on is taken at the beginning of the night to estimate the mean ADC offset of each capacitor.

from the boards.

Auxiliary Subsystem

Beside the aforementioned main components of an IACT, there are a number of additional subsystem ensuring MAGIC safe operations and correct data taking:

- *drive monitoring*: the tracking of a source, possible with a precision of $\sim 0.02\,^{\circ}$, is calibrated and monitored by two CCD cameras in the centre of the reflector. The first one, in dedicated operations, takes pictures of stars spanning all the movable range in Zenith and Azimuth by the telescope. These images are processed to build a bending model of the overall structure. The second camera monitors the telescope tracking in normal operations: it compares continuously the position of the camera, signalled by a ring of Light Emitting Diodes (LED) at the edge of the camera, with the position of fixed stars;

- a *calibration system* installed in the centre of the reflector uniformly illuminates the whole camera trough laser pulses with $\lambda = 355\,\mathrm{nm}$ and $\sim 0.5\,\mathrm{ns}$ duration; the intensity can be set from 1 to 10^3 phe. Besides a dedicated calibration run before each new pointing of the telescope, the calibration system fires at a regular frequency of 25 Hz. A controlled illumination of the camera allows: to adjust the HV settings of each PMTs to obtain a uniform gain; to obtain a conversion factor between ADC counts and phe; to calibrate the signal arrival time in the DRS4 chip (different positions in the ring buffer introduce delays with a spread of $1 - 4\,\mathrm{ns}$ on the readout signal);

- the *atmosphere and weather monitoring* is distributed over several instruments. Two instruments measure the atmospheric transmission, assessing the data quality. A pyrometer, mounted in the dish of M1, measures the sky temperatures in the pointing direction. If clouds are present, they reflect thermal radiation from Earth and an increase in the sky temperature is detected. A more refined transmission measurement is given by a LIght Detection And Ranging (LIDAR, Fruck et al. 2014). The MAGIC LIDAR is equipped with a laser firing light pulses up in the atmosphere and a photo detector allowing to measure the arrival time of the same light pulses backscattered by clouds and aerosols, thus inferring the transmission at different heights. A weather station installed on the roof of the CH measures temperature, pressure, humidity and wind speed every second, monitoring their compliance with safe operational requirements.

All the telescopes subsystems are orchestrated by a Central Control program (CC, cfr. Section 2.4 of Zanin 2011) equipped with a graphic interface used by the operators. The CC discipline each subsystem and receives reports on their status every 1 s.

Online Subsystems

The CH hosts several machines linking the telescope operations to the world outside the observatory and taking care of the data reduction and transfer:

- a *GRB monitoring alert system* (Berti et al., 2017) receives alerts from the Gamma-ray Coordinates Network[XII] (GCN). In case safe observational conditions are met the system is allowed to take control of the telescopes, automatically pointing and starting data acquisition;
- a *MAGIC Online Analysis* program (Tescaro et al., 2014) performs a real-time event reconstruction producing a first estimate of the observed source significance and flux, allowing the observers and schedulers to extend observations or to issue monitoring alerts towards other observatories;
- an *On Site Analysis* routine (Oya et al., 2010) starts with the data taking and reduces the data while they are produced. Raw and processed data are then transferred to an external cluster (the Port d'Informació Científica in Barcelona) after the observations are closed in the morning. Usually within few hours after the end of the observation high-level product are ready to be analysed.

2.3.3 Data Taking

The performance of an IACT varies with the observing conditions: zenith angle[XIII], atmosphere quality, the NSB level. These conditions can change in matter of minutes, data are usually collected in chunks of $\sim 20\,\mathrm{min}$ of stable acquisition, referred to as *runs*.

Duty Cycle

Dark moonless nights amount to a total of $\sim 1600\,\mathrm{h}$ / year. The moderate gain of the camera PMTs allows observations under moon conditions with NSB levels 12 times higher than in moonless night (for which the NSB is estimated to have a flux of $(2.3 \pm 0.15) \times 10^{12}\,\mathrm{m^{-2}\,s^{-1}\,sr^{-1}}$ between 300 and 600 nm by Mirzoyan and Lorenz 1994, we refer to it as $\mathrm{NSB_{dark}}$). Reducing the PMTs gain stretches the observational limit up to $20 \times \mathrm{NSB_{dark}}$, applying moon filters further to $100 \times \mathrm{NSB_{dark}}$. Moon operations extends the MAGIC duty cycle from the 18% of moonless night up to 40% as studied in Ahnen et al. (2017a).

Observation Mode

The first IACT observations were conducted in the so called *ON/OFF* pointing mode, i.e. the telescope is pointed at the coordinates of the source to be observed. To subtract the gamma-ray background from the ON source observation an additional OFF run, pointing to a patch of sky free of VHE emitters and following the same zenith-azimuth path of the ON observation for the same time, is needed. Dark time is thus lost to OFF runs, without even the certainty to reproduce the atmospheric conditions of the ON observation. Fomin et al. (1994) introduced the so called *wobble* mode observations, optimising IACTs observation strategy. The telescope is no longer pointed at the source but at a coordinate offset by $\sim 0.5°$ in Right Ascension (RA) with respect to the nominal source position. The successive run is taken with the same offset and with a rotation angle of 90° or 180°, depending on the number of pointings (or

[XII] https://gcn.gsfc.nasa.gov

[XIII] An inclined shower has a larger mass thickness to transverse compared to a vertical one. Hence, given the same inclination, only showers with a higher energy primary (hence a longer development) will not to be completely absorbed and trigger the telescope.

wobbles) needed. The source thus finds itself in mirrored points of the camera reference frame at each run, always at a fixed offset from the centre, the method is illustrated in Figure 2.13. The fundamental advantage of this strategy is the simultaneous estimation of the background from a position symmetric to the one occupied by the source and also the smearing out of systematics effects due to inhomogeneity of the camera response.

Most of the MAGIC observations are stereoscopic, although technical muon runs are taken with the telescopes triggering in mono mode. In these observations the thickness of the Cherenkov ring produced by muons in the camera is measured to monitor the optical PSF. The standard strategy for pointing is the wobble mode, with 0.4° offset. Special observations of some extended sources, dark patches of sky used for hadronic background estimation or even specific science cases, might require ON pointing observations (Ahnen et al., 2018; Acciari et al., 2018a).

2.4 IACT Data Analyis

The reduction and analysis of the MAGIC data is performed with the MAGIC Analysis and Reconstruction Software (MARS, Zanin et al. 2014), a collection of `C++` scripts built on the `ROOT`[XIV] framework Brun and Rademakers (1997). MARS is a proprietary software whose access is granted to collaboration members only. In the desire of keeping the discussion on a general level this section will illustrate the main analysis principles and the progressive data reduction using a scheme for IACT data levels introduced in Contreras et al. (2015). The latter, re-proposed in Table 2.2, is presented as a data model in view of the next generation of Cherenkov telescopes. Nevertheless it reasonably profiles the current IACT data processing structure and will hence be used as a guide in outlining this section.

2.4.1 MC Simulations

A foreword on MC simulations is mandatory, before illustrating the actual data levels. Though many of the electronic and optical subsystems can be calibrated separately, it is not possible to produce a gamma-ray shower specimen to measure the response of the instrument as a whole. MC simulations (Majumdar et al., 2005) are employed for this purpose, running through three stages: first, the shower is simulated with CORSIKA; second, the Cherenkov photons thus produced are passed to a dedicated program simulating the reflector response; third, the camera response and the trigger and readout systems are simulated, producing as a final output data files emulating the raw output of the DAQ (that can be then processed with MARS). Only gamma-ray showers are needed for most of the analyses, CR showers can be simulated for investigations oriented towards particle physics or for performance assessments. Most of MAGIC observations are conducted in wobble mode at a fixed offset of 0.4°; MC data, whose production is highly time consuming, are therefore mostly produced simulating events exactly at 0.4° from the camera centre, i.e. at the same offset the source happen to occupy in the observation. In this thesis only such MC simulations have been used. For the analysis of extended sources and for sources

[XIV] `https://root.cern.ch`

Data Level	Short Name	Description
Level 0 (DL0)	DAQ-RAW	Data from the data acquisition hardware/software.
Level 1 (DL1)	CALIBRATED	Physical quantities measured in each separate camera: photons, arrival times, etc., and per-telescope parameters derived from those quantities.
Level 2 (DL2)	RECONSTRUCTED	Reconstructed shower parameters (per event, no longer per-telescope) such as energy, direction, particle ID, and related signal discrimination parameters.
Level 3 (DL3)	REDUCED	Sets of selected (e.g. gamma-ray-candidate) events, along with associated instrumental response characterisations and any technical data needed for science analysis.
Level 4 (DL4)	SCIENCE	High level binned data products like spectra, sky maps, or light curves.
Level 5 (DL5)	OBSERVATORY	Legacy observatory data, as survey sky maps or the IACT source catalogue.

Table 2.2: Levels describing the data reduction of the next generation of Cherenkov telescopes, from Contreras et al. (2015). The scheme stands valid for the currently operating IACT and will be used for the MAGIC data analysis description.

that are not at the standard offset of 0.4°, MC simulations spanning the whole camera FoV are also produced.

2.4.2 Data Level 0: Raw Output of the DAQ

The lowest level of data is the raw output of the DAQ. For MAGIC, $\sim$ 1 TB of raw data per each telescope are produced per night. These are binary files containing the charge in the RoI of the DRS4 capacitors, for all the cameras pixels, for all the L3 triggered, interleaved pedestal and calibrated events. They are stored in a proprietary binary format and merged with the CC reports at the first step of the analysis, that saves them in a `ROOT` format.

2.4.3 Data Level 1: Calibration and Image Cleaning

The first step of the data processing consists in reducing the sampled waveform of each of the pixel (recorded in case of a stereo trigger) in integrated charge and arrival time. Charge and arrival time for each pixel are extracted with a *sliding window* algorithm after the pedestal of each capacitor has been subtracted. For each sampled waveform, the total charge is assumed to be the maximum of the sum of 5 consecutive time slices (50 time slices per event are saved with 1.64 GHz sampling speed). The arrival time is instead computed the average of the time slices weighted with the sampled charge. The charge in ADC counts is converted to photoelectrons (phe) using the *F-factor* method (Mirzoyan, 1997), with 1 phe typically producing 60 integrated ADC counts. At this stage the pixels containing NSB photons have to be removed in order for the discretised image of the shower to stand out. This operation is denoted as *cleaning* and relies, as the L1 trigger, on the concept that Cherenkov flashes trigger clusters of close-by

pixels in a few ns time window. The core of the image is identified by pixels in combination of 2, 3 or 4 NN whose summed charge lies above a certain threshold Q_{core} for a fixed time window Δt_{core} (both their values are given in Table 2.3). The charge of the individual pulses is clipped before summation to avoid contamination from eventual large PMT afterpulses. The image is completed by boundary pixels, these are pixels adjacent to core ones with a signal larger than 3.5 phe arriving within 1.5 ns from the signal arrival time in the core pixel. At this stage the charge information of the core and boundary pixels

Combination	Q_{core} / phe	Δt_{core} / ns
2NN	2×10.8	0.5
3NN	3×7.8	0.7
4NN	4×6	1.1

Table 2.3: Summed charge threshold, Q_{core}, and time window Δt_{core}, for a combination of nNN pixels to be accepted as a core pixels for the image.

can be used to compute the Hillas parameters, presented in Section 2.2.2. The cleaned image of an air shower recorded by one of the MAGIC cameras is shown in Figure 2.10, with the ellipse representing the Hillas parameters superimposed in red. After cleaning the shower image from the NSB background the pixelised information is lost, replaced by the Hillas parameters of each image. Storing only the Hillas parameters per each stereoscopic triggered event, per each telescope, reduces the total amount of data for a night of observations to ~ 8 GB. Each minute of observation per each telescope is written in a subrun file with size ~ 6 MB.

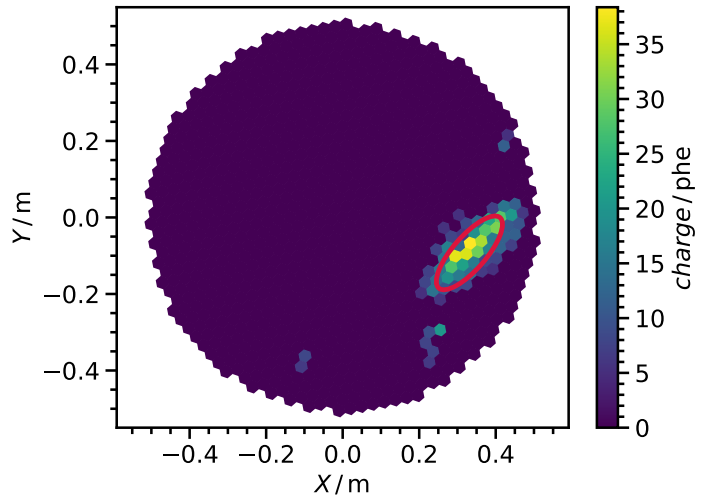

Figure 2.10: Cleaned image of an air shower recorded by one of the MAGIC cameras. The Hillas ellipse is overlayed in red to the major cluster of pixels which have survived the cleaning (their values are different than 0). Plot created reading DL1 MAGIC data with `ctapipe`[XV].

[XV] https://cta-observatory.github.io/ctapipe

2.4.4 Data Level 2: Direction and Energy Estimation, γ / Hadron Separation

At this level images surviving the cleaning in both telescopes are paired and stereoscopic parameters are computed. Most of the images are due to CR air showers; even when observing a source as bright as the Crab nebula, their number dominates by three orders of magnitude that of gamma ray events, a γ / hadron discrimination method is used to classify and distinguish the events. At this data level any information concerning the single telescope or the shower (enclosed in its Hillas parameters) is lost, the data are reduced to *events*: candidate gamma rays with arrival direction and time, estimated energy, γ / hadron classification outcome.

Stereoscopic Parameters

Distinctive of a stereoscopic system is the possibility to build a three-dimensional image of the shower, estimating the direction of its axis and the height of the shower maximum $h_{\max}$. The major axis of the Hillas ellipse identifies the axis of the shower development. Since the image point which corresponds to the shower direction must lie approximately on that axis, to estimate it one can intersect the major axes of the Hillas ellipses after translating them in a common camera frame (Hofmann et al., 1999). The impact point on the ground can be obtained instead intersecting the geometrical planes containing each telescope and the imaged shower axis, as shown in Figure 2.11. $h_{\max}$ can be computed using the CoG and the angular offset α of the image from the pointing position (see Section 2.2.2). The stereoscopic parameters most important for the energy reconstruction are: the impact parameters, $impact_{\mathrm{M1}}$, $impact_{\mathrm{M2}}$, i.e. the distances between the impact point on the ground and the telescopes positions; the Cherenkov radius r_{cher} and density ρ_{cher}, i.e. the radius of the Cherenkov annulus and the density of photons generated by an electron with critical energy E_e^c located at $h_{\max}$.

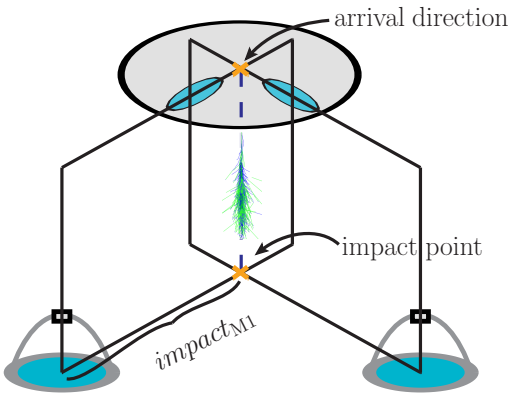

Figure 2.11: Stereoscopic reconstruction of shower parameters. If we were to move the Hillas ellipses recorded by the two telescopes in the same camera frame and cross their main axes, we will obtain an estimate of the arrival direction of the primary gamma ray. The planes containing each telescope and the main axis of the image intersect identifying the three-dimensional shower axis. In this sketch we assume the shower axis parallel to the optical axis of the telescopes (as in case 2 of Figure 2.6).

γ / Hadron Separation

A multi-variate classification algorithm based on multiple binary decision trees, presented in Albert et al. (2008a), is used for the γ / hadron discrimination. The training sample contains the two classes to

discriminate: gamma rays (MC simulation) and hadrons (events from any region of sky with no VHE emission, either dark patches or any non significant source observation can suffice this purpose). Both should match the zenith range of the data under investigation. The training process starts with a single node containing all the training data, tagged with a 1 if they are hadrons or with a 0 if they are gammas. Each event is characterised by a vector $\boldsymbol{v}$ containing the Hillas parameters. The tree is grown by iteratively splitting the sample in two branches: at each iteration a component of $\boldsymbol{v}$ is randomly selected and a cut value is chosen to separate the sample. This cut value minimises the Gini (1921) index: $G = 4\,N_\gamma\,N_{\rm hadron}/(N_\gamma + N_{\rm hadron})^2$, the smaller the Gini index, the better the separation (the index is 1 for a sample with equal number of events of each class, 0 for a branch with events of only one class). The growth stops when a branch is left either with a minimum number of events (usually 3) or with events of one class only. The *hadronness* value assigned to a terminal branch reflects its final hadron content: $hadronness = N_{\rm hadron}/N$. Usually a high number $\sim$ 100 of trees are trained, forming the so called Random Forest (RF). The RF is applied to the data under investigation (test sample) and associates to each event a *hadronness* value, classifying events from "most gamma-like" (0) to "most background-like" (1). This time, differently than in the training process, events have unknown nature. For each event its parameter vector $\boldsymbol{v}$ is processed through each tree until it reaches a terminal branch with a given *hadronness*. The final *hadronness* value for the event is simply the average of the *hadronness* scores achieved in all the trees.

Arrival Direction

The method of crossing the main axes of the Hillas ellipses to obtain the arrival direction can fail for low energy events or for very large impact parameters, that produce roughly parallel images. Since the arrival direction of a primary gamma ray lies somewhere on the main axis of the Hillas ellipse, Lessard et al. (2001) introduces the so called DISP method to estimate (using only the Hillas parameters) the arrival direction in the monoscopic case. The method is subject to the so called head-tail ambiguity, since the DISP only returns a distance (between the CoG and the estimated primary direction) not its direction on the image axis. This ambiguity can be easily broken using the skewness of the light distribution (note the Hillas ellipse is skewed for high impact values). In the MAGIC reconstruction chain an extension of the DISP method is used (Aleksić et al., 2010a): a RF trained with MC gamma ray simulations with known DISP, is used to estimate the DISP for each image in both telescopes (in this case, instead of the Gini index the DISP variance between nodes is minimised). Two possible arrival directions are thus estimated per each telescope, shown in Figure 2.12: $A_{\rm M1}$, $B_{\rm M1}$ for M1; $A_{\rm M2}$, $B_{\rm M2}$ for M2. The primary gamma ray direction lies on the segment identified by the minimum of the four distances given by the four points. If the smallest distance (in green in Figure 2.12) is greater than 0.22° the event is rejected (this enables higher rejection power against hadronic images), otherwise the estimated gamma ray coordinate is taken as the weighted average (with the charge content of the images) of the couple of selected points.

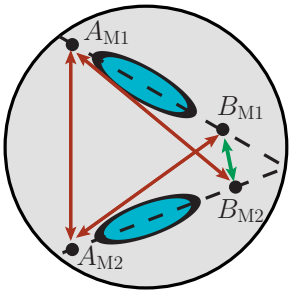

Figure 2.12: Given an image ellipse the DISP method returns the estimated distance between its CoG and the arrival direction of the gamma primary; the head-tail ambiguity (the direction on the image axis of the DISP is not known) creates two estimated coordinates for each image: A_{M1}, B_{M1} in M1; A_{M2}, B_{M2} in M2. These in turn identify four distances (double pointed arrows) the minimum of which (in green) contains the real event coordinate.

Energy Estimation

The energy of the events is estimated using a Look-Up Table (LUT) derived using gamma ray MC simulations. A two-dimensional table per each telescope is produced, binning the events in image size and in ratio of impact parameter to Cherenkov radius $impact_{M1}/r_{cher}$. The final estimated energy E_{est} is the weighted average of the energy value returned by both tables for the event parameters.

Quality Selection

The assessment of the quality of the data is also done at this level. Reading the reports of the LIDAR and pyrometer a list of good time intervals (GTI)s can be generated fixing a minimum atmospheric transmission value (usually around 80%). Other important criteria that could be used to generate GTI are the rate of events or the number of stars visible with one of the drive monitoring CCD cameras. Events whose timestamps do not fall within the GTIs are discarded.

At the DL2 stage the data size stays roughly the same of the DL1. Individual Hillas parameters are replaced by stereoscopic informations, direction and energy estimation. The data are grouped in runs covering a single wobble pointing (spanning typically 15 or 20 minutes of observation). Each data run has size $\sim 100\,\mathrm{MB}$.

2.4.5 Data Level 3: Event Lists and Instrument Response Functions

The DL3 data constitute the most reduced level products before the final scientific results as spectrum, light curve, and sky maps. As we shall see in Section 2.5.1 and Chapter 3, users provided with DL3 products and with science tools can self sufficiently obtain those results. After the DL2 has provided all the information relative to the events (e.g. direction, energy, hadronness) one can operate cuts to select a subset for a specific analysis (e.g. a given cut in hadronness to reject hadron-like events, zenith range, etc.). The events surviving the cuts tailored to a particular analysis constitute an *event list*, the first element of the DL3. The quantities attached to each photon are estimated (hatted in this notation), hence a knowledge of the instrument response function (IRF) is needed to convert them to their true physical value. The IRF, second element of the DL3, has several components, usually mathematical functions of the energy E and the direction $\boldsymbol{P}$ of the events, mapping the conversion between estimated

and true quantities. They are estimated from MC events subject to the same analysis cuts applied to the event list. An IRF for IACT has three components:

- the point spread function (PSF), $f_{\boldsymbol{P}}(\hat{\boldsymbol{P}}|E, \boldsymbol{P})$, representing the spatial probability distribution of the estimated coordinates for photons generated by a point source. A King (1971) function or a superposition of two Gaussian functions are typically used;

- the *energy dispersion*, $f_E(\hat{E}|E, \boldsymbol{P})$, representing the probability density function (PDF) for the energy estimator. For MAGIC it is estimated via the LUTs introduced in Section 2.4.4;

- the *effective area*, representing, the instrument collection area corrected by an efficiency depending on the analysis cuts, is typically expressed as

$$A_{\text{eff}}(E, \boldsymbol{P}) = \frac{N_{\text{MC, final}}(E, \boldsymbol{P})}{N_{\text{MC,total}}(E, \boldsymbol{P})} \times \pi \, impact^2_{\text{max}}, \tag{2.24}$$

  where $impact_{\text{max}}$ is the maximum impact parameters of the simulated air showers, $N_{\text{MC, total}}(E, \boldsymbol{P})$ is the total number of simulated events and $N_{\text{MC, final}}(E, \boldsymbol{P})$ the number of those surviving the analysis cuts.

The dependency on $\boldsymbol{P}$ of the IRF components can be expressed in camera coordinates or also as an offset from the FoV centre, in case of a symmetric camera acceptance. An IRF accounting for such a dependency is labelled as *full-enclosure* and it allows to perform analyses of any source in the FoV. As pointed out in Section 2.4.1, most of the observations of MAGIC are performed at a fixed offset from the camera centre (0.4°): due to the rotation of the wobbling scheme, the source can find itself only on a thin circular path in the camera frame (of 0.4° radius, see Figure 2.13). By applying a directional cut on the MC events (or simulating them at a fixed offset from the camera centre), one can obtain a similar thin ring of arrival directions on the camera. IRF computed from such simulations are labelled as *point-like* since they allow only the analysis of a point-like source with the same offset of the simulations. Assuming the acceptance uniform in such a thin ring, no PSF component is specified and effective area and energy dispersion depend solely on the energy $f_E(\hat{E}|E, \boldsymbol{P}) \rightarrow f_E(\hat{E}|E)$, $A_{\text{eff}}(E, \boldsymbol{P}) \rightarrow A_{\text{eff}}(E)$. All the MAGIC IRFs used in this thesis are of point-like type, an example of energy dispersion and effective area are displayed in Figure 2.15 and 2.17, respectively.

The only part of the DL3 data that is stored by MARS are the IRF components. They are attached to the final scientific products (spectra and light curves) that are contained in `ROOT` files of final size from hundreds of kB to few MB. The event lists for a given analysis are not stored separately but extracted on the fly during the computation of the scientific results from the DL2 data.

2.4.6 Data Level 4: Spectra and Light Curves

In this section we will present the data analysis steps performed in MAGIC to obtain the final scientific results. We will focus on spectra and light curves since these will be the results shown in this thesis,

pertaining only point-like sources. The reader interested in the methods for extended sources analyses and skymap computation is referred to Vovk et al. (2018).

Significance of the Observation

The first step of the analysis is to assess if the event list contains a significant gamma-ray signal. A common method in astronomy, known as aperture photometry, identifies two different sky regions: the signal, or ON region, enclosing the candidate source; the background, or OFF region, assumed to be devoid of gamma-ray sources, used to estimate the background counts to be subtracted from the source counts. The ON region is usually a circle around the source position with a radius comparable with the PSF of the instrument. The OFF region is commonly chosen as a ring concentric to the ON region (*ring background* method in Berge et al. 2007) or as multiple circular regions with the same size of the ON but mirroring its position with respect to the camera centre (*reflected regions* background method in Aharonian et al. 2001 and Berge et al. 2007). The latter case perfectly suits a wobble mode pointing strategy, as shown in Figure 2.13.

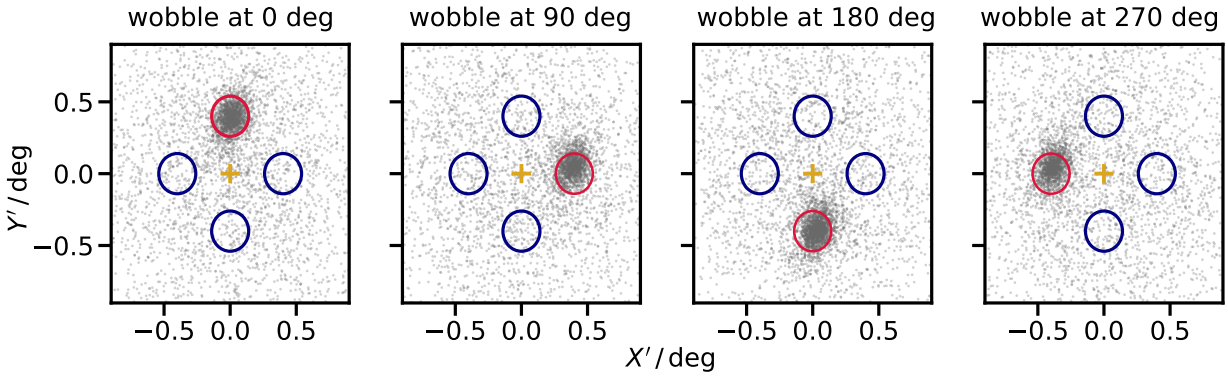

Figure 2.13: Signal estimation for wobble pointing strategy, or reflected regions method. In each panel estimated events coordinates are represented as grey dots. The telescope is not pointed to the source, whose position stands out due to the cluster of events, but to a point offset by 0.4 deg along its RA axis. In the following data runs (or wobbles) the source position is rotated by 90°. The acceptance of different camera sectors is thus sampled. The ON region is marked in red, the OFF regions to estimate the background to be subtracted in blue. In this particular scheme, per each wobble the OFF regions match the ON region positions in the remaining runs. The telescope pointing position is marked by a golden cross, the camera coordinates have been rotated such that the Y' axis matches the RA axis.

The arrival directions of the events are represented in camera coordinates with small grey dots, the source position is clearly identified by the cluster of events. At each run, due to the wobbling, the source (and the ON region enclosing it, in red) rotates of 90° in camera coordinates. The OFF regions (in blue) can then be chosen with the same offset from the camera centre as the ON (0.4°) and covering the same camera coordinates the source will occupy in the following runs (wobbles). In this way any inhomogeneity, due to a non-symmetric camera acceptance, is smeared out by testing different camera sections as signal and background regions. The probable signal, or excess, i.e. the number of photons

coming from the source is

$$N_{\mathrm{EX}} = N_{\mathrm{ON}} - \alpha\, N_{\mathrm{OFF}}, \tag{2.25}$$

where N_{ON} and N_{OFF} are the number of events in the ON and OFF regions, respectively, and α is the ratio of the ON to the OFF exposures. The significance of the source counts can be expressed as a S standard deviation result, using Eq. 17 of Li and Ma (1983)

$$S = \sqrt{2\left\{N_{\mathrm{ON}} \ln\left[\frac{1+\alpha}{\alpha}\left(\frac{N_{\mathrm{ON}}}{N_{\mathrm{ON}}+N_{\mathrm{OFF}}}\right)\right] + N_{\mathrm{OFF}} \ln\left[(1+\alpha)\left(\frac{N_{\mathrm{OFF}}}{N_{\mathrm{ON}}+N_{\mathrm{OFF}}}\right)\right]\right\}} \tag{2.26}$$

This is obtained from a likelihood ratio test where the null hypothesis is that no gamma-ray source exist and all the excess photons are due to the background, i.e. $< N_{\mathrm{EX}} >= 0$; Poisson distributions are assumed for N_{ON} and N_{OFF}. It is customary in the MAGIC analysis to evaluate the number of excesses and the significance by histogramming the events as a function of their squared angular distance, θ^2, from the ON / OFF region centre. An isotropic two-dimensional background should result in a flat θ^2 histogram, while the excess counts due to the source should increasingly pile up in the bins closer to 0 (i.e. close to the source nominal position), as shown in Figure 2.14. The θ^2_{cut} value defining the sizes of the ON and OFF regions (and N_{ON} and N_{OFF} via simple integration) is optimised, using an independent sample, to maximise the significance in similar observing conditions (energy range, zenith angle, etc.), as we will explain in Section 2.5.2.

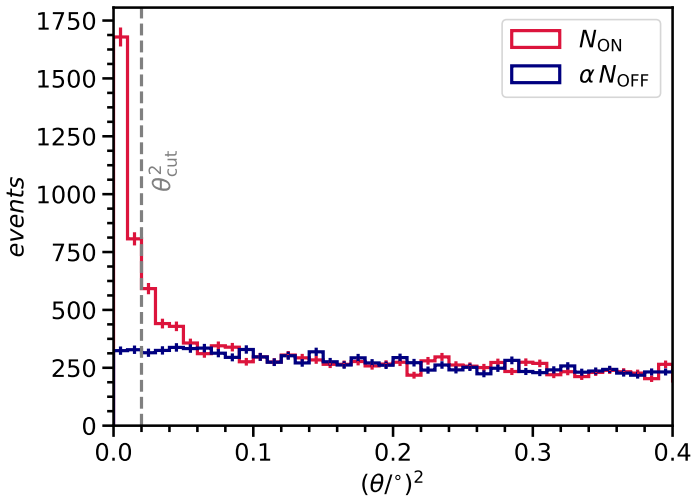

Figure 2.14: Example of a θ^2 plot. The histogram of the θ^2 distances of the events from the centre of the ON region is shown in red, events accumulate close to the source position. The histogram of the θ^2 distances of the events from the centres of each of the OFF regions, scaled by the exposures ratio α, is shown in blue. The background counts are isotropically distributed in the camera so they result in a flat distribution in θ^2.

Spectrum Evaluation I: Likelihood Method

To estimate the differential flux spectrum $\frac{\mathrm{d}\phi}{\mathrm{d}E}(E;\mathbf{\Lambda})$ of a gamma-ray source, i.e. the flux[XVI] per interval of gamma-ray energy (measured in $\mathrm{TeV}^{-1}\,\mathrm{cm}^{-2}\mathrm{s}^{-1}$), a binned maximum likelihood method, with $n_{\hat{E}}$

[XVI] Number of photons per unit area per unit time.

bins in estimated energy is used. The parameters $\mathbf{\Lambda}$ of the assumed spectral model are determined by maximising a likelihood whose data $\boldsymbol{\mathcal{D}}$ are the counts in the ON and OFF regions, assumed to be Poissonly distributed. In case the observation consist of j different observational runs, one has

$$\mathcal{L}(\mathbf{\Lambda}|\boldsymbol{\mathcal{D}}) = \prod_{j=1}^{n_{\text{runs}}} \prod_{k=1}^{n_{\hat{E}}} \text{Pois}(g_{jk}(\mathbf{\Lambda}) + b_{jk}; N_{\text{ON},jk}) \times \text{Pois}(b_{jk}/\alpha; N_{\text{OFF},jk}), \tag{2.27}$$

where:

- $N_{\text{ON},jk}$ and $N_{\text{OFF},jk}$ are the number of observed events within the ON and OFF regions, respectively, in the energy bin k, for the j-th run;
- $g_{jk}(\mathbf{\Lambda})$ and b_{jk} are the expected number of signal and background events, respectively, in the energy bin k, for the j-th run. $g_{jk}(\mathbf{\Lambda})$ depends on the assumed spectral model and is computed folding the latter with the IRF components

$$g_{jk}(\mathbf{\Lambda}) = T_{\text{eff},j} \int_{\Delta \hat{E}_k} \mathrm{d}\hat{E} \int_0^\infty \mathrm{d}E \, \frac{\mathrm{d}\phi}{\mathrm{d}E}(E; \mathbf{\Lambda}) \, A_{\text{eff},j}(E) \, f_{E,j}(\hat{E}|E), \tag{2.28}$$

  here $T_{\text{eff},j}$ is the effective time for the j-th run. It is computed fitting an exponential distribution to the histogram of the difference of arrival times between the events in a run[XVII]. $A_{\text{eff},j}(E)$ and $f_{E,j}(E|\hat{E})$ are the IRF components for the j-th run, they are both computed after re-weighting the MC simulations in order for them to have the same zenith angle distribution as the data. The expected number of background events b_{jk} can be either estimated with a similar convolution as the one in Eq. 2.28, if one has available IRF components for background events; or, more frequently, treated as a nuisance parameter and fixed solving $\frac{\partial \mathcal{L}}{\partial b_{jk}} = 0$ (as in Appendix A of Piron et al. 2001).

From Eq. 2.27 one can produce an average (or stacked) likelihood removing the dependence on the individual runs, i.e. j. In order to do this, the counts in each energy bin from the different runs are summed, $N_{\text{ON},k} = \sum_{j=1}^{n_{\text{runs}}} N_{\text{ON},jk}$ and the IRF components are averaged with a weight given by their effective time, e.g. for the effective area: $A_{\text{eff}} = \sum_{j=1}^{n_{\text{runs}}} T_{\text{eff},j} \, A_{\text{eff},j} / \sum_{j=1}^{n_{\text{runs}}} T_{\text{eff},j}$.

Astrophysical sources are powered by non-thermal processes whose spectra manifest a power-law energy (or wavelength) dependence, in contrast with the black body spectra of their thermal components. Hence it is common in gamma-ray astronomy, dominion of non-thermal processes, to use a power law of the energy for the assumed differential flux spectrum

$$\frac{\mathrm{d}\phi}{\mathrm{d}E}(E; E_0, \phi_0, \Gamma) = \phi_0 \left(\frac{E}{E_0} \right)^{-\Gamma}, \tag{2.29}$$

E_0 is referred to as reference energy, ϕ_0 (with the same units of $\mathrm{d}\phi/\mathrm{d}E$) as flux normalisation, Γ as spectral index. We will see in Chapter 5 that the VHE spectrum of PKS 1510-089 shows a simple power-law behaviour. For sources like the Crab Nebula (see Chapter 3) a simple power law is not sufficient to

[XVII] The difference of the arrival times between successive Poissonian events follows an exponential distribution

describe the spectrum over all the observed energy range: a second spectral index, variable with energy, is introduced to describe the curvature of the spectrum. This analytical function goes under the name of log parabola

$$\frac{\mathrm{d}\phi}{\mathrm{d}E}(E; E_0, \phi_0, \Gamma, \beta) = \phi_0 \left(\frac{E}{E_0}\right)^{-\Gamma-\beta\log_{10}(\frac{E}{E_0})}. \tag{2.30}$$

The spectrum of some sources shows a characteristic exponential suppression that is modelled, as in the case of NGC 1275 in Chapter 6, with a power law with an exponential cutoff at energy E_{cutoff}

$$\frac{\mathrm{d}\phi}{\mathrm{d}E}(E; E_0, \phi_0, \Gamma, E_{\mathrm{cutoff}}) = \phi_0 \left(\frac{E}{E_0}\right)^{-\Gamma} \exp\left(-\frac{E}{E_{\mathrm{cutoff}}}\right). \tag{2.31}$$

Spectrum Evaluation II: Unfolded Spectral Points

The result of a likelihood fit provides a spectral information valid over all the energy range considered, as shown in Figure 2.19 for the Crab nebula spectrum. A spectral feature narrower than an energy bin, e.g. a spectral line, would be undetectable by such method, if one were to fit a smooth, featureless, spectra[XVIII]. Discrete spectral flux points are hence computed as a comparison to the likelihood fit result. In the MAGIC collaboration an unfolding procedure, borrowed from high-energy particle physics and presented in Albert et al. (2007), is applied for this purpose.

Let $\boldsymbol{Y}$ be an array of length $n_{\hat{E}}$ containing the excess counts (Eq. 2.25) binned in estimated energy and $\boldsymbol{S}$ an array of length n_E defining the true energy bins in which the excess counts have to be reshuffled. We assume that the excess counts in each observational runs have been stacked. The components $\boldsymbol{S}$ and $\boldsymbol{Y}$ are connected by a $n_{\hat{E}} \times n_E$ matrix, $\boldsymbol{M}$, a binned version of the energy dispersion IRF component $f_E(\hat{E}|E)$

$$Y_k = \sum_{l=1}^{n_E} M_{kl}\, S_l. \tag{2.32}$$

and we will refer to $\boldsymbol{M}$, from now on as *migration matrix*. Its components M_{kl} represent the fraction of events with true energy in the bin l whose energy is estimated to be in the bin k. The migration matrix, shown in Figure 2.15, is normalised in estimated energy, i.e. along its rows: $\sum_{k=1}^{n_{\hat{E}}} M_{kl} = 1$. The unfolding method consists in inverting Eq. 2.32, but being $\boldsymbol{M}$ generally a non-invertible matrix, this constitute an ill-posed problem, whose numerical solution is the minimisation of the quantity

$$\chi_0^2 = (\boldsymbol{Y} - \boldsymbol{M}\cdot\boldsymbol{S})^T\, \boldsymbol{K}^{-1}\, (\boldsymbol{Y} - \boldsymbol{M}\cdot\boldsymbol{S}), \tag{2.33}$$

where $\boldsymbol{K}$ is the covariance matrix of $\boldsymbol{Y}$ and the free parameters in the minimisation are the n_E components of $\boldsymbol{S}$. The numerical minimisation is typically unstable and can produce large errors on $\boldsymbol{S}$. A regularisation procedure is hence introduced, the χ^2 to be minimised is now

$$\chi^2 = \frac{w}{2}\,\chi_0^2 + \mathrm{Reg}(\boldsymbol{S}), \tag{2.34}$$

[XVIII] And would show up as a large contribution to the χ^2 from the bin containing the line.

where $\mathrm{Reg}(S)$ is a regularisation function and w is a parameter regulating the weight of the regularisation term in the total χ^2 (a small w implies a strong regularisation and vice versa). In the MARS software, regularisation methods from Tikhonov and Arsenin (1977); Bertero (1989) and Schmelling (1994) are implemented. Once the unfolded excess $\boldsymbol{S}$ are obtained, the spectral points (now in true energy) are computed as

$$\left(\frac{\mathrm{d}\phi}{\mathrm{d}E}\right)_l = \frac{S_l}{T_{\mathrm{eff}}\,\Delta E_l\,A_{\mathrm{eff},l}} \tag{2.35}$$

Where T_{eff} is now the total observation time, ΔE_l the width of the true energy bin and $A_{\mathrm{eff},l}$ the effective area value in the true energy bin l. To optimise the unfolding procedure in MAGIC a finer binning in estimated rather than true energy is selected: $n_{\hat{E}} > n_E$; with ratios of bin widths $\Delta E_l/\Delta\hat{E}_k \approx \sqrt{2}$. A *forward unfolding* procedure is also implemented: in this case the values of $\boldsymbol{S}$ are parametrised by an analytical differential flux function $\mathrm{d}\phi/\mathrm{d}E$ as in Eq. 2.29 - Eq. 2.31, the minimisation in Eq. 2.34 returns the spectral parameters of $\mathrm{d}\phi/\mathrm{d}E$ instead of the single components S_l.

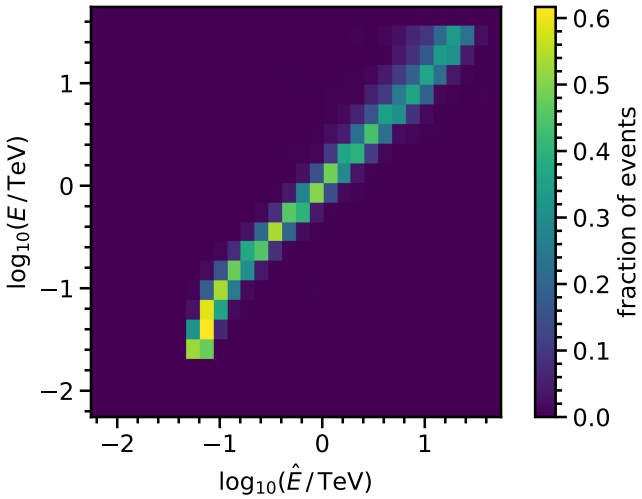

Figure 2.15: Values of the energy dispersion, $f_E(E|\hat{E})$, binned in true and estimated energies, also referred to as migration matrix. Given a certain true energy, E, the migration matrix returns the (binned) PDF of its estimator $\hat{E}$ (it is indeed normalised along the $\hat{E}$ axis).

Light Curves

A light curve represents the evolution of the flux of a source (expressed in $\mathrm{cm}^{-2}\,\mathrm{s}^{-1}$) as a function of time. This implies dividing the data in different time bins and integrating the differential flux $\mathrm{d}\phi/\mathrm{d}E$ above a certain energy E_0 in each of them, namely

$$\phi(E > E_0) = \int_{E_0}^{\infty} \frac{\mathrm{d}\phi}{\mathrm{d}E}\mathrm{d}E, \tag{2.36}$$

numerically estimated using

$$\phi(E > E_0) = \frac{N_{\mathrm{EX}}(\hat{E} > E_0)}{T_{\mathrm{eff}}\,A_{\mathrm{eff}}(E > E_0)}. \tag{2.37}$$

If the observation contains a robust gamma-ray signal, unfolded spectral points corresponding to the energy bins where the excesses stack up to a significant value (according to Eq. 2.26) are published. As we shall see in Chapter 5 for weak sources as PKS 1510-089, several tens of observation hours could be needed to reach such a result; for sources as bright as the Crab nebula or undergoing a sudden outburst of activity, as NGC 1275 in Chapter 6, even an hour can suffice. The situation is different when producing a light curve and dividing the data in daily bins (see Figure 5.2 and Figure 6.1), in that case it is difficult to obtain a significant amount of excesses. Hence an upper limit on the flux has to be expressed. The latter is computed by the MARS routines when the relative error obtained on Eq. 2.37 is more than 50 %. Confidence intervals on the expected number of source counts, let us denote it with g for consistency with the likelihood definition in Eq. 2.27, are obtained using the Rolke et al. (2005) method[XIX]. A two-sided confidence interval, $[g_{\rm low}, g_{\rm up}]$ is calculated assuming a Poissonian likelihood similar to the one in Eq. 2.27 but introducing a Gaussianly distributed nuisance parameter ε representing a systematic error on the gamma-ray detection efficiency. One should simply replace $g \to \varepsilon\, g$ and factor a final $\mathcal{N}(\varepsilon; \mu_\varepsilon, \sigma_\varepsilon)$, with $\mu_\varepsilon = 1$ and $\sigma_\varepsilon = 0.3$ (values conventionally used in MARS) in Eq. 2.27. An upper limit on the number of excess events, $g_{\rm up}$, can be converted to an upper limits on the integrated flux using Eq. 2.37.

2.4.7 Systematic Uncertainties

The systematic uncertainties associated with the IACT technique can be ascribed not only to the limited knowledge of certain essential instrument components (e.g. the atmosphere, the NSB, the light collection efficiency, the PMT response); but also to the methodologies inherent to the data reduction (e.g. the ADC counts conversion, the data-MC discrepancy, the background estimation). It is common to tackle the systematics evaluation by selecting the main sources of uncertainties and then study their impact, i.e. the distortion they produce, on the parameters of a spectral measurement. As an example, in Aleksić et al. (2012a) and Aleksić et al. (2016b) the distortion on the energy scale, on the spectral slope or on the flux normalisation are considered. It is possible either to measure their impact directly, e.g. the reflectivity can be monitored with star images in CCDs or with muon events; or to modify the MC simulation amplifying or decreasing one of these factors (e.g. the NSB background). Table 4 in Aleksić et al. (2012a) resumes such factors and their impact. Combining all these factors, the overall spectral distortion that the MAGIC collaboration claims on the spectral measurements are: $\lesssim 15\,\%$ for the energy scale, $11 - 18\,\%$ on the flux normalisation and ± 0.15 on the spectral slope. In Section 3.3.2 an example of how to include the uncertainty in the energy scale directly in the likelihood evaluation will be shown.

2.5 Technical Contributions

Completing the analysis technique description, this section illustrates the software contributions done for the MAGIC collaboration within the scope of this thesis.

[XIX] The Rolke method provides confidence intervals with physical insight since $g_{\rm up}$ is forced to be positive if a confidence interval happens to be entirely below 0 (it would not make sense physically to have a negative number of gamma-rays). This correction compromise the statistical coverage: confidence levels might be overestimated with respect to the level selected for the computation, 95% in most of the cases.

2.5.1 Implementing a DL3 FITS Format for the MAGIC data

The work presented here has been done in collaboration with T. Hassan, who implemented the code to export the MAGIC data in FITS format. My contributions was to modify the exporter with the objective to: reach full compatibility of the produced FITS files with the open-source science tool `gammapy`; ensure the correct storage of the IRF components and the reproduction of the MARS results. Results presented here have been approved by the MAGIC collaboration.

As described in Section 2.4 the MAGIC software and data format are based on the `ROOT` framework. The purpose of exporting the MAGIC data in a different format, with a more standardised data structure, is twofold. With a backward perspective, after the end of MAGIC scientific activity and the decommission of the experiment, legacy data can be provided to the astronomical community, ideally containing re-usable information without retaining the bulk of the raw data. Shifting the perspective forward, as we shall discuss in Chapter 3, the next generation of IACTs represented by the Cherenkov Telescope Array (CTA, whose construction is already ongoing) will be operated as an observatory, opening its operations to the astronomical community and hence calling for publicly available data products and analysis tools. In the construction phase of CTA, actual data from currently operating IACT provide one of the best tests for the future CTA analysis tools, already in development. The output of such tools can be tested on data whose scientific content has already being assessed by a certified collaboration software. The data level satisfying the previous desiderata of compactness and re-usability is the DL3. Standardising the DL3 format will allow, for example, the final scientific products to be re-obtained either by an investigator studying an archival MAGIC result or by a developer testing the reliability of the future IACT science tools.

From ROOT to FITS

`ROOT` is an Object Oriented (OO) framework, that incorporates a `C++` interpreter, and powerful tools for data analysis, data acquisition, event simulation and reconstruction. Introduced by Brun and Rademakers (1997), it has been extensively adopted by the particle physics community. `ROOT` files are system-independent binary data that can be organised in nested directories or directly store event trees. One can interface a `ROOT` file only through the `ROOT` software itself (even if the latter can be integrated with languages as `python` or `R`) and recently also with pure `pythonic` implementations[XX].

The Flexible Image Transport System (FITS), the format chosen to convert the MAGIC data into (for an historical overview see Chapter 3) is a 40-year consolidated standard to exchange and archive data in astronomy, introduced in Wells et al. (1981). Primarily used to exchange 2-dimensional and 3-dimensional images (2 coordinates plus a wavelength or energy or exposure time), the format can also be used to store non-image data as multidimensional tables. Each FITS file is partitioned in Header Data Units (HDUs), each of those capable of containing a different data extension: an Image Extension (an N-Dimensional

[XX] `uproot`, https://github.com/scikit-hep/uproot, allows for `ROOT` files I/O without the `ROOT` software installation.

array of pixels) or a Table Extension (a data table in binary or `ASCII` format). A peculiarity of the format is the possibility to encode metadata in `ASCII` format, ensuring a later human readable inspection of the files. As an example in Figure 2.16 we use NASA's interactive FITS viewer (`Fv`[XXI]) to open a MAGIC DL3 file. In the upper tab we can see a HDU for the event list and two for the IRF components, all the HDUs contain binary data table. FITS files can be manipulated through several programming language, among the many: `C`, `C++`, `C#`, `Fortran`, `IDL`, `Java`, `Julia`, `LabVIEW`, `Mathematica`, `MATLAB`, `Perl`, `Python` and `ROOT` itself.

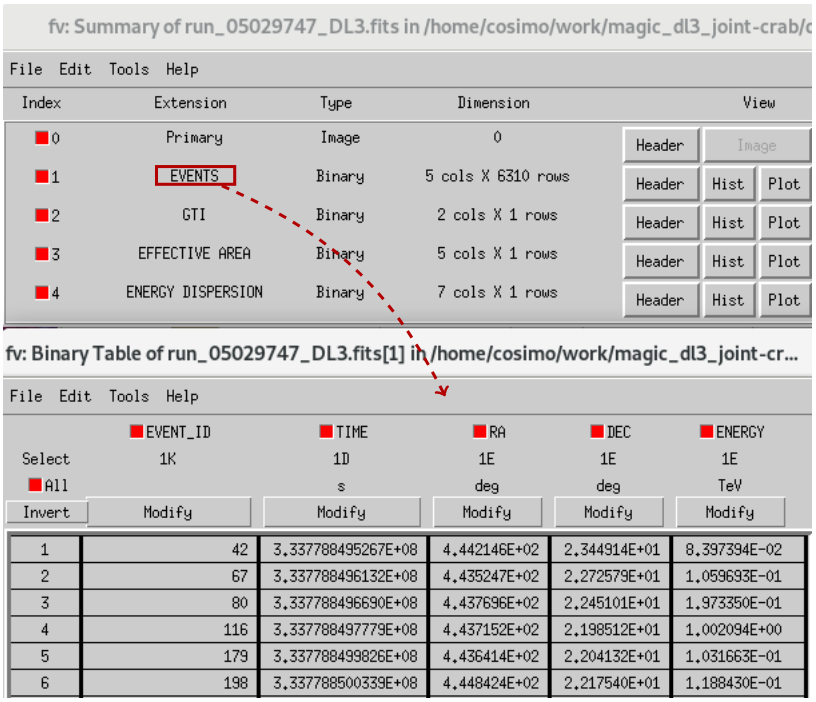

Figure 2.16: Example of FITS file, displayed with the NASA's interactive Fits viewer. A MAGIC DL3 file, covering an observational runs, has 5 HDUs: `Primary` pertains the file itself indicating the type of data stored, the `EVENTS` HDU contains the list of gamma rays surviving the analysis cuts, `EFFECTIVE AREA` and `ENERGY DISPERSION` the IRF components. The `GTI` HDU is at the moment not used since only good quality data are stored in FITS format. The `EVENTS` table and the column information it stores are expanded in the bottom half of the figure.

Analysis of MAGIC DL3 Data with `gammapy`

The discussion on the data format and the science tools implementation for CTA has already started. Most noticeably members of different gamma-ray astronomy experiments have channelled the dialogue in a "Data formats for gamma-ray astronomy" open-access forum[XXII] (Deil et al., 2017a). A first preliminary version of an IACT DL3 data format is therein defined, specifying the HDU extensions and the naming scheme to be used in the FITS file creation. We follow these prescriptions in the production of the MAGIC DL3 files. Science tools as `gammapy` (Deil et al., 2017b), developed in parallel to this a discussion, are compatible with data in the DL3 format and can therefore be used to analyse them.

The building blocks of the DL3 FITS files are created with the MARS software. As already mentioned in Section 2.4.5 the event lists are not stored by MARS but produced on the fly while computing the

[XXI] https://heasarc.gsfc.nasa.gov/ftools/fv
[XXII] https://gamma-astro-data-formats.readthedocs.io/en/latest

final scientific products. Therefore MARS was modified to retain at the final level a tuple per each event listing the properties to be stored in the columns of the `EVENTS` header (in this case RA, Dec, energy and arrival time per each event). We let the MARS routines compute the IRF components and then store the final output in the respective FITS binary table extensions. Each DL3 file covers an observational run, the size of the final DL3 FITS products is $\sim 200\,\mathrm{kB}$, a factor of 10^3 reduction with respect to the DL2 data. For the first production and test of DL3 data we select two runs out of the Crab nebula data sample used for the performance evaluation of MAGIC in Aleksić et al. (2016b) (referred to, from now on, as the performance paper), amounting to 40 minutes of data taking.

IRF components are computed and stored in binned values of true energy (and eventually offset in the *full-enclosure* case). Science tools perform an interpolation of these values in order to allow a successive analysis with a different, arbitrary, binning or to estimate a property for a specific energy value (as we shall see with the bias of the energy dispersion). The first task in our data conversion is to ensure that the interpolated IRF components are compatible with the stored values. The method for the multi-dimensional table interpolation performed by `gammapy` is borrowed from `scipy`[XXIII] and described in Weiser and Zarantonello (1988). The effective area depends only on the true energy so the comparison of the values stored by MARS and interpolated by `gammapy`, shown in Figure 2.17, is straightforward. Very good agreement is observed between the effective area computed with MARS (red points) and the one stored in the DL3 data and interpolated by `gammapy` (cyan).

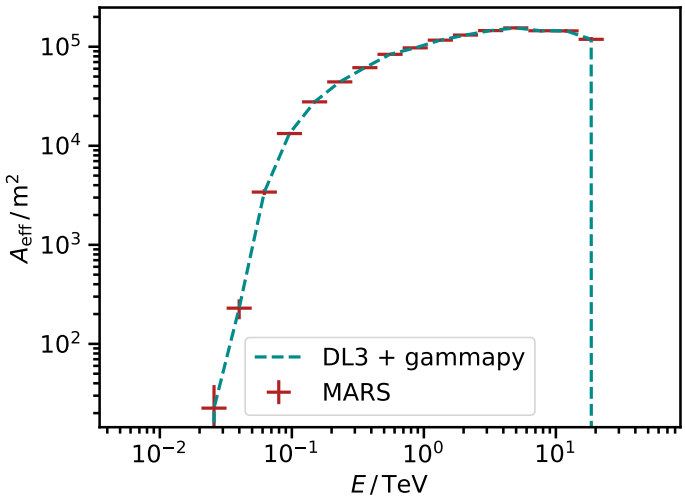

Figure 2.17: Comparison of the effective area computed with MARS (red points) with the one interpolated by `gammapy` from the DL3 data (dashed cyan line).

For the energy dispersion the comparison is not equally straightforward since a 2-dimensional distribution, function of true and estimated energy, is stored. We choose a comparison based on the mean and the variance of the distribution of the variable $z = (\hat{E} - E)/E$. These estimators are referred to as *bias* and *resolution*, respectively, their values obtained with `gammapy` and MARS are compared in Figure 2.18. Also for this IRF a good agreement is observed, the values obtained with `gammapy` (indicated with the

[XXIII] https://docs.scipy.org/doc/scipy/reference/index.html

cyan lines) deviate more than 30% from the ones computed with MARS only at energies $\sim 10\,\mathrm{TeV}$.

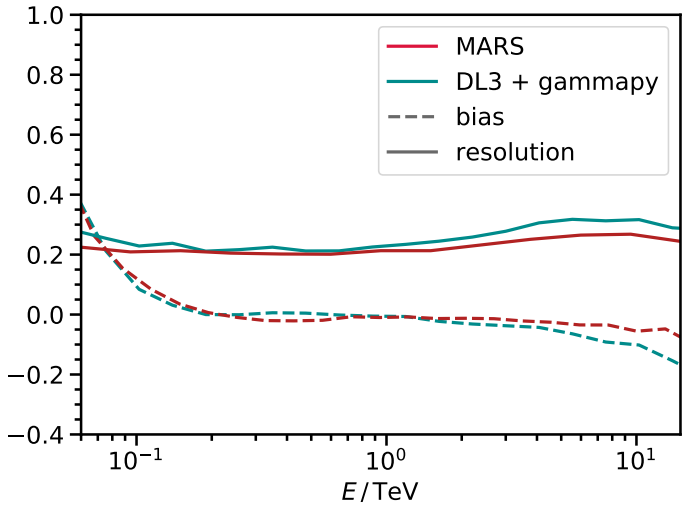

Figure 2.18: Comparison of the bias of the energy dispersion computed with MARS (solid red line) and with `gammapy` from the energy dispersion exported in the DL3 data (dashed cyan line).

Established the correct storage and reading of the interpolated IRF components, the final remaining check is a spectral analysis. The results for the two different softwares are compared in Figure 2.19, spectra are represented as Spectral Energy Distributions (SEDs): $E^2\,\mathrm{d}\phi/\mathrm{d}E$ i.e. as energy flux per logarithmic energy range ($\mathrm{erg\,cm^{-2}\,s^{-1}}$)[XXIV]. `gammapy` spectral result, shown with the dashed cyan line, is obtained with the likelihood method in Section 2.4.6; MARS spectral result, shown by the solid red line, instead relies on an average likelihood (i.e. instead of defining a likelihood term per each run, ON / OFF counts are summed and the IRF components are averaged). For both likelihood methods a log parabola, Eq. 2.30, has been used for the assumed spectrum $\mathrm{d}\phi/\mathrm{d}E$, whose fitted spectral parameters are shown in Table 2.4. The spectral points shown with red circles for MARS are obtained with the unfolding technique. The latter is not implemented in `gammapy` and its spectral points, shown with cyan diamonds, are obtained with a likelihood fit applied in each energy bin. The spectrum which results from the likelihood fit over the entire energy range is fed as the assumed spectrum to a likelihood minimisation with events in a single energy bin, and only the normalisation ϕ_0 is re-fitted. Spectral parameters obtained with the likelihood methods of MARS and `gammapy` are compatible within their statistical uncertainties. A very good agreement is also observed for the spectral points. Figure 2.19 shows the first MAGIC data analysed with open-source software, the two observational runs used for this test have been used in the larger project presented in Chapter 3.

[XXIV] Equivalent to the νF_ν used by astronomy at lower energies, where ν indicates the photon frequency (Hz) and F_ν the energy flux per unit frequency interval ($\mathrm{erg\,cm^{-2}\,s^{-1}\,Hz^{-1}}$), see Gehrels (1997).

parameter	MARS	gammapy
ϕ_0 / (TeV^{-1} cm^{-2} s^{-1})	$(4.02 \pm 0.29) \times 10^{-11}$	$(4.18 \pm 0.30) \times 10^{-11}$
Γ	2.56 ± 0.09	2.58 ± 0.09
β	0.36 ± 0.10	0.43 ± 0.11

Table 2.4: Spectral parameters results of the MARS and `gammapy` likelihood fit for a log-parabolic assumed spectrum, Eq. 2.30.

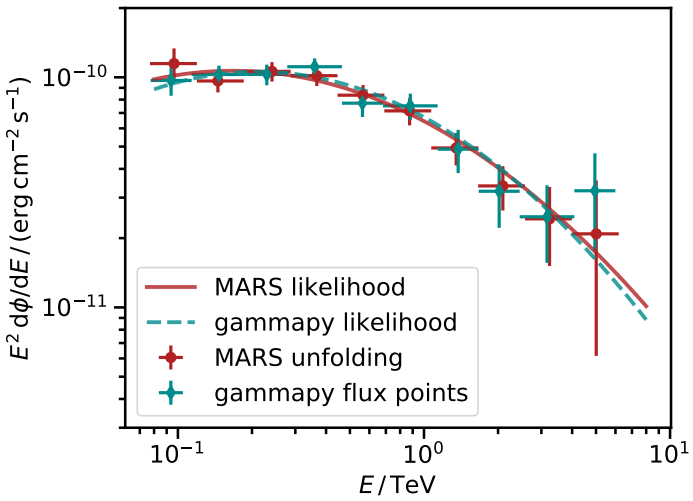

Figure 2.19: Comparison of the Crab Nebula SED obtained with MARS (red) and `gammapy` from the exported DL3 data (cyan). Spectra obtained from the likelihood method in Section 2.4.6 are shown as lines over the whole energy range considered. Spectral points are obtained for MARS (red circles) with the unfolding technique while for `gammapy` (cyan diamonds) repeating a likelihood fit separating the events in the individual energy bin.

2.5.2 Sensitivity of the Instrument

The work presented here has been done in collaboration with J. Sitarek, who provided a preliminary estimation of the sensitivity I used to cross-check my calculation, and A. Moralejo who contributed to the discussion. Results presented here have been approved by the MAGIC collaboration.

A second technical task undertaken during this thesis was the estimation of the sensitivity of the instrument as a function of the observation time. The sensitivity curves shown in this section represent, for a given observation time, the potential differential energy flux measurable with the instrument returning a significant detection. A detection is defined by the following three conditions:

- a significance, expressed as a S sigma result through the Li and Ma formula in Eq. 2.26, $S_{\text{Li Ma}} \geq 5$. We set $\alpha = 1/3$ by selecting three OFF reflected regions;
- a minimal number of 10 gamma ray counts within the ON region, $N_{\text{EX}} \geq 10$;
- a number of source counts above 5% of the background counts, expressed as $N_{\text{EX}} \geq 0.05\,\alpha\,N_{\text{OFF}}$, meaning a determination of the the background level with a 5% accuracy.

The Crab nebula data sample of the performance paper is used for this study, it consists of 11 hours of observation in the low zenith range $0° - 30°$, for which showers from photons with energies as low as $\sim 50\,\text{GeV}$ can be reconstructed.

The training procedure to estimate the significance starts by selecting half of the data sample, that we will refer to as the train sample, to optimise the analysis cuts. Given an energy bin, the rate of source and background counts, N_{EX} and N_{OFF}, and hence the significance, will depend on the size of the ON / OFF regions (expressed through the squared angular distance of the events from the centre of the region, θ^2) and the cut on the *hadronness* value (the variable returned by the RF classifier) chosen to accept the events as photons. The 2-dimensional histogram of the rates of source events, shown in Figure 2.20, illustrates such dependency in the (estimated) energy bin between 126 and 200 GeV.

As is expected the looser the analysis cuts, the larger the rate of source events surviving them. From the rates as a function of the (hadronness, θ^2) values, given a certain observation time t_{obs}, one can estimate the source and background counts expected from a source like the Crab nebula ($N_{\text{EX, Crab}} = rate_{N_{\text{EX}}} \times t_{\text{obs}}$, $N_{\text{OFF, Crab}} = rate_{N_{\text{OFF}}} \times t_{\text{obs}}$) and then the fraction of Crab excesses (i.e. the factor for which $N_{\text{EX, Crab}}$ has to be multiplied or divided) to verify all the detection conditions. In other words by using the rates of a Crab sample, for a given observation time, for each set of cuts, we obtain the factor of Crab excesses, or the flux in Crab Units (C.U.), corresponding to a $5\,\sigma$ detection. The pair (hadronness, θ^2) of cuts minimising the sensitivity is the one corresponding to the maximum C.U. fraction. To obtain an unbiased result, the optimised (hadronness, θ^2) cuts at each observation time are applied to the remaining half of the data sample, known as the test sample. The differential flux sensitivity at each observation time is converted from C.U. to SED units ($\text{erg}\,\text{cm}^{-2}\,\text{s}^{-1}$), using the Crab nebula SED from the performance

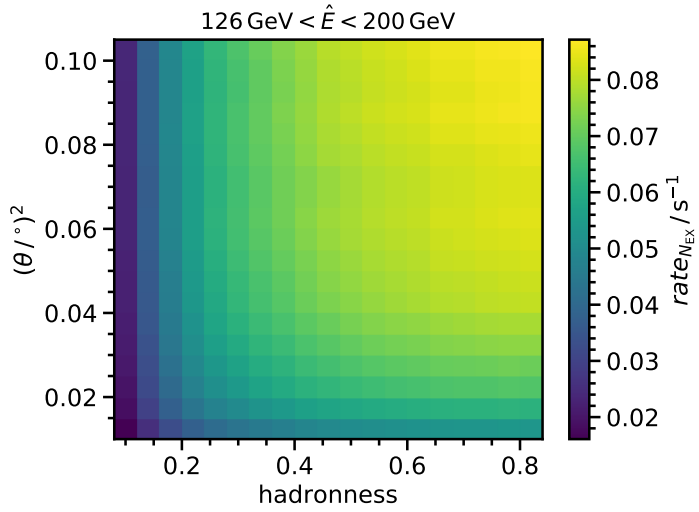

Figure 2.20: Rate of source events with estimated energy between 126 and 200 GeV, as a function of hadronness and θ^2 cuts, for the Crab nebula. The significance (in Crab nebula flux units) is computed, given a similar rate of background events, by finding in each (*hadronness*, θ^2) bin the fraction of Crab events verifying the detection conditions.

paper (Eq. 1 in Aleksić et al. 2016b). Figure 2.21 illustrates the differential flux sensitivity (in SED units) as a function of the observation time. Since this result is computed on the Crab nebula sample its extent is limited to sources with a Crab-like spectrum (i.e. with a log parabolic differential flux spectrum with the values in Aleksić et al. 2016b). A comparison with the prospect sensitivity for CTA is shown in the same plot. The order of magnitude improvement in sensitivity for the next generation of IACT is discussed in the next chapter introducing the CTA observatory.

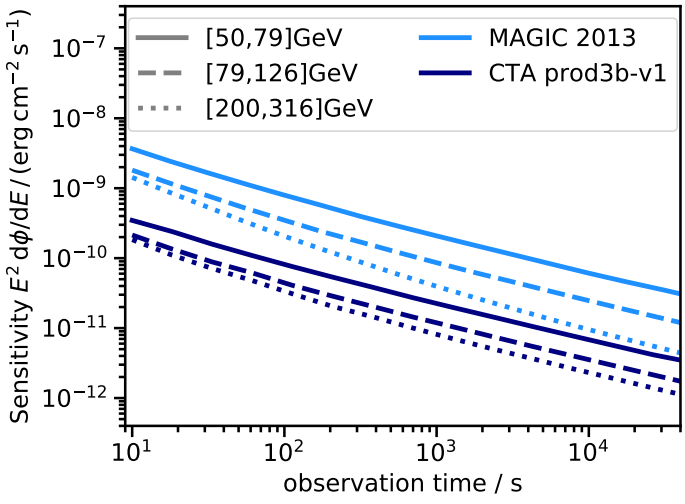

Figure 2.21: Differential flux sensitivity as a function of the observation time for MAGIC (light blue) and CTA (dark blue) in overlapping energy bins. The order of magnitude improvement in sensitivity is realised with arrays of tens of telescope each with a design optimised in a given energy range. In particular at energies up to few hundreds of GeV, the sensitivity is dominated by 4 IACTs of 23-meter diameter reflector: the Large Size Telescopes (see Figure 7 of Acharya et al. 2013), with a design very similar to MAGIC (Figure 2.22).

2.6 Towards the Future: The Cherenkov Telescope Array

After having discussed the VHE gamma-ray astronomy detection principles and analysis issues it is appropriate to close this chapter with an anticipation for the next generation of IACTs. Current IACTs have matured the imaging technique establishing the VHE gamma-ray domain as a legitimate branch of modern astronomy. The final step of this investiture will be the construction of the first VHE gamma-ray observatory: the Cherenkov Telescope Array (Acharya et al., 2013). Since 2006 gamma-ray astronomers from different collaborations have envisioned the next IACT experiment as an effort serving a global community rather than a few participating institutes. The community today counts almost 1500 scientist from 31 countries[XXV]. CTA will differentiate from the current experiments not only in technical, but also administrative and operational, aspects:

- a site in each hemisphere, the northern in the same site as MAGIC (as displayed in Figure 2.22) the second in Chile near the Paranal observatory, will grant full sky coverage;
- the installation of 19 telescopes in the Northern and 99 in the southern site, against the maximum of 5 of the current instrument will allow an order of magnitude boost in sensitivity, but also in the energy range covered that will span from tens of GeV to hundreds of TeV;
- the operation of CTA as an observatory foresee the allocation of part of its observational time through proposal of external scientist. The participation of a broad astronomical community, as explained in Section 2.5.1 and resumed in Chapter 3, calls for publicly available data and science tools.

CTA will progress the science cases explored so far in VHE gamma-ray astronomy (for a prospect of them see CTA Consortium 2019). Most noticeably the improved sensitivities will allow survey observations not only in the region of the galactic plane (as already performed by H.E.S.S., Abdalla et al. 2018a) but also, for the first time VHE extragalactic surveys (CTA could detect the current faintest extragalactic sources in 30 minutes, Dubus et al. 2013).

The different telescopes designs are shaped to cover different energy ranges relevant for different science cases. Large Size Telescopes (LSTs), 4 per site with 100 m spacing, a reflector of 23 m diameter and a design similar to MAGIC, will target the lower end of the energy range, $E_\gamma \leq 200\,\mathrm{GeV}$; they will be endowed with the fastest re-pointing targeting GRB follow-ups. Medium Size Telescopes (MSTs), with a reflector of 12 m diameter, will target the core energy range: $100\,\mathrm{GeV} \leq E_\gamma \leq 10\,\mathrm{TeV}$. Tens of MST with 100 m spacing will realise an array larger than the typical 150 m Cherenkov light pool, improving the direction reconstruction and the hadronic background rejection. Finally Small Size Telescopes SST, with a reflector of 4 m diameter will target the highest energies: $E_\gamma \geq 10\,\mathrm{TeV}$. Spaced as far as 200 m from each other they will cover the light pool of events with energies up to few $\sim 100\,\mathrm{TeV}$.

At the time of the writing of this thesis (early 2019) the construction of the first LST in the northern site has been completed, while the agreements for the southern site construction have been finalised. The

[XXV] Data from https://www.cta-observatory.org/about/cta-consortium/.

Figure 2.22: Artist view of CTA northern site at the ORM. Inverting the perspective of Figure 2.8, in ten years an observer sitting at the Gran Telescopio Canarias will see the MAGIC site populated with the CTA northern array. The central part of the array is occupied by the four Large Size Telescopes of 23-meter diameter reflectors, whose design is similar to the MAGIC one. Medium Size Telescopes with 12-meter diameter reflectors will complete the rest of the array. The installation of Small Size Telescopes is not foreseen at the moment for the northern site. Credit: Gabriel Pérez Diaz, image from https://www.cta-observatory.org/about/array-locations/la-palma/.

current CTA timeline foresees that operations will start in 2022 and that the array construction will be completed in 2025[XXVI].

[XXVI] https://www.cta-observatory.org/project/status/

3 | Towards a Multi-Instrument and Reproducible Gamma-Ray Astronomy

The work presented here is published in Nigro et al. (2019). I am the author of most of the analysis scripts (my contributions can be checked at this link) along with C. Deil. I was also editor of the paper in collaboration with R. Zanin. J.E. Ruiz set up all the on-line assets ensuring the reproducibility of this work. R. Bird, T. Hassan, T. T. Y. Lin and N. Kelley-Hoskins are responsible for the VERITAS DL3 data hereby used; K. Bruegge and M. Noethe for the FACT DL3 data and the authors in H.E.S.S. Collaboration (2018) for the the H.E.S.S. DL3 data. The remaining authors of Nigro et al. (2019) have contributed to the IACT standardisation to the FITS format or to the `gammapy` software.

This chapter, along with Chapter 2, constitute the technical section of this thesis. After having introduced VHE gamma-ray astronomy in the previous chapter, here we discuss its technical status, specifically in terms of reproducibility of its results and shareability and interoperability of its data. The work here presented shows how a multi-instrument gamma-ray analysis that is fully reproducible can be realised relying solely on open-source software and on-line repository systems. The scope of this work is purely technical, its objective is to illustrate that once the effort of defining a common data format for gamma-ray instruments is finalised, then the desiderata of multi-instrument and reproducible analysis supported by open-source tools can be simultaneously achieved. We present an example of such analysis using observations of the Crab nebula from *Fermi*-LAT and four of the currently operating IACTs. The material in Nigro et al. (2019) and hereby presented is supported by a set of `python` scripts and interactive notebooks available at `https://github.com/open-gamma-ray-astro/joint-crab`; we will refer to them, from now on, as on-line material. The chapter is structured as follow: Section 3.1 introduces the FITS format and the endeavour to standardise the IACTs data to adopt it; Section 3.2 presents the gamma-ray instruments involved in this project; Section 5.2 the analysis technique used to combine the data. Section 3.4 closes the chapter with a status of the current tools and an outlook on the shareability and reproducibility topic.

3.1 Data Formats for Gamma-ray Astronomy

As we shall see in Chapter 4, in the second half of the XX century, the possibility to share data between different observatories was essential in the identification and classification of the first extragalactic astronomical sources. What started as cross observations between optical and radio catalogues blossomed, after the rise of X-ray astronomy in the sixties and gamma-ray astronomy in the nineties, in what today we identify as multi-wavelength astronomy. The introduction of the FITS format, technically described in Section 2.5.1, in the late seventies addressed the need for a standardised support to exchange images between different observatories. The format definition paper was published in 1981 (Wells et al., 1981) and was formally ratified by a resolution of the International Astronomical Union in 1982[I] that later created a FITS working group. Along the eighties the format evolved to incorporate data tables other than simple images. In the nineties it was adopted by the High Energy Astrophysics Science Archive Research Center at NASA that fostered its usage for the data of several of its missions. As an example, today all the high level data of the *Fermi*-LAT telescope are publicly released in FITS format. The FITS standard is constantly reviewed, conventions on coordinates and dates system constantly updated, metadata for instruments added. The latest version of the format (4.0) dates 2018[II].

Ground based gamma-ray astronomy, born as a branch of particle physics, fell heir not only to its detection techniques but also to its data analysis methodologies and tools. As a matter of fact many VHE gamma-ray experiments adopted the `ROOT` framework (commonly used by particle physicists) for their software and data. Neither common analysis software nor common data structure is shared between

[I] `https://fits.gsfc.nasa.gov/iaufwg/history/IAU_1982_resolution_c1.html`
[II] `https://fits.gsfc.nasa.gov/fits_standard.html`

the different experiments though. Hence, from the perspective of the current ground based instruments, we are faced with two setbacks. First, each combination of data from different experiments needs new custom expansions of the collaborations proprietary software. Second, a release of public legacy data at the end of the scientific life of the instrument would be impossible to decouple from a release of the collaboration analysis software, that shall then in turn be also maintained. Shifting the perspective to the future Cherenkov telescopes, we are instead faced with a challenge since the operation of CTA (introduced in Section 2.6) as an observatory poses the VHE gamma-ray community the problem of producing public data and analysis tools.

The effort in both directions has already started. Concerning the data format, as already mentioned in Section 2.5.1, a first version of a unified format for high level gamma-ray astronomical data has been achieved with the "Data Formats for Gamma-ray Astronomy" forum (Deil et al., 2017a), from now on identified with the acronym GADF (Gamma Astro Data Formats). The GADF specifics focus on the DL3 (enclosing event lists and IRF, see Section 2.4.5), being the data level best suited to ensure at the same time data reduction along with reproducibility and extensibility of high level scientific results (e.g. spectra, light curves). The GADF specifics are in principle targeted on IACT data but, as we shall see in this work for *Fermi*-LAT, can be extended to satellite instruments. Concerning the open-source analysis tools there are currently two example in development: `ctools` (Knödlseder et al., 2016) and `gammapy` (Deil et al., 2017b), both compatible with the aforementioned DL3 format. `gammapy` is chosen for this work.

3.2 Instruments Involved in This Project

We show an example of a multi-instrument reproducible analysis by estimating the gamma-ray spectrum of the Crab nebula using observations from *Fermi*-LAT and four of the exisiting IACT: MAGIC, the Very Energetic Radiation Imaging Telescope Array System (VERITAS), the First G-APD Cherenkov Telescope (FACT) and the High Energy Stereoscopic System (H.E.S.S.). The Crab nebula is chosen as the analysis target since it represents the reference source of VHE gamma-ray astronomy, being the brightest steady object in the VHE gamma-ray sky (Aharonian et al., 2004, 2006; Albert et al., 2008b; Aleksić et al., 2012b, 2016b) and being visible from all the aforementioned IACTs. *Fermi*-LAT data are publicly available through the Fermi Science Support Center[III].

Differently than IACT, operating in pointing mode, *Fermi*-LAT operates in survey mode, orbiting at $\sim$ 700 km altitude and covering the whole sky in roughly 3 hours. Hence its data are not broken in observational runs, as for the IACTs, with each run providing a different IRF accounting for the change of observation condition. *Fermi*-LAT has instead a stable IRF incorporated in the science tools, that is marginalised accounting for the details of the analysis to be performed (observation time elapsed, portion of the sky observed etc.). We use the *Fermi*-LAT science tools and analysis guidelines available from the Science Support Center to produce an event list and an IRF that we make compliant with the GADF specifications using `gammapy`. Concerning the IACTs, each of the aforementioned experiments produced

[III] https://fermi.gsfc.nasa.gov/ssc/

the DL3 data using their own proprietary software. The H.E.S.S. observations are part of an already public DL3 data release (H.E.S.S. Collaboration, 2018) and the FACT data are a sub-sample of a week of Crab nebula observation made public in 2017[IV] and have been produced using open-source software. A more detailed description of each of these instruments, along with the data made available, is provided in the following subsections. The instruments data sets can be interactively accessed via the notebook `1_data.ipynb` in the on-line material.

3.2.1 *Fermi*-LAT

The Large Area Telescope on board the Fermi Gamma Ray Space Telescope spacecraft (*Fermi*-LAT from now on, Atwood et al. 2009), launched in orbit in June 2008, is a pair-conversion telescope (see introduction of Chapter 2) designed to detect gamma rays in the energy range from tens of MeV up to 2 TeV (according to the latest catalogue in Ajello et al. 2017). For this work we used observations of the Crab nebula from 8 August 2008 to 2 August 2015. We selected all the Source class[V] events within a 30° radius from the Crab nebula position, hitting the detector with an angle smaller than 105° from the telescope zenith (to suppress the background due to gamma rays emitted by CR secondary interacting in Earth's atmosphere) and estimated energy between 30 GeV and 2 TeV. The Crab emission in gamma rays is a superposition of radiative processes due to the pulsar and the nebula. Since the nebula emission starts to dominates at tens of GeV we select 30 GeV as minimum energy threshold since we estimate it reduces the pulsar flux contamination to 10%. This calculation is interactively shown in the notebook contained in the on-line material, `5_crab_pulsar_nebula_sed.ipynb`. We use the *Fermi*-LAT science tools to compute the IRF and then we reduce it to a GADF compliant format using `gammapy`. We use `gtpsf` to compute the PSF and `gtexpcube2` to estimate a full-enclosure (i.e. dependent on the sky position $\boldsymbol{P}$ and the energy E) exposure, which we reduce to an effective area by scaling it with the observation time. It is estimated that the energy dispersion should cause a distortion of $\sim 5\%$ on the estimated spectrum at the highest energies *Fermi*-LAT is sensitive to[VI]. We represent the energy dispersion as a Gaussian distribution for $\hat{E}$ with mean 0 and standard deviation 0.05, constant over the sky position $\boldsymbol{P}$ and the true energy E.

3.2.2 MAGIC

The production of the MAGIC DL3 data is described in Section 2.5.1. The MAGIC collaboration agreed to release 2 observational runs in DL3 format supporting this project, they are taken from the larger sample of observations of the Crab nebula used to assess the telescope performance after the 2012 upgrade (see Section 2.3.1 and, Aleksić et al. 2016b).

[IV] `https://fact-project.org/data/`
[V] Events with a high probability of being classified as photons and suited for most of the analyses.
[VI] `https://fermi.gsfc.nasa.gov/ssc/data/analysis/documentation/Pass8_edisp_usage.html`

3.2.3 VERITAS

VERITAS is an array of 4 IACTs with reflectors of 12 m diameter and a FoV of 3.5°, located near the site of the original Whipple 10 m telescope, at the Fred Lawrence Whipple Observatory in Arizona, USA. VERITAS started operations in 2007 (Holder et al., 2006) and underwent two major upgrades, namely the relocation of one of the telescopes in 2009 (Perkins et al., 2009) and the upgrade of the camera PMTs in 2012 (Kieda et al., 2014). As MAGIC, VERITAS released two observational runs, amounting to roughly 40 minutes of data acquisition, in DL3 format. The DL3 data belong to the period between the two aforementioned upgrades. Observation are performed in wobble mode with an offset of 0.5 deg from the camera centre, at small zenith angle $< 20°$. The IRF released are of point-like type, generated for a source sitting at 0.5° offset from the FoV centre, with a directional cut of 0.1° on the simulated events direction from the source position.

3.2.4 FACT

FACT (Anderhub et al., 2013) is a single imaging Cherenkov telescope with a reflector of 4 m diameter and a FoV of 4°. Reusing one of the old HEGRA mounts at the ORM, FACT has the objective to test the use of silicon photo-multipliers SiPM cameras in IACTs. It is also the first IACT with automatic remote operations (Nöthe et al., 2018) that does not require observers on site. The DL3 data used for this work were already made public from the collaboration, that in 2017 released a full week of Crab nebula observations dated 2013. The observations here used, amounting to ~ 10 hours of data acquisition, were conducted in wobble mode with an offset angle of 0.6° from the camera centre, at zenith angles smaller than 30°. The IRF of point-like type are generated with a directional cut of 0.17° on the simulated events direction from the source position.

3.2.5 H.E.S.S.

H.E.S.S. is a system of 5 IACTs located on the Namibian Khomas Highland. The array started operations in 2003 with 4 telescopes with reflectors of 12 m diameter and FoV of 3.5°. This stage of operations, referred to as Phase-I, ended in 2012 when a fifth telescope with a reflector of 28 m diameter and a FoV of 3.5° was added in the centre of the previous array initiating the so called Phase-II. For this work 4 data runs from the Crab nebula Phase-I observations were used, they are part of the first public DL3 data release (H.E.S.S. Collaboration, 2018). Observations are performed in wobble mode with 2 runs pointing the Crab nebula with an offset of 0.5°, and 2 runs with an offset of 1.5°, from the FoV centre. The zenith ranges from 45° to 50° given the location of the observatory in the southern hemisphere and the culmination of the Crab at high zenith angles. H.E.S.S. released full-enclosure IRF.

3.3 A Joint Analysis of The Crab Nebula

The likelihood method introduced in Section 2.4.6 is adopted to estimate the differential flux spectrum of the Crab nebula. Since most of the IACTs have made available point-like IRFs we perform a point-

like analysis, reducing the H.E.S.S. and *Fermi*-LAT full-enclosure IRFs to a point-like format. After presenting the results of this method, this section further discusses a simple sampling technique to estimate the error band on the differential flux and a modified likelihood method accounting for the systematic uncertainty on the energy scale of each instrument.

3.3.1 Likelihood Definition

We assume for the differential flux spectrum $\mathrm{d}\phi/\mathrm{d}E$ of the Crab nebula a log parabola function, Eq. 2.30, pointed out in the literature as the best analytical model to cover the broad spectrum of the source in gamma rays over several decades in energy (Aleksić et al., 2015). A joint likelihood is built factoring a term for each instrument

$$\mathcal{L}(\boldsymbol{\Lambda}|\boldsymbol{\mathcal{D}}) = \prod_{i=1}^{n_{\mathrm{instr}}} \mathcal{L}_i(\boldsymbol{\Lambda}|\boldsymbol{\mathcal{D}_i}). \tag{3.1}$$

Here the index i runs on each instrument and $\mathcal{L}_i(\boldsymbol{\Lambda}|\boldsymbol{\mathcal{D}_i})$ follows the definition in Eq. 2.27, $\boldsymbol{\Lambda}$ represents the log parabola parameters (same for all the data sets) and $\boldsymbol{\mathcal{D}}_i$ represent the i-th data set. The results of such a likelihood are referred to as *joint fit* results, from now on. For consistency we also obtain the spectrum of each data set separately (i.e. simply using Eq. 2.27 or fixing i in Eq. 3.1). The data set $\boldsymbol{\mathcal{D}}_i$ for the i-th likelihood term are the ON and OFF counts extracted for the i-th instrument.

The dimension of the ON region for all the data sets is reported in Table 3.1 as R_{ON}. For all the instruments that have provided point-like IRFs, R_{ON} coincides with the size of the directional cut applied on the MC simulations. The OFF region is defined differently for *Fermi*-LAT and for the IACT. As the IACTs have a small FoV and perform observations in wobble mode, the reflected regions method is particularly suitable for their background subtraction, as illustrated in Figure 2.13. For *Fermi*-LAT instead the ring background method is used defining the OFF region as an annulus of internal and external radius 1° and 2°, respectively. The same binning in estimated energy is selected for all the instruments: 20 bins per decade between 10 GeV and 100 TeV. The values of the minimum and maximum energy thresholds $\left[\hat{E}_{\mathrm{min}}, \hat{E}_{\mathrm{max}}\right]$ in Table 3.1 specify per each instrument i the energy bins outside which the Likelihood values are not computed. The choice of such limits for the *Fermi*-LAT data set are given in Section 3.2.1. For the IACTs, $\hat{E}_{\mathrm{min}}$ is an energy threshold for the analysis computed by each experiment and written in the metadata of the DL3 files. It depends on the observation conditions, mostly on the zenith angle of the observations. $\hat{E}_{\mathrm{max}}$ is instead fixed to 30 TeV to fully cover the energy range of the IACTs containing events.

Figure 3.1 illustrates the histograms of the estimated source events (or excesses) against the estimated energy, per each data set, computed using Eq. 2.25 and stacking over the observational runs. Table 3.1 also reports the total number of observed ON and background events (i.e. the OFF events scaled by the ratio of the exposures α) per each dataset, summed over all observations and over all the energy bins. Concerning the instrument IRFs, in order to perform a joint point-like analysis, and in particular in order to estimate the predicted counts with the same convolution in Eq. 2.28, the *Fermi*-LAT and H.E.S.S. full-enclosure IRFs have to be reduced to a point-like format, dismissing the dependency on the event coordinate $\boldsymbol{P}$. For *Fermi*-LAT, assuming that the effective area is uniform in a small area

Dataset	$T_{\rm obs}$	$\hat{E}_{\rm min}$ / TeV	$\hat{E}_{\rm max}$ / TeV	$N_{\rm ON}$	$N_{\rm BKG}$	$R_{\rm ON}$ / °
Fermi-LAT	∼7 yr	0.03	2	578	1.2	0.30
MAGIC	0.66 h	0.08	30	784	129.9	0.14
VERITAS	0.67 h	0.16	30	289	13.7	0.10
FACT	10.33 h	0.45	30	691	272.8	0.17
H.E.S.S.	1.87 h	0.71	30	459	27.5	0.11

Table 3.1: Crab nebula observations from the different instruments. $T_{\rm obs}$ represents the observation time. $\hat{E}_{\rm min}$ and $\hat{E}_{\rm max}$ identify the energy range of the analysis, i.e. the values within which the maximum likelihood method in is applied. $N_{\rm ON}$ and $N_{\rm BKG} = \alpha N_{\rm OFF}$ are the number of total and background events, respectively, estimated in the circular signal (ON) region with a radius $R_{\rm ON}$. Table from Nigro et al. (2019).

surrounding the source (i.e. in the 1°-radius ON region), the $\boldsymbol{P}$ dependency is removed simply taking the effective area value at the source position. Then, in each estimated energy bin, a containment efficiency is computed integrating the PSF over the signal region. In a similar way the $\boldsymbol{P}$ dependency is dismissed in the H.E.S.S. IRF by taking the value at the source offset and computing a containment correction in each estimated energy bin based on the PSF.

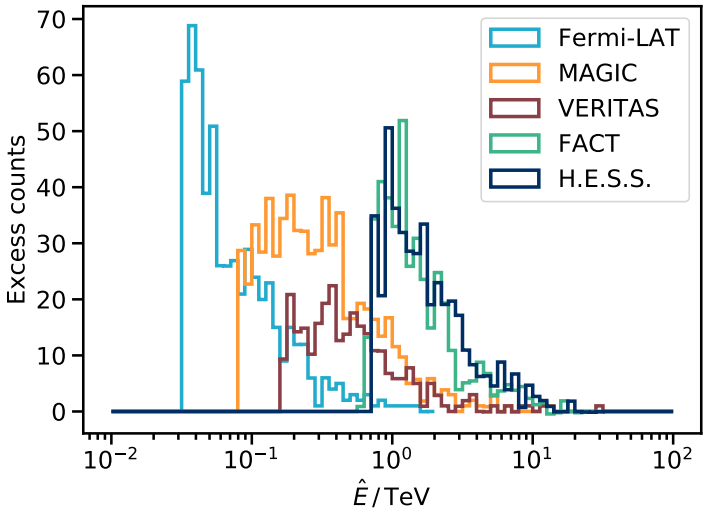

Figure 3.1: Histograms of the estimated energies of the Crab nebula source events for all the DL3 data set, from the left: *Fermi*-LAT (light-blue), MAGIC (yellow), VERITAS (brown), FACT (green), H.E.S.S. (dark purple). The $N_{\rm EX}$ for each energy bin is obtained from Eq. 2.25 summing over all the observational runs. Figure from Nigro et al. (2019).

Spectral Analysis Results

The parameters of the assumed spectral model left free to vary to maximise the likelihood are: normalisation, the first and the second spectral indexes of the log parabola, i.e. $\boldsymbol{\Lambda} = (\phi_0, \Gamma, \beta)$. The reference energy, E_0, is usually not fitted but chosen to have a value minimising the correlation between the other spectral parameters[VII]. In this case, in order to directly compare the value of the fitted parameters we

[VII] For a definition see Section 4 of H. E. S. S. Collaboration and LAT Collaboration (2017).

fix $E_0 = 1\,\mathrm{TeV}$ both for the joint and for the individual data set fits. This choice will introduce larger errors and strong correlation between the spectral parameters in the data sets for which E_0 is close to the edges of the allowed energy range (especially *Fermi*-LAT). The SEDs resulting from joint and individual likelihood fit are shown in Figure 3.2. As a comparison we show with a dotted gray line the spectrum of Meyer et al. (2010) obtained fitting the gamma-ray emission with an inverse Compton radiative process. The best-fit values for the spectral parameters are shown in Table 3.2, while Figure 3.3 shows the likelihood contours in the parameters space corresponding to the 68 % probability content. The effect of the afore-mentioned choice of E_0 is visible in the large and strongly correlated *Fermi*-LAT errors. The results of the fit can also be interactively explored in the on-line material `2_results.ipynb`.

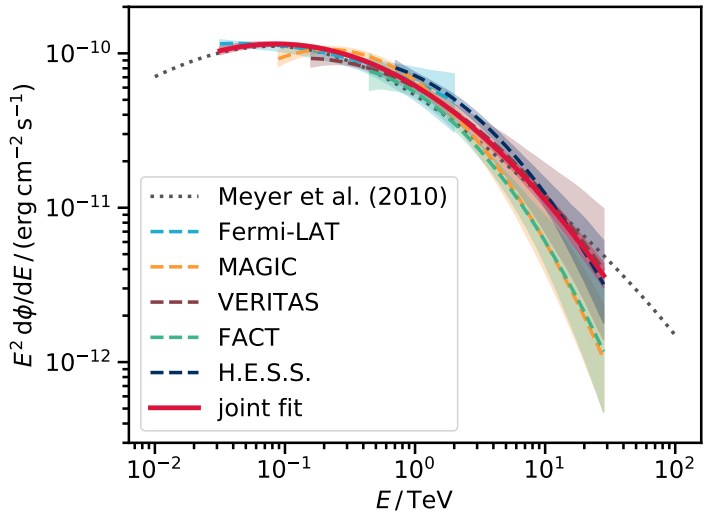

Figure 3.2: Log-parabolic SED of the Crab nebula obtained with the likelihood method of Eq. 3.1, combining all the data sets (thick red line) and fitting the data sets individually (dashed lines with same color code of Figure 3.1). The shadowed areas represent the differential flux error bands, their computation is described in Section 3.3.2, the theoretical flux spectrum from Meyer et al. (2010) is shown with a dashed gray line. Figure from Nigro et al. (2019).

Dataset	$\phi_0\,/\,(\mathrm{TeV^{-1}\,cm^{-2}\,s^{-1}})$	Γ	β
Fermi-LAT	$(4.04 \pm 1.01) \times 10^{-11}$	2.37 ± 0.24	0.14 ± 0.13
MAGIC	$(4.15 \pm 0.30) \times 10^{-11}$	2.60 ± 0.10	0.44 ± 0.11
VERITAS	$(3.76 \pm 0.36) \times 10^{-11}$	2.44 ± 0.09	0.26 ± 0.17
FACT	$(3.49 \pm 0.30) \times 10^{-11}$	2.54 ± 0.22	0.42 ± 0.31
H.E.S.S.	$(4.47 \pm 0.29) \times 10^{-11}$	2.39 ± 0.18	0.37 ± 0.22
joint	$(3.85 \pm 0.11) \times 10^{-11}$	2.51 ± 0.03	0.24 ± 0.02

Table 3.2: Best-fit values estimated with the likelihood in Eq. 3.1 for the spectral parameters (ϕ_0, Γ, β). Results from the individual instruments and from the joint-fit are shown. Table from Nigro et al. (2019).

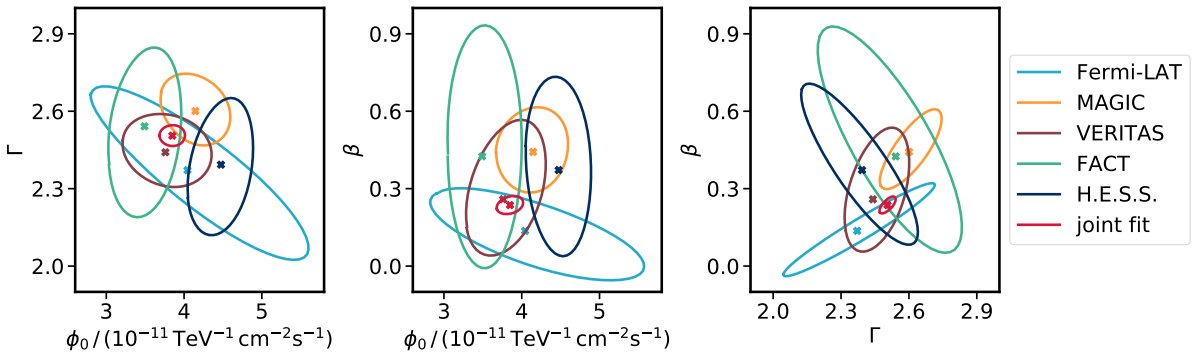

Figure 3.3: Likelihood contours estimated with the likelihood in Eq. 3.1 for the spectral parameters (ϕ_0, Γ, β) corresponding to 68 % probability content. Results from the individual instruments (same color code of Figure 3.1) and from the joint-fit (red) are shown. Figure from Nigro et al. (2019).

3.3.2 Statistical and Systematic Error Evaluation

SED Butterfly

A sampling technique is proposed here to propagate the error from the fitted spectral parameters to the differential flux spectrum. It is assumed that the likelihood of the spectral parameters has a multivariate normal distribution determined by the fit result. In particular, the mean of the distribution is defined by the array with the best-fit parameters $\boldsymbol{\mu} = \hat{\boldsymbol{\Lambda}} = (\hat{\phi_0}, \hat{\Gamma}, \hat{\beta})$ while the covariance of the distribution is given by the covariance matrix of the fitted parameters $\boldsymbol{\Sigma} = \hat{\boldsymbol{V}}_{\hat{\boldsymbol{\Lambda}}}$. This distribution is randomly sampled hundreds of times and the differential spectra corresponding to each sampled triple of spectral parameters are computed. The lower and upper errors on the differential flux $[(\mathrm{d}\phi/\mathrm{d}E)_{\mathrm{low}}, (\mathrm{d}\phi/\mathrm{d}E)_{\mathrm{up}}]$ at a given energy are obtained taking the upper and lower flux quantiles corresponding to a 68 % containment of all the different spectra realisations. Figure 3.4 shows the application of the method to the VERITAS dataset: the thin gray spectral represents 100 realisations of the log parabola obtained by randomly sampling the multivariate distribution. The black dashed line is the spectrum corresponding to the best-fit result, the thick solid lines delimit the error band containing, at each energy, 68 % of the fluxes values.

Systematic Uncertainty on the Energy Scale

Systematic uncertainties affecting IACTs system are commented upon in Section 2.4.7. In order to account for systematic uncertainties two approaches are followed. The first, remarked in Section 2.4.7 and applied in the MAGIC performance assessments (Aleksić et al., 2012a, 2016b), consists of selecting the main systematic factors and study how they distort a spectral measurement. This approach would add an additional uncertainty term in a spectral parameter result, e.g. for the flux normalisation: $\phi_0 \pm \sigma_{\phi_0,\mathrm{stat.}} \pm \sigma_{\phi_0,\mathrm{syst.}}$. The second approach is to incorporate such uncertainties in the likelihood, as Dickinson and Conrad (2013) do for the systematic uncertainty on the background subtraction. This approach returns

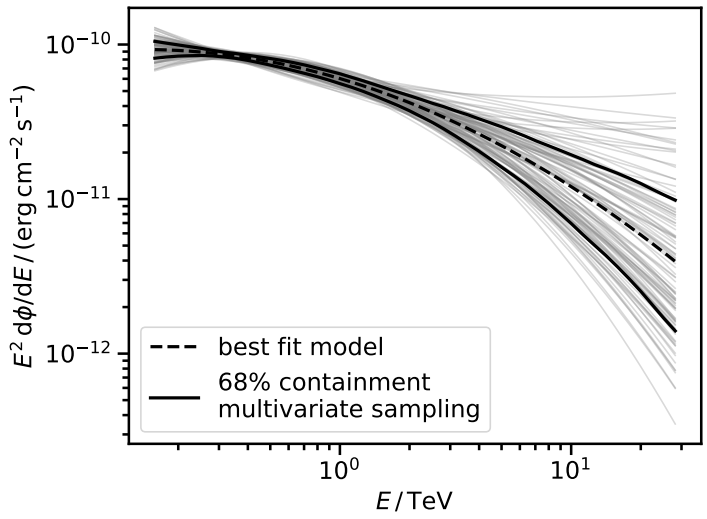

Figure 3.4: Multivariate sampling technique to determine the flux error band, VERITAS data set example. Each thin gray line correspond to a log parabola spectrum computed with a triple of parameters (ϕ_0, Γ, β) randomly sampled by a multivariate normal distribution defined with mean and covariance returned by the likelihood fit. The dashed black line corresponds to the spectra computed with the best-fit parameters $(\hat{\phi_0}, \hat{\Gamma}, \hat{\beta})$. The solid black lines mark, at each energy, the flux quantiles realising a 68 % containment of all the random spectra realisation. Figure from (Nigro et al., 2019).

for a spectral parameter a global uncertainty including both statistical and systematic effects, again, considering the flux normalisation as an example: $\phi_0 \pm \sigma_{\phi_0,\mathrm{stat.+syst.}}$. We choose the second of these approaches, modifying the likelihood in Eq. 3.1 to include the uncertainty on the energy scale of the different instruments. Following the approach of Dembinski et al. (2017), a constant relative bias on the energy of each instrument, z_i, is introduced

$$z_i = \frac{\tilde{E} - E}{E} = \frac{\tilde{E}}{E} - 1, \tag{3.2}$$

where $\tilde{E}$ is the energy reported by the instrument (the one the instrument evaluates as true energy after accounting for the energy dispersion after the IRF forward folding, Eq. 2.28) and E is the actual energy of each single event. z_i is Gaussianly distributed, with mean 0 and standard deviation δ_i, that is the systematic uncertainty on the energy scale that the experiment claims. The assumed spectral model for the differential flux is modified to account for the energy scale in

$$\frac{\mathrm{d}\tilde{\phi}}{\mathrm{d}\tilde{E}} = \frac{\mathrm{d}\phi}{\mathrm{d}E}\frac{\mathrm{d}E}{\mathrm{d}\tilde{E}} = \phi_0 \left(\frac{E/(1+z)}{E_0}\right)^{-\Gamma+\beta\log_{10}\left(\frac{E/(1+z)}{E_0}\right)} \left(\frac{1}{1+z}\right). \tag{3.3}$$

This is the spectral model that we will convolve with the IRF components, as in Eq. 2.28, to compute the predicted counts. The energy biases are included among the spectral parameters to be fitted: $\boldsymbol{\Lambda} = (\phi_0, \Gamma, \beta, z_1, ..., z_{n_{\mathrm{isntr}}})$, and the normal distribution ($\mathcal{N}$) of each parameter is factored in the likelihood

$$\mathcal{L}(\boldsymbol{\Lambda}|\boldsymbol{D}) = \prod_{i=1}^{n_{\mathrm{instr}}} \mathcal{L}_i(\boldsymbol{\Lambda}|\boldsymbol{\mathcal{D}_i}) \times \mathcal{N}(z_i; 0, \delta_i^2). \tag{3.4}$$

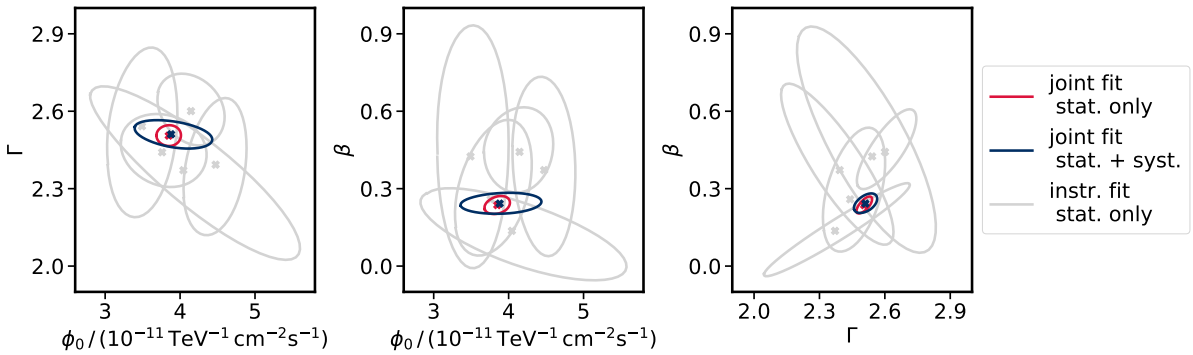

Figure 3.5: Likelihood contours estimated for the spectral parameters (ϕ_0, Γ, β) corresponding to 68 % probability content using the likelihood in Eq. 3.1 (red) and the modified likelihood in Eq. 3.4 (blue). The larger contours for the modified likelihood incorporate the uncertainty on the energy scale between the different instruments. The statistical likelihood contours from the individual instruments are displayed in gray, for comparison. Figure from Nigro et al. (2019).

The effect of the energy biases is that the spectral parameters are adjusted commonly to all dataset but an additional data-set-dependent shift in energy of the spectrum is allowed. This shift is constrained Gaussianly by the limits on the energy scale δ_i that the experiment claims. It is possible to revert the modified likelihood in Eq. 3.4 to the simple statistical likelihood of Eq. 3.1 by setting z_i to 0 for all the instruments. The spectral results and the probability contours for the modified likelihood are shown in Figure 3.5. The modified likelihood fit can be re-performed interactively with the notebook `3_systematics.ipynb` in the on-line material.

3.3.3 A Prototype For a Future Gamma-ray Astronomy Publication

In this section we focus on the on-line assets of this work and clarify how a public release of a material accompanying a future gamma-ray astronomy publication can be implemented.

Reproducibility

The `GitHub` repository containing the on-line material delivers all the DL3 data sets and the analysis scripts to reproduce the results of this chapter (and of Nigro et al. 2019). It also includes interactive `jupyter`[VIII] notebooks that act as supporting documentation: they clarify aspects of the analysis and illustrate the content of the data. They can be executed in a web browser without any software installation through the `Binder`[IX] service. The scripts are organised in order to be executable in a simple command-line fashion, e.g. one can perform the likelihood fit at Eq. 3.1 with the command `make.py fit-spectra`, or reproduce Figure 3.2 via `make.py plot-seds`. All the python software dependencies are accounted for through a `conda`[X] configuration file that can build a virtual environment installing all the required

[VIII] https://jupyter.org
[IX] https://mybinder.org/v2/gh/open-gamma-ray-astro/joint-crab/master?urlpath=lab/tree/joint-crab
[X] https://conda.io

packages. Instruments like `GitHub` and the `conda` environments ensure only a short term reproducibility, whose extent corresponds to the software maintenance. A longer, medium-term, preservation can be ensured with a `Docker` container (https://hub.docker.com/r/gammapy/joint-crab). A container is a light-weight image of an operative system, i.e. a standalone software unit that includes everything needed to run an application: software tools, libraries and code. Such medium-term reproducibility, independent of the software status (since a versioned copy of it is embedded in the container) is also limited by the maintenance of `Docker`, or of similar container systems, themselves. Finally, archival services as `zenodo`[XI] can host any digital artefact associated with a publication, making it open access and tagging it with a permanent Data Object Identifier (DOI), making the code and data citable exactly as any other scientific publication. The digital artefacts associated with this work can be for example cited as Nigro et al. (2018).

Extensibility

As it is understandable from the likelihood formulation in Eq. 2.27 and Eq. 3.1 the ON and OFF counts distributions and the reduced IRFs are the only information needed to perform a likelihood estimation of the spectrum. Hence releasing the results of the spectrum extraction as we do in this work using the `OGIP`[XII] format enhance their re-usability (the latter can be examined in the notebook `1_data.ipynb` in the on-line material). As a side note, such a format is also compatible with the `sherpa` tools (Freeman et al., 2001). Releasing the products of the spectral extraction can be very valuable for astronomers not associated with a collaboration. If they were to fit a spectra with a radiative model they would often have access only to the final published spectral points (without correlation matrix attached). Having access instead to the ON and OFF and IRF arrays (in OGIP format) would grant them the possibility to build a likelihood as in Eq. 2.27 or Eq. 3.1 assuming for $\mathrm{d}\phi/\mathrm{d}E$ any arbitrary radiative model. In the notebook `4_naima.ipynb` attached to the on-line material we show a practical implementation: we load the results of the spectrum extraction and re-perform the likelihood fit this time using for the assumed spectrum $\mathrm{d}\phi/\mathrm{d}E$ a theoretical synchrotron-self Compton radiative model computed with the `naima` Python package (Zabalza, 2015).

3.4 Outlook: Common, Open and Reproducible, the Future of Gamma-Ray astronomy

This work represents the first multi-instrument, fully-reproducible gamma-ray analysis. The gamma-ray spectrum of the Crab nebula is estimated using data from *Fermi*-LAT and four of the current generation IACTs. Given the DL3 data files compliant with the GADF format provided by the collaborations, this work achieves all its results relying exclusively on open-source assets: science tools and archival systems. It also represents the first joint release of data from the major operating VHE gamma-ray instruments.

[XI] https://zenodo.org
[XII] https://gamma-astro-data-formats.readthedocs.io/en/latest/spectra/ogip/index.html

From the point of view of the status of the tools, having all the IACTs but H.E.S.S. released point-like IRFs, with the current status of the DL3 data only joint point-like analysis can be performed, i.e. of sources at a given position of the FoV with IRFs pre-computed accordingly. Additionally the data format definition itself can be improved, particularly regarding the IRF dependency on the event position $\boldsymbol{P}$. The latter is now expressed as a radial offset from the centre of the FoV, hence assuming an azimuthally symmetric acceptance in the FoV. This is not the case for experiments as MAGIC (Prandini et al., 2015) and thus the actual data format does not suffice to produce full-enclosure IRFs for them.

The spirit of this work also remarks a general approach to share and publish results we wish the gamma-ray community would strive for. This approach can be conveyed through the three concepts of *common-data format*, *open-source software* and *reproducible results*. A common-data format allows for combination of data between different observatories. Given the common DL3 format we have performed an illustrative spectrum analysis of the Crab nebula using data from space and ground based telescopes. Once the common format is been finalised, open-source analysis tools can be developed or modified to support it; this will be of crucial interest for the future operations of CTA as an observatory. Reproducible results are an effortless consequence of open data and software and we practically show, using open access on-line repository system, how to release the data and software artefacts for a gamma-ray astronomy publication. A `GitHub` repository including data and scripts suffices for a short term preservation. To survive a loss of maintenance one can rely on standalone software container as the one provided by the `Docker` or on longer term archival systems as `zenodo` which also allow for a proper bibliographic acknowledgement. An open data release is also of crucial interest for physicists working on the theoretical interpretation as they can, for example, re-use the result of the spectrum extraction to test their models with proper likelihood methods instead of simple chi-square fit of spectral points.

4 High Energy Radiation from Active Galactic Nuclei

The broadband electromagnetic emission of Active Galactic Nuclei (AGN) constitutes the scientific focus of this dissertation. Galaxies hosting a massive[I] black hole (BH, $M_{\mathrm{BH}} > 10^5\,M_\odot$[II]) in their centre are identified as active if they display a central core with a continuum emission spanning, both in energy and luminosity, far beyond what is expected from typical stellar processes. Additionally, emission lines with line ratios characteristic of excitation by non-stellar fields are present. Both lines and continuum emission show significant variability over time. The highest energies of the continuum emission can reach the VHE gamma-ray regime. After having introduced the instruments and the methods of gamma-ray astronomy in Chapter 2 and 3, we will make use of them in Chapter 5 and 6 to characterise the VHE gamma-ray emission of two AGN observed by the MAGIC telescopes: PKS 1510-089 and NGC 1275. This Chapter therefore connects the technical and scientific sections of this thesis, providing an introduction to the objects analysed and to the mechanisms involved in the production of astrophysical gamma radiation. Section 4.1 outlines a brief observational history introducing the nomenclature developed with the progressive discovery of the same objects at different wavelengths. The latter will be overcome in Section 4.2 by providing a unified model for AGN. As introduced in Chapter 1 extragalactic sources as AGN can be considered responsible for the acceleration of CR particles at energies above the *ankle*. Section 4.3 illustrates how the typical power-law energy distribution of particles, paramount signature of astrophysical acceleration, is obtainable with the mechanism introduced in 1949 by Fermi. Section 4.4 introduces the notation to describe BHs and their immediate proximities, later used in Section 4.5 to describe the radiative processes modelling the broadband electromagnetic emission of AGN. A particular focus will be put on the processes framing the emission in a plasma of electrons that streams in a relativistic flow stretching outward from the centre of the galaxy.

4.1 Early Discoveries and Taxonomy

4.1.1 Seyfert galaxies

Before their existence as "Island Universes" (introduced by Kant 1755) became a common notion, galaxies were inadvertently included in the catalogues of nebulae and star clusters by Messier (1781) and in the New General Catalogue (NGC) by Dreyer (1888). NGC 1068 and NGC 4151, provided the first evidence that such objects were emitting broad optical lines (Fath, 1909; Campbell and Paddock, 1918). Their widths, interpreted as due to the Doppler effect (Slipher, 1917), pointed out to gas motion at velocities of several thousands of $\mathrm{km\,s^{-1}}$ ($3600\,\mathrm{km\,s^{-1}}$ for NGC 1068 and $7500\,\mathrm{km\,s^{-1}}$ for NGC 4151). Short exposures of some NGC sources revealed bright unresolved optical nuclei. Peculiarly, in Messier 87 the latter was accompanied by a slender optical jet (Curtis, 1918), as visible in Figure 4.1.

Hubble (1925), studying variable stars in NGC 6822, was the first to assign such objects "to a region outside the galactic system". Seyfert (1943) later noticed that 10 out of 12 selected NGC nebulae appeared in spiral galaxies, thus outlining the same class of objects. Khachikyan and Weedman (1971) distinguished

[I] For the BH nomenclature we follow Meier (2012), defining as *massive* BHs with $M_{\mathrm{BH}} = 10^5 - 10^8\,M_\odot$ and as *supermassive* BHs with $M_{\mathrm{BH}} = 10^8 - 10^{10}\,M_\odot$.

[II] $M_\odot = 1.989 \times 10^{33}\,\mathrm{g}$.

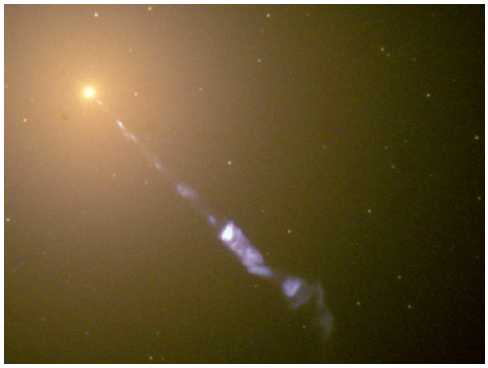

Figure 4.1: Hubble Space Telescope image of M87, the bright unresolved optical nucleus corresponding to the central engine is visible in yellow, the slender jet seemingly streaming away from it, in blue. Credit: J. A. Biretta et al., Hubble Heritage Team.

Seyfert objects as occurring in two different fashions. Both showed permitted and forbidden emission lines[III] but in the type 1 objects the permitted lines were considerably larger than the forbidden ones, reaching widths above few thousands of $\mathrm{km\,s^{-1}}$. Type 2 objects were instead characterised by narrow permitted lines, with the same width of the forbidden lines, i.e. below $1000\,\mathrm{km\,s^{-1}}$. With the partial data of the time, the picture emerged of a central source with a power $10^{42-44}\,\mathrm{erg\,s^{-1}}$ (the bright unresolved optical nucleus), surrounded, both in Seyfert 1 and 2 galaxies, by a gas streaming at velocities up to $1000\,\mathrm{km\,s^{-1}}$ and manifesting as a Narrow Line Region (NLR). In Seyfert 1 galaxies, an additional region of gas, on sub-parsec scales from the central source, a Broad Line Region (BLR) signalled the presence of gas flowing at even higher velocities, up to $0.1\,c$.

4.1.2 Radio Galaxies

The progresses in the radio technology driven by the Second World War fostered the development of radio astronomy in the second half of the twentieth century. Galaxies observed in radio displayed a typical dumbbell shape, with a central hotspot corresponding to the optical galaxy and two detached extended lobes, as visible in the Cygnus A radio image in Figure 4.2a. Readhead et al. (1978), employing the Very Long Baseline Interferometry VLBI technique, showed that the nucleus of NGC 6251 was actually connected to the lobes by a slender radio jet (similar to the thin radio filament visible between the lobes and the core of Cygnus A in Figure 4.2b).

The finding of a radio jet, similar to the one observed in optical for M 87, confirmed the theory of Blandford and Rees (1974) foreseeing the jet activity as arising from the nucleus. The first systematic sample of radio objects with known luminosities and distances was provided by the Third Cambridge Catalogue (3C) and its Revised edition (3CR, Bennett 1962), collecting all the sources with Dec$> -5°$ and spectral flux density $F_\nu(178\,\mathrm{MHz}) > 9\,\mathrm{Jy}$[IV]. Fanaroff and Riley (1974) classified the sample from the morphological point of view, distinguishing two classes of radio galaxies: the Fanaroff-Riley I class,

[III] Permitted and forbidden lines are the result of transitions between atomic states. In the first case the time scales for such transitions are smaller than the time scale between atomic collisions, therefore their probability of happening is high (hence "permitted"). Hydrogen and Carbon emission lines provide an example of permitted lines. The emission of "forbidden" lines is, on the contrary, hampered by time scales longer than the average atomic collision times, an example is the 500.7 nm line of doubly-ionised Oxygen. See Chapter 5 of Netzer (2013) for a review.

[IV] $1\mathrm{Jy} = 10^{-26}\,\mathrm{W\,m^{-2}\,Hz^{-1}}$.

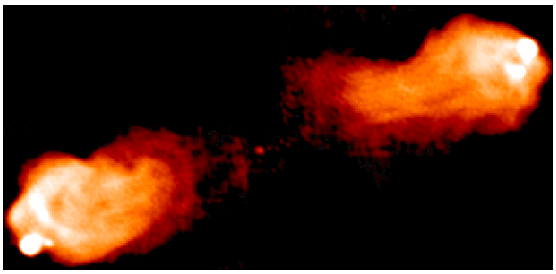

(a) 21 cm radio image of Cygnus A.

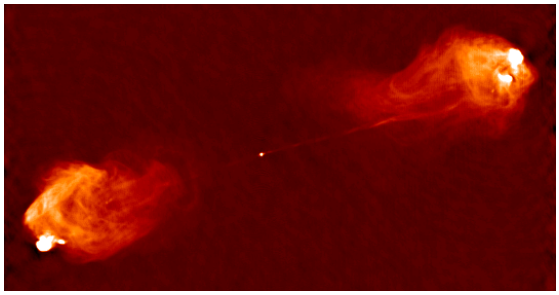

(b) 6 cm radio image of Cygnus A.

Figure 4.2: Radio image of Cygnus A at two different wavelengths. In the 21 cm image the sources appears as a Fanaroff-Riley II type, as its brightest emission is produced by the lobes. The image at 6 cm shows a thin radio jet connecting the central core to the massive outflow of the lobes. Credit: Philip Blanco and Chris Carilli, from https://cass.ucsd.edu/hexte/people/pblanco/cyga.html.

or "core dominated", with the brightest radio emission occurring near the position of the central optical galaxy; the more luminous Fanaroff-Riley II class, or "lobes dominated", with the brightest radio emission found in correspondence of the lobes (Cygnus A, in Figure 4.2a, is an example of Fanaroff-Riley II radio galaxy). Osterbrock et al. (1976) classified instead the optical counterparts of the 3CR sources identifying: Broad Line Radio Galaxies (BLRGs), showing emission lines similar to Seyfert 1 galaxies (pointing to velocities $> 10^4\,\mathrm{km\,s^{-1}}$) and Narrow Line Radio Galaxies (NLRGs), with narrow emission lines corresponding to those of Seyfert 2 galaxies (velocities $< 10^3\,\mathrm{km\,s^{-1}}$).

4.1.3 Quasi-Stellar Radio Sources

Many 3CR sources did not show an optical galaxy in spatial correspondence with the radio core. Among them, 3C 273, whose position was refined by Hazard (1962) with the lunar occultation technique[V], was found coincident to an optical point source with spectral lines that did not match any of the known elements. Schmidt (1963) and Oke (1963) interpreted them as compatible with the Hydrogen spectral series if the wavelength were to be shifted towards the red by a quantity

$$z = \frac{\lambda_{\mathrm{obs}} - \lambda_{\mathrm{em}}}{\lambda_{\mathrm{em}}} = 0.158. \tag{4.1}$$

According to the cosmological expansion of Hubble (1926), the object was receding at 16% of the speed of light and sitting at a distance of $\sim 700\,\mathrm{Mpc}$. Given the measured optical and radio fluxes, its distance implied a power (or luminosity) in those bands of 10^{46} and $10^{44}\,\mathrm{erg\,s^{-1}}$, respectively. Objects similar to 3C 273 (among them 3C 9 at $z = 2.012$), lacking an optical galaxy host and sitting at cosmological distances implying luminosities $> 10^{44}\,\mathrm{erg\,s^{-1}}$, were baptised "quasi-stellar radio sources" (QSRs) or shortly "quasars". During the first Texas Symposium (Robinson et al., 1965) John Wheleer suggested that the only engine capable of producing such luminosities could be a black hole accreting matter (see Section 4.4). QSRs showed many similarities with BLRGs: they presented the same broad emission lines and occurred in powerful Fanaroff-Riley II objects but they missed a detectable optical host galaxy. Hutchings et al. (1988) and Hutchings and Neff (1991) were able to resolve the optical "fuzz" surrounding some QSRs, showing their density profiles were compatible with those of normal optical and spiral galaxies. Therefore it was concluded that QSRs were the same object as a BLRGs but the optical emission of their nuclei outshined the host.

4.2 Unified Model

Trying to solve the puzzle of the compact appearance in radio of some QSRs, Roger Blandford introduced the cornerstone idea that different classes of AGN could be traced back to the same object with the different osbervational features arising because of the different viewing angle with respect to our line of sight.

[V] The size of an emitting object can be inferred from the diffraction pattern in its light curve that is generated by a non emitting source temporarily shadowing its image.

4.2.1 Unification of Compact Quasar and Radio Galaxies by Viewing Angle

Some of the 3CR sources observed in radio did not show the classical dumbbell appearance of Cygnus A in Figure 4.2. They were either compact, elongated of only few arcmin, as 3C 273, or were unresolved, as 3C 345. The spectral flux density of these sources in radio was also flat $F_\nu \propto \nu^0$, hence they were labelled Flat Spectrum Radio Quasars (FSRQs). Even observing them with the VLBI technique, capable at the time of arcmin resolution, all FSRQs displayed a point-like core with a single radio jet, of tens of arcmin. Blandford and Königl (1979) proposed that compact and unresolved QSRs were the same object as the extended dumbbell radio galaxies: the first being the same source as the latter but viewed with a small angle between their jet and the line of sight of the observer. The theory of Blandford and Königl elegantly accommodates two of the features observed in QSRs sources described in the following subsections.

Superluminal Motion

Tracing the path of a jet component in the sky and dividing the distance by the observational time occurred to cover it, an apparent velocity greater than c, i.e. a *superluminal motion*, can be obtained. The effect is illustrated in for 3C 279 in Figure 4.3: it seems the jet components traced by the red arrow has moved by 20 l.y.[VI] in 8 years (from 1992 to 1998), corresponding to a velocity of $\approx 10 \times 10^{10}\,\mathrm{cm\,s^{-1}}$.

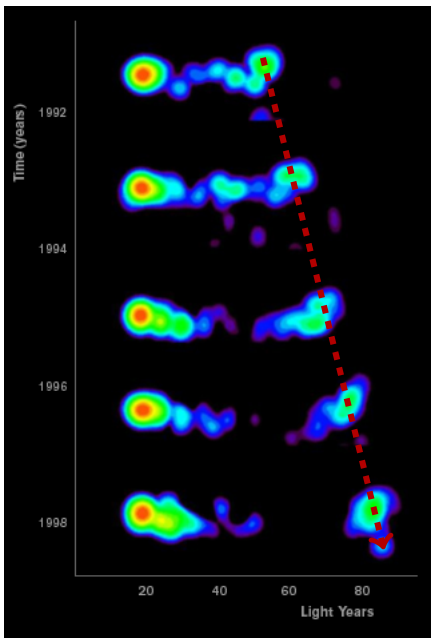

Figure 4.3: Superluminal motion visible in 3C 279. From 1992 to 1994 the source has moved 0.3 arcmin corresponding, given the distance, to 20 l.y.. This implies a velocity roughly 3 times the speed of light. Image from `http://user.astro.columbia.edu/~jules/UN2002/superluminal.html`.

The effect was predicted by Rees (1966) and observed by Cohen et al. (1971). The computational error resides in dividing the distance by the elapsed time on Earth. The formula to predict the apparent

[VI] 1 l.y. = 1 light year = 9.46×10^{18} cm.

velocity (accounting for the inclination angle between the jet and our line of sight, θ) reads

$$v_{\rm app} = \frac{\Delta x_{\rm app}}{\Delta t_{\rm app}} = \frac{v_{\rm jet}\sin\theta}{1-\frac{v_{\rm jet}}{c}\cos\theta}, \tag{4.2}$$

where the apparent distance between two points separated by emission times $\Delta t_{\rm em}$ is $\Delta x_{\rm app} = \Delta t_{\rm em} v_{\rm jet}\sin\theta$, with $v_{\rm jet}$ jet velocity, and the denominator is the apparent elapsed time $\Delta t_{\rm app} = \Delta t_{\rm em}(1 - v_{\rm jet}/c\,\cos\theta)$ accounting for the motion of the source.

Beaming

Let us consider a jet streaming with relativistic velocity $\mathcal{B} = v_{\rm jet}/c$ and bulk Lorentz factor $\Gamma = 1/\sqrt{1-\mathcal{B}^2}$[VII] in the observer frame. In the frame comoving with the jet a photon is emitted with frequency ν' and dimensionless energy $\epsilon' = h\nu'/m_e c^2$ (with h Planck's constant and m_e electron mass) at an angle $\theta' = \arccos\mu'$ from the jet axis. One can use the relativistic transformation in Appendix B (Eq. B.5) to obtain the energy and the angle under which this photon will be detected in the observer frame. Observed energies (or frequencies, equivalently) can be related with comoving emitted energies via $\epsilon = \delta_D \epsilon'$, defining the Doppler factor

$$\delta_D = \frac{1}{\Gamma(1-\mathcal{B}\mu)} \xrightarrow[\Gamma\gg1,\theta\ll1]{} \frac{2\Gamma}{1+\Gamma^2\theta^2}, \tag{4.3}$$

where the last limit stands for large jet Lorentz factors and small viewing angle. Two important observational features of compact QSRs are recovered:

- a photon emitted perpendicular to the jet direction $\mu' = 0$ will be observed at $\mu = \mathcal{B}$ (Eq. B.5). In the limit of large jet Lorentz factors and small viewing angles,

$$\mu = \mathcal{B} \xrightarrow[\Gamma\gg1,\theta\ll1]{} 1 - \frac{\theta^2}{2} = 1 - \frac{1}{2\Gamma^2}, \tag{4.4}$$

  hence the radiation emitted in a relativistic jet is collimated in the forward direction in a cone of angle $\theta \lesssim 1/\Gamma$;

- by proving that the emitted intensity I_ϵ[VIII] transforms as ϵ^3, hence with δ_D^3 one can derive that the luminosity (related to I_ϵ by an integration over the solid angle, see Section 4.5.1) transforms with the fourth power of the Doppler factor. Luminosities of jetted sources are boosted by δ_D^4 when transforming from the frame comoving with the jet to the one of the observer. Being $\delta_D \propto 1/(1+\Gamma^2\theta^2)$, it is then explained why the compact 3CR sources (with the smallest viewing angle θ) appear as the brightest in the radio catalogues and, if the optical radiation is produced in the jet, can even outshine their host.

[VII] As in Appendix B we indicate with capital letters $\mathcal{B}$, Γ the velocity and Lorentz factor, respectively, of the reference frames that we use for Lorentz boost transformation. Lower case β, γ are reserved for the particles velocity and Lorentz factor, respectively.

[VIII] Measured in erg cm^{-2} s^{-1} sr^{-1}, see Section 4.5.1 for its definition.

Blazars

FSRQs were not the only sources to display a quasar-like behaviour. Schmitt (1968) found that BL Lacertae, an object initially identified as a variable star, was actually a flat-spectrum radio galaxy, without an evident optical host. In contrast to FSRQs, optical emission lines were weak or almost absent in BL Lacertae. A red, strongly polarised continuum was observed in their place. Contrarily to most active galaxies, objects similar to BL Lacertae (from now identified as BL Lacs) and FSRQs could be detected all across the electromagnetic spectrum up to gamma-ray energies. BL Lacs and FSRQs were grouped under the common name of *blazars*, a term merging the BL Lacertae and the quasar attributes. Their broadband SED consists of two continuum components, displayed in Figure 4.4: the lower, peaking in the optical to X-ray regime, is due to synchrotron radiation of electrons accelerated in the jet; the higher, peaking in the gamma-ray regime, is often described with inverse Compton scattering of the same electrons on different target fields (a deeper discussion of the radiative processes is given in Section 4.5).

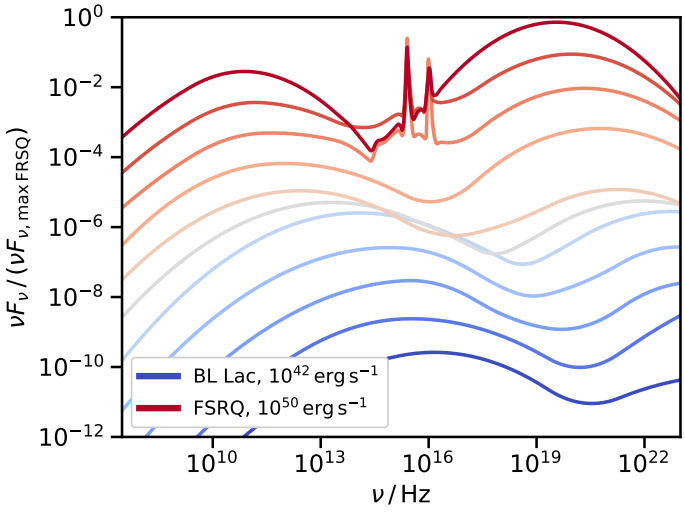

Figure 4.4: Blazar sequence from Rodrigues et al. (2018). The bolometric luminosities of the blazars seemingly anticorrelates with the peak frequency of their continuum components. BL Lacs (in blue) are the faintest objects of the sequence but also the ones with the highest frequency of the continuum peaks. Increasing the luminosity shifts the spectral peaks towards lower energies and the sequence culminates with FSRQs. In the latter emission lines produced by the BLR overlaps the continuum emission. The fluxes are normalzied to the maximum flux emitted by the brightest object. Spectra kindly provided by X. Rodrigues.

Fossati et al. (1998) and Ghisellini et al. (1998), collecting radio, X-ray data and the limited γ-ray observations provided by EGRET, found a remarkable negative correlation between the radio luminosities of the objects and the peak frequency of their SED components. The so-called *blazar sequence* was re-identified by Ghisellini et al. (2017) using the complete Third Catalogue of Active Galactic Nuclei (3LAC) detected by *Fermi*-LAT (Ackermann et al., 2015). The trend is nicely illustrated in Figure 4.4: BL Lac type objects show the lowest luminosities and present the synchrotron peak, ν_{syn}, in a range spanning from optical to X-ray frequencies while the Compton peak, ν_{C}, easily attains the VHE regime. Increasing the luminosities, ν_{syn} and ν_{C} shift towards lower frequencies reaching the THz and the MeV, respectively, for the most powerful objects completing the sequence, i.e. FSRQs. Figure 4.4 also displays the appearance of optical broad line emission for such objects, in contrast to the optical featureless spectra of the BL Lacs. Some authors have pointed out selection biases that could arise as a result of grouping blazars according

to their properties in different energy bands. An overview of these objections can be found in Section 6.6 of Padovani et al. (2017) and references therein.

4.2.2 Unification of Seyfert Galaxies by Viewing Angle

The viewing angle scheme introduced by Blandford and Königl (1979) for radio sources was applied also to unify Seyfert galaxy types by Antonucci and Miller (1985). They observed that in NGC 1608, a Seyfert 2 galaxy, broad emission lines were visible in polarised light, hinting at the fact that they were scattered by free electrons. The authors suggested Seyfert 1 and 2 galaxies could be considered as the same object if an obscuring structure, containing free electrons scattering the broad lines in polarised light, was introduced for the Seyfert 2 type. This dusty toroidal structure, tens of pc in radius, was surrounding the BLR. Seyfert 1 galaxies are therefore viewed with an angle above such obscuring torus (see Figure 4.5), displaying directly the lines emitted by the BLR. Seyfert 2 galaxies, instead, are viewed at a higher inclination angle, with the torus seen sideways, covering the BLR. The NLR lies outside the torus, presumably in a ionisation cone that is therefore visible in both sources. Direct imaging by the Hubble Space telescope of the narrow line ionisation cone of NGC 1068 (Evans et al., 1991) and of the dust torus of NGC 4261 (Jaffe et al., 1993) confirmed Antonucci and Miller's obscuration model.

4.2.3 Assembling a Global Picture

Despite the variety of observational appearances, the picture that arises from all the AGN typologies previously presented underlines the same components. Figure 4.5 attempts to illustrate them:

- the centre of the AGN and its gravitational fulcrum is a supermassive black hole, discussed in more detail in Section 4.4 and displayed as a black sphere in Figure 4.5. Its mass typically exceeds $10^5\,M_\odot$;
- the matter falling in the BH is accreted in an equatorial flow, depicted with the blue wings in proximity of the BH in Figure 4.5. The so-called *accretion disk* sits at distances smaller than a parsec (see Section 4.4) from the BH and in non-jetted AGNs is (directly and indirectly) responsible for the whole EM radiation. The thermal radiation from the gas in the disk results in a black-body spectrum peaking in the UV (Shields, 1978). Hot and diluted gas regions can form a corona around the disk in which the very same UV photons can be Compton up-scattered to X-ray energies. The radiation from the disk produces photoionisation of surrounding gas, generating large and narrow emission lines. Finally the UV radiation from the disk is absorbed and re-emitted in the IR by the dust torus (see Chapter 4-5 and 7 of Netzer 2013);
- gas clouds rotating with velocities of thousands of $\mathrm{km\,s^{-1}}$ form the BLR (represented with light blue ellipses in Figure 4.5). Typical distances from the BH are $0.01 - 1\,\mathrm{pc}$, densities reach values $> 10^9\,\mathrm{cm^{-3}}$. The origin of the clouds is not clear, it is suggested they could be generated by a flow of warm gas, a funnelled wind, rising from a small range of disk radii and driven by radiation pressure (Elvis, 2000);

- the NLR, represented as small azure points in Figure 4.5, is a region of photoionised gas less dense and fast than the BLR clouds ($v \lesssim 1000\,\mathrm{km\,s^{-1}}$, densities $10^{3-5}\,\mathrm{cm^{-3}}$). It expands in a conical area not obscured by the dust torus up to hundreds of pc along the torus axis. It is thought that the NLR is gas in the host galaxy photoionised by the accretion disk (Groves, 2007);

- the dust torus, the large red structure surrounding the disk in Figure 4.5, sits at distances $1-10\,\mathrm{pc}$ from the central source. It lies outside the sublimation radius of the central source and contains molecular and atomic dust. Its origin is the inflow of galactic material that eventually find its way to the central BH via the accretion disk. Alternatively, the torus is considered related to the disk by the same wind generating the BLR clouds (see Section 7.5.4 of Netzer 2013);

- extended radio galaxies and blazars present a relativistic outflow of plasma collimated up to the kpc scales and broadening in plumes up to Mpc scale. The mechanism launching the jet and the barionic content of the streaming material is still under debate, a broad overview on the topic is provided by Blandford et al. (2018). There is nonetheless a common understanding that the magnetic field transported by the disk from large scale distances is whirled by the environment just outside the BH and spun up to form a funnel of magnetic field lines collimating the jet. The extraction of angular momentum by the EM field lines threading the BH is described in yet another seminal paper due to Blandford and Znajek (1977). It is also clear that jets are the site of the acceleration of particles and an immediate example can be displayed using M 87 jet. The jet stretches as far as 1500 pc, even with the particles moving at almost the speed of light ($\beta \to 1$), it would have required more than 5000 years to reach that position. Now suppose that locally in the jet magnetic fields of the order $B = 0.01 - 10\,\mathrm{G}$ (range of values commonly used for modelling the synchrotron emission of AGN) can be found. The time over which a particle would lose all of its energy via synchrotron radiation is given by

$$t_{\mathrm{syn}}^{-1} = \frac{Z^4}{(m/m_e)^3}\frac{4}{3}c\sigma_{\mathrm{T}}u_B\beta^2\gamma, \tag{4.5}$$

  where Z is the charge of the particle in elementary charge units, m is the mass of the particle and m_e is the electron mass, σ_{T} is the Thomson cross section and $u_B = B^2/(8\pi m_e c^2)$ is the magnetic field energy density divided by the electron rest mass energy, β and γ are dimensionless velocity and Lorentz factor of the particle. Electrons and positrons (commonly deemed responsible for the synchrotron emission) with energies $\gamma = 10^2$ ($\approx 50\,\mathrm{MeV}$) would take 24 years in a 0.01 G magnetic field and only 8 days in a 10 G magnetic field to lose all their energy via synchrotron radiation. Increasing the energy to $\gamma = 10^5$ ($\approx 50\,\mathrm{GeV}$) would reduce the radiative time scale to 8 days for the 0.01 G magnetic field and 12 minutes for the 10 G magnetic field. Synchrotron radiative time scales are therefore incompatible with the millennial times required to reach kpc distances, the electrons could not reach such distances without losing all their energy to synchrotron radiation. This is an elementary demonstration, quoting Meier (2012), that particles are accelerated *in situ*.

Given the AGN components presented in this section, a unified model grouping all the aforementioned typologies can be identified. The latter is built by selecting a parameter that groups active galaxies in a

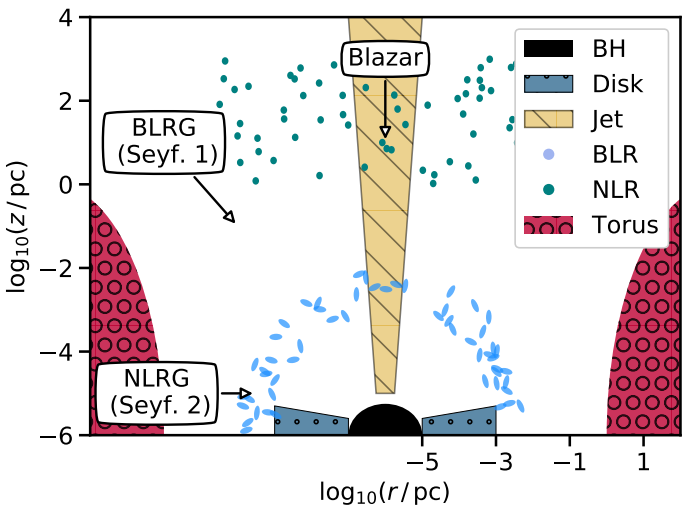

Figure 4.5: AGN can be classified based on their viewing angle and the presence of a relativistic jet. An observer sideways with respect to a jetted AGN would see the ionisation cone of the NLR and the extended radio jet. This is the observational appearance of a NLRG. Raising the viewing angle above the obscuring torus will make the BLR visible, and the jetted AGN will appear as a BLRG. Aligning the viewing angle with the jet axis, will return the compact and luminous observational appearance of blazars. Non-jetted Seyfert galaxies can be accommodated within the same NLRG / BLRG viewing scheme. Adapted from Zier and Biermann (2002).

class as general and as independent as possible from the various accidental observational features (Urry and Padovani, 1995).

Viewing Angle

The unification by *viewing angle* is the path traced by Blandford and Königl (1979) and Antonucci and Miller (1985). Following Netzer (2013), objects presenting obscuration of the central engine are defined as Type 2 AGNs (like Seyfert 2 galaxies and NLRG, see Figure 4.5), on the other hand objects in which the central engine is viewed without obscuration are defined as Type 1 AGN (Seyfert 1 galaxies and BLRG, see Figure 4.5 would belong to this class). The difference between Seyfert 1 / 2 and NLRG / BLRG is merely the presence of a relativistic jet, which leads us to the second unifying parameter.

Radio Loudness

Another remarkable distinction between different AGNs is the presence or absence of a relativistic jet. This modifies the type and extent of the emitted electromagnetic radiation. Jetted objects (that are the focus of this thesis) like extended radio galaxies and QSRs, display non-thermal power-law-like emission processes (see Figure 4.4) over a large range of the EM spectrum, from radio frequencies to gamma rays. Radiative processes for jetted AGNs will be described in Section 4.5. Non jetted objects are instead dominated by thermal black-body-like emission (also by emission lines and by Compton scattering to a smaller extent, as already pointed out in the disk description). Their emission spectrum usually spans from the IR to the X-ray regime. A common proxy used to make quantitative the presence or absence of jets is the *radio loudness* parameters. Following Meier (2012) we define it as the ratio of the

monochromatic flux densities (F_ν measured in Jy) at 1.4 GHz and in the optical b band

$$R = \frac{F_\nu(1.4\,\mathrm{GHz})}{F_\nu(b)} \tag{4.6}$$

An object is defined as radio-loud if $R > 100$, as radio-quiet in the opposite case. Radio loud objects are roughly 10% of all the observed AGNs. On top of the radio-loud / quiet scheme we can still invoke viewing angle scheme to justify the enormous apparent luminosities observed for blazars, consequence of their small jet viewing angle. Blazars constitute $\sim 1\%$ of all the observed AGN (Padovani et al., 2017).

Although the introduction to the historical AGN observations and unification schemes traced in this sections is very simplified and partial, it serves the purpose of introducing the two science cases discussed in this thesis: PKS 1510-089, that is a FSRQ and NGC 1275, that is a Fanaroff-Riley I extended radio galaxy with optical emission lines intermediate between those produced by Seyfert 1 and 2 types. Covering the full AGN taxonomy is outside the scope of this dissertation but the interested reader is referred to: Netzer (2015) and Padovani et al. (2017) for a review of the unification schemes; Meier (2012) and Netzer (2013) for a thorough treatment of the AGN physics.

4.3 Particle Acceleration

Acceleration of particles in astrophysical environments is commonly described as due to relativistic *shocks* perturbing the source plasma. The simple example of M 87 in Section 4.2.3 illustrated that we can consider the relativistic outflows of plasma in AGN jets as a locus of acceleration. The paramount signature of astrophysical acceleration is the production of non-thermal power-law distributions of particles that we can directly detect in CR experiments, or indirectly observe in the EM spectrum through the non-thermal photon spectra ascribable to their radiative processes (examined in Section 4.5). We will illustrate that this essential power-law distribution is recovered by the simple acceleration mechanism proposed by Fermi. Plasma instabilities generating the environment for the acceleration are directly imaged in jetted AGN. Indeed one can distinctly observe, as in the superluminal motion of Figure 4.3, distinct plasma components detaching the central radio core and relativistically streaming along the jet. In this simplified treatment we will assume that the shock front accelerating the particles is generated at the interface between these plasma instabilities, approximated with a spherical *blob*, and the rest of the jet material.

4.3.1 Fermi Acceleration

Enrico Fermi's article of 1949 *On the Origin of the Cosmic Radiation* (Fermi, 1949) was a major turning point in a debate that until then had seen as prominent ideas for the CR acceleration Millikan's proposal for production in nuclear reactions and Lemaître's evocative theory of disintegration from a *primordial nucleus*. Swann (1933) discussed a simple model for acceleration of particles through electro-magnetic forces generated by variable magnetic fields similar to those present in sunspots, providing a precious insight into the role that non-constant magnetic fields play in the acceleration mechanisms. According to Fermi's original treatment, CRs are accelerated in the interstellar (galactic) space by interactions with

wandering magnetic fields occupying it. These magnetic fields are carried by parsec-sized regions of the interstellar galactic medium with densities $10^{-24}\,\mathrm{g\,cm^{-3}}$, $10-100$ times higher than the average. These regions can move, as estimated via the Doppler broadening of their lines, as fast as $\sim 10\,\mathrm{km\,s^{-1}}$. They constantly stir the lower density interstellar medium, whose magnetic field lines (of intensity $\sim 5\,\mu\mathrm{G}$) "will form a very crooked pattern, since they will be dragged by the streaming motions of the matter to which they are attached". The diffusion of charged particles on the magnetic irregularities dragged by the clouds is responsible for the acceleration: in the cloud rest frame the scattering the CR particle undergo is elastic ($M_{\mathrm{cloud}} >> m_{\mathrm{CR}}$), therefore the net effect of the interaction cloud-particle is the randomisation of the particle direction. We will show that applying Fermi's prescriptions an energy gain proportional to the β of the cloud squared will be obtained. Therefore the results will be called *II order Fermi acceleration*. Limiting aspects of the original theory were underlined and modified by later authors in order to obtain more efficient acceleration processes. A remarkable result is due to Bell (1978), the first to consider particle acceleration in shock waves. This last model produces an energy gain linear in β factor, thus defining a *I order Fermi acceleration*.

Energy Distribution

What makes Fermi's theory canonical is that it naturally produces the power-law function characterising the energy distribution observed for CRs. In what follows no assumptions will be made on the dynamics of the acceleration or on the nature of the objects involved, such that the results will stand valid both for I and II order mechanisms. We will use the term *cloud* and *interaction* to refer, respectively, to the source of the acceleration and its interaction with the test particle. Let us consider a process in which a test particle has an energy gain for interaction ΔE, proportional to its energy: $\Delta E = \xi E$, after n interactions the energy is $E_n = E_0(1+\xi)^n$, where E_0 is the energy of the particle at the injection in the *acceleration region*. If we denote with P_{esc} the probability at each interaction for the particle to escape the acceleration region, the probability to be still in it after n encounters is $(1-P_{\mathrm{esc}})^n$. The number of interaction needed to reach an energy E is

$$n = \frac{\ln\left(\frac{E}{E_0}\right)}{\ln\left(1+\xi\right)}. \tag{4.7}$$

The total number of particles accelerated at energies $\geq E$ is

$$N(\geq E) \propto \sum_{m=n}^{\infty}(1-P_{\mathrm{esc}})^m = \frac{(1-P_{\mathrm{esc}})^n}{P_{\mathrm{esc}}} = \frac{(1-P_{\mathrm{esc}})^{\ln\left(\frac{E}{E_0}\right)/\ln(1+\xi)}}{P_{\mathrm{esc}}}, \tag{4.8}$$

using Eq. 4.7 in the last equality. With some manipulation, the numerator of Eq. 4.8 becomes

$$(1-P_{\mathrm{esc}})^{\ln\left(\frac{E}{E_0}\right)/\ln(1+\xi)} = \left\{\exp\left[\ln\left(\frac{E}{E_0}\right)\right]\right\}^{\frac{\ln(1-P_{\mathrm{esc}})}{\ln(1+\xi)}} = \left(\frac{E}{E_0}\right)^{-\alpha}, \tag{4.9}$$

where we have denoted α as

$$\alpha = -\frac{\ln(1-P_{\rm esc})}{\ln(1+\xi)} = \ln\left(\frac{1}{1-P_{\rm esc}}\right) / \ln(1+\xi) \approx \frac{P_{\rm esc}}{\xi} = \frac{1}{\xi}\,\frac{T_{\rm cycle}}{T_{\rm esc}}. \tag{4.10}$$

In the last equality of Eq. 4.10 we assumed that $P_{\rm esc} = T_{\rm cycle}/T_{\rm esc}$, i.e. that the escape probability from the acceleration region can be expressed as a ratio between a typical acceleration time $T_{\rm cycle}$, and a typical escape time $T_{\rm esc}$. Plugging the simplification obtained in Eq. 4.9 back into Eq. 4.8, we obtain an energy spectrum described by a power law,

$$N(\geq E) \propto \frac{1}{P_{\rm esc}}\,\left(\frac{E}{E_0}\right)^{-\alpha}. \tag{4.11}$$

4.3.2 II Order Fermi Acceleration

Let us consider first the *wandering magnetic fields* of the original treatment as responsible for the acceleration. A particle with energy E_1 in the observer frame enters a cloud that moves with velocity $\beta = V/c$ (and Lorentz factor γ) and starts its diffusion. If θ_1 is the entering angle of the particle in the cloud, as in Figure 4.6, we can write the transformation of the particle energy to the rest frame of the cloud, Eq. B.1, as

$$E_1' = \gamma E_1(1-\beta\cos\theta_1). \tag{4.12}$$

All the scatterings in the comoving frame are due to deflections in a magnetic field, therefore are elastic and when the particle comes out of the cloud: $E_1' = E_2'$. Performing a Lorentz transformation for E_2' back to the observer frame (see Eq. B.5) returns

$$E_2 = \gamma E_2'(1+\beta\cos\theta_2'), \tag{4.13}$$

where θ_2' is the departure angle from the cloud as seen in the comoving frame. The energy gain per interaction, ΔE, is proportional to the energy. We can obtained it from Eq. 4.13 and Eq. 4.12 as

$$\begin{aligned}\frac{\Delta E}{E_1} = \frac{E_2-E_1}{E_1} = \frac{\gamma E_1'(1+\beta\cos\theta_2') - E_1}{E_1} = \frac{\gamma^2 E_1(1-\beta\cos\theta_1)(1+\beta\cos\theta_2') - E_1}{E_1} = \\ = \frac{1-\beta\cos\theta_1+\beta\cos\theta_2'-\beta^2\cos\theta_1\cos\theta_2'}{1-\beta^2} - 1\end{aligned} \tag{4.14}$$

The energy gain depends only on the velocity β of the cloud and most importantly on the cosines of the ingress and egress angles θ_1 and θ_2. As we shall see, their average distributions will differentiate the final energy gain in Eq. 4.14 for I and II order accelerations. In the II order Fermi mechanism the deflections are completely random and the egress angle θ_2' has an isotropic distribution. For such a distribution $\mathrm{d}n/\mathrm{d}\cos\theta = \text{const}$. The mean value of $\cos\theta_2'$ is then

$$< \cos\theta_2' >= \int_{-1}^{1} \mathrm{d}\cos\theta_2'\ \cos\theta_2'\,\frac{\mathrm{d}n}{\mathrm{d}\cos\theta_2'} = 0. \tag{4.15}$$

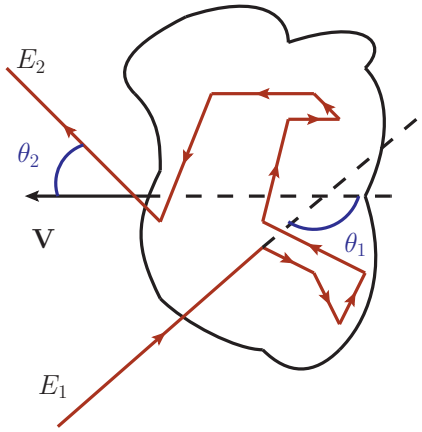

Figure 4.6: II order Fermi mechanism. A particle with energy E_1 enters with angle θ_1 a cloud with density 10 times higher than the interstellar galactic medium and moving at relativistic velocity $\beta = V/c$. Within the frame comoving with the cloud the particle is scattered along crooked magnetic field lines with the net effect being only a change of direction: the particle departs the cloud with energy $E_2' = E_1'$ and angle θ_2'.

The number of particles in the infinitesimal cosine band $\cos\theta_1 + \mathrm{d}\cos\theta_1$ depends instead on the rate of collisions between particle and cloud and it is proportional to their relative velocity $\mathrm{d}n/\mathrm{d}\cos\theta_1 \propto c - V\cos\theta_1$, therefore the mean value of $\cos\theta_1$ reads

$$< \cos\theta_1 >= \frac{\int_{-1}^{1} \mathrm{d}\cos\theta_1 \ \cos\theta_1 \frac{\mathrm{d}n}{\mathrm{d}\cos\theta_1}}{\int_{-1}^{1} \mathrm{d}\cos\theta_1 \ \frac{\mathrm{d}n}{\mathrm{d}\cos\theta_1}} = \frac{\int_{-1}^{1} \mathrm{d}\cos\theta_1 \ \cos\theta_1 (c - V\cos\theta_1)}{\int_{-1}^{1} \mathrm{d}\cos\theta_1 \ (c - V\cos\theta_1)} = \frac{-2/3V}{2c} = -\frac{\beta}{3}. \tag{4.16}$$

Plugging the expressions obtained for the average $\cos\theta_2'$ and $\cos\theta_1$ back into Eq. 4.14 one obtains

$$\xi = \frac{< \Delta E >}{E_1} = \frac{1 + \frac{\beta^2}{3}}{1 - \beta^2} - 1 \sim \frac{4}{3}\beta^2 \tag{4.17}$$

where in the last step we have considered $\beta \ll 1$. We have obtained that the energy gain depends on β squared.

4.3.3 I Order Fermi Acceleration

In the I order Fermi mechanism the source of the acceleration is a shock wave propagating in an astrophysical medium. This can be produced e.g. by the expanding remnant of a Supernova explosion or also at the interface between a relativistically streaming blob and the jet material in an AGN, i.e. objects with streaming velocities $\sim 10^4\,\mathrm{km\,s^{-1}}$ or higher. A shock wave is an interface of discontinuity in a fluid generated by a medium that is moving at velocity V greater than the speed of sound in the fluid c_s[IX]. Essentially new waves are generated at velocity V by the medium motion but cannot reach the sections of the fluid that have not been yet informed (or heated, since $c_s \propto \sqrt{T}$) of (by) the perturbation. Therefore they tend to squash in a surface that manifests as jump in the field variables of density, velocity and temperature (ρ, v and T, respectively) between the region of the gas not informed of the perturbation,

[IX] For an ideal gas: $c_s = \sqrt{\gamma_{\mathrm{ad}} k_{\mathrm{B}} T/m}$, where γ_{ad} is the adiabatic index, ratio of specific heats of the gas at constant pressure and constant volume, $\gamma_{\mathrm{ad}} = 5/3$ for a monoatomic gas, k_{B} is the Boltzmann constant, T the temperature and m the mass of a molecule.

indicated as *upstream* (quantities subscripted with 1), and region already shocked, indicated as *downstream* (quantities subscripted with 2). Landau and Lifshitz (1959) obtain from the Rankine–Hugoniot equations a velocity of the shock front

$$v_s = \frac{\gamma_{\rm ad}+1}{4}V + \left[c_s^2 + \frac{(\gamma_{\rm ad}+1)^2 V^2}{16}\right]^{1/2} \xrightarrow[V\gg c_s]{} \frac{\gamma_{\rm ad}+1}{2}V, \tag{4.18}$$

where $\gamma_{\rm ad}$ is the adiabatic index and the limit $V \gg c_s$ denotes *strong shocks*. For a monoatomic gas $\gamma_{\rm ad} = 5/3$ and $v_s = 4/3\,V$. In the frame comoving with the shock we would see particles approaching the shock with velocity $v_1 = v_s$ and flowing in the downstream region with velocity $v_2 = v_1 - V$, from this, the ratio of the velocities in the frame comoving with the shock results

$$\frac{v_1}{v_2} = \frac{v_1}{v_1 - V} = \frac{v_s}{v_s - V} = \frac{\gamma_{\rm ad}+1}{\gamma_{\rm ad}-1} = \mathcal{R}. \tag{4.19}$$

We name $\mathcal{R}$ *compression ratio*, $\mathcal{R} = 4$ for a monoatomic gas. Let us now consider a particle entering the shock front and being scattered as in Figure 4.7.

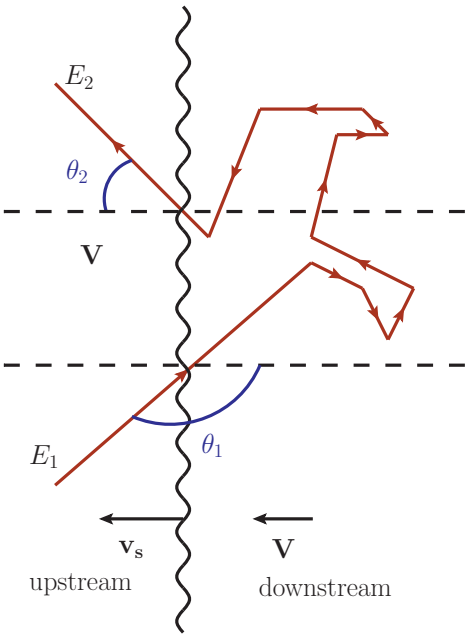

Figure 4.7: I order Fermi mechanism. A medium moving at velocity $V \gg c_s$ generates a shock with velocity v_s. The term *downstream* denotes the region that has already been shocked, while the region *upstream* denotes the medium beyond the discontinuity, not yet informed of the perturbation. A particle entering the shock with energy E_1 and at an angle θ_1 is scattered outside with energy E_2 at an angle θ_2. In the frame comoving with the discontinuity there is a flux of particles entering with velocity $v_1 = v_s$ and moving in the downstream region with velocity $v_2 = v_1 - V$.

We recall Eq. 4.14, that was obtained without any assumption neither on the test particle nor on the acceleration region. This time we pose $\beta = V/c = (1 - 1/R)\, v_s/c$ for the velocity, and will recompute the mean values of $\cos\theta_2'$ and $\cos\theta_1$ showing the different energy gain obtainable for the I order mechanism. Since we assume a plane geometry for the profile of the shock the ingress and egress angles will have a distribution of cosines given by the projection of an isotropic flux (a sphere) on the shock front (a plane) returning a normalised distribution $\mathrm{d}n/\mathrm{d}\cos\theta = 2\cos\theta$. The mean values for $\cos\theta_2'$ and $\cos\theta_1$ are in this

case

$$\begin{aligned} < \cos\theta_1 >= \int_{-1}^{0} \mathrm{d}\cos\theta_1 \ \cos\theta_1 \frac{\mathrm{d}n}{\mathrm{d}\cos\theta_1} = -\frac{2}{3}, \\ < \cos\theta_2' >= \int_{0}^{1} \mathrm{d}\cos\theta_2' \ \cos\theta_2' \frac{\mathrm{d}n}{\mathrm{d}\cos\theta_2'} = \frac{2}{3}. \end{aligned} \tag{4.20}$$

Where, given the geometry in Figure 4.7, the limits of integration are defined such that θ_1 and θ_2 are an ingress and egress angle, respectively. The energy gain from Eq. 4.14 is then

$$\xi = \frac{< \Delta E >}{E_1} = \frac{1 + \frac{4}{3}\beta + \frac{4}{9}\beta^2}{1 - \beta^2} - 1 \sim \frac{4}{3}\beta = \frac{4}{3}\left(1 - \frac{1}{R}\right)\frac{v_s}{c}, \tag{4.21}$$

that returns exactly v_s/c in the monoatomic case. We have derived an energy gain linear in β, hence the denomination *I order Fermi mechanism.*

4.3.4 Comparison

The main criticality of the II order mechanism is the slow energy gain, we illustrate it with an order of magnitude estimation. Consider a cloud with velocity $V = 30\,\mathrm{km\,s^{-1}}$ and suppose we want a test particle to attain an energy gain of $E/E_0 = 10^6$. The number of interactions in a time t is $n = t/T_{\mathrm{cycle}}$ with T_{cycle} a typical acceleration time (as in Eq. 4.10), from Eq. 4.7

$$n = \frac{\ln(E/E_0)}{\ln(1+\xi)} = t/T_{\mathrm{cycle}}. \tag{4.22}$$

A velocity of $30\,\mathrm{km\,s^{-1}}$ returns a $\xi = 4/3\,\beta^2 \approx 10^{-8}$. Let us consider the typical acceleration time for the II order mechanism as the average scattering time in the interstellar medium: $T_{\mathrm{cycle}} = c/\lambda_{\mathrm{ISM}}$, with the particle being ultrarelativistic $v \to c$ and $\lambda_{\mathrm{ISM}} \sim 1\,\mathrm{pc}$ the mean free path in the interstellar medium. Evaluating t from Eq. 4.22 returns

$$t = \frac{\ln(E/E_0)}{\ln(1+\xi)}\frac{\lambda_{\mathrm{ISM}}}{c} \approx 4.3\,\mathrm{Gyr}, \tag{4.23}$$

the same order of magnitude of the age of the universe, therefore unsuitable for justifying the acceleration of CRs, being their time of permanence in our galaxy estimated as $\tau \sim 6 \times 10^6\,\mathrm{yr}$ (Chapter 6 of Gaisser et al. 2016).

On the other hand a strength of the I order mechanism is that correctly reproduce the spectral index observed for the CRs (Chapter 1). In the reference frame comoving with the shock let us consider an isotropic distribution of particles with density ρ_{CR}, moving with velocity $v \to c$. We can express the rate of particles crossing the shock as

$$f_{\mathrm{cross}} = \frac{1}{4\pi}\int_0^1 \mathrm{d}\cos\theta \int_0^{2\pi} \mathrm{d}\phi \ c\rho_{\mathrm{CR}}\cos\theta = \frac{c\rho_{\mathrm{CR}}}{4}. \tag{4.24}$$

Since such density of particles streams in the second region with velocity u_2, the rate of particle leaving the shock is

$$f_{\rm loss} = \rho_{\rm CR} u_2. \tag{4.25}$$

We can express $P_{\rm esc}$ as the ratio $f_{\rm loss}/f_{\rm cross}$ and obtain from Eq. 4.10, for the I order mechanism

$$\alpha = \frac{P_{\rm esc}}{\xi} = \frac{4\frac{v_2}{c}}{\frac{4}{3}\frac{V}{c}} = \frac{3}{\frac{v_1}{v_2} - 1} = \frac{3}{\mathcal{R} - 1}, \tag{4.26}$$

returning $\alpha = 1$ for the monoatomic case. And we observe that for the I order mechanism the spectral index does not depend on the velocity of the plasma. CR experiments report usually differential spectra as they directly measure the fluxes of particle is energy bins to which they are sensitive, recalling Eq. 4.8: $N(\geq E) \propto (E/E_0)^{-\alpha} \implies {\rm d}N/{\rm d}E \propto E^{-\alpha-1}$. Therefore a source accelerating particle according to a I order Fermi mechanism produces a differential power law energy spectrum with index 2 (if the shock propagates in a monoatomic gas). Experimentally it is found (see Chapter 1) that in the energetic range from few GeV to 100 TeV, the CR spectrum is characterised by a power law $\frac{{\rm d}N}{{\rm d}E} \propto E^{-2.7}$. Such a result is perfectly in agreement with what we have derived, accounting that the diffusion of CRs distort the energy spectrum generated at the source with a variable addend term $0.5 - 0.7$.

4.4 The Environment Around the Central Engine

In this section we focus on the formalism used to describe the black hole and the accretion disk that will be used in the rest of this chapter for the derivation of the radiative processes.

4.4.1 Black Hole Formalism

A black hole can be mathematically described by three quantities: mass, angular momentum and charge. Many properties we will derive in what follows are independent of charge, therefore it will be neglected. The mass directly determines a fundamental quantity, the *gravitational radius*

$$R_g = \frac{GM}{c^2} \approx 1.5 \times 10^{13} M_8 \,{\rm cm}, \tag{4.27}$$

where G is the gravitational constant, M the BH mass and M_8 its value in $10^8\, M_\odot$ units, c the speed of light. It is common to express quantities in the proximity of the BH in terms of R_g. Schwarzschild (1916) solved Einstein's general relativity equation (see Chapter 3 of Bergström and Goobar 2004) obtaining the metric around a static body of mass M as

$${\rm d}s^2 = \left(1 - \frac{R_s}{r}\right) c^2\, {\rm d}t^2 - \frac{1}{1 - R_s/r}\, {\rm d}r^2 - r^2({\rm d}\theta^2 + \sin^2\theta\, {\rm d}\phi^2), \tag{4.28}$$

where the Schwarzschild radius is $R_{\rm S} = 2\, R_g$. The Schwarzschild metric presents a singularity at $r = R_s$. Let us consider a photon travelling radially away from the central mass. For a light-ray the line element

$ds^2 = 0$, therefore Eq. 4.28 reduces to $cdt = dr/(1 - R_s/r)$ which explodes to ∞ at $r = R_S$. Light-ray emitted by any object with size smaller than its Schwarzschild radius (or emitted in their proximity) will take infinite time to reach R_S, this boundary is referred to as *event horizon*. Kerr (1963) generalises Schwarzschild's case to a rotating BH. In describing the latter an additional quantity is introduced, the BH angular momentum J. A maximally spinning Kerr BH has angular momentum

$$J_{\max} = \frac{GM^2}{c}, \tag{4.29}$$

and usually angular momenta are expressed as a dimensionless fraction of $J_{\max}$: $a = J/J_{\max}$, with J the actual BH angular momentum. For the static Schwarzschild case $a = 0$, while for an extreme Kerr case $a = 1$. Introduced the angular momentum, the Kerr metric in Boyer and Lindquist (1967) coordinates reads

$$\begin{aligned} ds^2 = &\left(1 - \frac{2rR_g}{\Sigma}\right) c^2\, dt^2 + \frac{4\alpha r R_g \sin^2\theta}{\Sigma}\, c dt d\phi \\ &- \frac{\Sigma}{\Delta}\, dr^2 - \Sigma\, d\theta^2 - \left(r^2 + \alpha^2 + \frac{2rR_g\alpha^2 \sin^2\theta}{\Sigma}\right) \sin^2\theta\, d\phi^2. \end{aligned} \tag{4.30}$$

where $\alpha = aR_g$, $\Sigma = r^2 + \alpha^2 \cos^2\theta$ and $\Delta = r^2 - 2rR_g + \alpha^2$. The polar coordinate system is defined such that θ is the angle with respect to the BH rotational axis. As for the Schwarzschild metric there is a singularity when the radial component g_{rr} (i.e. the one associated with dr^2) explode, this occurs at the *event horizon*

$$R_H = R_g(1 + \sqrt{1 - a^2}), \tag{4.31}$$

which reduces to $R_H = 2\,R_g = R_S$, the Schwarzschild radius, for $a = 0$ and $R_H = R_g$ for the extreme Kerr case with $a = 1$. Another singularity of the metric is given by the change of sign of the component g_{tt} (the one associated with dt^2), solving $g_{tt} = 0$ returns

$$R_E = R_g(1 + \sqrt{1 - a^2 \cos^2\theta}). \tag{4.32}$$

The space between R_H and R_E defines the so-called *ergosphere*. Any particle within the ergosphere is forced to co-rotate with the BH, since no stationary frame can exist, this effect is commonly referred to as *frame-dragging*[X]. Given Eq. 4.32, the ergosphere appears like an ellipsoid containing the event horizon

[X] If we consider a photon at a radius r, moving in an equatorial orbit ($\theta = \pi/2$ and $d\theta = 0$), we can write the metric as ($ds^2 = 0$ for photons):

$$0 = g_{tt}\, dt^2 + 2g_{t\phi}\, dt d\phi + g_{\phi\phi}\, d\phi^2.$$

Solving for $d\phi/dt$, the tangential velocity:

$$\frac{d\phi}{dt} = -\frac{g_{t\phi}}{g_{\phi\phi}} \pm \left[\left(\frac{g_{t\phi}}{g_{\phi\phi}}\right)^2 - \frac{g_{tt}}{g_{\phi\phi}}\right]^{1/2}.$$

The ergosphere occurs where $g_{tt} = 0$, this returns two solutions: $d\phi/dt = 0$, and $d\phi/dt = -2g_{t\phi}/g_{\phi\phi}$. One can prove that the second solution has same sign of a (or α), i.e. the BH angular momentum. One can think to $d\phi/dt = 0$ as representing the photon that is trying to move in the direction opposite to the BH rotation and to the solution $d\phi/dt$ with the same sign as a (or α) as representing the photon moving in the same direction of the BH rotation. Any particle slower than a

sphere, larger at the equator, $R_E(\theta = \pi/2) > R_H$, and squashed at the poles, $R_E(\theta = 0) = R_H$. Outside the BH, the innermost circle on which a stable orbital motion is possible (abbreviated as ISCO, innermost stable circular orbit) is defined by the *marginal stability radius*, from Zhang et al. (1997),

$$R_{\rm ms} = R_g \left\{ 3 + A_2 - \frac{|a|}{a} \left[(3 - A_1)(3 + A_1 + 2A_2) \right]^{1/2} \right\}, \tag{4.33}$$

where $A_1 = 1 + (1 - a^2)^{1/3} \times [(1 + a)^{1/3} + (1 - a)^{1/3}]$ and $A_2 = \sqrt{3a^2 + A_1^2}$.
The *radiative efficiency* is defined as the efficiency in converting rest mass energy in EM radiation, considering the work done to attract a mass m from ∞ to $R_{\rm ms}$, it can be expressed as $\eta = [E(\infty) - E(R_{\rm ms})]/mc^2$. After the in-fall of the test particle m, the mass of the BH increases by $(1 - \eta)m$. The Newtonian limit on the efficiency is $\eta = 1/(2x)$, where $x = R_{\rm ms}/R_g$, hence 1/12 for a Schwarzschild BH (for which $R_{\rm ms} = 6\, R_g$). The correct result from General Relativity can be expressed, following Rieger (2011) and Netzer (2013), as

$$\eta = 1 - \left(1 - \frac{2}{3x} \right)^{1/2}. \tag{4.34}$$

Table 4.1 illustrates the values of the marginal stable orbit and radiative efficiency for BH with different angular momenta. A negative angular momentum $a < 0$, denotes the case of *retrograde accretion*, in which the accreting material rotates in the direction opposite to the BH. The faster the BH is spinning the closer the ISCO approaches the event horizon and the higher the radiative efficiency becomes. A remarkable value of 0.42 is reached for a Kerr BH, almost two orders of magnitude above the typical 0.007 efficiency of nuclear fusion process in stars[XI].

a	$R_{\rm ms}\,/\,R_g$	η
-1.0	9.0	0.038
0	6.0	0.057
0.1	5.67	0.061
0.5	4.23	0.082
0.9	2.32	0.156
0.998	1.24	0.321
1.0	1.00	0.423

Table 4.1: Radius of marginal stability and radiation efficiency for BHs with different angular momenta, from Netzer (2013).

4.4.2 Accretion

Having introduced the radiative efficiency we can express the luminosity of an object powered by accretion, the disk in this case, as

$$L_{\rm disk} = \eta \dot{M} c^2, \tag{4.35}$$

photon is forced to co-rotate with the BH.

[XI] Let us consider the main form of He production by fusion of 4 protons in the sun: $4\,{}^1{\rm H} \rightarrow {}^4{\rm He}$. The efficiency for this process can be written as: $\eta = (4m_{^1{\rm H}} - m_{^4{\rm He}})\,/\,4m_{^1{\rm H}} = (4{\times}1.6726{\times}10^{-24}\,{\rm g} - 6.642{\times}10^{-24}\,{\rm g})\,/\,4{\times}1.6726{\times}10^{-24}\,{\rm g} \approx 0.007$.

where $\dot{M} = \mathrm{d}M/\mathrm{d}t$ is the rate at which the object is accreting matter. The maximum luminosity attainable by a celestial object before ripping itself apart by internal radiation pressure was expressed by Eddington (1917). The limit is obtained balancing the gravitational attraction on a test particle $F = GMm/R^2$ with the radiation pressure at distance R, $P_{\mathrm{rad}} = L/(4\pi R^2 c)$, where L is the luminosity of the source. Let us consider that the test particle, say a cloud, is opaque to the radiation with a cross-section per unit mass (or opacity) k, the balance of the forces is given by $F = mkP_{\mathrm{rad}}$. The Eddington luminosity is then

$$L_{\mathrm{Edd}} = \frac{4\pi GMc}{k}. \tag{4.36}$$

Considering that in an accretion process the material is mostly constituted by ionised hydrogen and the opacity is provided by Thomson scattering we can write $k = \sigma_{\mathrm{T}}/m_p$ and simplify Eq. 4.36 in

$$L_{\mathrm{Edd}} = \frac{4\pi GMm_p c}{\sigma_{\mathrm{T}}} = 1.25 \times 10^{46}\, M_8\, \mathrm{erg\,s^{-1}}. \tag{4.37}$$

Eq. 4.37 sets an upper limit on the luminosity in case of spherical accretion. The critical accretion rate required to sustain such luminosity is, using Eq. 4.35,

$$\dot{M}_{\mathrm{Edd}} = \frac{L_{\mathrm{Edd}}}{\eta c^2} \approx 2.2\, M_8\, M_\odot\, \mathrm{yr^{-1}}, \tag{4.38}$$

where in the last equality we have used a typical efficiency of $\eta = 0.1$. Very often the normalised Eddington accretion rate, indicated as $\dot{m} = \dot{M}/\dot{M}_{\mathrm{Edd}}$, is used in place of $\dot{M}$. The upper limits just set are valid for spherical accretion, we examine now in more detail the two major different modality of accretion disks.

Standard (Shakura Sunyaev) Accretion Disk

We can picture a geometrically thin accretion disk ($H \ll R$, where H is half of the disk height and R the radial coordinate) as composed by a series of infinitesimal rings. In the standard accretion disk description viscous frictional stresses are assumed to transform gravitational potential energy in thermal radiation: as the material infalls towards the BH in concentric orbits, at the interface between rings friction generates thermal radiation emitted locally as black-body spectrum. This model of geometrically thin accretion was introduced by Shakura and Sunyaev (1973) to describe the X-ray emission of binary star systems. The energy flux emitted locally at R can be derived, as in Section 4.1 of Netzer (2013), assuming the mechanical energy and the work done by the local torque at the disk interface convert to electromagnetic radiation

$$\frac{\mathrm{d}\mathcal{E}}{\mathrm{d}A\mathrm{d}t} = \frac{3GM\dot{M}}{8\pi R^3}\,\varphi(R), \tag{4.39}$$

where

$$\varphi(R) = 1 - \sqrt{\frac{R_{\mathrm{in}}}{R}}, \tag{4.40}$$

and R_{in} is the inner radius of the disk, commonly chosen equal to the marginal stability radius in Eq. 4.33 ($R_{\mathrm{in}} = R_{\mathrm{ms}}$). The outer radius of the disk can be obtained, following Netzer (2013), as the point where

the vertical component of the self-gravity overcomes the vertical component of the central BH gravity. This happens roughly at: $R_{\rm out} = 2 \times 10^3 \, (\alpha/0.03)^{1/2} \, R_g$. α is a coefficient parametrising the viscosity ν (in $\mathrm{cm^2 s^{-1}}$) of the disk, according to Shakura and Sunyaev (1973),

$$\nu = \alpha c_s H = \alpha \frac{c_s^2}{\Omega_{\rm K}} \tag{4.41}$$

with c_s speed of sound in the disk gas, H half-height of the disk and $\Omega_{\rm K}^2 = GM/R^3$ Keplerian angular velocity. The temperature profile of the disk can be expressed relying on the assumption of local black-body emission and equating the energy flux Eq. 4.39 with the Stefan-Boltzmann law: $\mathrm{d}\mathcal{E}/\mathrm{d}A\mathrm{d}t = \sigma_{\rm SB} T(R)^4$. One obtains

$$T(R) = \left[\frac{3GM\dot{M}\varphi(R)}{8\pi R^3 \sigma_{\rm SB}} \right]^{1/4}, \tag{4.42}$$

values typically range between 10^{5-7} K. Expressing the temperature in terms of the dimensionless energy ϵ_0 in electron rest-mass energy units, $m_e c^2 \epsilon_0 = k_{\rm B} T$,

$$\epsilon_0(R) = 2.7 \times 10^{-4} \left(\frac{l_{\rm Edd}}{M_8 \eta} \right)^{1/4} \left(\frac{R}{R_g} \right)^{-3/4}, \tag{4.43}$$

where $l_{\rm Edd} = L_{\rm disk}/L_{\rm Edd} = \eta \dot{M} c^2 / L_{\rm Edd}$.

Radiatively Inefficient Accretion Disk

The Shakura Sunyaev disk is an example of a more general *cooling dominated* flow. The latter is a high-density gas in which Coulomb collisions between ions and electrons are fast and efficient in sharing the total kinetic energy (increased by the local viscosity). Particle cooling is due to the electrons, through several atomic processes (listed in Section 5.3 of Netzer 2013) that have efficiencies proportional to n_e^2, where n_e is the electron density, and time scales much smaller than the inflow time. An accretion disk with a low accretion rate can have densities so small that the cooling time scale becomes larger than the inflow time. A radiatively inefficient accretion flow (RIAF) forms as cooling becomes negligible with respect to heating and most of the energy is stored in the flow and advected in the central source. Narayan and Yi (1994, 1995) studied the case of a two-temperatures advection dominated accretion flows (ADAF), in which the accretion rate and the particle density are so low that the Coulomb coupling between ions and electrons breaks and the viscous energy goes mostly into ion heating. Ions can eventually achieve virial temperatures $T_p \sim 3 \times 10^{12} (R/R_g)\,\mathrm{K}$[XII], while the electrons stay at temperatures typically 2 orders of magnitude lower, $T_e \sim 5 \times 10^9$ K. Narayan and Yi (1994) show that the sound speed in the heated accreting gas ($c_s \propto \sqrt{T}$) is comparable to the Keplerian velocity $c_s \sim \Omega_{\rm K} R$. Using this to obtain H from Eq. 4.41, one gets $H \sim R$. ADAF disks have a geometrically thick configuration, as the heat advected with the gas inflates them. They are characterised by viscosity parameters $\alpha \sim 0.2 - 0.3$ and typically

[XII] A system of mass M and radius R with constant density has *virial temperature*: $T_{\rm vir} = \frac{1}{3} \frac{GMm_p}{k_{\rm B} R}$ obtained applying the virial theorem $E = W/2$ considering the kinetic energy per unit mass $E = \frac{k_{\rm B} T}{\mu}$ (with μ mean molecular weight) and the gravitational energy per unit mass $W = \frac{GM}{R}$.

occur for normalised accretion rates: $\dot{m} \sim \alpha^2$. They are less luminous than Shakura Sunyaev disks, being their total luminosity (Rieger, 2011)

$$L_{\mathrm{ADAF}} = \frac{2 \times 10^{-2}}{\alpha^2} \frac{\dot{M}^2}{\dot{M}_{\mathrm{Edd}}} c^2, \tag{4.44}$$

proportional to $\dot{M}^2$ instead of $\dot{M}$ as for the standard case (see Eq. 4.39). ADAF were introduced to explain the hard X-ray spectrum in the emission of binary systems (Narayan and Yi, 1994), they proved to be adaptable to describe the broad band spectrum of the lowest luminosity AGN. The cooling processes of the electrons are responsible for the broadband emission of the ADAF disk, as visible in Figure 4.8, showing the luminosity as a function of frequency for different values of the normalised accretion rate $\dot{m}$. The spectrum has three components: in radio to sub-millimeter regime the synchrotron emission of the electrons dominates. The synchrotron photons produced are upscattered by the relativistic electrons up to energies $h\nu_{\mathrm{C}}^{\mathrm{max}} \sim k_{\mathrm{B}} T_e \sim (100 - 500)\,\mathrm{keV}$ via inverse Compton effect. For high values of $\dot{m}$ (as in the orange spectra corresponding to $\dot{m} = 10^{-1}$ in Figure 4.8) the optical depth for the Compton scattering is high and the inverse Compton component can dominate the spectrum. As the accretion rate decreases, Compton scattering becomes inefficient and individual Compton peaks (visible for $\dot{m} = 10^{-2}$) starts to appear in the spectrum. The X-ray regime is instead dominated by bremsstrahlung emission due to electron-electron and ion-electron interaction up to $\sim k_{\mathrm{B}} T_e$ energies.

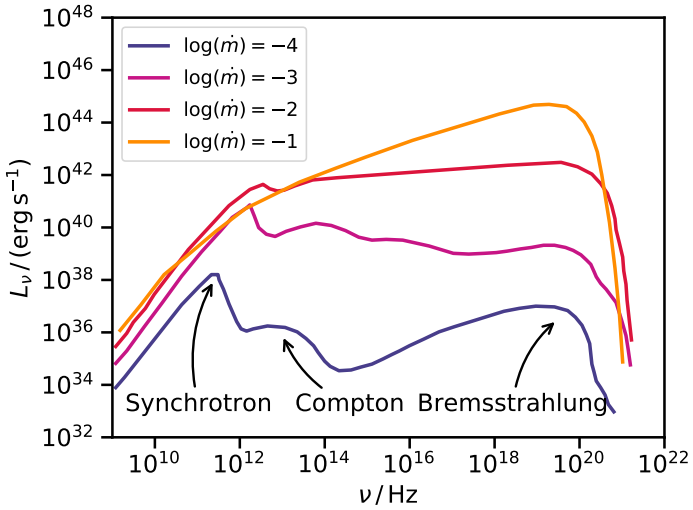

Figure 4.8: SEDs displaying the luminosity of an ADAF disk for different normalised accretion rates $\dot{m}$. For low $\dot{m} \lesssim 10^{-3}$ we can distinguish three continuum contributions: electron synchrotron in the radio regime, synchrotron self Compton up to $\sim 100\,\mathrm{keV}$ and bremsstrahlung dominating at X-ray energies. For higher accretion rates the Compton efficiency increases and the Compton peaks widens in a power law. Adapted from (Narayan et al., 1998).

4.5 Non Thermal Radiative Processes

The description of the radiative processes is supported by a `python` package I have developed: `agnpy`. At the moment the code models synchrotron radiation and inverse Compton scattering by electrons over different target fields for which also the optical depth to $\gamma\gamma$ pair creation is computed. The code has as only dependencies `numpy` (Oliphant, 2006) and `astropy` (Astropy Collaboration, 2013). The implementation of the code and the notation in the section follow the works of Dermer and Menon (2009); Dermer et al. (2009); Finke (2016).

As underlined in Section 4.3, the direct detection of CRs does not constitute the only path to study the acceleration of particles in astrophysical environments. The observation of broadband EM spectra, manifestation of the interaction of such particles with their environments, provides additional insights to the identification of the acceleration sites. In this section we will focus on the EM emission of electrons (and positrons), hence labelled as *leptonic*, as they will be used to explain the gamma-ray emission of the objects analysed in this thesis. Section 4.5.6 provides a comment on the radiative processes involving protons and their importance.

4.5.1 Notation

In this section we introduce the notation that will be used in the radiative models description:

- the energy or frequency dependence of all quantities is expressed as a function of the dimensionless energy in electron rest-mass energy units: $\epsilon = h\nu/(m_e c^2)$;
- the *intensity* I_ϵ, measured in $\mathrm{erg\,cm^{-2}\,s^{-1}\,sr^{-1}}$, is defined such that the infinitesimal energy $\mathrm{d}\mathcal{E}$ carried by photons with energy between ϵ and $\epsilon + \mathrm{d}\epsilon$ contained within the solid angle $\mathrm{d}\Omega$, impinging on an area $\mathrm{d}A$ for a time $\mathrm{d}t$ reads $\mathrm{d}\mathcal{E} = I_\epsilon \,\mathrm{d}\epsilon \,\mathrm{d}A \,\mathrm{d}t \,\mathrm{d}\Omega$;
- the *spectral energy density*, $u(\epsilon, \Omega)$, is defined such that the infinitesimal energy carried by the photons is $\mathrm{d}\mathcal{E} = u(\epsilon, \Omega)\,\mathrm{d}\epsilon \,\mathrm{d}V \,\mathrm{d}\Omega$, and considering a ray of light that is moving in a cylinder of volume $\mathrm{d}V = c\mathrm{d}t\mathrm{d}A$, can be related to the intensity via $I_\epsilon = c\,u(\epsilon, \Omega)$;
- the *emissivity* j is analogous to the intensity but defined over a differential volume rather than a differential area: $j(\epsilon, \Omega) = \mathrm{d}\mathcal{E}/\mathrm{d}\epsilon \,\mathrm{d}V \,\mathrm{d}t \,\mathrm{d}\Omega$. It is measured in $\mathrm{erg\,cm^{-3}\,s^{-1}\,sr^{-1}}$. When indicated with a capital letter, J, will denote an emissivity multiplied by the volume of the emitting region, i.e. $J(\epsilon, \Omega) = V_b\, j(\epsilon, \Omega)$ (the blob volume in our case) and measured in $\mathrm{erg\,s^{-1}\,sr^{-1}}$. J integrated over the solid angle subtended by the source returns the *luminosity* $L(\epsilon)$ (also simply indicated as $J(\epsilon)$, in $\mathrm{erg\,s^{-1}}$);
- the SED of astronomical sources is typically expressed with the νF_ν formulation, that is the energy flux per natural logarithmic frequency interval (see Gehrels 1997). ν is the frequency in Hz and F_ν

the flux density measured in erg cm^{-2} s^{-1} Hz^{-1} or Jy. It is equivalent to the $E^2\,\mathrm{d}\phi/\mathrm{d}E$ formulation used in experimental gamma-ray astronomy, with the differential flux $\mathrm{d}\phi/\mathrm{d}E$ usually measured in TeV^{-1} cm^{-2} s^{-1}. Recalling the beaming properties derived in Section 4.2.1, a source with an intrinsic luminosity $J'(\epsilon')$ (primed quantities refer to the reference frame comoving with the source) has a measured SED on Earth:

$$\nu F_\nu \equiv f_\epsilon = \frac{\delta_D^4}{4\pi d_L}\,\epsilon' J'(\epsilon'). \tag{4.45}$$

In the last expression δ_D is the Doppler factor introduced in Eq. 4.3, its fourth power is returned by a factor δ_D transforming the energies and a factor δ_D^3 transforming the intensities (see 5.2 of Dermer and Menon 2009). d_L is the *luminosity distance*. Observed (unprimed) and comoving (primed) energies are connected by the transformations: $\epsilon' = (1+z)\epsilon/\delta_D$ accounting both for Doppler boosting and redshift of the source;

– the particle populations we will consider for the radiative processes will generally have densities (cm^{-3}) that are power laws of the Lorentz factor, as we have derived from the Fermi mechanism,

$$n_e(\gamma) = k_e \gamma^{-p}\, H(\gamma;\gamma_1,\gamma_2), \tag{4.46}$$

where k_e is the normalisation constant, measured in cm^{-3}, p is the spectral index and $H(\gamma;\gamma_1,\gamma_2)$ is a Heaviside function ensuring that n_e assumes null values in the range $\gamma \leq \gamma_1$ and $\gamma \geq \gamma_2$. The particle density can be also denoted with the capital letter N_e, indicating that the latter has been multiplied by the volume of the emitting region (same convention for the emissivities) $N_e(\gamma) = V_b\, n_e(\gamma)$. We may also consider broken power-law densities, i.e. power-law distributions with different spectral indexes (p_1, p_2) below and above a certain spectral break given by γ_b

$$n_e(\gamma) = k_e \left[\left(\frac{\gamma}{\gamma_b}\right)^{-p_1} H(\gamma;\gamma_1,\gamma_b) + \left(\frac{\gamma}{\gamma_b}\right)^{-p_2} H(\gamma;\gamma_b,\gamma_2) \right]. \tag{4.47}$$

The *energy density* u_e and the *total energy* W_e in non-thermal electrons are defined as

$$\begin{aligned} u_e &= m_e c^2 \int_1^\infty \mathrm{d}\gamma\; \gamma\, n_e(\gamma), \\ W_e &= m_e c^2 \int_1^\infty \mathrm{d}\gamma\; \gamma\, N_e(\gamma). \end{aligned} \tag{4.48}$$

4.5.2 Synchrotron Radiation

Particles accelerated in presence of a magnetic field $\boldsymbol{B}$ will emit radiation that we identify as *cyclotron radiation* if the motion is non relativistic and with *synchrotron radiation* in the complementary case. Let us focus on the second case: the covariant form of the Lorentz force, using the metric $(1, -1, -1, -1)$,

reads[XIII]

$$\frac{\mathrm{d}p^\mu}{\mathrm{d}\tau} = \frac{Q}{c} F^{\mu\nu} u_\nu, \tag{4.49}$$

where $p^\mu = (\gamma mc,\, p_x,\, p_y,\, p_z) = (\gamma mc,\, \gamma m v_x,\, \gamma m v_y,\, \gamma m v_z)$ is the four-momentum, τ the proper time, Q the electric charge, $F^{\mu\nu}$ the electromagnetic tensor, $u_\nu = \gamma(c,\, -v_x,\, -v_y,\, -v_z)$ the four-velocity. Suppose the electric field is null ($E = 0$) and the magnetic field is parallel to the z-axis of the observer frame. The electromagnetic tensor simplifies in

$$F^{\mu\nu} = \begin{pmatrix} 0 & -E_x & -E_y & -E_z \\ E_x & 0 & -B_z & B_y \\ E_y & B_z & 0 & -B_x \\ E_z & -B_y & B_x & 0 \end{pmatrix} \xrightarrow[E=0,\, B_z=B]{} \begin{pmatrix} 0 & 0 & 0 & 0 \\ 0 & 0 & -B & 0 \\ 0 & B & 0 & 0 \\ 0 & 0 & 0 & 0 \end{pmatrix}. \tag{4.50}$$

Eq. 4.49 can be solved in the form

$$\begin{pmatrix} \frac{\mathrm{d}\gamma mc}{\mathrm{d}\tau} \\ \frac{\mathrm{d}p_x}{\mathrm{d}\tau} \\ \frac{\mathrm{d}p_y}{\mathrm{d}\tau} \\ \frac{\mathrm{d}p_z}{\mathrm{d}\tau} \end{pmatrix} = \frac{Q}{c} \begin{pmatrix} 0 \\ B\gamma v_x \\ -B\gamma v_y \\ 0 \end{pmatrix} \Longrightarrow \begin{matrix} \frac{\mathrm{d}\gamma}{\mathrm{d}t} = 0 \\ \frac{\mathrm{d}v_x}{\mathrm{d}t} = \omega_\mathrm{L} v_x \\ \frac{\mathrm{d}v_y}{\mathrm{d}t} = -\omega_\mathrm{L} v_y \\ \frac{\mathrm{d}v_z}{\mathrm{d}t} = 0 \end{matrix}, \tag{4.51}$$

where we have used the relation $\mathrm{d}t = \gamma \mathrm{d}\tau$ and introduced the *Larmor frequency*

$$\omega_\mathrm{L} = \frac{QB}{\gamma mc}. \tag{4.52}$$

In Eq. 4.51 we have derived the equations of a *helical motion* composed of a uniform linear motion along the magnetic field direction, $\mathrm{d}v_z/\mathrm{d}t = 0$, and a uniform circular motion in the orthogonal plane $v_x(t) \propto \cos(\omega_\mathrm{L} t)$, $v_y(t) \propto \sin(\omega_\mathrm{L} t)$. The Lorentz factor of the particle does not increase since $\mathrm{d}\gamma/\mathrm{d}t = 0$.

Energy Losses

The Larmor formula expresses the power radiated by an accelerated charged particle as (Eq. 4.92 in Rybicki and Lightman 1986)

$$\frac{\mathrm{d}E}{\mathrm{d}t} = \frac{2Q^2}{3c^3} \gamma^4 (a_\perp^2 + \gamma^2 a_\parallel^2). \tag{4.53}$$

As we can see from the x and y components of the velocities obtained for a motion in a uniform magnetic field (Eq. 4.51), there is acceleration only perpendicularly to the velocity, if θ is the pitch angle between the particle direction and the B orientation: $a_\perp = \omega_\mathrm{L} v_\perp = \omega_\mathrm{L} \beta c \sin\theta$, therefore

$$\frac{\mathrm{d}E}{\mathrm{d}t} = \frac{2Q^2}{3c^3} \gamma^4 \omega_\mathrm{L}^2 v_\perp^2 = \frac{16\pi}{3} \left(\frac{Q^2}{mc^2}\right)^2 c \left(\frac{B^2}{8\pi}\right) \gamma^2 \beta^2 \sin^2\theta \underset{e^\pm}{\longrightarrow} 2\sigma_\mathrm{T} U_B c \gamma^2 \beta^2 \sin^2\theta, \tag{4.54}$$

[XIII] The factor $1/c$ is to keep a CGS system of units, see notation in Section 7.1 of Dermer and Menon (2009) or Section 6 of Rybicki and Lightman (1986).

where to obtain the last term we have assumed that the particle is an electron, such that $\frac{8}{3}\pi\left(\frac{e^2}{m_e c^2}\right)^2 = \frac{8}{3}\pi r_e^2$ is the Thomson cross section $\sigma_{\rm T}$ (with r_e classical electron radius) and we have also introduced the *magnetic field energy density*: $U_B = B^2/(8\pi)$. Averaging $\sin^2\theta$ over the whole solid angle, in order to account for all the possible pitch angles, we obtain $< \beta_\perp^2 >= \beta^2/4\pi \int {\rm d}\Omega \ \sin^2\theta = 2/3\,\beta^2$, that replaced in Eq. 4.54 returns the canonical expression

$$-\left\langle \frac{{\rm d}E}{{\rm d}t} \right\rangle_{\rm syn} = \frac{4}{3} c\sigma_{\rm T} U_B \beta^2 \gamma^2, \tag{4.55}$$

and we have added a minus sign to consider it as an energy loss. Expressing Eq. 4.55 in terms of the particle Lorentz factors

$$-\left\langle \frac{{\rm d}\gamma}{{\rm d}t} \right\rangle_{\rm syn} = -\dot{\gamma}_{\rm syn} = \frac{4}{3} c\sigma_{\rm T} u_B Z^4 \left(\frac{m_e}{m}\right)^3 \beta^2\gamma^2 \xrightarrow[e^\pm]{} \frac{4}{3} c\sigma_{\rm T} u_B \beta^2\gamma^2 \xrightarrow[\gamma\gg 1]{} \frac{4}{3} c\sigma_{\rm T} u_B \gamma^2, \tag{4.56}$$

where the first expression is valid for any particle with charge Z and mass m, the second for an electron and the third for an ultrarelativistic electron, we have also introduced the *normalised magnetic field energy density*: $u_B = U_B/(8\pi m_e c^2)$. One can easily obtain Eq. 4.5, the formula we used in the jet discussion to estimate the cooling time by synchrotron losses, from Eq. 4.56. A rule-of-thumb estimate of the synchrotron frequency emitted by a particle with Lorentz factor γ can be obtained considering that an observer receives the radiation collimated in a cone of aperture $\theta_{\rm syn} \sim 1/\gamma$ (derived in Eq. 4.4), with a time scale given by the giration time $t_L = 2\pi/\omega_{\rm L}$ but compressed by a factor $(1-\beta)$ (as for the apparent time in the superluminal motion, Eq. 4.2)

$$\nu_{\rm peak}^{\rm syn} = \frac{1}{\Delta t_{\rm syn}} = \frac{1}{(2\theta_{\rm syn}) t_{\rm L}(1-\beta)} = \frac{eB}{2\pi m_e c}\gamma^2 = \nu_B \gamma^2, \tag{4.57}$$

with $\nu_B = eB/(2\pi m_e c)$ that can be expressed in terms of dimensionless energy as

$$\epsilon_B = \frac{h\nu_B}{m_e c^2} = \frac{e\hbar B}{m_e^2 c^3} = \frac{B}{B_{\rm cr}} \tag{4.58}$$

introducing the critical magnetic field: $B_{\rm cr} = 4.414 \times 10^{13}$ G.

Synchrotron Radiation in a Random Magnetic Field

The exact contribution at each frequency of a population of electrons can be obtained invoking the derivations in Section 6.2 - 6.4 of Rybicki and Lightman (1986) and writing the emitted spectral power via synchrotron by a single electron in vacuum as

$$P(\nu,\theta,\gamma) = \frac{\sqrt{3} e^3 B \sin\theta}{m_e c^3} F\left(\frac{\nu}{\nu_c}\right), \tag{4.59}$$

where the θ is the pitch angle in the magnetic field and the frequency ν_c is

$$\nu_c = \frac{3eB}{4\pi m_e c}\gamma^2 = \frac{3}{2}\nu_B\gamma^2. \tag{4.60}$$

The emissivity function $F(\nu/\nu_c)$, is an integral of a modified Bessel function of order 5/3

$$F\left(\frac{\nu}{\nu_c}\right) = \frac{\nu}{\nu_c}\int_{\nu/\nu_c}^{\infty} \mathrm{d}t\ K_{5/3}(t). \tag{4.61}$$

By integrating Eq. 4.59 over all the possible pitch angles θ, Crusius and Schlickeiser (1986) derived the luminosity emitted in synchrotron photons by an electron distribution N_e in a large-scale random magnetic field, here expressed as a function of ϵ,

$$\epsilon' J'_{\rm syn}(\epsilon') = \epsilon' \frac{\sqrt{3}e^3 B}{h}\int_1^{\infty} \mathrm{d}\gamma'\ N'_e(\gamma')\, R(x), \tag{4.62}$$

where the new emissivity function R is introduced

$$\begin{aligned} R(x) &= \frac{x}{2}\int_0^{\pi} \mathrm{d}\theta\ \sin\theta \int_{x/\sin\theta}^{\infty} \mathrm{d}t\ K_{5/3}(t), \\ x &= \frac{4\pi\epsilon' m_e^2 c^3}{3eBh\gamma'^2}. \end{aligned} \tag{4.63}$$

One can obtain the synchrotron νF_ν spectrum from Eq. 4.62 by using Eq. 4.45. In the implementation of `agnpy` the approximation provided in Eq. D7 of Aharonian (2010) is used for $R(x)$. The latter achieves an accuracy of 0.2% with respect to the exact solution of Eq. 4.63 and is represented with a solid red line in Figure 4.9 against tabulated values of $R(x)$ from Crusius and Schlickeiser (1986), represented with a dot-dashed line. An example of synchrotron spectrum for a simple power law of electrons is shown in Figure 4.10.

Synchrotron Self Absorption

The photon flux due to synchrotron radiation can be suppressed either by re-absorption by the emitting electrons or by stimulated emission, i.e. by emission induced preferentially in a certain direction and at a certain frequency. Such processes are incorporated under the term of Synchrotron Self Absorption (SSA). In general terms, absorption and emission processes over a path length ds are regulated by the equation of radiative transfer

$$\frac{\mathrm{d}I_\epsilon}{\mathrm{d}s} = -k_\epsilon\, I_\epsilon + j(\epsilon, \Omega) = -I_\epsilon + \mathcal{S}_\epsilon, \tag{4.64}$$

where I_ϵ is the intensity, attenuated by an *absorption coefficient* k_ϵ, and $j(\epsilon, \Omega)$ is the source emissivity (see Section 4.5.1). In the last equality of Eq. 4.64 we have introduced the *opacity* $\tau_\epsilon = k_\epsilon \mathrm{d}s$ and the source function $\mathcal{S}_\epsilon = j(\epsilon, \Omega)/\tau_\epsilon$. The *absorption coefficient* due to SSA (whose complete derivation can

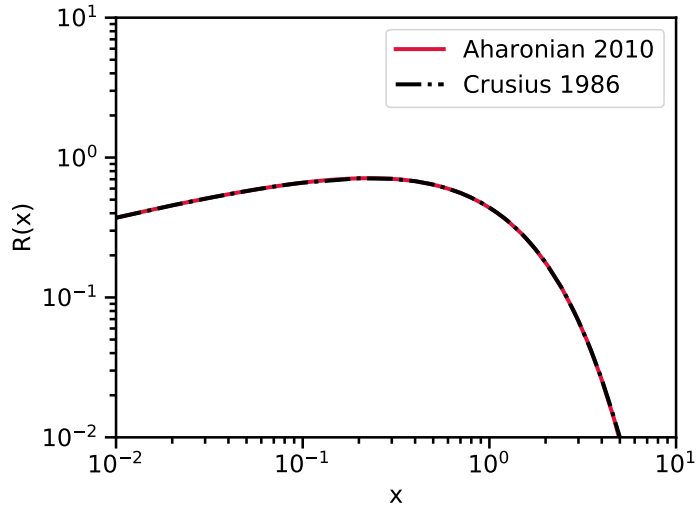

Figure 4.9: Emissivity function for the synchrotron emission of an electron distribution in a random magnetic field, $R(x)$. The black dot-dashed line represents the values computed and tabulated by Crusius and Schlickeiser (1986). The solid red line represents the approximation in Eq. D7 of Aharonian (2010).

be found in Section 6.8 of Rybicki and Lightman 1986), is expressed by as

$$k_\epsilon = -\frac{1}{8\pi m_e \epsilon^2}\left(\frac{\lambda_C}{c}\right)^3 \int \mathrm{d}\gamma\, P^{\mathrm{syn}}(\epsilon;\gamma)\left[\gamma^2 \frac{\partial}{\partial\gamma}\left(\frac{n_e(\gamma)}{\gamma^2}\right)\right]. \tag{4.65}$$

The SSA opacity for the spherical blob can be obtained (Dermer and Menon, 2009) as

$$\tau_{\mathrm{SSA}} = 2k_\epsilon R_b \tag{4.66}$$

where R_b is the blob radius. The emissivity of sources encountering an external radiation field is attenuated by a factor $\exp(-\tau_\epsilon)$, if the absorption is instead due to the same region of space producing the emission, then the appropriate *attenuation* reads

$$\frac{3\,u(\tau)}{\tau} = \frac{1}{\tau}\left(\frac{1}{2} + \frac{\exp(-\tau)}{\tau} + \frac{1-\exp(-\tau)}{\tau^2}\right). \tag{4.67}$$

Hence a self absorbed synchrotron νF_ν spectrum will be computed as

$$f_\epsilon^{\mathrm{SSA\,syn}} = \frac{3\,u(\tau)}{\tau}\,\frac{\delta_D^4}{4\pi d_L^2}\,\epsilon'\,J'_{\mathrm{syn}}(\epsilon'), \tag{4.68}$$

with $J'_{\mathrm{syn}}(\epsilon')$ from 4.62. The νF_ν synchrotron spectrum due to a simple power law of electrons 4.46 is shown in Figure 4.10, its self-absorbed version is displayed with the dashed line. The curves are obtained with a numerical integration of Eq. 4.62 and Eq. 4.65, in the absorbed case.

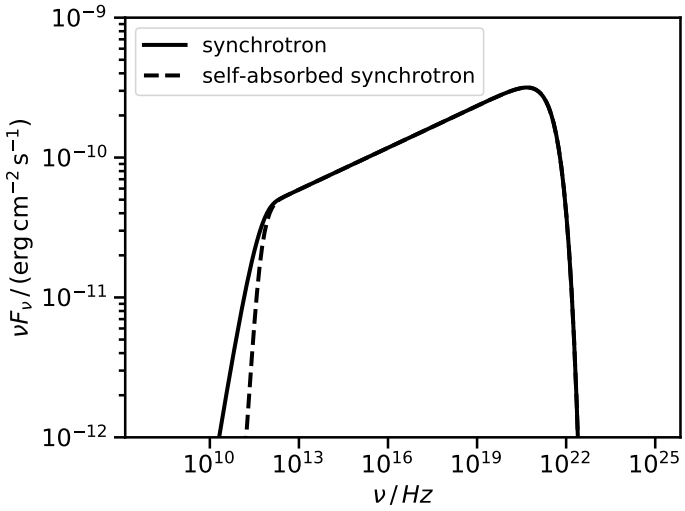

Figure 4.10: Example of synchrotron (solid line) and self-absorbed synchrotron (dashed line) νF_ν spectra obtained from a simple power-law electron density Eq. 4.46, with spectral index $p = 2.8$, defined between $\gamma'_1 = 10^2$ and $\gamma'_2 = 10^7$, with total energy content $W'_e = 10^{48}$ erg (primed quantities are computed in the blob rest frame. The blob has size $R'_b = 10^{16}$ cm and a uniform magnetic field $B = 1$ G. The jet has parameters $\Gamma = \delta_D = 10$ and resides in a galaxy sitting at $d_L = 10^{27}$ cm.

4.5.3 Compton Scattering

Elementary Compton Formula and Cross Section

The classical Compton effect, depicted in Figure 4.11, foresees a photon of energy ϵ scattering an electron at rest. The photon is scattered with energy ϵ_s at an angle χ with respect the incident direction and the electron acquires Lorentz factor γ_e and departs at an angle θ_e with respect to the photon incident direction.

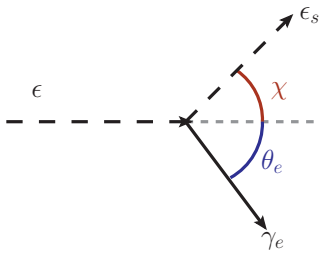

Figure 4.11: Elementary Compton scattering. A photon of energy ϵ scatters an electron at rest. After the scattering the photon has energy ϵ_s and forms and angle χ with respect to its initial direction. The electron acquires energy γ_e and departs at an angle θ_e with respect to the photon incoming direction.

From simple relativistic kinematics considerations (see Section 6.1 of Dermer and Menon 2009) one can obtain the scattered photon energy

$$\epsilon_s = \frac{\epsilon}{1 + \epsilon(1 - \cos\chi)}. \tag{4.69}$$

The latter can have values between $\epsilon/(1+2\epsilon)$ for backward scattering ($\chi = \pi$) or ϵ for forward scattering ($\chi = 0$). If $\epsilon \ll 1$, the scattering is elastic $\epsilon_s = \epsilon$, independently of χ. We denote the regime in which $\epsilon \ll 1$ as *Thomson* regime and the regime in which $\epsilon \gg 1$ as *Klein-Nishina* regime. The polarisation-averaged

Compton cross section is given by Dermer and Menon (2009), as

$$\frac{\mathrm{d}\sigma_{\mathrm{C}}}{\mathrm{d}\epsilon_s\,\mathrm{d}\Omega_s} = \frac{r_e^2}{2}\left(\frac{\epsilon_s}{\epsilon}\right)^2\left(\frac{\epsilon_s}{\epsilon}+\frac{\epsilon}{\epsilon_s}-1+\cos^2\chi\right)\delta\left(\epsilon_s-\frac{\epsilon}{1+\epsilon(1-\cos\chi)}\right), \tag{4.70}$$

the latter is differential in the scattered energy $\mathrm{d}\epsilon_s$ and the solid angle $\mathrm{d}\Omega_s = \mathrm{d}\phi\mathrm{d}\cos\chi$. Integrating over both variables one obtains the total cross section

$$\begin{aligned}\sigma_{\mathrm{C}}(\epsilon) &= \int_0^\infty \mathrm{d}\epsilon_s \oint \mathrm{d}\Omega_s \frac{\mathrm{d}\sigma_{\mathrm{C}}}{\mathrm{d}\epsilon_s\,\mathrm{d}\Omega_s} \\ &= \frac{\pi r_e^2}{\epsilon^2}\left(4+\frac{2\epsilon^2(1+\epsilon)}{(1+2\epsilon)^2}+\frac{\epsilon^2-2\epsilon-2}{\epsilon}\ln(1+2\epsilon)\right) \to \begin{cases}\sigma_{\mathrm{T}}\left(1-2\epsilon+\frac{26}{5}\epsilon^2\right) & \text{for } \epsilon \ll 1,\\ \frac{\pi r_e^2}{\epsilon^2}\left[\ln(2\epsilon)+\frac{1}{2}\right] & \text{for } \epsilon \gg 1.\end{cases}\end{aligned} \tag{4.71}$$

where we have also reported the asymptotic behaviours in the Thomson and Klein-Nishina regimes. The total cross section and its asymptotes are displayed in Figure 4.12.

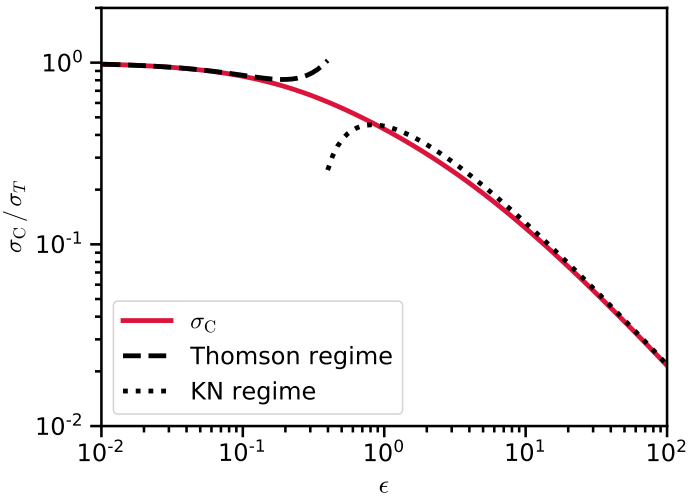

Figure 4.12: The solid red line shows the total Compton cross section obtained integrating the differential expression in Eq. 4.70 over the energy ϵ and the solid angle Ω_s. The dashed and dotted lines show the Thomson ($\epsilon \ll 1$) and Klein-Nishina ($\epsilon \gg 1$) asymptotes written in Eq. 4.71.

Transformation of The Cross Section, Head-On Approximation

For the radiative model evaluation we will actually consider an inverse Compton mechanism, i.e. a populations of photons being scattered by relativistic electrons accelerated in the blob. The relations obtained for the scattered energy and the cross section (Eq. 4.69 and Eq. 4.70, respectively) will stay valid in the electron rest frame (ERF), the quantities there defined will be indicated with an over bar. Let us consider the reference frame in Figure 4.13 that sketches the inverse Compton scattering in three dimensions. An electron with Lorentz factor γ and zenith and azimuth angles (θ_e, ϕ_e) scatters a seed photon with energy ϵ and polar angles (θ, ϕ) to energy ϵ_s and polar angles (θ_s, ϕ_s). The angle between

the electron and seed photon incident directions, ψ, is

$$\cos\psi = \mu\mu_e + \sqrt{1-\mu^2}\sqrt{1-\mu_e^2}\cos(\phi-\phi_e), \tag{4.72}$$

where $\mu = \cos\theta$, $\mu_s = \cos\theta_s$ and one can always define the coordinate system such that the electron azimuth angle $\phi_e = 0$. The seed photon energy in the ERF reads, applying the relativistic transformations in Eq. B.4,

$$\bar{\epsilon} = \gamma\epsilon(1-\beta\cos\psi) \tag{4.73}$$

and now it is $\bar{\epsilon}$ that discriminates between the Thomson and Klein-Nishina regimes. It is interesting also to consider the transformation of μ, in the ERF (Eq. B.4)

$$\bar{\mu} = \frac{\cos\psi - \beta}{1-\beta\cos\psi} \xrightarrow[\gamma\gg1,\,\beta\to1]{} -1. \tag{4.74}$$

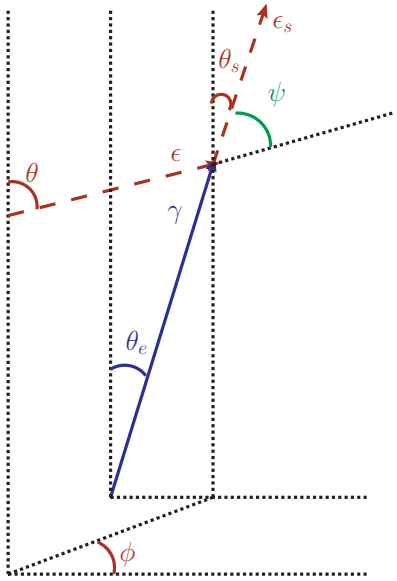

Figure 4.13: Inverse Compton scattering scheme in the observer frame. An electron with energy γ, forming an angle θ_e with the z-axis of the observer frame scatters an incoming seed photon with energy ϵ and directions θ, ϕ to energies ϵ_s and direction θ_s. In the head-on approximation the scattered photon travels in the same direction of the scattering electron $\theta_s = \theta_e$, $\phi_s = \phi_e$. Their azimuth angle is not indicated in the picture as one can define a reference system where $\phi_s = 0$. Adapted from Finke (2016).

The limit $\gamma \gg 1$, $\beta \to 1$ in Eq. 4.74 defines the so-called *head-on approximation* (Reynolds, 1982), i.e. once transformed in the ERF the seed photons appear collimated, as they assume the same angle $\bar{\theta} = \pi$. The angle between the incoming and scattered photon directions in the ERF is $\bar{\chi} = \bar{\theta} - \bar{\theta}_s = \pi - \bar{\theta}_s$, hence one obtains $\cos\bar{\chi} = -\bar{\mu}_s$, and in a moment we shall see how to simplify the Compton emissivity formulation using such approximation. The general Compton spectral emissivity is given by (Dermer and Menon, 2009; Dermer et al., 2009; Finke, 2016) as

$$\epsilon_s J_{\rm C}(\epsilon_s,\Omega_s) = m_e c^3 \epsilon_s^2 \oint \mathrm{d}\Omega \int_0^\infty \mathrm{d}\epsilon\; n_{\rm ph}(\epsilon,\Omega) \oint \mathrm{d}\Omega_e \int_1^\infty \mathrm{d}\gamma\; N_e(\gamma,\Omega_e) \times (1-\cos\psi)\,\frac{\mathrm{d}\sigma_{\rm C}}{\mathrm{d}\epsilon_s \mathrm{d}\Omega_s}, \tag{4.75}$$

where $n_{\rm ph}(\epsilon,\Omega)$ is the volumetric density of seed photons (obtainable from the spectral energy density

as $n_{\rm ph} = u(\epsilon)/(m_e c^2 \epsilon)$) and N_e the numeric density of scattering electrons. We convolve these two densities with the differential cross section, integrating over their angular ($\mathrm{d}\Omega$, $\mathrm{d}\Omega_e$) and energy ($\mathrm{d}\epsilon$, $\mathrm{d}\gamma$) distributions. The general expression for the cross section $\frac{\mathrm{d}\sigma_{\rm C}}{\mathrm{d}\epsilon_s \mathrm{d}\Omega_s}$ relates to Eq. 4.70, valid in the ERF, via[XIV]

$$\frac{\mathrm{d}\sigma_{\rm C}}{\mathrm{d}\epsilon_s \mathrm{d}\Omega_s} = \frac{\epsilon_s}{\bar{\epsilon}_s} \frac{\mathrm{d}\sigma_{\rm C}}{\mathrm{d}\bar{\epsilon}_s \mathrm{d}\bar{\Omega}_s}, \tag{4.76}$$

and adopting the head-on approximation one should replace $\cos\bar{\chi} \to -\bar{\mu}_s$. The advantage of using the head-on approximation is that photons are preferentially scattered in the electron direction $\Omega_s \approx \Omega_e$, therefore one can replace the differential cross section in Eq. 4.75 with

$$\frac{\mathrm{d}\sigma_{\rm C}}{\mathrm{d}\epsilon_s \mathrm{d}\Omega_s} \approx \frac{\mathrm{d}\sigma_{\rm C}}{\mathrm{d}\epsilon_s} \delta(\Omega_s - \Omega_e), \tag{4.77}$$

where, following Dermer and Menon (2009); Dermer et al. (2009),

$$\frac{\mathrm{d}\sigma_{\rm C}}{\mathrm{d}\epsilon_s} = \oint \mathrm{d}\Omega_s \, \frac{\mathrm{d}\sigma_{\rm C}}{\mathrm{d}\epsilon_s \mathrm{d}\Omega_s} = \frac{\pi r_e^2}{\gamma\bar{\epsilon}} \, \Xi_{\rm C} \, H\left(\epsilon_s; \frac{\bar{\epsilon}}{2\gamma}, \frac{2\gamma\bar{\epsilon}}{1+2\bar{\epsilon}}\right). \tag{4.78}$$

The Compton Kernel $\Xi_{\rm C}$ is introduced

$$\begin{aligned} \Xi_{\rm C} &= y + y^{-1} - \frac{2\epsilon_s \gamma}{\gamma\bar{\epsilon}y} + \left(\frac{\epsilon_s}{\gamma\bar{\epsilon}y}\right)^2, \\ y &= 1 - \frac{\epsilon_s}{\gamma}. \end{aligned} \tag{4.79}$$

The Compton emissivity in Eq. 4.75 can be simplified in

$$\epsilon_s J_{\rm C}(\epsilon_s, \Omega_s) = c\pi^2 r_e^2 \epsilon_s^2 \oint \mathrm{d}\Omega \int_0^{\epsilon_{\rm hi}} \mathrm{d}\epsilon \, \frac{u(\epsilon, \Omega)}{\epsilon^2} \int_{\gamma_{\rm low}}^{\infty} \mathrm{d}\gamma \, \gamma^{-2} N_e(\gamma, \Omega_s) \, \Xi_{\rm C}. \tag{4.80}$$

and the integration limits on the lower γ and the higher ϵ are given by the kinematic limits on y posed by the Heaviside function in Eq. 4.78

$$\gamma_{\rm low} = \frac{\epsilon_s}{2}\left(1 + \sqrt{1 + \frac{2}{\epsilon\epsilon_s(1-\cos\psi)}}\right) \tag{4.81}$$

and

$$\epsilon_{\rm hi} = \frac{2\epsilon_s}{1-\cos\psi}. \tag{4.82}$$

Given the head-on approximation $\cos\psi$ can be obtained from Eq. 4.72 by replacing $\mu_e \to \mu_s$.

[XIV] Using the invariance for Lorentz transformations (see Section 5.2 of Dermer and Menon 2009) of $\mathrm{d}\sigma \,/\, (\epsilon \, \mathrm{d}\epsilon \, \mathrm{d}\Omega)$.

Energy Losses

The energy loss rate for inverse Compton scattering is defined as, following (Dermer and Menon, 2009),

$$
\begin{aligned}
-\left\langle \frac{\mathrm{d}\gamma}{\mathrm{d}t} \right\rangle_{\mathrm{C}} = -\dot{\gamma}_{\mathrm{C}} &= c \oint \mathrm{d}\Omega \int_0^\infty \mathrm{d}\epsilon\, n_{\mathrm{ph}}(\epsilon,\Omega)(1-\beta\mu) \oint \mathrm{d}\Omega_s \int_0^\infty \mathrm{d}\epsilon_s\, (\epsilon_s - \epsilon)\, \frac{\mathrm{d}\sigma_{\mathrm{C}}}{\mathrm{d}\epsilon_s \mathrm{d}\Omega_s} \\
&= c \oint \mathrm{d}\Omega \int_0^\infty \mathrm{d}\epsilon\, n_{\mathrm{ph}}(\epsilon,\Omega)(1-\beta\mu)\, (\langle \epsilon_s^1 \sigma_{\mathrm{C}} \rangle - \epsilon \langle \epsilon_s^0 \sigma_{\mathrm{C}} \rangle)
\end{aligned}
\tag{4.83}
$$

where the n-th moment of the Compton cross section is introduced as

$$
\langle \epsilon_s^n \sigma_{\mathrm{C}} \rangle = \oint \mathrm{d}\Omega_s \int_0^\infty \mathrm{d}\epsilon_s\, \epsilon_s^n \left(\frac{\mathrm{d}\sigma_{\mathrm{C}}}{\mathrm{d}\epsilon_s \mathrm{d}\Omega_s} \right). \tag{4.84}
$$

The $n = 0$ moment corresponds to the total cross section in Eq. 4.71: $\langle \epsilon_s^0 \sigma_{\mathrm{C}} \rangle = \sigma_{\mathrm{C}}(\bar{\epsilon})$. The $n = 1$ moment is the average cross section weighted with the photon energy. The average scattered photon energy will therefore read:

$$
\langle \epsilon_s \rangle = \frac{\langle \epsilon_s^1 \sigma_{\mathrm{C}} \rangle}{\langle \epsilon_s^0 \sigma_{\mathrm{C}} \rangle}. \tag{4.85}
$$

Values of $\langle \epsilon_s^0 \sigma_{\mathrm{C}} \rangle$, $\langle \epsilon_s^1 \sigma_{\mathrm{C}} \rangle$, $\langle \epsilon_s \rangle$ and $\dot{\gamma}_{\mathrm{C}}$ for the Thomson $\bar{\epsilon} \ll 1$ and Klein-Nishina $\bar{\epsilon} \gg 1$ regimes, are listed in Table 4.2. We see that in the Thomson regime of elastic scattering the average scattered energy is

quantity	Thomson regime $\bar{\epsilon} \ll 1$	Klein-Nishina regime $\bar{\epsilon} \gg 1$
$\langle \epsilon_s^0 \sigma_{\mathrm{C}} \rangle$	σ_{T}	$\pi r_e^2 (\ln 2\bar{\epsilon} + 1/2)/\bar{\epsilon}$
$\langle \epsilon_s^1 \sigma_{\mathrm{C}} \rangle$	$\gamma \bar{\epsilon} \sigma_{\mathrm{T}}$	$\gamma \langle \epsilon_s^0 \sigma_{\mathrm{C}} \rangle - (4\gamma \pi r_e^2)/(3\bar{\epsilon})$
$\langle \epsilon_s \rangle$	$\gamma \bar{\epsilon} = \gamma^2 \epsilon (1 - \cos\psi)$	$\approx \gamma$
$\dot{\gamma}_{\mathrm{C}}$	$4/3 c \sigma_{\mathrm{T}} \gamma^2 \int_0^{1/\gamma} \mathrm{d}\epsilon\, \epsilon n_{\mathrm{ph}}(\epsilon)$	$c \pi r_e^2 \int_{1/\gamma}^\infty \mathrm{d}\epsilon\, n_{\mathrm{ph}}(\epsilon)/\epsilon\, (\ln 4\gamma\epsilon - 11/6)$

Table 4.2: Table of n-th moment of the Compton cross section, average scattered energy and energy losses in the Thomson and Klein-Nishina regimes.

proportional to γ^2. This is obtainable, as for the Fermi mechanism, with a back and forth transformations to the object rest frame and using the elastic scattering assumption (see Eq. 4.14). If we were to write the energy density of the seed field as $u_{\mathrm{T}} = \int_0^{1/\gamma} \mathrm{d}\epsilon\, \epsilon n_{\mathrm{ph}}(\epsilon)$, then the Thomson energy losses would assume the same expression of the Synchrotron energy losses, Eq. 4.56: $4/3\, c \sigma_{\mathrm{T}} u_{\mathrm{T}} \gamma^2$. In the Klein-Nishina regime, due to the drop of the cross section, the average scattered energy goes linearly in γ.

Synchrotron Self Compton

The first target we could consider for the inverse Compton scattering is given by the photons produced via synchrotron radiation of the electron themselves in the blob. Jones (1968) obtains an emissivity for the Synchrotron Self Compton (SSC) mechanism

$$
\epsilon_s' J_{\mathrm{SSC}}'(\epsilon_s') = \frac{3}{4} c \sigma_{\mathrm{T}} \epsilon_s'^2 \int_0^\infty \mathrm{d}\epsilon' \frac{u'(\epsilon')}{\epsilon'^2} \int_{\gamma'_{\mathrm{min}}}^{\gamma'_{\mathrm{max}}} \mathrm{d}\gamma' \gamma'^{-2} N_e'(\gamma')\, F_{\mathrm{C}}(q', \Gamma_e'). \tag{4.86}
$$

Primed quantities refer to the rest frame of the blob: $u'(\epsilon')$ is the energy density given by the synchrotron photons, $N'(\gamma')$ the numeric density of electrons in the blob. F_C is a simplified Compton Kernel computed by (Jones, 1968) accounting for both the distributions of target photons and scattering electrons being isotropic,

$$F_C(q', \Gamma'_e) = \left(2q' \ln q' + (1+2q')(1-q') + \frac{1}{2}\frac{(\Gamma'_e q')^2}{(1+\Gamma'_e q')}(1-q')\right) \times H\left(q'; \frac{1}{4\gamma'^2}, 1\right), \tag{4.87}$$

with

$$q' = \frac{\epsilon'_s/\gamma'}{\Gamma'_e(1-\epsilon'_s/\gamma')} \text{ and } \Gamma'_e = 4\epsilon'\gamma'. \tag{4.88}$$

The energy density in synchrotron photons, $u'(\epsilon')$, can be obtained from the emissivity (Eq. 8 in Finke et al. 2008)

$$u'(\epsilon') = \frac{3d_L^2 f_\epsilon^{\rm syn}}{cR_b'^2 \delta_D^4 \epsilon'} = \frac{3J'(\epsilon')}{4\pi c R'_b}. \tag{4.89}$$

One can obtain the observed νF_ν spectrum from Eq. 4.86 with the transformation in Eq. 4.45. Figure 4.14 shows an example of synchrotron and SSC νF_ν spectra obtained integrating numerically the emissivities in Eq. 4.62 and Eq. 4.86, respectively. In order to validate the implementation of the SSC in `agnpy`, the same plot in Figure 7.4 of Dermer and Menon (2009) is generated.

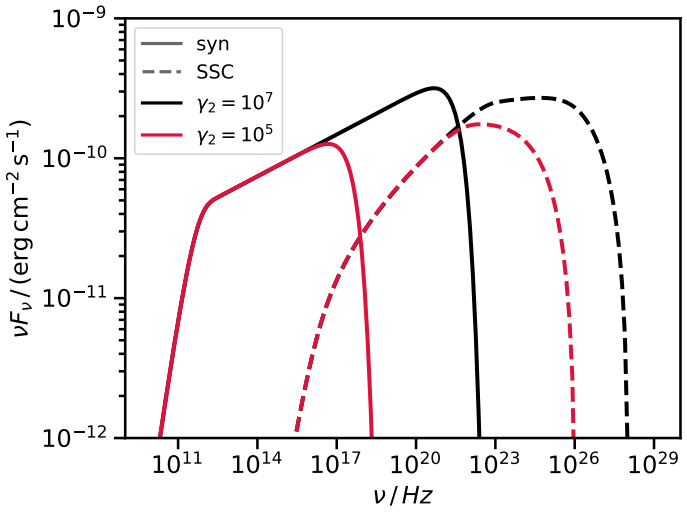

Figure 4.14: Example of synchrotron (solid line) and SSC (dashed line) νF_ν spectra obtained from a simple power-law of electrons. In the red SED the maximum Lorentz factor assumed by the electron distribution is $\gamma_2 = 10^5$, $\gamma_2 = 10^7$ for the black SED. The remaining parameters of the electron distribution and of the jet are reported in Table 4.3. Reproduction of Figure 7.4 of Dermer and Menon (2009) using `agnpy`.

A simple power-law distribution of electrons, Eq. 4.46, is considered. The parameters used for the blob and the electron density are reported in Table 4.3, primed quantities are expressed in the blob frame.

4.5.4 Compton Scattering in External Radiation Fields

The full Compton emissivity expression, Eq. 4.80, stands valid for electrons and photons distributions (N_e, $n_{\rm ph}$) computed in the same reference frame, as a particular case we have seen in Eq. 4.86 the scattering of

quantity	symbol	value
total energy in electrons	W'_e	10^{48} erg
power law spectral index	p	2.8
minimum Lorentz factor	γ'_1	10^2
maximum Lorentz factor	γ'_2	$10^5(10^7)$
blob radius	R'_b	10^{16} cm
blob magnetic field	B	1 G
jet bulk Lorentz factor	Γ	10
Doppler factor	δ_D	10
luminosity distance	d_L	10^{27} cm

Table 4.3: Parameters for the SSC model in Figure 4.14.

the synchrotron photons by the same electrons that have produced them. Dermer and Schlickeiser (1993) suggested that the high energy emission of some blazars, especially of FSRQs as 3C 273 and 3C 279, could be explained via inverse Compton scattering by the jet electrons of photon fields external to the blob, i.e. the radiation produced from the accretion disk or reprocessed by the BLR or the dust torus. We will refer to such scenario as external Compton (EC) from now on. If we were to compute the EC emissivity using Eq. 4.80, then a relativistic transformation of one of the two densities in the rest frame of the other would be in order before performing the integration. One could follow two approaches: either transform the photon distribution to the blob frame (as in Dermer and Schlickeiser 1993) or, conversely, transform the electron distribution in the stationary frame of the target (as in Georganopoulos et al. 2001). The second approach is more convenient for isotropic electron distributions that do not evolve in time and will be adopted in this work. N_e can be transformed[XV], following Georganopoulos et al. (2001), as

$$N_e(\gamma,\Omega) = \frac{\gamma^2}{\gamma'^2}\frac{\mathrm{d}V}{\mathrm{d}V'}N'_e(\gamma',\Omega) = \delta_D^3\, N'_e(\gamma',\Omega') \xrightarrow[\text{isotropic}]{} \delta_D^3\,\frac{N'_e(\gamma')}{4\pi}, \tag{4.90}$$

where, with the usual convention, primed quantities refer to the reference frame comoving with the blob. The general inverse Compton emissivity for scattering over a generic photon field external to the jet is, from Eq. 4.80

$$\epsilon_s J_{\mathrm{C}}(\epsilon_s,\Omega_s) = \epsilon_s^2\frac{cr_e^2}{4}\delta_D^3\int_0^{2\pi}\mathrm{d}\phi\int_{-1}^{1}\mathrm{d}\mu\int_0^{\epsilon_{\mathrm{high}}}\mathrm{d}\epsilon\,\frac{u(\epsilon,\Omega)}{\epsilon^2}\int_{\gamma_{\mathrm{low}}}^{\infty}\mathrm{d}\gamma\,\gamma^{-2}N'_e(\gamma/\delta_D)\,\Xi_{\mathrm{C}}, \tag{4.91}$$

and we recall that the spectral energy density is related to the photon density via $u(\epsilon) = \epsilon m_e c^2 n_{\mathrm{ph}}(\epsilon)$. In what follows we will consider three different photon targets, namely the accretion disk, the BLR and the dust torus, described in Section 4.2.3, whose photon fields become progressively more effective for Compton scattering as the blob moves farther away from the base of the jet.

[XV] Using the invariance for Lorentz transformation of the phase space volume

$$\frac{\mathrm{d}N}{\mathrm{d}\mathcal{V}} = \frac{\mathrm{d}N}{\mathrm{d}V\mathrm{d}^3\boldsymbol{p}} = \frac{\mathrm{d}N}{\mathrm{d}V\,\mathrm{d}p^2\,\mathrm{d}p\,\mathrm{d}\Omega} = \frac{1}{(m_e c^2)^3}\,\frac{1}{\gamma^2}\,\frac{\mathrm{d}N}{\mathrm{d}V\,\mathrm{d}\gamma\,\mathrm{d}\Omega} = \mathrm{inv.}$$

External Compton on Standard Disk

The first external photon field the blob will encounter moving away from the base of the jet will be the accretion disk, see Figure 4.5. Following Dermer et al. (2009), we show the result only for a standard, Shakura-Sunyaev, accretion flow. The geometry for this problem is sketched in Figure 4.15. We consider the reference frame outlined in Figure 4.13 and we set the origin in the BH.

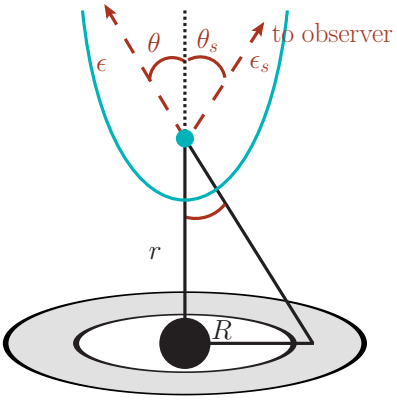

Figure 4.15: Sketch of the geometry for the inverse Compton scattering on Shakura-Sunyaev Disk. The blob (light blue dot) is at a distance r from the BH (black sphere), R defines the radial coordinate of the disk. A photon from the disk field intercepting the blob with energy ϵ and angle θ, is scattered with energy ϵ_s at an angle θ_s. r, R and θ are related by Eq. 4.92.

The blob (the light blue dot) is at height r above the BH, a photon emitted by the disk at distance R from the BH, will form an angle θ with the direction of the blob. The three quantities are related via

$$R = r\sqrt{\mu^{-2} - 1}, \tag{4.92}$$

where $\mu = \cos\theta$. These quantities are often expressed in units of the gravitational radius: $\tilde{r} = r/R_g$ and $\tilde{R} = R/R_g$. The intensity emitted by the disk at a distance R from the BH can be derived from Eq. 4.39, as

$$I^{\rm SS}(R,\Omega) = \frac{3}{16\pi^2}\frac{L_{\rm disk}}{\eta \tilde{R} R^2}\,\varphi(\tilde{R})\,\delta(\epsilon - \epsilon_0(\tilde{R})), \tag{4.93}$$

where $L_{\rm disk}$ is the disk luminosity and η its accretion efficiency, Eq. 4.35, φ is expressed in Eq. 4.40 and the delta function ensures that the photons have the dimensionless energy in Eq. 4.43, given by the disk temperature. Obtaining $u(\epsilon,\Omega)$ as $c\,I_\epsilon(\epsilon,\Omega)$ from Eq. 4.93 and plugging it into Eq. 4.91, one obtains the SED due to inverse Compton on disk photons, given a blob at distance r from the BH, as (Dermer et al., 2009)

$$f_{\epsilon_s^{\rm obs}}(r) = \frac{3^2}{2^9\pi^3}\frac{\sigma_{\rm T}\epsilon_s^2}{d_L^2 R_g^2}\frac{L_{\rm disk}}{\eta\tilde{r}^3}\int_0^{2\pi}{\rm d}\phi\int_{\mu_{\rm min}}^{\mu_{\rm min}}{\rm d}\mu\,\frac{\varphi(\tilde{R})}{(\mu^{-2}-1)^{3/2}\,\epsilon_0(\tilde{R})}\int_{\gamma_{\rm low}}^{\infty}{\rm d}\gamma\,\gamma^{-2}N_e'(\gamma/\delta_D)\,\Xi_{\rm C}, \tag{4.94}$$

where:

– the limits of integration on μ are given by

$$\mu_{\min\,(\max)} = \frac{1}{\sqrt{1 + \left(\frac{R_{\text{out (in)}}}{r}\right)^2}}, \tag{4.95}$$

and R_{in} and R_{out} are the inner and outer radius of the accretion disk, respectively;

– $\epsilon_0(\tilde{R})$ also enters the Compton Kernel computation, Eq. 4.79, with: $\bar{\epsilon} = \gamma\epsilon_0(\tilde{R})(1 - \cos\psi)$;

– since we are employing the head-on approximation ($\Omega_s \approx \Omega_e$): $\cos\psi = \mu\mu_s + \sqrt{1-\mu}\sqrt{1-\mu_s}\cos\phi$. In this case scattered photons have the same directions of the jet electrons, therefore μ_s indicates also the angle with which the electrons, and the blob, are travelling with respect to the jet axis. This result is therefore valid for any jetted AGN, not only blazars, and μ_s represents the cosine of the angle of the jet with respect our line of sight;

– the Compton emissivity is computed in the galaxy stationary frame with the BH as centre, scattered energies ϵ_s and energies observed at earth ϵ_s^{obs} (for which we compute the SED) are related via $\epsilon_s = \epsilon_s^{\text{obs}}\,(1+z)$.

Figure 4.16 proposes an example of SED due to inverse Compton on Shakura-Sunyaev disk photons, obtained performing a numerical integration of Eq. 4.94. In order to validate the implementation of the EC on disk in `agnpy`, the same plot in Figure 8 of Finke (2016) is generated. Three different distances of the blob are considered: $r = 10^{17}$, 10^{18} and 10^{19} cm. A broken power-law electron density, Eq. 4.47, is considered. Its parameters, along with those used for the disk and the AGN, are reported in Table 4.4.

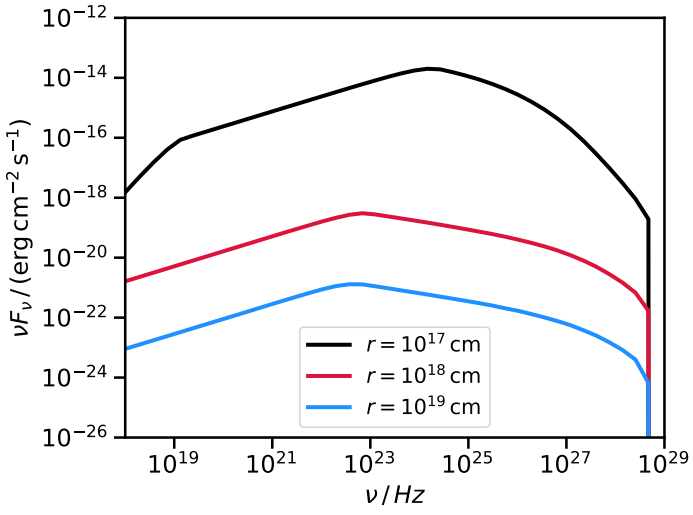

Figure 4.16: Example of νF_ν spectra due to inverse Compton on a Shakura-Sunyaev accretion disk for three different blob distances: $r = 10^{17}$ cm (black), 10^{18} cm (red) and 10^{19} cm (light blue). The parameters characterising the electron distribution and the disk are given in Table 4.4. Reproduction of Figure 8 of Finke (2016) using `agnpy`.

External Compton on Reprocessing Material

As we move along the jet axis, away from the central BH and the accretion disk photon field, we encounter sources of reprocessed radiation. The accretion disk emission is absorbed by the BLR and re-radiated as emission lines and by the dust torus that instead produces an infrared-peaked black body. Figure 4.17 introduces the geometry for this case.

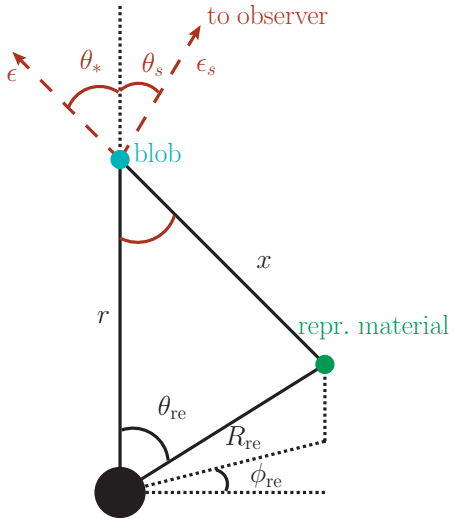

Figure 4.17: Geometry for inverse Compton scattering on reprocessing radiation field. The blob sits at distance r from the BH, the location of the infinitesimal element of reprocessing material is defined by the polar coordinates $(R_{\rm re}, \theta_{\rm re}, \phi_{\rm re})$, and has a distance x from the blob given by Eq. 4.96. A photon from the reprocessing field intercepting the blob with energy ϵ and angle θ_*, is scattered with energy ϵ_s at an angle θ_s. The disk is assumed to emit isotropically as a point-source located in the origin, heating the reprocessed material. Adapted from Finke (2016).

It is assumed that the disk is viewed by the reprocessing fields as a point-like source at the BH position emitting isotropically. The reprocessing material is identified by the polar coordinates $(R_{\rm re}, \theta_{\rm re}, \phi_{\rm re})$; x denotes its distance from the blob and it is given by

$$x^2 = R_{\rm re}^2 + r^2 - 2rR_{\rm re}\mu_{\rm re}, \tag{4.96}$$

where r is the height of the blob above the BH and $\mu_{\rm re} = \cos\theta_{\rm re}$. $\theta_* = \arccos\mu_*$ indicates the collision angle between target photon and blob electrons

$$\mu_*^2 = 1 - \left(\frac{R_{\rm re}}{x}\right)^2 (1 - \mu_{\rm re}^2). \tag{4.97}$$

θ_s indicates the emission angle of the scattered photon and, at the same time, the direction of the blob motion (given the head-on approximation). Assuming that the disk emits isotropically as a point source and that the reprocessing material isotropically scatters such radiation the energy density of the reprocessed emission (Finke, 2016) reads

$$u_{\rm re}(\epsilon) = \int {\rm d}V_{\rm re}\, \frac{j_{\rm re}(\epsilon, \Omega_{\rm re}; R_{\rm re})}{4\pi^2 x^2 c} \tag{4.98}$$

and the angle dependence can be found imposing the delta function constrains in Boettcher and Dermer

(1995) as

$$
\begin{aligned}
u_{\rm re}(\epsilon, \Omega) &= \int \mathrm{d}V_{\rm re} \frac{j_{\rm re}(\epsilon, \Omega_{\rm re}; R_{\rm re})}{4\pi^2 x^2 c} \delta(\phi - \phi_{\rm re}) \, \delta(\mu - \mu_*) \\
&= \frac{1}{4\pi c} \int_0^{2\pi} \mathrm{d}\phi_{\rm re} \int_{-1}^{1} \mathrm{d}\mu_{\rm re} \int_0^{\infty} \mathrm{d}R_{\rm re} \left(\frac{R_{\rm re}}{x}\right)^2 j_{\rm re}(\epsilon, \Omega_{\rm re}; R_{\rm re}) \, \delta(\phi - \phi_{\rm re}) \, \delta(\mu - \mu_*).
\end{aligned}
\tag{4.99}
$$

External Compton on BLR

Observations with the reverberation mapping technique[XVI] seems to indicate that individual emission lines are emitted in a narrow distance range from the central BH (Peterson and Wandel, 1999; Peterson et al., 2014). For this reason, following Finke (2016), we model each emission line of the BLR as produced by a spherical shell of radius $R_{\rm li}$, radiating monochromatically with dimensionless energy $\epsilon_{\rm li}$ given by the emission line (any Doppler broadening is neglected), the emissivity reads

$$
j_{\rm re}(\epsilon, \Omega_{\rm re}; R_{\rm li}) = \frac{\xi_{\rm li} L_{\rm disk}}{4\pi R_{\rm li}^2} \delta(\epsilon - \epsilon_{\rm li}) \, \delta(R_{\rm re} - R_{\rm li}),
\tag{4.100}
$$

where $\xi_{\rm li}$ is the fraction of the disk radiation reprocessed. From Eq. 4.99 one can obtain

$$
u_{\rm re}(\epsilon, \Omega_{\rm re}; R_{\rm li}) = \frac{\xi_{\rm li} L_{\rm disk}}{(4\pi)^2 c} \delta(\epsilon - \epsilon_{\rm li}) \int_{-1}^{1} \frac{\mathrm{d}\mu_{\rm re}}{x^2} \delta(\mu - \mu_*).
\tag{4.101}
$$

The SED can be computed from 4.91 as

$$
f_{\epsilon_s^{\rm obs}}(r) = \frac{3}{8} \sigma_{\rm T} \xi_{\rm li} L_{\rm disk} \frac{\delta_D^3}{(4\pi)^3 d_L^2} \left(\frac{\epsilon_s}{\epsilon_{\rm li}}\right)^2 \int_0^{2\pi} \mathrm{d}\phi \int_{-1}^{1} \frac{\mathrm{d}\mu_{\rm re}}{x^2} \int_{\gamma_{\rm low}}^{\infty} \mathrm{d}\gamma \, \gamma^{-2} N_e'(\gamma/\delta_D) \, \Xi_{\rm C},
\tag{4.102}
$$

keeping in mind that for the Compton Kernel (Eq. 4.79) and $\gamma_{\rm low}$ (Eq. 4.81) calculation we will use $\cos\psi = \mu_*\mu_s + \sqrt{1-\mu_*^2}\sqrt{1-\mu_s^2}\cos\phi$ and $\bar{\epsilon} = \gamma\epsilon_{\rm li}(1-\cos\psi)$. Figure 4.18 proposes an example of SED due to inverse Compton on BLR emission lines, obtained performing a numerical integration of Eq. 4.102. In order to validate the implementation of the EC on BLR in `agnpy`, the same plot in Figure 10 of Finke (2016) is generated. Three different distances of the blob are considered: $r = 10^{16}$, 10^{18} and 10^{19} cm. A broken power-law electron density, Eq. 4.47, is considered. Its parameters, along with those used for the BLR and the AGN, are reported in Table 4.4. We have considered for simplicity only the contribution due to the shell corresponding to the Lyman α hydrogen emission line: $\epsilon_{\rm li} = 2 \times 10^{-5}$ and $R_{\rm li} = 10^{17}$ cm.

External Compton on Torus

The dust torus, described in Section 4.2.3, can be modelled for the purpose of the Compton Scattering as a ring orthogonal to the jet axis, with radius $R_{\rm dt}$. We assume, following Finke (2016), that the torus emits monochromatically at $\epsilon_{\rm dt}$, which represents the peak of the black-body reprocessed distribution.

[XVI] The radius corresponding to the emission of a certain line in the BLR can be measured timing the delay between a continuum variation in the accretion disk, and a variation of the consequently excited (reverberating) line emission.

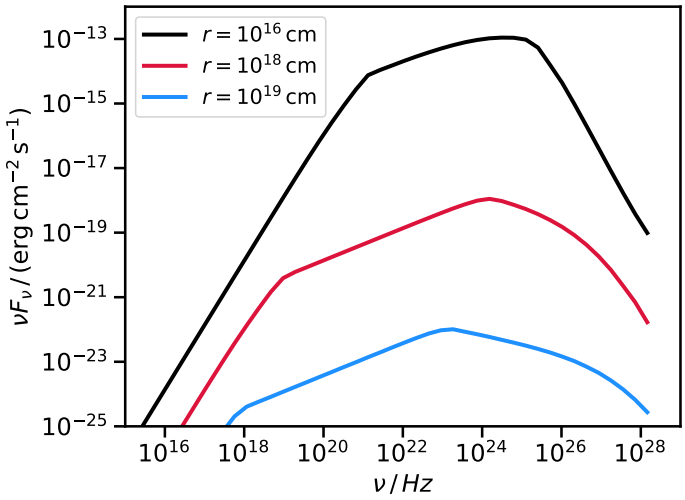

Figure 4.18: Example of νF_ν spectra due to inverse Compton on a spherical shell BLR emitting the hydrogen Lyman α line for three different blob distances: $r = 10^{16}$ cm (black), 10^{18} cm (red) and 10^{19} cm (light blue). The parameters characterising the electron distribution and the BLR are given in Table 4.4. Reproduction of Figure 10 of Finke (2016) using `agnpy`.

$\epsilon_{\rm dt} = 2.7\Theta$, where $\Theta = k_{\rm B}T_{\rm dt}/(m_e c^2)$ is the dimensionless torus temperature. The emissivity of the ring dust torus is

$$j_{\rm re}(\epsilon, \Omega_{\rm re}; R_{\rm dt}) = \frac{\xi_{\rm dt} L_{\rm disk}}{4\pi R_{\rm re}^2}\, \delta(\epsilon - \epsilon_{\rm dt})\, \delta(R_{\rm re} - 0), \tag{4.103}$$

and $\xi_{\rm dt}$ is the fraction of the disk radiation reprocessed. From Eq. 4.99 one can obtain

$$u_{\rm re}(\epsilon, \Omega) = \frac{\xi_{\rm dt} L_{\rm disk}}{(4\pi)^2 c x^2}\, \delta\left(\mu - \frac{r}{x}\right)\, \delta(\epsilon - \epsilon_{\rm dt}). \tag{4.104}$$

The SED can be computed from 4.91 as

$$f_{\epsilon_s^{\rm obs}}(r) = \frac{3}{8}\sigma_{\rm T}\xi_{\rm dt} L_{\rm disk}\, \frac{\delta_D^3}{(4\pi)^3 d_L^2} \left(\frac{\epsilon_s}{\epsilon_{\rm dt}}\right)^2 \int_0^{2\pi} {\rm d}\phi \int_{\gamma_{\rm low}}^{\infty} {\rm d}\gamma\, \gamma^{-2} N_e'(\gamma/\delta_D)\, \Xi_{\rm C}, \tag{4.105}$$

Being the torus ring orthogonal to the jet axis, Eq. 4.96 reduces to $x^2 = R_{\rm dt}^2 + r^2$, and Eq. 4.97 to r/x. For the Compton Kernel (Eq. 4.79) and $\gamma_{\rm low}$ (Eq. 4.81) calculation we will use $\cos\psi = \frac{r}{x}\mu_s + \sqrt{1 - (\frac{r}{x})^2}\sqrt{1 - \mu_s^2}\cos\phi$ and $\bar{\epsilon} = \gamma\epsilon_{\rm dt}(1 - \cos\psi)$. Figure 4.19 presents an example of SED due to inverse Compton over a dust torus with temperature $T_{\rm dt} = 10^3$ K. The radius of the ring is estimated at the sublimation radius, given by Nenkova et al. (2008) as

$$R_{\rm dt} = 3.5 \times 10^{18} \left(\frac{L_{\rm disk}}{10^{45}\,{\rm erg\,s^{-1}}}\right)^{1/2} \left(\frac{T_{\rm dt}}{10^3\,{\rm K}}\right)^{-2.6} {\rm cm}. \tag{4.106}$$

In order to validate the implementation of the EC on dust torus in `agnpy`, the same plot in Figure 11 of Finke (2016) is generated. Three different distances of the blob are considered: $r = 10^{19}$, 10^{20} and 10^{21} cm. A broken power-law electron density, Eq. 4.47, is considered. Its parameters, along with those used for the dust torus and the AGN, are reported in Table 4.4.

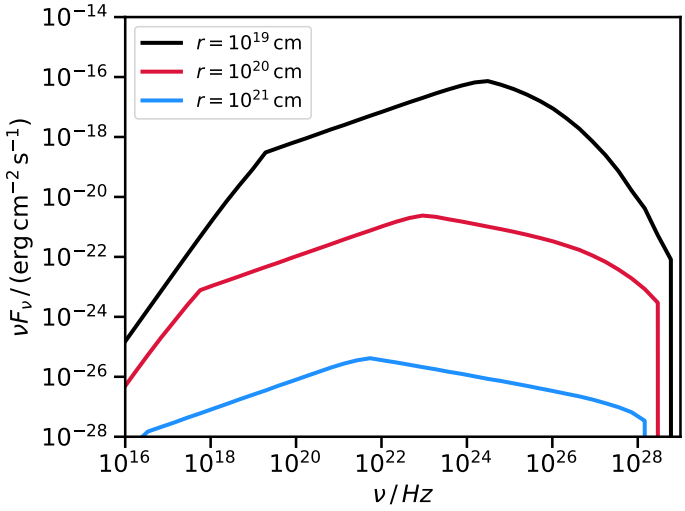

Figure 4.19: Example of νF_ν spectra due to inverse Compton on a dust torus for three different blob distances: $r = 10^{19}$ cm (black), 10^{20} cm (red) and 10^{21} cm (light blue). The parameters characterising the electron distribution and the torus are given in Table 4.4. Reproduction of Figure 11 of Finke (2016) using `agnpy`.

quantity	symbol	value
total energy in electrons	W_e	5×10^{42} erg
1st power law spectral index	p_1	2
2nd power law spectral index	p_2	3.5
spectral break	γ'_b	10^4
minimum Lorentz factor	γ'_1	20
maximum Lorentz factor	γ'_2	5×10^7
blob radius	R'_b	10^{16} cm
jet bulk Lorentz factor	Γ	10
Doppler factor	δ_D	10
redshift	z	1
BH mass	$M_{\rm BH}$	$1.2 \times 10^9\, M_\odot$
BH gravitational radius	R_g	1.8×10^{14} cm
disk luminosity	$L_{\rm disk}$	2×10^{46} erg s^{-1}
disk accretion efficiency	η	1/12
disk inner radius	$R_{\rm in}$	$6\, R_g$
disk outer radius	$R_{\rm out}$	$200\, R_g$
BLR dimensionless energy	$\epsilon_{\rm li}$	2×10^{-5}
BLR scattering fraction	$\xi_{\rm li}$	0.024
BLR emission radius	$R_{\rm li}$	10^{17} cm
dust torus temperature	$T_{\rm dt}$	10^3 K
dust torus scattering fraction	$\xi_{\rm dt}$	0.1

Table 4.4: Parameters for the EC scattering model in Figure 4.16, 4.18 and 4.19.

4.5.5 Photon-Photon Opacity

The discussion on gamma-ray emission from cosmic sources cannot be exempt from considering the pair production process $\gamma\gamma \to e^+e^-$ attenuating their intrinsic fluxes. To account for this phenomenon a $\gamma\gamma$ optical depth or *opacity*, $\tau_{\gamma\gamma}$, has to be computed. The latter depends on the gamma ray energy, on the energy of the target photon and on the path traversed in the absorbing field. The observed flux can be obtained attenuating the intrinsic one with a factor $\exp(-\tau_{\gamma\gamma})$. The cross section for the $\gamma\gamma \to e^+e^-$ process (Finke, 2016) reads[XVII]

$$\begin{aligned} \sigma_{\gamma\gamma}(s) &= \frac{3}{8}\sigma_{\mathrm{T}}(1-\beta_{\mathrm{cm}}^2)\left[(3-\beta_{\mathrm{cm}}^4)\ln\left(\frac{1+\beta_{\mathrm{cm}}}{1-\beta_{\mathrm{cm}}}\right) - 2\beta_{\mathrm{cm}}(2-\beta_{\mathrm{cm}}^2)\right], \\ \beta_{\mathrm{cm}} &= \sqrt{1-s^{-1}}. \end{aligned} \tag{4.107}$$

and is represented in Figure 4.20. The variable s is the squared value of the Lorentz factor the produced $e^{\pm}$ pair has in the centre-of-momentum frame

$$s = \gamma_{\mathrm{cm}}^2 = \epsilon\epsilon_1(1-\cos\psi), \tag{4.108}$$

where ϵ_1 is the dimensionless observed energy of the gamma ray corrected by the redshift $\epsilon_1 = (1+z)\,\epsilon_1^{\mathrm{obs}}$, ϵ is the dimensionless energy of the target and ψ the angle between the photons.

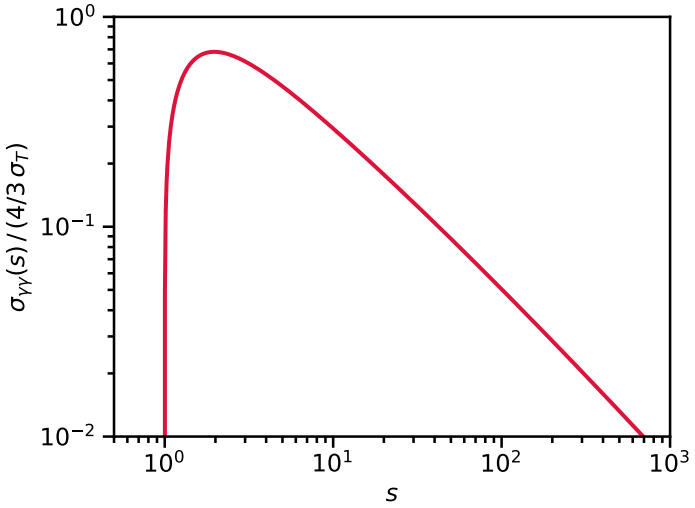

Figure 4.20: Cross section for the $\gamma\gamma \to e^+e^-$ process as a function of the kinematic variable $s = \epsilon\epsilon_1(1-\cos\psi)$, using Finke (2016) formulation.

As the $\gamma\gamma$ cross section rises for $s > 1$, as a rule of thumb we could use $\epsilon_1 \approx s/\epsilon \approx 1/\epsilon$ to obtain the energy ϵ_1 of a photon field absorbing a gamma ray with energy ϵ. The $\sim$ GeV to $\sim$ TeV gamma rays measured by HE and VHE instruments are therefore best absorbed by photon fields in the UV to IR.

[XVII] Note there is a factor 4/3 between the definition in Eq. 17 of Dermer et al. (2009) and in Eq. 119 of Finke (2016) for the $\gamma\gamma$ cross section. The latter is chosen as the approach of Finke (2016) is followed for the opacity calculations in this work.

This means that the same photon fields providing the target for the external Compton can attenuate the highest-energy radiation. Additionally, in their route to Earth, gamma rays can be absorbed by the extragalactic cosmic radiation permeating the universe. The latter, identified in the wavelength range between 0.1 and 1000 μm as extragalactic background light (EBL), contains the cumulative energy all stars and galaxies (and their progenitors) emitted through the history of the universe (Dwek and Krennrich, 2013). The correction for the EBL absorption is implemented in the MAGIC software. The source modelling in this thesis can therefore rely directly on intrinsic spectra and flux points, corrected with the EBL models of Franceschini et al. (2008) or Domínguez et al. (2011).

We concentrate on the gamma-ray absorption caused by the AGN components producing the fields for the inverse Compton scattering. The $\gamma\gamma$ opacity (Dermer and Menon, 2009) is introduced as

$$\tau_{\gamma\gamma}(\epsilon_1, r) = \int_r^\infty \mathrm{d}l \int_0^{2\pi} \mathrm{d}\phi \int_{-1}^{1} \mathrm{d}\mu \int_0^\infty \mathrm{d}\epsilon \, \frac{u(\epsilon, \Omega; l)}{\epsilon m_e c^2} \, \sigma_{\gamma\gamma}(s) \, (1 - \cos\psi), \tag{4.109}$$

where $u(\epsilon, \Omega; l)$ is the energy density of the seed photon field and one has to integrate over the solid angle (θ, μ), over the seed energy ϵ and over the distance l between the emitting region (located at r) and the observer, located at ∞. ψ is the angle between the two photons. In what follows we will consider the optical depths produced by the target fields that we considered in Section 4.5.4 for the external Compton scattering. Each target will attenuate the flux produced at the source by a factor $\exp(-\tau_{\gamma\gamma})$. To simplify the calculations we will assume that the blob electrons travel along the jet axis $\mu_s \to 0$, i.e. that we are in a blazar scenario, this implies $\cos\psi = \mu$ (from Eq. 4.72).

Absorption by (Standard) Accretion Disk Photons

First we consider the $\gamma\gamma$ opacity of a standard Shakura-Sunyaev accretion disk. The energy density can be obtained from the intensity in Eq. 4.93. One obtains for the opacity, from Eq. 4.109,

$$\tau_{\gamma\gamma}(\epsilon_1^{\mathrm{obs}}; r) = 10^7 \, \frac{l_{\mathrm{Edd}}^{3/4} M_8^{1/4}}{\eta^{3/4}} \int_{\tilde{r}}^\infty \frac{\mathrm{d}\tilde{l}}{\tilde{l}^2} \int_{\tilde{R}_{\mathrm{in}}}^{\tilde{R}_{\mathrm{out}}} \frac{\mathrm{d}\tilde{R}}{\tilde{R}^{5/4}} \, \frac{\varphi(\tilde{R})}{\left(1 + \tilde{R}^2/\tilde{l}^2\right)^{3/2}} \left[\frac{\sigma_{\gamma\gamma}(\tilde{s})}{\sigma_{\mathrm{T}}}\right] (1 - \mu). \tag{4.110}$$

Distances with the tilde are scaled by the gravitational radius, i.e. $\tilde{r} = r/R_g$, $\tilde{l} = l/R_g$ and $\tilde{R} = R/R_g$, the kinematic variable s is now obtained via

$$\tilde{s} = \frac{\epsilon_0(\tilde{R})\epsilon_1(1 - \mu)}{2}, \tag{4.111}$$

$\epsilon_0(\tilde{R})$ is the dimensionless energy of the accretion disk in Eq. 4.43 and $\mu = \sqrt{1 + \tilde{R}^2/\tilde{l}^2}$ is the cosine of the angle under which the disk is viewed at height l (see Eq. 4.92 and Eq. 4.15).

Absorption by Spherical Shell BLR

The energy density of a BLR approximated as a spherical shell emitting monochromatically is given in 4.101. From Eq. 4.109 one finds

$$\tau_{\gamma\gamma}(\epsilon_1^{\rm obs};r) = 900\,\frac{\xi_{\rm li} l_{\rm Edd}}{\epsilon_{\rm li}}\int_{\tilde{r}}^{\infty} {\rm d}\tilde{l}\int_{-1}^{1}\frac{{\rm d}\mu_{\rm re}}{\tilde{x}^2}\left[\frac{\sigma_{\gamma\gamma}(\tilde{s})}{\sigma_{\rm T}}\right](1-\mu_*), \tag{4.112}$$

where, following Eq. 4.96 and Eq. 4.97,

$$\begin{aligned}\tilde{x}^2 &= \frac{R_{\rm li}^2 + l^2 - 2lR_{\rm li}\mu_{\rm re}}{R_g^2},\\ \mu_*^2 &= 1-\left(\frac{R_{\rm li}}{R_g\tilde{x}}\right)^2(1-\mu_{\rm re}^2),\\ \tilde{s} &= \frac{\epsilon_{\rm li}\epsilon_1(1-\mu_*)}{2}.\end{aligned} \tag{4.113}$$

Absorption by Dust Torus

Considering the energy density obtained in Eq. 4.104 for the dust torus, the $\gamma\gamma$ opacity reads

$$\tau_{\gamma\gamma}(\epsilon_1^{\rm obs};r) = 900\,\frac{\xi_{\rm dt} l_{\rm Edd}}{\epsilon_{\rm dt}}\int_{\tilde{r}}^{\infty}\frac{{\rm d}\tilde{l}}{\tilde{x}^2}\left(1-\frac{\tilde{l}}{\tilde{x}}\right)\left[\frac{\sigma_{\gamma\gamma}(\tilde{s})}{\sigma_{\rm T}}\right], \tag{4.114}$$

where, following Eq. 4.96 and Eq. 4.97,

$$\begin{aligned}\tilde{x}^2 &= \frac{R_{\rm dt}^2}{R_g^2} + \tilde{l}^2,\\ \tilde{s} &= \frac{\epsilon_{\rm dt}\epsilon_1\left(1-\frac{\tilde{l}}{\tilde{r}}\right)}{2}.\end{aligned} \tag{4.115}$$

Figure 4.21 presents the opacities, as a function of the observed energy E, for the Shakura-Sunyaev disk (solid line), the BLR (dashed line) and the dust torus (dot-dashed) fields and considering three blob distances expressed in units of the Lyman α radius, $R({\rm Ly}\alpha) = 1.1\times10^{17}$ cm. Values are obtained solving numerically Equations 4.110, 4.112 and 4.114. Parameters of the target fields are listed in Table 4.4. On subparsec scales, $r\sim0.01-0.1$ pc, the opacity for gamma-rays is dominated by the BLR photons. The effect of the disk photons intervenes only after hundreds of GeV, even in the closes scenario $r\sim0.1\,R({\rm Ly}\alpha)$, where the spectra of many FSRQs (see Chapter 5) significantly softens, reaching the maximum of detectability with the current sensitivities. The absorption by the dust torus photon field is instead relevant only for $\sim$ TeV gamma-rays, and seems equal at all distances within the Torus radius. The torus opacity becomes the only dominant component outside the BLR, $r\sim1$ pc.

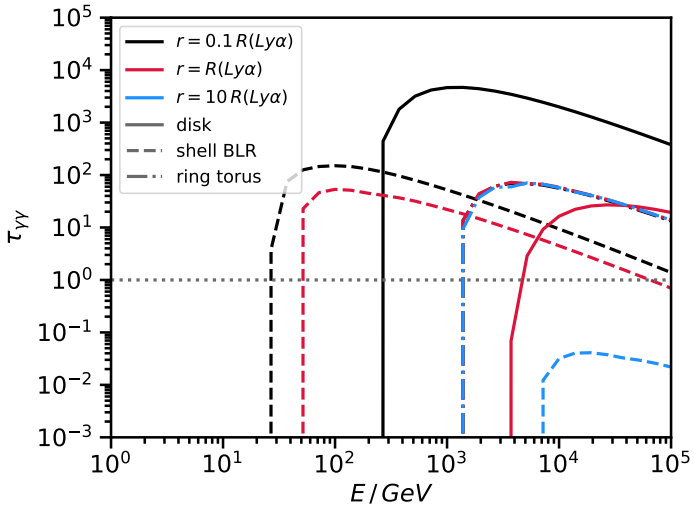

Figure 4.21: $\gamma\gamma \to e^{\pm}$ opacity for different photon fields: Shakura-Sunyaev accretion disk (solid line), a spherical shell Lyman α BLR (dashed line), a dust torus (dot-dashed line). Parameters of the target fields are listed in Table 4.4. Results for three distances of the blob are considered: $r = 0.1\,R(\mathrm{Ly}\alpha) \approx 10^{16}\,\mathrm{cm}$) (in black), $r = R(\mathrm{Ly}\alpha) \approx 10^{17}\,\mathrm{cm}$) (in red), $r = 10\,R(\mathrm{Ly}\alpha) \approx 10^{18}\,\mathrm{cm}$) (in light blue). Reproduction of Figure 14 of Finke (2016) using `agnpy`.

4.5.6 Hadronic Models

The radiative processes involving electrons and positrons, focus of this dissertation, are commonly labelled as leptonic. They provide a reasonable fit to the broadband spectra of most observed blazars: the dicothomy adopted in the literature foresees the SSC mechanism as responsible of the high-energy continuum emission of BL Lacs (given the observational absence of broad emission lines or strong seed fields) while the EC is invoked to model the high-energy spectral hump of FSRQs. Although contributing to picture the mechanisms and the environments of astrophysical particle acceleration, leptonic radiative processes leave AGN decoupled from the hadronic and neutrino cosmic fluxes observed at Earth (see Chapter 1). Hadronic radiative models recover such connection and provide, beside EM spectra, also a prediction on the astrophysical neutrino fluxes to be expected from this class of sources. The discussion on hadronic models has started in the early nineties (Mannheim and Biermann, 1989; Kirk and Mastichiadis, 1992; Mastichiadis and Kirk, 1995), although the literature has prominently focused on leptonic ones as they provided adequate reproduction of the broad-band AGN spectra with fewer assumptions. After the detection of the broadband flaring activity of the blazar TXS 0506+056 in spatial and temporal coincidence with an astrophysical high-energy neutrino (IceCube Collaboration et al. 2018, in addition to the discovery of a significant excess of astrophysical neutrinos from the same position in archival IceCube data, IceCube Collaboration 2018), the adoption of hadronic models has blossomed again in the literature (Ansoldi et al., 2018a; Cerruti et al., 2019; Gao et al., 2019; Keivani et al., 2018; Liu et al., 2019). Here we provide a brief overview of the mechanisms suggested, focusing on the historical papers introducing the seminal ideas. Given that the environments of AGN are mostly constituted by photon fields (see Section 4.2.3) $p - \gamma$ interactions are mostly considered for hadronic radiative models. $p - p$ interactions are seldomly used as they require some ad-hoc proton target entering the jet, e.g. a star (Bednarek and Protheroe, 1997) or a red giant (Barkov, 2010). Essentially an hadron accelerated in the jet (let us

consider a proton for simplicity) will interact with a target photon field via photo-pion production or Bethe-Heitler pair production

$$p+\gamma \rightarrow \begin{cases} \text{photo-pion} & \Delta^+ \rightarrow \begin{cases} p+\pi^0 \\ n+\pi^+ \end{cases} \qquad \sqrt{s} = (m_p + m_\pi)\, c^2, \\ \text{Bethe-Heitler} & p + e^+ + e^- \qquad\qquad \sqrt{s} = (m_p + 2\, m_e)\, c^2, \end{cases} \tag{4.116}$$

and we have reported also the threshold in the centre-of-mass system, $\sqrt{s}$, for such processes. Given a photon target with energy 10 eV a proton of energy 10^2 TeV is needed to start Bethe-Heitler while the threshold rises to 10 PeV for photo-meson production. The target fields providing the photons for $p-\gamma$ interaction can be (exactly as for the inverse Compton scattering) internal to the jet itself (Mannheim and Biermann, 1992; Mücke and Protheroe, 2001) or external, provided by the accretion disk (Bednarek and Protheroe, 1999) or by its radiation reprocessed by the BLR (Atoyan and Dermer, 2003). In addition to $p-\gamma$ and $p-p$ model, there are also *proton synchrotron models* (Aharonian, 2000), describing the dominant contribution to the high-energy emission with synchrotron radiation from protons. In this case, however, very intense magnetic fields, $B \gtrsim 10$ G, are required. Such intense B fields would make also relevant the synchrotron emission of the secondary products of the photo-meson production e.g. π and μ. The emission region can be optically thick to $\gamma\gamma$ pair production and an EM cascade can be initiated by: the p-synchrotron photons (p-synchrotron cascade), the $2\,\gamma$ from π_0 decay (π_0 cascade), electrons from μ decay, synchrotron radiation by photo-meson secondary products (e.g. π- or μ-synchrotron cascades). Mücke and Protheroe (2001); Mücke et al. (2003) illustrated that only p-synchrotron and μ-synchrotron cascades produce significant features in a VHE spectrum.

5 | Detection of a Gamma-ray Low State of PKS 1510-089 between 2012 and 2017

The MAGIC data analysis presented here is published in Acciari et al. (2018b) of which I am corresponding author. Together with J. Sitarek I was responsible of the MAGIC data analysis. At least two independent and compatible analysis are requested by the MAGIC collaboration in order to publish any scientific results. Figures and numbers from J. Sitarek's analysis are used in Acciari et al. (2018b), while in this chapter I present mine. They are both compatible and approved by the MAGIC collaboration. The Swift-XRT data shown were analysed by V. Fallah Ramazani, the *Fermi*-LAT data by J. Becerra González. Multi-wavelength data were provided by collaborators listed after J. Becerra González in the author list of Acciari et al. (2018b). The radiative model presented in this chapter is original.

Flat Spectrum Radio Quasars represent the most luminous sources of the blazar sequence. Despite their brightness, their detection in VHE gamma-rays is hampered by two circumstances. First, the peak of their high-energy continuum emission occurs in the $\sim$ MeV$-$GeV regime and, as a result, a steeply falling power-law flux manifests in VHE gamma-rays (see Figure 4.4). Second, they are characterised, on average, by larger cosmological distances with respect to the rest of the blazar objects (see their redshift distribution in Figure 12 of Ackermann et al. 2015) and hence suffer a higher gamma-ray attenuation by the EBL. Only 7 FSRQs have been detected to date in VHE gamma rays (they are listed, along with their redshifts and the instrument that first detected them, in Table 5.1) predominantly during flaring episodes or broad-band enhanced states.

source	redshift	discovered	reference
3C 279	$z = 0.5362$	MAGIC	Albert et al. (2008b)
PKS 1222+216	$z = 0.432$	MAGIC	Aleksić et al. (2011)
PKS 1510-089	$z = 0.36$	H.E.S.S.	Abramowski et al. (2013)
PKS 1441+25	$z = 0.939$	MAGIC	Ahnen et al. (2015)
S3 0218+35	$z = 0.954$	MAGIC	Ahnen et al. (2016a)
PKS 0736+017	$z = 0.18941$	H.E.S.S.	Cerruti et al. (2017)
TON 0599	$z = 0.747$	MAGIC	Mirzoyan (2017)

Table 5.1: FSRQs detected in VHE gamma-rays.

The FSRQ subject of this study, PKS 1510-089, represents the first FSRQ showing a persistent emission in VHE. In Section 5.2 we will show that relying on *Fermi*-LAT integral flux measurements it is possible to individuate a low state of gamma-ray emission simultaneous to several dozens of MAGIC observational hours building up a significant VHE gamma-ray signal. The VHE flux level of the thus identified low state is compatible with a constant flux over the 5 years (2012-2017) in which the source has been monitored by MAGIC. The spectral index of the low state is remarkably similar to those characterising past VHE flaring episodes. In Section 5.2.3 we will list the observations at lower energies (from X-ray to radio), collected for this work, simultaneous to the identified VHE low gamma-ray state that will be used in Section 5.3 to compile the multi-wavelength SED. Its highest-energy continuum emission will be modelled, in line with the previous literature on this source, with a scenario foreseeing inverse Compton over the photon field generated by the disk radiation reprocessed by the dust torus (described in Section 4.5.4). Also in agreement with the interpretational history of this source is the lack of evidence for gamma-ray absorption feature produced by the BLR photon field. Our study reinforces the hypothesis that the region responsible for the gamma-ray emission of FSRQs resides at sub-pc distances from the BH, outside the BLR clouds.

5.1 Gamma-ray Observational History

The first gamma-ray instrument to discover PKS 1510-089 was EGRET (Hartman et al., 1999). The first variability in HE gamma rays was detected by the AGILE team between 2007 and 2009 (reported in Verrecchia et al. 2013). In 2009 the source underwent a broad band flaring activity, from gamma rays

(Abdo et al., 2010; D'Ammando et al., 2011) to radio (Marscher et al., 2010). Follow-up observations by H.E.S.S. resulted in the discovery of the source in VHE gamma rays (reported in Abramowski et al. 2013). The brightest radio flare was recorded in 2011 (Orienti et al., 2013) and was accompanied by fast HE gamma-ray variability characterised by time scales as low as 20 minutes (Saito et al., 2013). MAGIC detected PKS 1510-089 in VHE gamma rays with observations gathered between February and April 2012 and triggered by the high flux measured by AGILE (Lucarelli et al., 2012). The flux above 200 GeV was $\sim 3\%$ of the Crab nebula flux integrated above the same energy. After its first detection MAGIC initiated a multi-year monitoring campaign of 2 to 6 observations (1 to 3 hours long) in each of the 6 months (February-August) in which the source is visible at the ORM. Results presented in this chapter use the whole stereo observations collected in this monitoring programme over 5 years: from 2012 to 2017. Variability in the VHE regime was not detected until May 2015, when MAGIC observed a VHE flare with a flux 5 times higher than the one measureds in 2012. Observations were once more triggered by a HE satellite, *Fermi*-LAT in this case (Ahnen et al., 2017b). A peculiar flare occurred in May 2016 with the flux, integrated above 200 GeV, reaching a value $\sim 80\%$ the Crab nebula flux. This time the VHE flaring activity had a mild HE counterpart. Joint observations by H.E.S.S. and MAGIC are reported in Zacharias et al. (2017).

5.2 Data Analysis

In this section the data sets used for this work are presented. Considering the unstable observing conditions (subject to weather variations) and being the source observable only for half a year, the VHE data sampling is very sparse. Additionally, excluding flaring episodes, PKS 1510-089 is characterised by low flux values that build a significant VHE gamma-ray signal only collecting tens of observation hours. Since the source is not detectable on a nightly basis it is therefore impossible to infer any information on the gamma-ray flux behaviour over time using the VHE data alone. In order to identify a low gamma-ray state of the source, *Fermi*-LAT flux measurements over the five-year period monitored by MAGIC are considered. Being the *Fermi*-LAT analysis preliminary to the selection of MAGIC data, its description will be presented first.

5.2.1 *Fermi*-LAT Analysis

A description of the *Fermi*-LAT instrument can be found in Section 3.2.1. For this data analysis, observations performed between 5 December 2011 and 7 August 2017 (MJD: 55900-57972) were selected, considering all the photons from a RoI with radius 10° centred on PKS 1510-089 coordinates. Additional cuts were posed on the events energy: $100\,\mathrm{MeV} \leq E_\gamma \leq 300\,\mathrm{GeV}$, and their angle with respect to the satellite local zenith $< 90°$, to reduce the background of gamma rays produced by CRs interactions in Earth atmosphere. To extract the spectrum and the light curve, differently than in Chapter 3, the full likelihood analysis described in Mattox et al. (1996) is employed. Differently than the likelihood in Eq. 2.27, that we may call one-dimensional as it foresees only a binning in energy, the likelihood for the standard *Fermi*-LAT analysis is three-dimensional as the events are additionally binned according

to their coordinates (pixels). Such likelihood allows to model several sources in the FoV and to consider their spatial extension at once with the spectral parameters. For the likelihood computation, spectral and morphological parameters modelling the sources within 20° from PKS 1510-089 coordinates are taken from the *Fermi*-LAT Third Source Catalog (3FGL, Acero et al. 2015). The residual gamma-ray background due to the galactic plane and to non-resolved extragalactic sources is modelled following Acero et al. (2016) and Ackermann et al. (2016), respectively. A more detailed description of this data analysis, and the optimisation steps performed can be found in Section 2.1 of Acciari et al. (2018b), here we will simply list the main results. In order to identify a low state of gamma-ray emission, a light curve in time bins of 30 days is computed. In each time bin the differential flux spectrum is estimated with the aforedescribed likelihood method and then integrated from 1 GeV to 300 GeV. Fluxes in monthly time bins have relative uncertainties as low as 20%, thus reducing variations due to statistical fluctuations with respect to the intrinsic ones. Building a histogram of the monthly fluxes, shown by the the blue line in Figure 5.1, indicates there is a low state of fluxes between 1 and $3 \times 10^{-8}\,\mathrm{cm^{-2}s^{-1}}$, distinct from the flaring periods seemingly occurring with flux values $> 3 \times 10^{-8}\,\mathrm{cm^{-2}s^{-1}}$. This trend is confirmed by building the histogram of the daily fluxes, shown by the the red line in Figure 5.1: a cut at

$$\phi(E > 1\,\mathrm{GeV}) < 3 \times 10^{-8}\,\mathrm{cm^{-2}s^{-1}}, \tag{5.1}$$

marks the beginning of a power-law distribution characterising high-flux episodes. We note that the relative error on daily fluxes can be as high as 50%.

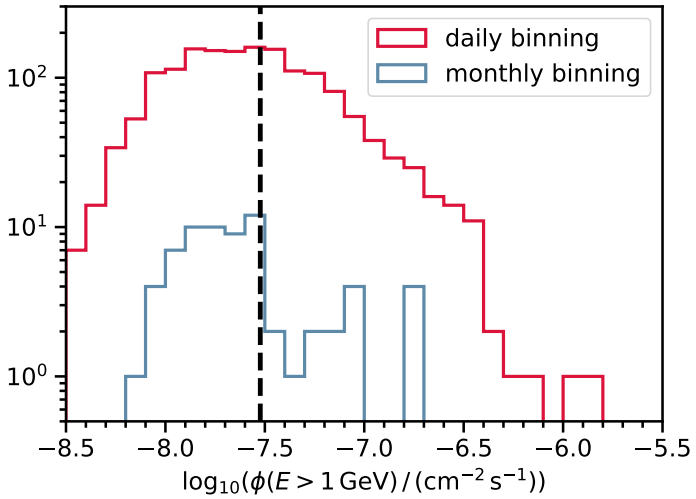

Figure 5.1: Histograms of the daily (red) and monthly (blue) fluxes integrated above 1 GeV, estimated from *Fermi*-LAT data. A consistent accumulation of fluxes is visible in the monthly histograms below the value $3 \times 10^{-8}\,\mathrm{cm^{-2}s^{-1}}$, marked by the black dashed line. The same value marks a break between a rising and falling power-law trend in the histogrammed daily fluxes. Adapted from Acciari et al. (2018b).

The separation between periods of low and high HE gamma-ray fluxes is also displayed in the uppermost panel of the multi-wavelength light curve in Figure 5.2. The monthly flux values are shown as light grey steps, only daily flux points simultaneous to MAGIC observations are displayed: in blue if they fulfil Eq. 5.1 (low state), in red in the opposite case. The value of 1 GeV as threshold for the flux integration

in the light curve is chosen as a proxy for the tens of GeV regime in which MAGIC becomes sensitive. PKS 1510-089 is indeed a source with a soft spectrum typically detected as a power-law stretching (i.e. having significant excesses) up to hundreds of GeV (Abramowski et al., 2013; Aleksić et al., 2014a; Zacharias et al., 2017). Therefore the flux distribution above the GeV in HE is chosen as a representation of the flux distribution in the sub-TeV regime in which the source shines in VHE. Combining the *Fermi*-LAT data simultaneous to the MAGIC observations and fulfilling Eq. 5.1 (indicated as blue points in Figure 5.2), the differential flux model $\mathrm{d}\phi/\mathrm{d}E$ giving the best likelihood fit between 100 MeV and 300 GeV, is a power law (Eq. 2.29) with spectral index 2.56 ± 0.04. The test statistics (TS)[I] of the fit is 1656, corresponding to a significance of $\approx 41\,\sigma$. A fit with a log-parabolic spectral model (Eq. 2.30) does not produce a significant improvement of the TS, therefore the presence of spectral curvature is discarded.

5.2.2 MAGIC Analysis

MAGIC observed PKS 1510-089 for 151 nights in the five-year period between 2012 and 2017. Among those, 115 nights survived the data quality selection cuts: atmospheric transmission $> 85\%$, mean current in the M2 camera pixels $< 2000\,\mu$A (to suppress NSB background). The atmospheric depth (Eq. 2.7) increases with the zenith angle and so does the minimum energy of a gamma ray primary for its shower to penetrate to trigger the telescopes. The negative declination of the source makes it observable from the ORM at zenith angles $> 38°$ and most of the observations are taken while the source culminates, i.e. at angles $< 40°$. We estimate, given the zenith angle spanned by the observations, that the appropriate energy threshold for the flux integration for the light curve computation is 150 GeV[II]. We then reconstruct spectral points below 100 GeV relying on the unfolding procedure.

Selection of the Low State

Selecting the MAGIC observations whose simultaneous *Fermi*-LAT flux measurement verifies Eq. 5.1 leaves 76 nights in the data set, amounting to ≈ 76 hours of observation. We label these observations as VHE *low state*. For the other wavelengths introduced in Section 5.2.3 we will define their data sets as simultaneous to the VHE low state, if they verify the condition

$$\text{simultaneous to MAGIC observation} \;\wedge\; \phi(E > 1\,\mathrm{GeV}) < 3 \times 10^{-8}\,\mathrm{cm}^{-2}\mathrm{s}^{-1}. \tag{5.2}$$

The low state selection removes from the MAGIC data set most of the observations used in the 2012 detection (Aleksić et al., 2014a) as well as the 2015 (Ahnen et al., 2017b) and 2016 (Zacharias et al., 2017) flares. The MAGIC data analysis was performed with MARS (see Section 2.4), the low state data set is divided in 6 periods during which significant hardware changes have occurred. In each period a RF

[I] The test statistics is derived from the likelihood ratio testing the source / no source hypothesis, i.e. built form a sky model including or neglecting the source under study.

[II] For this estimate the energy distribution of the simulated MC events is re-weighted with the spectrum of the source considered and the peak of this energy distribution is considered as the threshold for the flux integrations (see Section 4.1 and Figure 6 of Aleksić et al. 2016b).

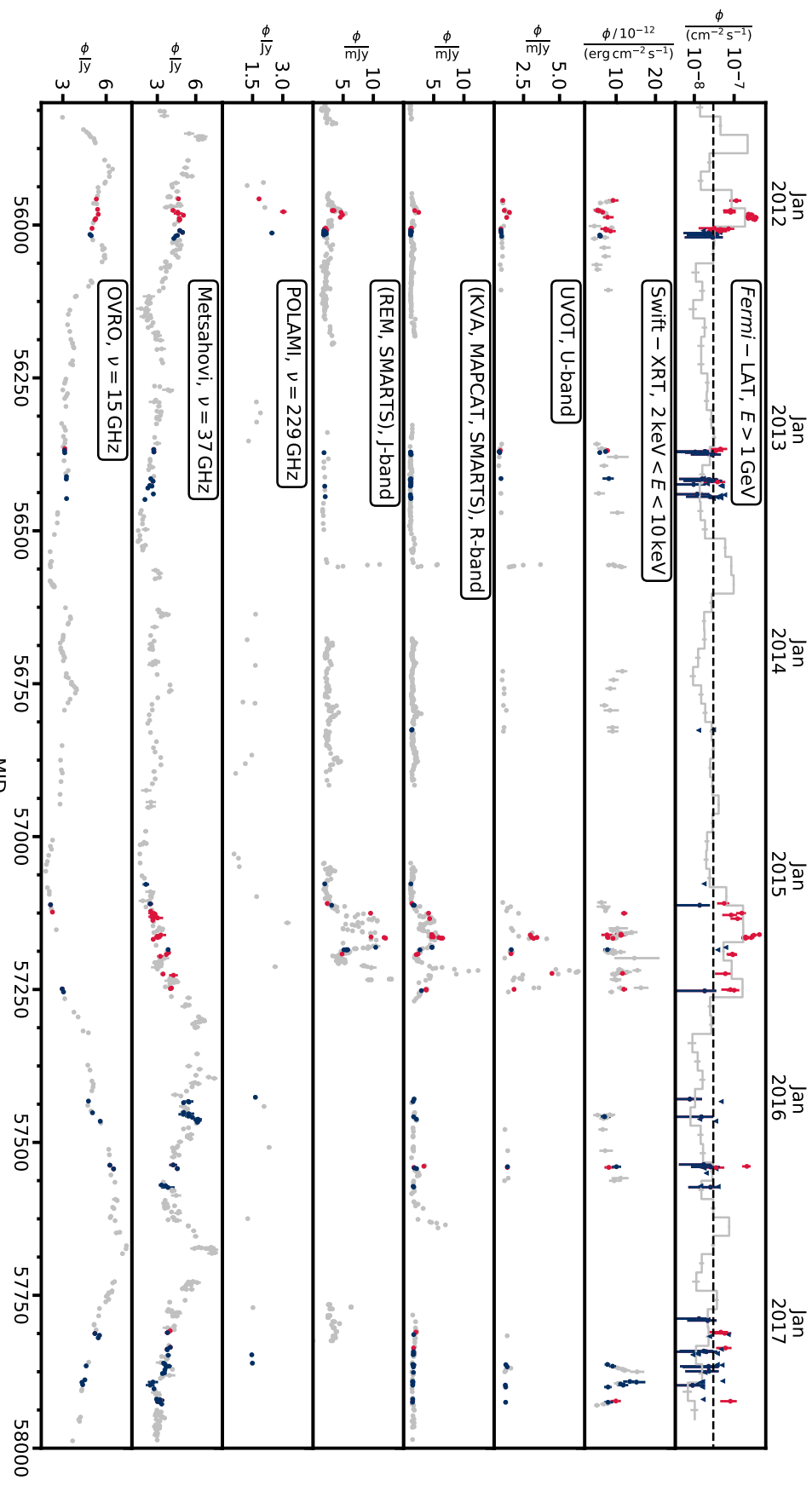

Figure 5.2: Multi wavelength light curve of PKS 1510-089 between 2012 and 2017. The panels are presented in order of decreasing frequency. Only flux points simultaneous to MAGIC observations are coloured, in blue if they are simultaneous to the VHE low state condition in Eq. 5.2, in red on the contrary.

is trained with the proper hadron data and MC simulations (see Section 2.4.4). Data are merged for the final scientific results production. Building the θ^2 histogram of the 76 nights with simultaneous low flux in HE, illustrated in Figure 5.3, returns a significance of $9.7\,\sigma$, computed according to Eq. 2.26.

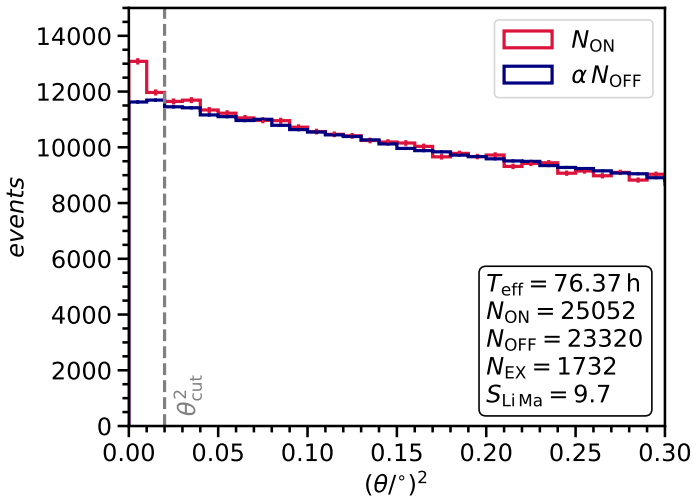

Figure 5.3: Histogram of the squared angular distances θ^2 from the centre of the ON (red) and OFF (blue) regions used for the background subtraction (see Section 2.4.6). The ON and OFF regions have sizes $R^2_{\mathrm{ON/OFF}} = 0.02^{\circ^2}$ and only one OFF control region is used.

The spectrum is estimated both with the likelihood method and the unfolding procedure described in Section 2.4.6 assuming a power law function. Spectral results are shown in Table 5.2: in the column labelled as "EBL-corrected", the spectrum to be fitted is multiplied by the attenuation factor $\exp[-\tau_{\gamma\gamma,\,\mathrm{EBL}}(E)]$ due to pair production of gamma rays with the EBL, modelled following Domínguez et al. (2011).

	forward unfolding		likelihood method	
parameter	observed	EBL-corrected	observed	EBL-corrected
ϕ_0 / $(10^{-11}\mathrm{TeV}^{-1}\,\mathrm{cm}^{-2}\,\mathrm{s}^{-1})$	5.37 ± 0.51	8.95 ± 0.98	5.19 ± 0.45	9.40 ± 0.94
Γ	3.96 ± 0.18	3.29 ± 0.23	4.1 ± 0.15	3.29 ± 0.24
E_0 / GeV	175 (fixed)	175 (fixed)	175 (fixed)	175 (fixed)

Table 5.2: Spectral parameters estimated with the forward folding and likelihood methods for the PKS 1510-089 VHE low state.

We estimate the signal to background ratio to be of the order of 7%, resulting in a systematic uncertainty on the flux normalisation of $\approx 20\%$ and on the spectral index of ± 0.4 (see Section 5.1 of Aleksić et al. 2016a or Section 2.4.7). The uncertainty on the energy scales stays $\pm 15\%$. Figure 5.4 compares the MAGIC low state SED, with previous VHE measurements. In blue spectral points unfolded with the Tikhonov and Arsenin (1977) method and the flux error band obtained with the forward unfolding method are shown. The high state detected by MAGIC between February and April 2012 (reported in Aleksić et al. 2014a) is shown in light violet. The 2012 state is compatible with the flux measured in 2009 by H.E.S.S. (Abramowski et al., 2013), represented by red diamonds. The flux during 2012 is 1 to 3 times

the low state. The flux measured during the May 2015 flare (Ahnen et al., 2017b), represented by light blue points, is instead from 3 to 10 times higher. The 2016 May flare (Zacharias et al., 2017) reaches instead a factor from 40 to 80 higher. Remarkably, on the other hand, the intrinsic spectral index of the low gamma-ray state: -3.29 ± 0.24, is consistent within statistical uncertainties with the ones measured in the aforementioned active periods: -2.5 ± 0.6, for the 2012 detection, -3.17 ± 0.80 for the May 2015 flare and -3.37 ± 0.09 for the May 2016 flare.

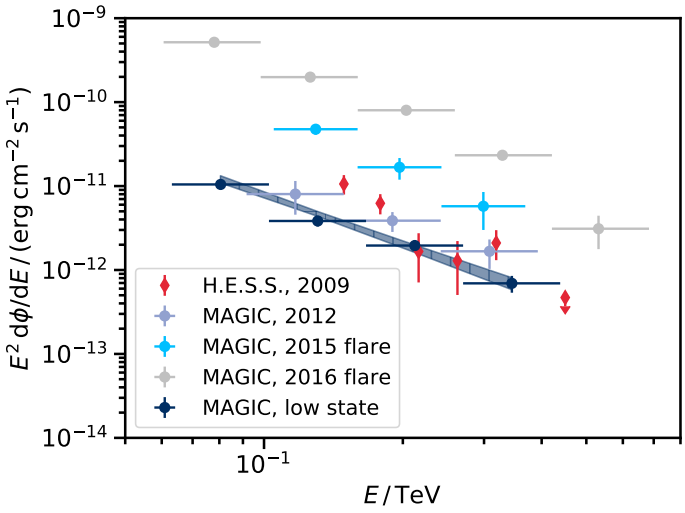

Figure 5.4: Comparison of PKS 1510-089 SEDs in different VHE states. The VHE low state identified in this work is represented in dark blue: flux points represent the result of the Tikhonov and Arsenin (1977) unfolding method, the band shows instead the results of the forward folding. Spectral points from previous observations are reported: the 2009 detection by H.E.S.S. (in red), the 2012 active state (light purple), the 2015 and 2016 flares (light blue and grey, respectively).

No flux variability over time is observed for the VHE low state: both the daily-binned and yearly-binned MAGIC light curves, shown in Figure 5.5, can be fitted by a constant function returning $\chi^2/N_{\mathrm{d.o.f}} = 63.61/74$ and $\chi^2/N_{\mathrm{d.o.f}} = 3.94/5$, respectively. The fit to the yearly-binned points returns an estimated flux of $(4.10 \pm 0.49) \times 10^{-12}\,\mathrm{cm^{-2}\,s^{-1}}$.

To test against biases introduced by the threshold selected for the integrated *Fermi*-LAT flux, we repeat the selection procedure building a histograms of integrated fluxes above 100 MeV, instead of 1 GeV. The peak of the flux distribution, chosen for the low gamma-ray state selection as in Eq. 5.1, moves in this case to $\phi(E > 0.1\,\mathrm{GeV}) < 10^{-6}\,\mathrm{cm^{-2}s^{-1}}$. The MAGIC observation nights simultaneous to *Fermi*-LAT data verifying such conditions are again 76, with 9 night changing with respect to the previous sample. Using the sample selected with the *Fermi*-LAT integrated flux above 100 MeV would return a spectral normalisation and index varying with respect to the values reported in Table 5.2 by 7% and 3%, respectively, hence well within the statistical uncertainties.

5.2.3 Multi-Wavelength Data Set

In this section we list, in order of decreasing energy, the multi-wavelength data sets simultaneous to the VHE low state that were gathered for this project.

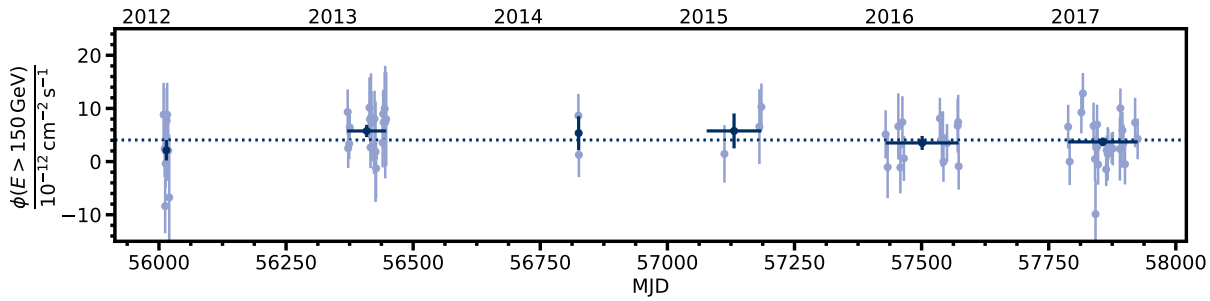

Figure 5.5: VHE light curve of PKS 1510-089 between 2012 and 2017. Daily binning of the MAGIC observations is displayed with light blue points, yearly binning with dark blue points. The (overlapping) results of a fit with a constant function to the daily and yearly light curve points are displayed by the dashed line.

X Ray

PKS 1510-089 is monitored in the X-ray band by the *Neil Gehrels Swift* Observatory (Swift-XRT, Burrows et al. 2004). 243 raw images including the source could be fetched from the `SWIFTXRLOG`[III] data base. 17 of these, amounting to 30 ks, are simultaneous to the VHE low state. They are represented as blue points in the second panel from the top of Figure 5.2. The remaining data simultaneous to MAGIC observation nights are plotted in red. Spectrum and light curve are obtained with the method in Section 2.4 of Fallah Ramazani et al. (2017), assuming $n_H = 6.89 \times 10^{20}\,\mathrm{cm}^{-2}$ for the Galactic hydrogen column density. Fitting the light curve points simultaneous to the VHE low state with a constant function returns a $\chi^2/N_{\mathrm{d.o.f.}} = 84/16$, the amplitude of the variability is moderate: the RMS of the points is 30 % of the mean flux. The average spectrum is a power law with spectral index 1.382 ± 0.020 and flux normalisation $F_{2-10\,\mathrm{keV}} = 8.14^{+0.25}_{-0.19} \times 10^{-12}\,\mathrm{erg\,cm^{-2}\,s^{-1}}$. The Pearson coefficient for a linear correlation between index and flux measurements is 0.81 between 2 and 10 keV, hinting at the harder-when-brighter behaviour reported in Kataoka et al. (2008) or Aleksić et al. (2014a).

Ultraviolet

Observations in the wavelength band between 180 and 600 nm are available from another instrument on board the *Neil Gehrels Swift* Observatory: the Ultraviolet/Optical Telescope (Swift-UVOT, Poole et al. 2008). The wavelength range is covered by six filters, whose description can be found in Table 1 of Poole et al. (2008). The data reduction is performed according to Section 3.1 of Raiteri et al. (2010), the number of Swift-UVOT observations contemporaneous to the VHE low state are 9 to 13, depending on the filter. The light curve in the third panel from the top of Figure 5.2 represent the flux in the u photometric band filter. The same color convention of the other light curve panels is adopted. Flux variations in the UV band are minor during the night simultaneous to the VHE low state.

[III] https://heasarc.gsfc.nasa.gov/W3Browse/swift/swiftxrlog.html

Optical Data

The optical data were provided by the three following instruments:

- the 35 cm Kunglinga Vetenskaps Akademien (KVA) telescope, located at the ORM, monitors the source in the R band, within the Tuorla blazar monitoring programme [IV]. KVA covers the 2012-2017 period with observations almost simultaneous to the MAGIC ones. For the data reduction see Section 5.2 of Aleksić et al. (2014a) and references therein;
- the Calar Alto telescope situated in Andalusia, Spain, that runs the "Monitoring AGN with Polarimetry at the Calar Alto 2.2 m Telescope " (MAPCAT) programme[V] (Agudo et al., 2012). Data are reduced and analysed with the procedure in Jorstad et al. (2010);
- the Small and Moderate Aperture Research Telescope System (SMARTS) located at Cerro Tololo Interamerican Observatory in Chile. Calibration and data reduction procedures are described in Bonning et al. (2012).

The light curves in the R band from the three instruments are jointly displayed in the fourth panel from the top of Figure 5.2, with the same aforementioned color code. To produce a spectral measurement in the R-band, for the physical discussion, we average measurements from 53 nights that are simultaneous to the VHE low state (47 of KVA observations, 3 of MAPCAT, 13 of SMARTS), obtaining a flux value of 1.55 ± 0.57 mJy. The statistical uncertainty is taken from the RMS of the flux values. We apply the same procedure to the B band in which we have measurements from one of the Swift-UVOT filters and SMARTS. 20 nights simultaneous to the VHE low state result in an average flux of 1.22 ± 0.46 mJy. PKS 1510-089 shows low optical emission at the level of ~ 1 mJy from 2012 to 2014 and again in 2017. The flaring periods of 2015 and 2016 correspond to high GeV states simultaneous with the VHE flares reported in Ahnen et al. (2017b) and Zacharias et al. (2017).

Infrared

In the IR band, data from the Rapid Eye Mount (REM, Zerbi et al. 2001), 60 cm telescope located in La Silla, Chile, in the J, K and H photometric bands were used. Additional observations in the J and K bands are provided by SMARTS. Only 5 nights of REM data in the H band and 13 nights for both telescopes in the J and K bands are simultaneous to the VHE low state. A light curve jointly displaying REM and SMARTS data in the J band is shown in the fifth panel from the top of Figure 5.2. One night in the SMARTS data set simultaneous to the MAGIC low state (MJD 57181) presented an IR flare with a value ~ 6 higher than the rest of the values. This flux measurement is removed from the flux averaging used to obtain the spectral points, the latter returned in the three bands: $F_K = 7.3 \pm 2.7$ mJy, $F_H = 4.2 \pm 2.4$ mJy and $F_J = 2.3 \pm 1.0$ mJy. Including the flaring night would change the average flux values in the H and K band by less than 30 %, but would increase the error (obtained from the RMS of the measurements) to a value compatible with the average.

[IV] http://users.utu.fi/kani/1m
[V] http://www.iaa.es/~iagudo/_iagudo/MAPCAT.html

Radio

We have collected radio data from the following four radio instruments monitoring PKS 1510-089 during the 2012-2017 period:

- observations at 3.5 mm and 1.3 mm performed by the 30 m diameter telescope of the Institut de Radioastronomie Millimétrique (IRAM), in the Spanish Sierra Nevada, performing the "Polarimetric Monitoring of AGN at Millimetre Wavelengths" [VI] programme (POLAMI). See Agudo et al. (2018a) for the programme description and Agudo et al. (2018a); Thum et al. (2018) and Agudo et al. (2018b) for the data reduction and main scientific results, respectively;
- observations at 37 GHz performed between 2012 and 2014 by the Combined Array for Research in Millimeter-Wave Astronomy (CARMA), already published in Ramakrishnan et al. (2016);
- observations at 37 GHz performed by the 13.7 m diameter Aalto University Metsähovi radio telescope[VII], located in Finland. The instrument and its data reduction are described in Teraesranta et al. 1998;
- observations at 15 GHz performed by the 30 m diameter telescope at the Owens Valley Radio Observatory (OVRO, see Richards et al. 2011 for the observations and data reduction descriptions);

The radio measurements by POLAMI, Metsähovi and OVRO are displayed in the last three panels of Figure 5.2, with the same color code introduced for the other light curves. Slow flux variations, with time scales of months, are visible at 37 and 15 GHz in 2012-2013 and after 2015. As for the other wavebands, we obtain a flux spectral point in a given band by averaging observations from different instruments simultaneous with the MAGIC low state. For the radio case, though, the simultaneity window is stretched to ±3 days. We obtain: $F_{15\,\mathrm{GHz}} = 4.4 \pm 1.2$ Jy (from 22 observations), $F_{37\,\mathrm{GHz}} = 3.9 \pm 1.1$ Jy (from 59 observations), $F_{86\,\mathrm{GHz}} = 3.14 \pm 0.86$ Jy (from 6 observations), $F_{95\,\mathrm{GHz}} = 2.16 \pm 0.13$ Jy (from 9 observations), $F_{229\,\mathrm{GHz}} = 1.76 \pm 0.42$ Jy (from 4 observations).

5.3 Physical Discussion

The broad-band SED of PKS 1510-089 simultaneous with the VHE low state is compiled adding the multi-wavelength data in Section 5.2.3 and displayed with black points in Figure 5.6. The black butterfly represents the spectral measurement obtained with Swift-BAT over 105 months (Oh et al., 2018). The highest energy emission of FSRQs is usually explained in the literature with the EC mechanism (Dermer and Schlickeiser, 1993). In the case of PKS 1510-089, the target fields considered are the BLR and the torus (Kataoka et al., 2008; Abdo et al., 2010; Aleksić et al., 2014a; Ahnen et al., 2017b; Acciari et al., 2018b), as the emission region is typically placed between their radii, $R_{\mathrm{li}} < r < R_{\mathrm{dt}}$. `agnpy`, whose implementation is described in Section 4.5, is used to reproduce the "close" scenario in Acciari et al.

[VI] http://polami.iaa.es
[VII] http://metsahovi.aalto.fi/en/

(2018b) that considers the emission region located at $r = 7 \times 10^{17}$ cm. A broken power-law electron distribution is assumed, Eq. 4.47: a change in the spectral index is commonly imputed to the energy losses via synchrotron and inverse Compton radiation concurrent with the acceleration process (see Kirk et al. 1998; Chiaberge and Ghisellini 1999). The electron distribution assumes values between $\gamma'_1 = 2$ and $\gamma'_2 = 3 \times 10^5$ and has spectral index $p_1 = 1.9$ before the break, occurring at $\gamma'_b = 130$ and $p_2 = 3.5$ after. The emission region has size $R'_b = 2 \times 10^{16}$ cm and a uniform magnetic field $B = 0.35$ G. The aforementioned electron distributions and blob parameters are taken from Acciari et al. (2018b). The Doppler and bulk Lorentz factor are fixed to the values $\delta_D = 35.5$ and $\Gamma = 22.5$, respectively, measured in Liu et al. (2006). The total energy content of the electrons, $W'_e = 8 \times 10^{47}$ erg, is instead fixed in order for the global model to reproduce the data points. Referring to Figure 5.6 we introduce the individual SED components starting from the lower energies. The electron distribution parameters fixed to reproduce the high-energy hump via inverse Compton results in a strongly self-absorbed spectrum (indicated with the dashed dark blue line) that underestimates the radio spectral points ($\nu < 10^{12}$ THz). The underestimation of the synchrotron fluxes is a difficulty commonly encountered in literature, see e.g. the modelling of the same source by Kataoka et al. (2008); Abdo et al. (2010); Barnacka et al. (2014); Ahnen et al. (2017b). It is due to the simplistic attribution of the synchrotron emission to a single region of the jet (the spherical blob in this case). Potter and Cotter (2012) addresses this issue by integrating synchrotron radiation and opacity over a conical representation of the jet. The dip in the flux measured from IR to UV frequencies (10^{14} Hz $\lesssim \nu \lesssim 10^{15}$ Hz) can be modelled with the falling part of the black body spectrum due to the torus (dot-dashed grey line) and the rising part of another black body spectrum, due to the disk (dot-dashed green line). A torus of temperature $T_{\rm dt} = 10^3$ K, with a reprocessing efficiency $\xi_{\rm dt} = 0.6$ and a radius $R_{\rm dt} = 6.5 \times 10^{18}$ cm is considered. Such parameters are estimated in Ahnen et al. (2017b) with the scaling laws for the BLR and torus radii in Ghisellini and Tavecchio (2009). A Shakura-Sunyaev disk is considered, with total luminosity $L_{\rm disk} = 6.7 \times 10^{45}$ erg s^{-1} (as estimated in Aleksić et al. 2014a) typical accretion efficiency $\eta = 0.1$, inner radius six times the gravitational radius, $R_{\rm in} = 6\, R_g$ (as in Abdo et al. 2010), and outer radius fixed to $R_{\rm out} = 10^3\, R_g$ to reproduce the UV points. The SSC component (displayed with the light blue dashed line) spans from 10^{11} to 10^{26} Hz but its contribution is negligible at high energies. The X-ray to VHE gamma-ray regime is entirely dominated by the EC on the dust torus (dot-dashed yellow line). This is due to the emission region positioned outside the BLR. At $r = 7 \times 10^{17}$ cm $\approx 3 \times 10^4\, R_g$ the disk photon field is too far for efficient Compton scattering and its EC contribution (light red dot-dashed line) reaches 10^{-15} erg cm^{-2} s^{-1}. As the emission region is outside the BLR, $r \approx 3\, R_{\rm li}$, the EC on the BLR (dot-dashed brown line) becomes also sub-dominant. The BLR is modelled as a spherical shell Section 4.5.4 with $R_{\rm li} = 2.6 \times 10^{17}$ cm and $\xi_{\rm li} = 0.1$ (as in Aleksić et al. 2014a). The BLR target field is considered due to Lyman α line, as in Kataoka et al. (2008), adopting $\epsilon_{\rm li} = 2 \rightarrow 10.22$ eV. The parameters used for the model are resumed in Table 5.3 along with the reference from which they were adopted. Missing references indicates parameters that have been fixed to reproduce the model to the data points. Parameters from Acciari et al. (2018b) are modelled on this very same data set, the remaining on previous observations.

The effects of the $\gamma\gamma$ absorption are considered at once with the global model. The red line in the plot

indeed represents the sum of the aforementioned SED components attenuated with the opacities due to the BLR and dust torus, i.e. multiplied by $\exp[-(\tau_{\gamma\gamma,\,\mathrm{BLR}} + \tau_{\gamma\gamma,\,\mathrm{torus}})]$. Given the blob distance from the BH, the $\gamma\gamma$ opacity from the disk photons is completely negligible, the opacities of the dominant fields for the EC process are represented as shaded grey area on the right side of Figure 5.6. At $r = 7 \times 10^{17}$ cm, the absorption produced by the BLR photon field does not affect the spectrum observed by MAGIC and the unabsorbed EC on torus smoothly connects it with the *Fermi*-LAT points. The absorption by BLR photons becomes dominant at several hundreds of GeV, already beyond the MAGIC reach.

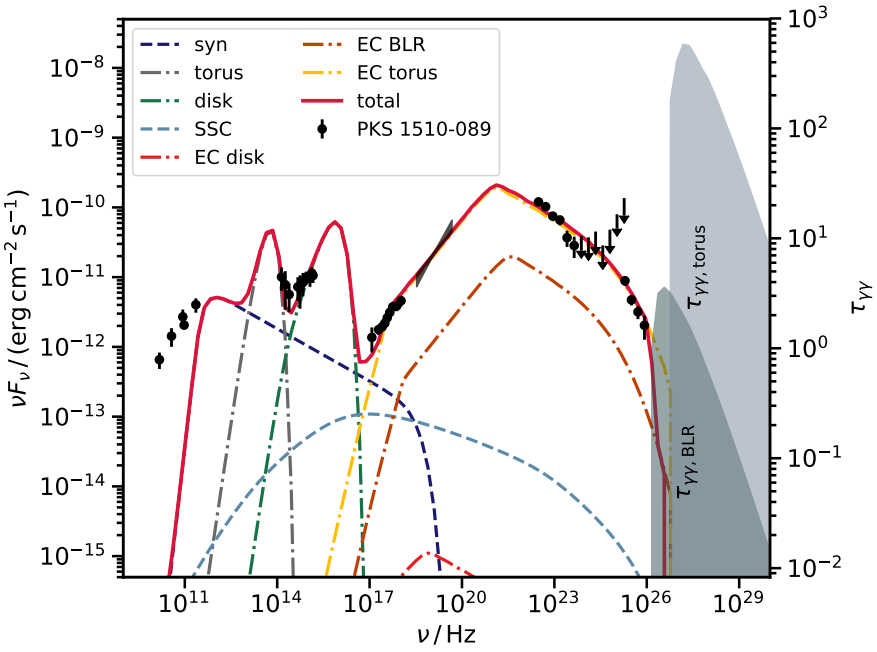

Figure 5.6: Multi-wavelength SED of the VHE low state of PKS 1510-089. Dashed lines represent synchrotron and SSC emission (dark and light blue, respectively). The dot-dashed lines at low energies ($\nu < 10^{17}$ Hz) display the black-body spectra of the torus (grey) and disk (green). The dot-dashed lines at high energies ($\nu > 10^{17}$ Hz) display instead the Compton-scattered target fields of the disk (orange, bottom of the figure), of the BLR (brown) and the torus (yellow). The opacities of the BLR and the torus are indicated as grey shaded areas, with the right $y-$axis returning their scale. The total model (in red) is the sum of all the components due to the individual radiative processes, exponentially attenuated with the opacities.

5.4 Conclusion

A significant low state of VHE gamma-ray emission for the FSRQ PKS 1510-089 was discovered analysing the whole stereo observations gathered by MAGIC between 2012 and 2017 on this source. Such state is identified using the *Fermi*-LAT flux above 1 GeV as a proxy on the tens of GeV regime in which MAGIC

quantity	symbol	value	reference
total energy in electrons	W_e	8×10^{47} erg	-
1st power law spectral index	p_1	1.9	Acciari et al. (2018b)
2nd power law spectral index	p_2	3.5	Acciari et al. (2018b)
spectral break	γ'_b	130	Acciari et al. (2018b)
minimum Lorentz factor	γ'_1	2	Acciari et al. (2018b)
maximum Lorentz factor	γ'_2	3×10^5	Acciari et al. (2018b)
blob radius	R'_b	2×10^{16} cm	Acciari et al. (2018b)
blob magnetic field	B	0.35 G	Acciari et al. (2018b)
blob distance from BH	r	7×10^{17} cm	Acciari et al. (2018b)
jet bulk Lorentz factor	Γ	22.5	Liu et al. (2006)
Doppler factor	δ_D	35.5	Liu et al. (2006)
redshift	z	0.36	Tanner et al. (1996)
BH mass	$M_{\rm BH}$	$1.58 \times 10^8\, M_\odot$	Liu et al. (2006)
BH gravitational radius	R_g	2.34×10^{13} cm	computed from $M_{\rm BH}$
disk luminosity	$L_{\rm disk}$	6.7×10^{45} erg s^{-1}	Aleksić et al. (2014a)
disk accretion efficiency	η	0.1	-
disk inner radius	$R_{\rm in}$	$6\, R_g$	Abdo et al. (2010)
disk outer radius	$R_{\rm out}$	$10^3\, R_g$	-
BLR dimensionless energy	$\epsilon_{\rm li}$	2×10^{-5}	Kataoka et al. (2008)
BLR scattering fraction	$\xi_{\rm li}$	0.1	Ahnen et al. (2017b)
BLR emission radius	$R_{\rm li}$	2.6×10^{17} cm	Aleksić et al. (2014a)
dust torus temperature	$T_{\rm dt}$	10^3 K	Ahnen et al. (2017b)
dust torus scattering fraction	$\xi_{\rm dt}$	0.6	Ahnen et al. (2017b)
dust torus emission radius	$R_{\rm dt}$	6.5×10^{18} cm	Ahnen et al. (2017b)

Table 5.3: Parameters for the PKS 1510-089 SED model.

detects the source emission. Selecting the MAGIC nights simultaneous to *Fermi*-LAT integrated fluxes $< 3 \times 10^{-8}\,\mathrm{cm}^{-2}\,\mathrm{s}^{-1}$ reduces the stereo observations sample to 76 individual nights. The VHE spectrum can be fit to a simple power-law function, with index compatible with all the previous observations in different active or flaring states. The normalisation is $1-3$ times lower with respect to the first detection by MAGIC in 2012, $3-10$ times lower than the 2015 flare and $40-80$ times lower than the historical highest VHE flare. After this study PKS 1510-089 results the first FSRQ manifesting a persistent VHE gamma-ray emission compatible with a constant flux over 5 years. Compatibly with most of the previous literature, the high-energy continuum emission of the source can be modelled with an EC scenario dominated by the scattering over the photon field provided by the dust torus. The dominance of such target field is realised by placing the emission region outside the BLR, assumption supported by the lack of any observable absorption feature in the gamma-ray spectra due to the BLR soft photons. The location of the emission region outside the BLR is in agreement with the more general studies performed by Costamante et al. (2018) and Meyer et al. (2019) showing that most of the *Fermi*-LAT detected blazars have HE emission lacking absorption features due to BLR photon fields.

6 | Gamma-ray Flaring Activity of the Radio Galaxy NGC 1275

The MAGIC data analysis presented here is published in Ansoldi et al. (2018b) of which I am corresponding author. Together with D. Glawion and K. Pfrang I was responsible of the MAGIC data analysis. At least two independent and compatible analysis are requested by the MAGIC collaboration in order to publish any scientific results. Figures and numbers from D. Glawion's analysis are used in Ansoldi et al. (2018b), while in this chapter I present mine. They are both compatible and approved by the MAGIC collaboration. I was also responsible of the *Fermi*-LAT analysis and one of the editor of the paper. The KVA data shown were reduced by V. Fallah Ramazani.

The observation of VHE gamma-ray emission from radio galaxies (RGs, presented in Section 4.1.2) challenges the class of jet-dominated radiative models described in Section 4.5 as such objects are characterised by a large angle between their jet axis and the line of sight of the observer, resulting in very low Doppler factors (Eq. 4.3) and hence poor boosting of their intrinsic luminosity. The VHE census of RGs is scarce. Similarly to what is done for FSRQs in the introduction of Chapter 5, we list in Table 6.1 the RGs detected in VHE along with their distance, central BH mass, instrument of discovery and reference.

source	distance	$M_{\rm BH}/M_{\odot}$	discovered	reference
M 87	16 Mpc	$20-60\times10^{8}$	HEGRA	Aharonian et al. (2003)
Centaurus A	3.7 Mpc	$0.5-1\times10^{8}$	H.E.S.S.	Aharonian et al. (2009)
IC 310	80 Mpc	3×10^{8}	MAGIC	Aleksić et al. (2010b)
NGC 1275	70 Mpc	3×10^{8}	MAGIC	Aleksić et al. (2012c)
PKS 0625-35	220 Mpc	10^{9}	H.E.S.S.	Abdalla et al. (2018b)
3C 264	95 Mpc	$4-5\times10^{8}$	VERITAS	Mukherjee (2018)

Table 6.1: RGs detected in VHE gamma-rays.

VHE-detected RGs have in common relatively close distances, $z \lesssim 0.05$, central BHs with masses $10^{8-9}\,M_{\odot}$ and a radio appearance as Fanaroff-Riley I objects (low luminosity, core dominated emission). The broad-band emission of RGs can be interpreted as the one produced by a BL Lac with a large viewing angle (Aleksić et al., 2014b), eventually invoking the presence of multiple emitting regions (Lenain et al., 2008; Abdalla et al., 2018b). Defying jet-dominated scenarios, some RGs have shown peculiarly bright VHE flares characterised by variability time scales smaller or $\sim$ few times the light crossing time at the event horizon (see IC 310 in Aleksić et al. 2014c or M 87 in Acciari et al. 2009, respectively). Causality implies that the size of the emission region has to be smaller or few times the size of the event horizon (R_H, Eq. 4.31), making difficult to locate the radiation source within the jet. The latter is indeed usually represented as a conical outflow with basis larger than the ISCO (Eq. 4.33) $R_{\rm jet} > R_{\rm ms} > R_H$ (Donea and Biermann, 2002).

In this chapter we report the observations performed by MAGIC in the period between September 2016 and February 2017 of an enhanced gamma-ray state of the RG NGC 1275. The MAGIC data analysis, described in Section 6.2.1, finds an average VHE gamma-ray flux marking the historical maximum of this source. In the night corresponding to the brightest flux, 1 January 2017, a variability time scale of tens of hours is measured. The whole data set is characterised by significant emission at energies > 1 TeV, another record for this source. Gamma-ray data from *Fermi*-LAT and optical data from KVA are collected and analysed in Section 6.2.2 and 6.2.3, respectively, in order to constraint the most luminous gamma-ray state and to search for correlation between optical and gamma-ray fluxes. Two evidences can be obtained from the data against the location of the emitting region within the jet. First, the lack of significant correlation between optical and gamma-ray fluxes hints at the absence of a synchrotron component produced by an hypothetical blob and simultaneously growing with the flaring high energy continuum. Second, the small size of the emission regions inferred from variability would

lead to a consistent absorption of TeV photons via pair production with the low energy emission of the hypothetical blob. In order to escape such absorption, Doppler factors in tension with those usually observed for RG (Hovatta et al., 2009) and adopted in previous leptonic models (Aleksić et al., 2014b) should be invoked. We attempt to reconcile such observational features in Section 6.3.2 discussing the high-energy radiation as produced in the vicinity of the BH, by a gap in the magnetosphere created by the frame dragging (Section 4.4.1) the BH exerts on the disk magnetic field lines threading it.

6.1 Gamma-ray Observational History

NGC 1275 resides at the centre of the Perseus cluster of galaxies (Abell 426), the same hosting IC 310. It is a known AGN, included both in the Seyfert (1943) and 3CR catalogues. Very distinctively, the optical image of the galaxy shows $\sim$ kpc scale filament emitting Hydrogen lines (Lynds, 1970). In radio, NGC 1275 has the appearance of a core dominated Fanaroff-Riley I galaxy with an angle between the jet axis and the line of sight of the observer of $30-50^\circ$ (Asada et al., 2006; Hovatta et al., 2009). HE Gamma-ray emission from NGC 1275 was first observed by COSB (Strong and Bignami, 1983) and re-detected in the *Fermi*-LAT era (Abdo et al., 2009) with variability on weekly time scales found by Kataoka et al. (2010) and Brown and Adams (2011). The first detection at VHE is due to stereoscopic observations by MAGIC (Aleksić et al., 2012c) that later presented a a broad-band study of the source in Aleksić et al. (2014b). The Perseus cluster was also considered by the MAGIC collaboration to investigate fundamental physics: a sample of 253 hours of observations was employed to search for diffuse gamma-ray emission due to CR interactions in the intra-cluster medium (Ahnen et al., 2016b); 400 hours of data were instead used to search for gamma-ray decay of dark matter particles in Acciari et al. (2018c).

6.2 Data Analysis

6.2.1 MAGIC Analysis

The MAGIC data set here analysed was gathered between September 2016 and February 2017, as a part of a monitoring programme of NGC 1275. Out of the 63 hours collected, 56 satisfied the quality cuts: atmospheric transmission ($> 85\%$), mean current in the M2 camera pixels $< 2000\,\mu$A (low NSB background), zenith angle $< 50^\circ$. The positive declination of the source makes it visible from the ORM at relatively low zenith angles. Most of the data were collected between 12° and 50°, with only 7 nights having zenith above 35°. Hence, being most of the shower reconstructed at low zenith angles (small atmospheric depths), we estimate that 100 GeV represents a safe energy threshold for the light curve integration. The unfolding procedure Section 2.4.6 allows us to reconstruct spectral points down to 70 GeV.

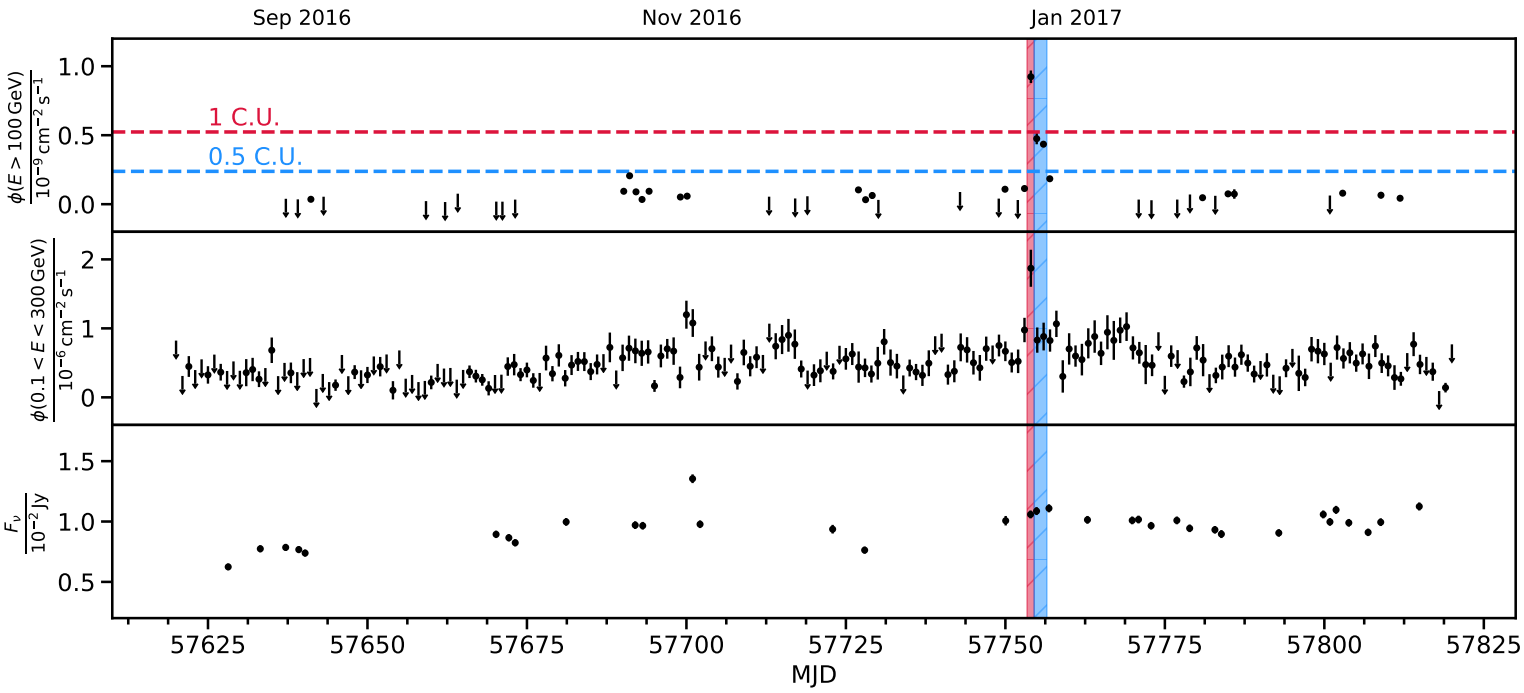

Figure 6.1: γ-ray and optical light curve of NGC 1275 between September 2016 and February 2017. In the top panel the MAGIC flux measurements above 100 GeV are displayed. Flux upper limits correspond to a 95% confidence level and are computed assuming a total systematic uncertainty of 30% using the Rolke et al. (2005) method. Middle panel: Daily binned fluxes (black data points) calculated from *Fermi*-LAT observations in an energy range of 0.1–300.0 GeV. Flux upper limits were estimated at 95% confidence level in the case of TS<25 and are shown in blue. Bottom panel: R-band flux density measurements host-galaxy subtracted and corrected for galactic extinction by KVA.

VHE flux variability

The mean VHE flux of the entire data set is $(1.16 \pm 0.03) \times 10^{-10}\,\mathrm{cm}^{-2}\,\mathrm{s}^{-1}$, previous measurements by MAGIC resulted in mean fluxes of $(1.6{\pm}0.3){\times}10^{-11}\,\mathrm{cm}^{-2}\,\mathrm{s}^{-1}$ in 2009-2010 and $(1.3{\pm}0.2){\times}10^{-11}\,\mathrm{cm}^{-2}\,\mathrm{s}^{-1}$ in 2010-2011 (Aleksić et al., 2014b), i.e. $7-9$ times lower the one reported here. The uppermost panel of Figure 6.1 shows the integrated flux above 100 GeV, measured by MAGIC in daily bins. Flux points and upper limits are computed according to the methods in Section 2.4.6, assuming a power-law spectrum with index -3, and a systematic error of 30% on the gamma-ray detection efficiency. Since November 2016, NGC 1275 displays an active VHE state culminating in a major flaring event on 1 January 2017. To search for intra-night variability, in each of the night with high flux a zoomed light curve with time bins matching the span of the observational runs is built. Even for the brightest night, 1 January 2017, the run-wise light curve can be fitted with a constant function. The variability is therefore larger than the usual $1-3$ hours covered by a single night observation. We estimate the night-to-night variability computing the *flux doubling timescale* using the two approaches outlined in Aleksić et al. (2014c) (see supplementary material):

– we directly compute the bin-to-bin doubling time scale as

$$\tau_D = \Delta t \times \frac{\ln 2}{\ln \left| \frac{\phi_i}{\phi_{i+1}} \right|}, \tag{6.1}$$

where $\Delta t = t_{i+1} - t_i$ is the difference between the bin centres and $\phi_i/\phi_{i+1} = \phi(t_i)/\phi(t_{i+1})$ the ratio between their fluxes. The fastest variability is obtained for the night between 31 December 2016 and 1 January 2017, with a value $\tau_D = (496 \pm 75)$ minutes;

– we fit to different time intervals of the light curve the exponential function

$$\phi(t) = \phi(t_0) \times 2^{\frac{t-t_0}{\tau_D}}, \tag{6.2}$$

where t_0, and the corresponding flux $\phi(t_0)$ are fixed and τ_D is fitted. The only time interval compatible with such a fit lies in the region of the major flare, i.e. between MJD $57751.0-57754.02$. Setting t_0 to MJD 57753.99 and $\phi(t_0) = 9.5 \times 10^{-10}\,\mathrm{cm}^{-2}\,\mathrm{s}^{-1}$, returns $\tau_D = (611 \pm 101)$ minutes with a χ^2 / d.o.f. $= 0.49/1$

Both methods return values consistent within their uncertainties. In what follows we will conservatively adopt the second, returning the largest time scale, for discussing the variability.

VHE spectral analysis

In order to extract the spectral information, we divide the data in three sub-samples according to their integral flux (expressed in C.U., e.g. as a fraction of the Crab Nebula spectrum integrated above the same energy):

– the first sub-sample contains the observations with integral flux $\phi(E > 100\,\mathrm{GeV}) > 1\,\mathrm{C.U.}$, i.e. only the night of 1 Jan 2017. Such flux level is indicated with a dashed red line in the uppermost panel of Figure 6.1. The time span of the VHE flux verifying such condition is indicated by a background area shaded in red in all the light curve panels. The number of source counts computed from this sub-sample using the signal extraction method discussed in Section 2.4.6 has a significance of $56.10\,\sigma$. Flux points and forward folded spectrum obtained from this sub-sample are shown in red in Figure 6.2;

– the second sub-sample contains the observations with integral flux $0.5\,\mathrm{C.U.} < \phi(E > 100\,\mathrm{GeV}) < 1\,\mathrm{C.U.}$, i.e. the nights of 2 and 3 Jan 2017. Such flux level is indicated with a dashed light blue line in the uppermost panel of Figure 6.1. The time span of the VHE flux verifying such condition is indicated by a background area shaded in light blue in all the light curve panels. The number of source counts extracted from this sub-sample has a significance of $33.81\,\sigma$. Flux points and forward folded spectrum obtained from this sub-sample are shown in light blue in Figure 6.2;

– the last sub-sample contains the remaining observations, characterised by integral flux $\phi(E > 100\,\mathrm{GeV}) < 0.5\,\mathrm{C.U.}$. Such flux level averages together minor active states, e.g. those standing out among the upper limits in October and November 2016. The number of source counts extracted from this sub-sample has a significance of $31.36\,\sigma$. Flux points and forward folded spectrum obtained from this sub-sample are shown in black in Figure 6.2. We refer from now on to this sub-sample as *flares excluded*.

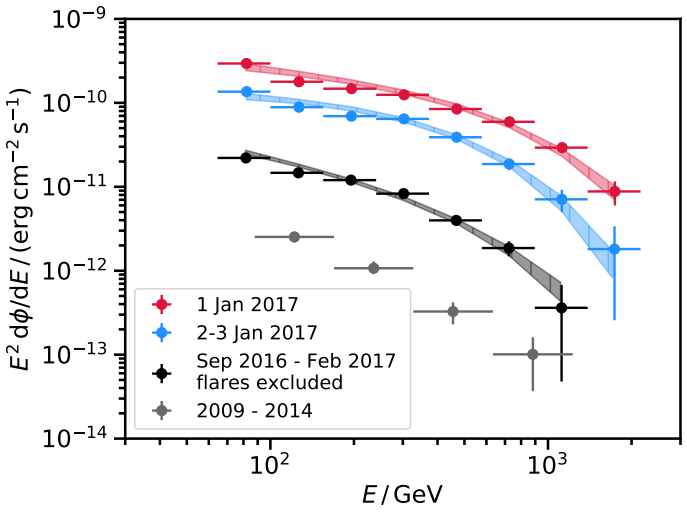

Figure 6.2: Spectra of NGC 1275 reconstructed from different sub-samples gathered in the September 2016 - February 2017 observational campaign. The flux points display the results of the Schmelling (1994) unfolding method, in red for the night of 1 January 2017, in blue for the nights between 2 and 3 January 2017 and in black for the rest of the data set, after removing the aforementioned nights. The same color code is applied to the results of the forward unfolding, assuming an EPL spectrum, represented with bands. The grey points represents the result of 253 hours gathered by MAGIC in previous observational campaigns.

The flux points of the three spectra display a clear curved trend. In order to parametrise it, we apply a forward unfolding procedure (Section 2.4.6) using both a log parabola (LP, Eq. 2.30) and a power law with exponential cutoff (EPL, Eq. 2.31) as assumed spectra. Parameters results of such procedure for all

the sub-samples, along with the χ^2 they yield, are reported in Table 6.2. We do not consider the effect of the EBL absorption on the gamma-ray spectrum of the source as it should become significant only above 10 TeV (Aleksić et al., 2014b), given the small cosmological distance of NGC 1275: $z = 0.01756$ (Falco et al., 1999), i.e. ~ 70 Mpc. For all the sub-samples the EPL seems best suited to model the data, and we choose to represent the result of the forward unfolding with such assumed spectrum as coloured band in Figure 6.2. The grey spectral points are obtained in Ahnen et al. (2016b) from 253 hours data set collected in the previous MAGIC observational campaigns, conducted between 2009 and 2014. We note that before this work, no significant emission above the TeV was ever detected. Considering instead only the source counts in our data set with energies above 1 TeV a significance of $8\,\sigma$ (Eq. 2.26) can still be obtained. The systematic uncertainties on the spectral parameters stays the same as in Section 2.4.7, i.e.: 11% on the flux normalisation, ±0.15 on the spectral index and 15% on the energy scale.

	1 Jan 2017		2-3 Jan 2017		flares excluded	
parameter	LP	EPL	LP	EPL	LP	EPL
$\frac{\phi_0}{10^{-10}\,\mathrm{TeV}^{-1}\,\mathrm{cm}^{-2}\,\mathrm{s}^{-1}}$	9.35 ± 0.45	15.64 ± 1.88	4.29 ± 0.23	10.65 ± 2.17	0.48 ± 0.03	0.99 ± 0.22
Γ	2.90 ± 0.04	2.24 ± 0.10	3.03 ± 0.06	1.99 ± 0.16	3.36 ± 0.07	2.60 ± 0.16
β	0.58 ± 0.10	-	0.91 ± 0.16	-	0.59 ± 0.17	-
E_{cutoff} / GeV	-	602.6 ± 101.9	-	344.8 ± 65.0	-	447.4 ± 127.1
E_0 / GeV	300 (fixed)	300 (fixed)	300 (fixed)	300 (fixed)	300 (fixed)	300 (fixed)
χ^2 / d.o.f.	29.31/10	16.06/10	17.44/10	9.70/10	20.78/10	14.93/10
p value	10^{-3}	0.1	0.07	0.47	0.02	0.13

Table 6.2: NGC 1275 spectral parameters on the three different sub-samples identified by their integrated flux level (1 Jan 2017, 2-3 Jan 2017 and flares excluded), obtained with the forward folding method employing both a log parabola LP and a power law with exponential cutoff EPL for the assumed spectrum.

6.2.2 *Fermi*-LAT Analysis

We perform an analysis of the data collected by *Fermi*-LAT simultaneously to the MAGIC observations here described, precisely within the time span between 9 August 2016 (MJD 57619.5) and 8 March 2017 (MJD 57820.5). The analysis of HE gamma-ray data has two objectives. First, a search for correlation between the gamma-ray and optical fluxes (the optical data will be described in the next section) provides significant insights for the physics discussion as certain models (like the SSC) are characterised by a very strong correlations between these observables. Second, it serves to further investigate the presence of a cutoff using the whole, (100 MeV − 10 TeV), gamma-ray spectrum. We choose the 1 Jan 2017 for this study as it is the brightest observation and also the only case in which the LP seems disfavoured. *Fermi*-LAT data are reduced and analysed using the python package `fermipy` (Wood et al., 2017). We build the event list considering all the photons in a RoI of radius 10°, centred on NGC 1275 coordinates. Both for the light curve and the spectrum estimation we perform a binned likelihood with 3 bins per energy decade between 100 MeV and 300 GeV. In building the model for the likelihood we consider all the sources from the 3FGL within a 15 deg-radius area from NGC 1275 coordinates. We account for the residual galactic and extragalactic background with the models in Acero et al. (2016) and Ackermann

et al. (2016), respectively.

Fermi-LAT Light Curve

The *Fermi*-LAT data set is sub-divided in time bins spanning 24 hours, centred on midnight. In each of them a binned likelihood analysis is performed. For the likelihood minimisation the flux normalisation of all the sources within 5° from the RoI centre are left free to vary, while the spectral indexes are kept fixed to the catalogue values. NGC is modelled with a simple power law. The integral of such spectrum between 100 MeV and 300 GeV in each of the time bins is displayed with black points in the middle panel of Figure 6.1. For the time bins in which the likelihood fit returned a TS<25 upper limits at 95% confidence level are displayed.

Fermi-LAT Spectrum on 1 Jan 2017

To investigate the presence of a cutoff in the brightest state we evaluate the HE spectra in a 12 hour time span centred on midnight of 1 January 2017 (MJD 57753.75 − 57754.25). Such a time interval is simultaneous to MAGIC observation and consistent with the ~ 10 hour variability observed in VHE. For the likelihood minimisation we let free to vary the spectral normalisations of the sources within 5° from the RoI centre, while we fix their spectral indexes to the catalogue values. In such a small time interval it is difficult to adjust the flux normalisations of the diffuse background components in the likelihood minimisation, therefore we keep them fixed. A variant of the power law in Eq. 2.29 is chosen to model NGC 1275 spectrum

$$\frac{\mathrm{d}\phi}{\mathrm{d}E} = \frac{\Phi_0(\Gamma+1)E^{-\Gamma}}{E_{\mathrm{max}}^{\Gamma+1} - E_{\mathrm{min}}^{\Gamma+1}}, \tag{6.3}$$

where now the flux normalisation Φ_0 is an integral flux (expressed in $\mathrm{cm}^{-2}\,\mathrm{s}^{-1}$ units). With this power-law function one can estimate the error on the integral flux directly from the likelihood procedure. We fix $E_{\mathrm{min}} = 100\,\mathrm{MeV}$ and $E_{\mathrm{max}} = 10\,\mathrm{GeV}$, as there are no gamma rays above this energy in the 12 hour sample. Converting Eq. 6.3 to a simple power-law function Eq. 2.29 and selecting E_0 as the *decorrelation* energy, i.e. as the point where ϕ_0 and Γ show the minimum correlation, the likelihood minimisation returns the following parameters: $\phi_0 = (7.03 \pm 1.26) \times 10^{-10}\,\mathrm{MeV}^{-1}\,\mathrm{cm}^{-2}\mathrm{s}^{-1}$, $\Gamma = 1.80 \pm 0.17$, and $E_0 = 0.56\,\mathrm{GeV}$. In such small dataset the source shows a TS of 55.83, i.e. a significance of $\approx 7.5\,\sigma$. *Fermi*-LAT flux points, computed iterating the likelihood fit in separate energy bands are displayed as black diamonds in Figure 6.3.

Combined gamma-ray spectrum for 1 January 2017

A method to constrain the VHE one-dimensional likelihood in Eq. 2.27 relying on the HE spectral information provided by *Fermi*-LAT is illustrated in Acciari et al. (2019). It is assumed that the MAGIC and *Fermi*-LAT spectra can be described by the same differential flux $\mathrm{d}\phi/\mathrm{d}E$, which manifests as a simple straight power law in the HE regime. Therefore, given the power-law fit results from a *Fermi*-LAT likelihood analysis: $\phi_{0,Fermi} \pm \sigma_{\phi_{0,Fermi}}$ and $\Gamma_{Fermi} \pm \sigma_{\Gamma_{Fermi}}$, one would multiply the VHE likelihood in

Eq. 2.27 by their normal distributions: $\mathcal{N}(\phi_0; \phi_{0,Fermi}, \sigma_{\phi_{0,Fermi}})$ and $\mathcal{N}(\Gamma; \Gamma_{Fermi}, \sigma_{\Gamma_{Fermi}})$. In this way the parameters of the VHE spectrum are anchored to vary Gaussianly within the interval returned by the fit to the *Fermi*-LAT data. We apply such method to the 1 January 2017 observation, considering both the LP and EPL as assumed spectra. Results for the constrained likelihood are reported in Table 6.3. Again the EPL seems more adequate to reproduce the data and the cutoff value is statistically compatible with the one obtained from MAGIC data alone. In Figure 6.3 we see that the spectrum estimated for the EPL with the *Fermi*-LAT constraint (solid red line) is in agreement with the independent estimates of the unfolding procedures (displayed by circular markers and the curved band). We conclude that in the high state of 1 January 2017 the spectrum presents a cutoff at $E_{\rm cutoff} = 492\,\mathrm{GeV}$.

parameter	LP	EPL
$\frac{\phi_0}{10^{-10}\,\mathrm{TeV}^{-1}\,\mathrm{cm}^{-2}\,\mathrm{s}^{-1}}$	34.2 ± 1.1	41.7 ± 2.2
Γ	2.76 ± 0.03	2.05 ± 0.03
β	0.26 ± 0.22	-
$E_{\rm cutoff}$	-	492 ± 35
E_0	180.77	198.21
χ^2/d.o.f.	66.97/11	19.18/11
p value	$< 10^{-9}$	0.06

Table 6.3: NGC 1275 spectral parameters on the the 1 January 2017 sub-samples obtained constraining the likelihood with the spectral information obtained from *Fermi*-LAT.

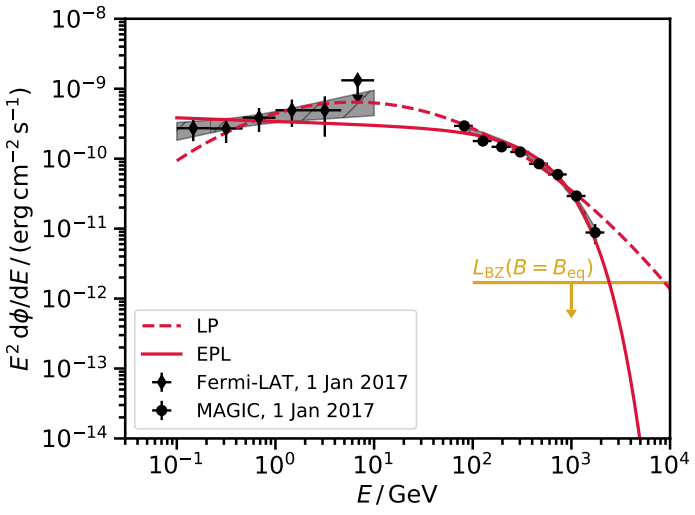

Figure 6.3: 1 January 2017 MAGIC SED constrained with *Fermi*-LAT data. The *Fermi*-LAT flux points are represented by diamonds, overlaid to the butterfly representing the fitted flux and statistical error obtained with the likelihood analysis. Unfolded MAGIC flux points are represented with circles, overlaid to the band representing the result of the forward unfolding. The red lines represent the outcome of the VHE likelihood constrained with the *Fermi*-LAT spectral fit, assuming a LP (dashed line) or a EPL (solid line). The yellow upper limit represents the maximum energy flux obtainable from the Blandford-Znajek mechanism (see discussion in Section 6.3.2).

6.2.3 KVA

In this work we consider optical observations gathered by KVA within the Tuorla Blazar Monitoring programme (see Section 5.2.3), covering the 2016-2017 MAGIC observations. For the KVA data reduction, differential photometry with an aperture of 5.0″ is used to measure the magnitude, comparison stars are taken from Fiorucci et al. (1998). Flux densities, corrected accounting for the host galaxy and the galactic extinction (Schlafly et al., 2011), are displayed in the bottom panel of Figure 6.1. We can observe that there is no increase of optical activity in correspondence with the VHE flares (shaded red and blue area), the optical flux is instead consistent with the mean of the entire period, $(0.95 \pm 0.13) \times 10^{-2}$ Jy. The mean flux is 1.6 higher the one reported in Aleksić et al. (2014b), simultaneous to the 2009-2011 MAGIC observational campaign. In correspondence with the highest optical flux in November 2016 (MJD 57700) a moderate increase of the *Fermi*-LAT flux is visible while there are no simultaneous MAGIC observations.

Correlation between Optical and Gamma-ray fluxes

After the qualitative examination of the light curve we provide a quantitative estimate of the correlation between optical and gamma-ray fluxes. In Figure 6.5 we plot the gamma-ray fluxes measured by MAGIC (in black) and *Fermi*-LAT (in red) against the simultaneous measurement by KVA.

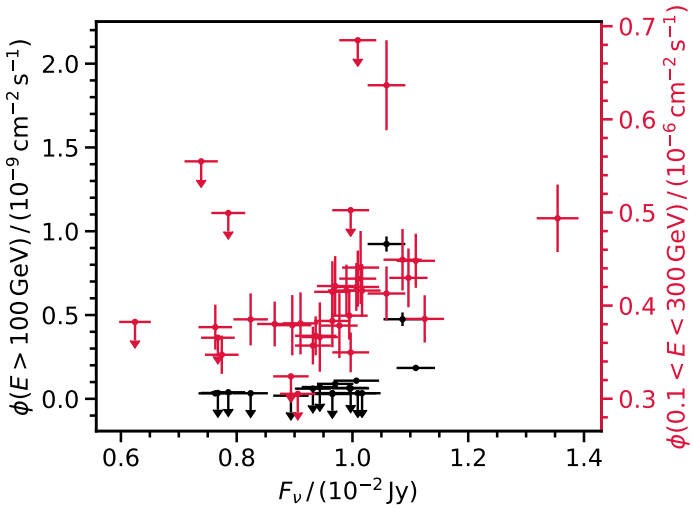

Figure 6.4: The black points indicate simultaneous flux measurements in VHE (y-axis) and optical (x-axis). The red points simultaneous flux measurements in HE and optical, their y scale is reported on the right y-axis.

We define a gamma-ray flux point to be simultaneous to an optical flux point if the MJD value in the centre of its time bin is within ±0.5 MJD (i.e. ±12 hours) of an optical measurement. The Pearson correlation coefficient for the VHE and optical points is 0.49; 0.55 when considering the HE and optical points (upper limits are not included in these calculations). The correlation is lower than the one observed in the 2009-2011 campaign (Aleksić et al., 2014b), where a value of 0.79 was found for the HE-optical correlation. Removing the flaring nights from 1 to 3 January 2017 from the *Fermi*-LAT and MAGIC data sets increases the VHE-optical correlation coefficient to 0.64 and the HE-optical to

0.72. We also attempt at fitting the correlation plots with a linear ($\phi_\gamma = c_0 + c_1\phi_{\rm optical}$) and a quadratic function ($\phi_\gamma = c_0 + c_1\phi_{\rm optical} + c_2\phi^2_{\rm optical}$). In a flaring scenario in which the optical and gamma-ray continuum components are regulated by synchrotron and SSC mechanism, respectively, linear or quadratic correlations are expected between those fluxes depending on the parameter whose variation is producing the flare (Aleksić et al., 2014b). None of the χ^2/d.o.f. returned by the aforementioned fits returns a p value greater than 10^{-3}. Given these results and the computed Pearson coefficient we conclude that correlation between gamma-ray and optical fluxes is not observed.

6.3 Physical Discussion

6.3.1 Size of the Emission Region

The size of the emission region R'_b (primed as measured in the frame comoving with the blob) can be inferred from the time scale of the flux variability $t_{\rm var}$, using a simple causality argument

$$R'_b \lesssim \frac{c\delta_D t_{\rm var}}{(1+z)}, \tag{6.4}$$

considering it has to be at least as large as the distance a photon could travel within the observed $t_{\rm var}$, corrected by Doppler boosting δ_D and redshift z. We adopt for $t_{\rm var}$ the conservative estimate of 611 min in Section 6.2.1, returning

$$R'_b \lesssim \delta_D \times 1.1 \times 10^{15}\,{\rm cm}, \tag{6.5}$$

and we leave the Doppler factor as a variable for the sake of the following discussion. What we can already see is that the variability is larger than the light crossing time at the BH event horizon $t_{\rm BH} = R_H/c = (2\times)\,R_g/c = (2\times)\,8.2\,M_8$ min, where the factor $(2\times)$ has to be taken into account depending on whether we consider a maximally spinning ($R_H = R_g$) or a Schwarzschild BH ($R_H = 2\times R_g$). From the BH mass measured by Wilman et al. (2005) and Scharwächter et al. (2013), $M_{\rm BH} = 3.4\times10^8\,M_\odot$ and $M_{\rm BH} = 8^{+7}_{-2}\times10^8\,M_\odot$, respectively, we obtain light crossing times of $t_{\rm BH} = 27.9$ min and 65.7 min. The variability time scale observed is one order of magnitude larger than $t_{\rm BH}$, hence a distinctive feature other RGs have shown in flaring or active states, i.e. VHE flux variability comparable or smaller than $t_{\rm BH}$ (Acciari et al., 2009; Aleksić et al., 2014c) is not encountered here. Nonetheless the size of the emission region is $1-2$ orders of magnitude smaller than the one proposed in previous modelling of the source (Aleksić et al., 2014b; Tavecchio and Ghisellini, 2014) adopting leptonic scenarios.

From this an important point of further discussion can be derived by considering if the size of the emitting region would allow observation of TeV gamma rays or would absorb them via $\gamma\gamma$ pair production. We simplify the opacity in Eq. 4.109 considering that the target emission is isotropic in the blob and peaks at $\epsilon_{\rm seed}$ with SED value $f_{\epsilon_{\rm seed}}$ (i.e. a monochromatic spectrum). For a gamma ray with dimensionless energy ϵ_γ the condition not to be absorbed reads (Eq. 9 in Abdo et al. 2011b)

$$\tau_{\gamma\gamma} \sim \frac{\sigma_{\rm T} d_L^2 f_{\epsilon_{\rm seed}} \epsilon_\gamma (1+z)}{10 R_b m_e^2 c^5 \delta_D^5} < 1. \tag{6.6}$$

We can rearrange Eq. 6.6 in order to obtain directly the Doppler factor necessary to avoid $\gamma\gamma$ absorption

$$\delta_D^5 > \frac{\sigma_T d_L^2 f_{\epsilon_{seed}} \epsilon_\gamma (1+z)}{10 R'_b m_e^2 c^5} \Rightarrow \delta_D > \left[\frac{\sigma_T d_L^2 f_{\epsilon_{seed}} \epsilon_\gamma (1+z)}{(11 \times 10^{15}\,\mathrm{cm})\, m_e^2 c^5} \right]^{1/6} \tag{6.7}$$

where in the last relation we have replaced R'_b with its expression Eq. 6.5. The dimensionless energy of the observed photons, since we question the absorption of 1 TeV photons, is $\epsilon_\gamma \approx 2 \times 10^6$. The cross section for $\gamma\gamma$ absorption is not null for $s > 1$ (Eq. 4.108), in this case, considering head-on collisions $s = \epsilon_\gamma \epsilon_{seed} > 1$, and the ideal target for $\gamma\gamma$ absorption of TeV gamma-rays are $\epsilon_{seed} = 0.5 \times 10^6 \rightarrow E_{seed} \approx 0.3\,\mathrm{eV}$ photons. A flux measurement in the $\sim$ eV energy range is available within the KVA dataset ($E_{R-band} \approx 2\,\mathrm{eV}$). For the night of 1 January 2017 a νF_ν flux of $4.96 \times 10^{-11}\,\mathrm{erg\,cm^{-2}\,s^{-1}}$ is observed, which returns, using Eq. 6.7, a Doppler factor of $\delta_{D,\,KVA} > 4.7$. Given the lack of correlation between optical and gamma-ray fluxes observed in Section 6.2.3 one could argue that the KVA measurement is related to an emission region different than the one responsible for the VHE flare. We provide then another lower limit on the Doppler factor, assuming a leptonic scenario. Both in case of SSC or EC scenario, the Compton dominance, i.e. the ratio of the peaks of the synchrotron and Compton νF_ν distributions rarely exceeds two orders of magnitude (Zacharias and Schlickeiser, 2012; Ghisellini et al., 2010). We therefore derive $f_{\epsilon_{seed}}$ as the peak of an hypothetical unresolved synchrotron component, assuming that NGC 1275 is undergoing a SSC-regulated flare with maximum Compton dominance 100. The peak of the gamma-ray SED is estimated from the fit in Section 6.2.2 as $\nu_{peak} F_{\nu_{peak}} = 6.42 \times 10^{-10}\,\mathrm{erg\,cm^{-2}\,s^{-1}}$[I]. We hence obtain $\delta_{D,\,SSC} > 3.3$, with the assumption $f_{\epsilon_{seed}} = \nu_{peak} F_{\nu_{peak}} / 10^2$. In Figure 6.5 the Doppler factor values resulting for different values of jet bulk Lorentz factor Γ and inclination angle θ is shown. The regions of (Γ, θ) values allowed to accommodate the lower limits that we computed on δ_D are enclosed by dashed and dot-dashed lines, the cross represents instead the values of (Γ, θ) measured by Hovatta et al. (2009). We conclude that Doppler values required to avoid internal absorption of TeV photons in the blob itself are incompatible with the large viewing angles and low bulk Lorentz factors measured by Hovatta et al. (2009) but also in tension with previous values used to model the source in the literature ($\delta_D = 2$ and 4 in Aleksić et al. 2014b).

6.3.2 Magnetospheric Model

Given the scarcity of multi-wavelength data gathered simultaneously to the VHE observations presented here, it is difficult to provide a broad-band modelling as done for PKS 1510-089 in Chapter 5. Especially having only the optical measurement for the low-energy continuum, it would be impossible to constrain the electron distribution via their synchrotron SED. The lack of correlation between optical and gamma-ray fluxes and the consistent absorption expected for TeV photons provide nonetheless insights for further discussion, hinting at the difficulty of accommodating the emission region within the jet. Brightest flares produced by RGs have been explained with the so called *megnetospheric* models (see Neronov and Aharonian 2007 and Levinson and Rieger 2011 for M 87; Aleksić et al. 2014c and Hirotani and Pu 2016 for IC 310). This model falls outside the jet-dominated acceleration and radiation processes examined

[I] The fitted log parabola is used in this case as the EPL does not present a local maximum.

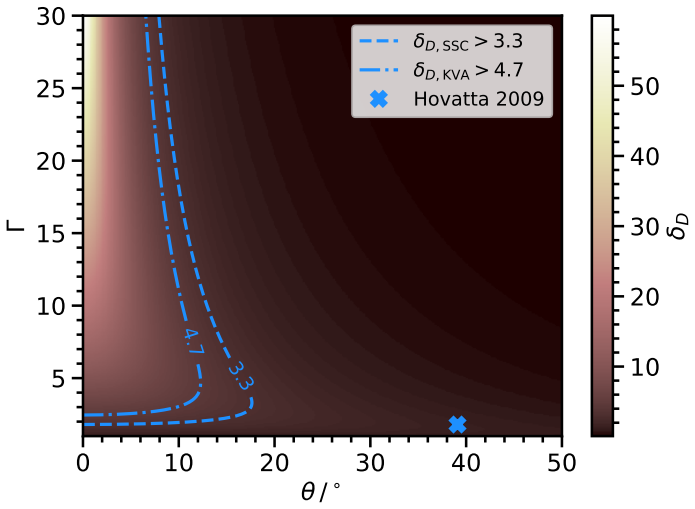

Figure 6.5: The two-dimensional plot shows the dependence of the Doppler factor δ_D on the jet bulk Lorentz factor Γ and the viewing angle θ. The regions of values necessary to avoid $\gamma\gamma$ absorption of TeV photons are enclosed with blue lines. The dot-dashed line considers as a target for the absorption the optical flux measured by KVA, the dashed line considers an hypothetical synchrotron components with peak luminosity 100 times smaller than the one observed in gamma rays. The cross indicates the (Γ, θ) values reported by Hovatta et al. (2009).

in Chapter 4, nonetheless an elementary understanding of it (and an upper limit on the radiated flux) can be obtained recalling the BH formalism introduced in Section 4.4.1 and the accretion processes of Section 4.4.2.

Gap Acceleration

Along with matter, the accretion disk drags towards the central engine poloidal magnetic field lines attached to the disk. When these thread the BH they start to rigidly rotate with the frame dragging velocity $\Omega_H = ac/(2R_H)$, where R_H is the event horizon radius (Eq. 4.31) and a is the dimensionless black hole angular momentum (Eq. 4.29). An electric field $\boldsymbol{E}$ and a voltage drop across the horizon are induced

$$\begin{aligned} |\boldsymbol{E}| &= \frac{v_{\mathrm{rot}}}{c} \times B = \frac{\Omega_H R_H}{c} B, \\ \Phi &= R_H \, |\boldsymbol{E}| = (a/2) R_H B. \end{aligned} \tag{6.8}$$

If the potential Φ was to be tapped for particle acceleration, ultra high energies could be easily achieved $E = Ze\Phi = 3 \times 10^{19} Z M_8 B_4$ eV where the Black Hole mass is expressed in $M_8 = M/(10^8 \, M_\odot)$ units and the magnetic field in $B_4 = B/(10^4 \, \mathrm{G})$. For the Gauss' law such an electric field is supported by a particle number density commonly referred to as Goldreich and Julian (1969) density

$$n_{\mathrm{GJ}} = \frac{\boldsymbol{\Omega_H B}}{2\pi e c} = 5 \times 10^{-2} \, \dot{m}^{-1/2} \, M_9^{-3/2} \, \mathrm{cm}^{-3}. \tag{6.9}$$

with e elementary electric charge. This density can be provided either by direct inflow from the accretion disk (see Section 2.5 of Rieger 2011) or by $e^{\pm}$ pairs generated by self-annihilating MeV photons produced by an ADAF accretion disk. As we have seen in Section 4.4.2 and Figure 4.8 such disks can emit $\sim$ MeV

photons via bremsstrahlung. If the charge density is greater than the Goldreich-Julian density $n_{\pm} > n_{\rm GJ}$ then the charges move freely around the field lines, neutralising the electric field component parallel to the magnetic field lines $E_{\parallel} = 0$ i.e. $\mathbf{E} \cdot \mathbf{B} = \mathbf{0}$. Such magnetosphere is labelled as *force-free*. In case the charge density supply is provided by the $e^{\pm}$ pairs produced by the ADAF photons, if the accretion rates becomes much smaller than the Eddington rate then a charge-starved region, or *gap*, can form in the magnetosphere. Here the $E_{\parallel}$ is not null and particles are efficiently accelerated along the magnetic field lines. Moving along the field lines the charged particles emit synchro-curvature radiation and can Compton scatter the ADAF MeV photons to VHEs. The pair production of the accelerated particle can cascade out of the magnetosphere were further synchrotron and inverse Compton emission will add-up to the radiative emission. If we define the gap height as h, the fraction of the potential drop (Eq. 6.8) available for acceleration scales with $(h/R_H)^2\Phi$.

Blandford-Znajek Limit

The maximum electromagnetic output of the gap is limited by the Blandford-Znajek power (Blandford and Znajek, 1977) that establishes the maximum EM energy extractable by a rotating BH. Rieger (2011) derives it (see Section 3.1) considering the potential in Eq. 6.8 and assuming the BH having the impedance of the free space

$$L_{\rm BZ} = 10^{37} a^2 \, M_9^2 \, B^2 \, {\rm erg \, s^{-1}}, \tag{6.10}$$

with $M_9 = M_{\rm BH}/(10^9 M_{\odot})$. In a RIAF, Levinson and Rieger (2011), assume that the magnetic field is at the equipartition value given by half the gas pressure $B^2/(8\pi) = 1/2\rho c_s^2$, where ρ is the disk material density and c_s the speed of sound. Hirotani (2018) simplifies $B_{\rm eq}$ to

$$B_{\rm eq} \approx 4 \times 10^4 \, \dot{m}^{1/2} \, M_9^{-1/2} \, {\rm G}. \tag{6.11}$$

Replacing Eq. 6.11 in 6.10 returns a Blandford-Znajek power dependent only on the BH mass, spin and accretion rate

$$L_{\rm BZ} = 1.6 \times 10^{46} \, a^2 \, \dot{m} \, M_9 \, {\rm erg \, s^{-1}}. \tag{6.12}$$

Assuming that the supply of charge to the magnetosphere is due to self-annihilating MeV photons emitted by bremsstrahlung in the ADAF, Levinson and Rieger (2011) compute (Eq. 6) a particle density dependent only on the accretion rate

$$n_{\pm} = 3 \times 10^{11} \, \dot{m}^4 \, M_9^{-1} \, {\rm cm^{-3}}. \tag{6.13}$$

Recovering the expression for the Goldreich-Julian density at Eq. 6.9 we obtain a ratio of particle densities dependent only on the accretion rate $\dot{m}$ and the BH mass. It is precisely this ratio that determines the upper limit on $\dot{m}$ to starve the magnetosphere and open the gap

$$\frac{n_{\pm}}{n_{\rm GJ}} < 1 \Rightarrow \dot{m} < 2.2 \times 10^{-4} \, M_9^{-1/7}. \tag{6.14}$$

Plugging this result back into Eq. 6.15 we obtain the maximum gap luminosity as

$$L_{\rm BZ} = 3.7 \times 10^{42}\, a^2\, M_9^{6/7}\, {\rm erg\,s^{-1}}. \tag{6.15}$$

Using for NGC 1275 $M_{\rm BH} = 3.4 \times 10^8\, M_\odot$ and assuming $a = 0.9$ we obtain $L_{\rm BZ} = 1.2 \times 10^{42}\, {\rm erg\,s^{-1}}$. This luminosity corresponds to a SED value $f_{\rm BZ} = L_{\rm BZ}/(4\pi d_L^2)$ (with d_L luminosity distance of the source), plotted as a yellow upper limit in 6.3. The upper limit is represented in the $0.1 - 10\,{\rm TeV}$ band as Hirotani et al. (2017) foresee the peak of the cascaded synchrotron and inverse Compton emission in this energy range. The maximum flux allowed by the Blandford-Znajek limit on the gap luminosity is 2 orders of magnitude lower than the maximum flux observed for 1 January 2017, the night with the strongest flux ad shortest variability. Hirotani and Pu (2016) encountered the same issue while modelling with magnetospheric emission the gamma-ray outburst observed in IC 310 (Aleksić et al., 2014c). A luminosity in gamma rays of $L_{\rm VHE,\,IC\ 310} \sim 10^{44}\, {\rm erg\,s^{-1}}$ was measured by MAGIC at odds with the maximum Blandford-Znajek power $L_{\rm BZ,\,IC\ 310} = 5.3 \times 10^{41} {\rm erg\,s^{-1}}$ (given $M_{\rm BH,\,IC\ 310} = 0.3\, M_9$). The critical assumption that allowed us to get a Blandford-Znajek luminosity dependent only on the accretion rate and BH mass was the use of a magnetic field at equipartition (simplifications from Eq. 6.10 to Eq. 6.15). Hirotani and Pu (2016), in order to achieve magnetospheric luminosities comparable to those observed for IC 310, discuss that a BH with extreme values of angular momentum, $a > 0.998$, could produce a pile-up of plasma threading the horizon, intensifying the magnetic field up to values of $B \approx 10^4\,{\rm G} \approx 14\, B_{\rm eq}$. Although not yet confirmed by a thorough numerical simulation, such scenario is hinted by two factors. The first is the divergence of plasma density at the horizon of a Kerr BH, described in Hirotani et al. (1992). The second is the increase of magnetic energy by a factor 30 at R_H obtainable by increasing the angular momentum from $a = 0.9$ to $a = 0.998$, as shown by magneto-hydrodynamic simulations in Hirose et al. (2004). Such a high value of magnetic field would push the Blandford-Znajek luminosity, i.e. the maximum extractable electro-magnetic power, beyond the jet luminosity[II] commonly observed for AGN (Ghisellini et al., 2014). Such magnetic field enhancement can therefore be only contemplated with small duty cycles, e.g. during episodic flares. A closing remark on magnetospheric model is that the cascaded radiative processes naturally result in a high-energy continuum emission with a cutoff spectra (see Figure 11 of Hirotani and Pu 2016), hence the cutoff observed in the flaring state of 1 January 2017 could constitute another hint in favour of such processes.

6.4 Conclusion

The MAGIC telescopes monitored the radio galaxy NGC 1275 in an enhanced state of VHE gamma-ray emission in the period from September 2016 to March 2017. The average integrated flux above $100\,GeV$ is almost an order of magnitude above the one measured from the 253 hours collected in previous observational campaigns (Aleksić et al., 2014b; Ahnen et al., 2016b). Particular bright flares are observed on the night of 1 and 2-3 January 2017 where the source attains an integrated flux greater than 1 and

[II] The jet luminosity is commonly computed as the sum of the kinetic energy of the electron distribution and the energy of the magnetic field in the jet.

0.5 C.U., respectively, marking the highest VHE flux measured for this source. The time variability in coincidence of the brightest flare is estimated to be of $\sim$ 10 hours. The spectra evaluated for the flaring nights and on the rest of the dataset clearly show curvature describable both with a log parabola or a cutoff power law. With the exception of the brightest night, where the spectrum is constrained with a simultaneous HE measurement and a cutoff of $\approx 500\,\mathrm{GeV}$ is found. Analysing HE and optical measurements provided by the *Fermi*-LAT and KVA telescopes, respectively, we do not find correlation between simultaneous optical and gamma-ray fluxes (both in the HE and VHE bands). The size of the emission region, R'_b, inferred from the variability is $\sim$ 20 times large than the BH horizon, but still one order of magnitude below the value used in previous leptonic modelling of the source (Aleksić et al., 2014b; Tavecchio and Ghisellini, 2014). Additionally the small R'_b would complicate for TeV gamma rays, significantly detected in the whole data set, to escape the absorption by eV photons. Doppler values $\delta_D \gtrsim 4$ would be required to escape such absorption, in tension with values assumed in previous modelling and with the bulk Lorentz factor and viewing angle measured by Hovatta et al. (2009). Intense gamma-ray flares observed from radio galaxies (e.g. IC 310 and M 87) have been accommodated with magnetospheric models, that foresee particle acceleration in charge-starved regions of a force-free magnetosphere. An upper limit on these models is posed by the Blandford-Znajek luminosity, which accounts for the maximum electromagnetic power extractable from a rotating BH. The case of NGC 1275 is similar to the one of IC 310 in Aleksić et al. (2014c), as VHE luminosities exceeding this power by two order of magnitudes are observed. In case of an extremely rotating BH, a pile-up of plasma near the event horizon can form, increasing the magnetic energy available for the Blandford-Znajek process. The maximum extractable luminosity in such scenario can even overcome the jet power, a state that can be contemplated only on small time scales, like those characterising these distinctively bright flares.

7 | Conclusions

7.1 Summary

Jetted active galaxies present an electromagnetic spectrum spanning over 20 orders of magnitude in energy, from radio frequencies to TeV gamma rays. Modelling their non-thermal radiative processes allows us to expand our knowledge on acceleration and interactions of particles in astrophysical environments. The multi-wavelength spectral energy distribution of jetted AGN (radio galaxies and blazars) can be modelled considering the region of particle acceleration located within the jet and reproducing the broad-band electromagnetic spectrum with the radiative processes of electrons and positrons. This thesis focuses on the examination of these leptonic models.

We study the electromagnetic emission of a blazar and a radio galaxy, driving the interpretation with MAGIC observations in the VHE regime, supported by multi-wavelength data sets collected from lower energy instruments. The objective is to investigate the validity of the aforementioned jet-dominated leptonic scenario by examining two sources rarely detected in VHE gamma-rays. These sources also provide complementary science cases as PKS 1510-089 manifests a persistent low-state gamma-ray emission while NGC 1275 is observed undergoing a record flaring activity.

PKS 1510-089 is studied in a low gamma-ray state identified using flux measurements densely sampled over time by the *Fermi*-LAT telescope. Within 5 years (2012-2017) of monitoring of the source MAGIC has gathered ≈ 80 hours simultaneous to such HE low state. This VHE data set yields a significant signal that allows to identify PKS 1510-089 as the first FSRQ to show *persistent* VHE emission. The multi-wavelength SED is assembled with data collected from X-ray, UV, optical, IR and radio telescopes. The low-energy continuum of the spectrum can be modelled with the synchrotron radiation of jet electrons, overlapping with the thermal components of the disk and torus photon fields. The high-energy continuum can be well represented by the inverse Compton of the jet electrons on the photon field provided by IR radiation produced by the dust torus. HE and VHE gamma-ray spectral points can be smoothly connected by the spectrum of this radiative process seemingly presenting no features of $\gamma\gamma$ absorption by low-energy photon field.

NGC 1275 is instead studied in a gamma-ray flaring period closely monitored by MAGIC. Between September 2016 and February 2017 the source has shown an unprecedented VHE activity, peaking the night of 1 January 2017, when the sources manifested variability time scale of the order of 10 hours and flux higher than the Crab nebula. Emission of TeV gamma rays is detected over the entire period.

Fermi-LAT data are analysed to better characterise the spectrum in the night with the highest energy flux and to search for correlation with optical fluxes, whose measurements are provided by the KVA telescope. Two arguments can be inferred in this case against a jet-dominated scenario. The first is the absence of correlation between optical and gamma-ray fluxes. The latter should instead be present if the optical photons are due to the synchrotron radiation of the same relativistic electrons responsible for the gamma-ray spectrum via Comptonisation of soft photon fields. The second is the size of the emitting region inferred from the variability time scales that would result in a consistent absorption of TeV gamma rays by the synchrotron photons filling the blob. This attenuation could be avoided only assuming values of the Doppler factor $\delta_{\rm D} \gtrsim 4$ that are actually incompatible with previous measurements for this source (and other radio galaxies in general). Given the difficulty to accommodate the emission region in the jet we suggest that electrons might be accelerated and radiate in a gap opened in the BH magnetosphere.

The physical discussion of PKS 1510-089 conforms to the jet-dominated, leptonic, scenario. The spectrum of the external Compton on the torus photon field can smoothly connect the HE and VHE flux points. To obtain the dominance of the torus photon field for the EC, we place the emitting region outside the BLR and reasonably reproduce the gamma-ray flux measurements without encountering any $\gamma\gamma$ absorption feature either produced by the BLR or by the torus photon field. Therefore our observations confirm, in the VHE regime, what Costamante et al. (2018) and Meyer et al. (2019) found analysing HE gamma-ray data from *Fermi*-LAT. They both claim that since no absorption features due to the BLR photon field are observed in HE spectra, the region responsible for the gamma-ray emission of FSRQs must lie outside the BLR. Costamante et al. (2018) deduces, analysing both low-state and flaring HE spectra, that the claim on the emission region position is valid "on average and during high/flaring or low-flux states". We recognise this in our observations since in the low state we measure a spectral index in VHE that is remarkably similar (compatible within statistical errors) to the ones measured in previous VHE active or flaring states. We can therefore exclude that the previously observed VHE flares were due to the blob emerging from the BLR and overcoming its $\gamma\gamma$ absorption. Our SED model, even if reasonably reproducing the multi-wavelength SED manifests a limitation inherent to assigning all the emission to a single region in the jet. The electron population reproducing the high-energy continuum via EC produces a synchrotron emission underestimating the flux actually observed in radio. To overcome this limitation a modelling that integrates the radiative processes along the jet geometrical dimension, as illustrated by Potter and Cotter (2012), would have to be implemented.

Even if a jet-dominated radiation can explain baseline spectra like the one observed for PKS 1510-089, extreme flares like the one characterising NGC 1275 are difficult to accommodate in this scenarios. We consider an alternative model foreseeing electron acceleration and radiation in gaps opened in the BH magnetosphere. Supporting our suggestion, magnetospheric models to describe the gamma-ray emission of RGs have been already proposed by Neronov and Aharonian (2007) and Levinson and Rieger (2011) for M 87, and by Aleksić et al. (2014c) and Hirotani and Pu (2016) for IC 310. Hirotani and Pu (2016) critically realise that the luminosities observed for IC 310 in VHE exceeds by two orders of magnitude the Blandford-Znajek power, reckoning the maximum EM power extractable from a rotating BH. This tension derives from a fundamental assumption that we make in order to reduce the Blandford-Znajek

power to a function of the spin, the accretion and the mass of the BH (such that a rule-of-thumb estimate can be derived knowing only the main BH properties). It is indeed assumed that the magnetic field that the accretion flows drags towards the BH is at equipartition with the gas pressure in the disk. Considering a magnetic field far from the equipartition increases the upper limit posed by the Blandford-Znajek luminosity but such a possibility has not yet been confirmed by numerical simulation. A difference we encounter between the flaring activity of NGC 1275 and the one of M 87 and IC 310 is that for these sources a straight power-law spectrum was measured in VHE, while for NGC 1275 we observe a spectral cutoff at $\approx 500\,\mathrm{GeV}$. Such cutoff can be indeed a result of the magnetospheric cascaded emission. Its appearance at VHE could depend on the curvature radius of the particles around the magnetic field lines (see Figure 15 and 16 of Hirotani and Pu 2016). To assess with more confidence if the flaring activity is magnetospheric in origin a full modelling on the line of Hirotani and Pu 2016 is mandatory, with special care in numerically addressing the possibility of departure of the magnetic field in the accretion flow from the equipartition value.

For both the sources analysed the combined analysis of HE and VHE gamma-ray data is fundamental to the interpretation. Such combination is nowadays limited by the absence of a unified, standardised format for high-level gamma-ray astronomy data and case-by-case methods have to be considered (e.g. fit of spectral points for PKS 1510-089, likelihood constrained with HE spectral parameters for NGC 1275).

The technical work of this thesis is concerned with interoperability of gamma-ray data and reproducibility of their results. This thesis presents the effort of VHE gamma-ray data standardisation applied on the MAGIC observations, illustrating the first production of DL3 data in FITS format. These are later employed in a project that combines data sets from *Fermi*-LAT and four of the operating IACTs, made compliant with the same specifications, and delivers the first example of a reproducible, multi-instrument gamma-ray publication. A prototypical analysis (the estimation of the Crab Nebula spectrum) illustrates how to deliver data, scripts and results to the community relying on open access assets only: `gammapy` for the analysis, `GitHub` and `Docker` for the data dissemination and results reproduction.

7.2 Outlook

As a concluding remark I would like to stress the importance that the production of DL3 data from the current gamma-ray instruments will assume in the next years. From a merely technical point of view they provide a critical test for the reliability of the evolving CTA science tools in producing scientific results. Furthermore the status of the actual tools already realises the possibility to produce combined gamma-ray analysis of point-like sources like AGN.

It would be interesting to try to expand the gamma-ray studies as those performed for PKS 1510-089 and NGC 1275 into a multi-instrument context. Combining archival data from different IACTs could play a crucial role in detecting sources that are not intrinsically bright in VHE (beside sporadic flaring episodes) and better characterising their spectra and time evolution. Additionally, the approaching closure of the current instruments opens up the possibility to leave a final statement after two decades of observations of these objects. In this sense, the tools developed here would even allow to build standardised catalogues

for single or multi-instrument gamma-ray objects, if a consistent overlap of sources observed by different IACTs exists.

The development of open-source software for gamma-ray astronomy can proceed also on the physics side. In this thesis a prototypical python-based module that reproduces some established radiative processes is presented. The latter is employed, as a test case, to model the SED of PKS 1510-089. This code will be made available in the near future, after validation with further cases has been performed.

Continuing the effort of standardisation of analysis and interpretation tools would benefit the last years of the current VHE science and prepare us for the era that the full operation of CTA will unfold.

A | Physical Constants

In this appendix we express the numerical values of the physical constants used in this work. In 2018 the Bureau International des Poids et Mesures voted to redefine the International System of Units changing the definition of all the base units in terms of constants that define the natural world, see https://www.bipm.org/en/measurement-units/rev-si and references therein. Table A.1 contains the new fixed numerical values of the Physical constants at the base of the SI redefinition that will become effective on 20 May 2019. Most of the formulas concerning the radiative processes have been derived from classical electrodynamic, anchored to centimeter-gram-second (CGS) based system of units. We convert the SI units to a Gaussian CGS system. For clarity in such a system the Coulomb Law is expressed simply as:

$$F = \frac{Q_1\, Q_2}{r^2}, \tag{A.1}$$

with Q_1 and Q_2 electrical charges in statC and r distance between the charges in cm.

symbol	name	International System of Units (SI)	Gaussian CGS Units
k_B	Boltzmann constant	$1.380649 \times 10^{-23}\,\mathrm{J\,K^{-1}}$	$1.38064852 \times 10^{-16}\,\mathrm{erg\,K^{-1}}$
e	elementary charge	$1.602176634 \times 10^{-19}\,\mathrm{C}$	$4.80320425 \times 10^{-10}\,\mathrm{statC}$
c	speed of light in vacuum	$299792458\,\mathrm{m\,s^{-1}}$	$2.99792458 \times 10^{10}\,\mathrm{cm\,s^{-1}}$
h	Planck constant	$6.62607015 \times 10^{-34}\,\mathrm{J\,s^{-1}}$	$66260701.5\,\mathrm{erg\,s^{-1}}$
m_p	proton mass	$1.67262192369 \times 10^{-27}\,\mathrm{kg}$	$1.67262192369 \times 10^{-24}\,\mathrm{g}$
α	fine structure constant	$\approx 1\,/\,137$	$\approx 1\,/\,137$
m_e	electron mass	$9.1093837015 \times 10^{-31}\,\mathrm{kg}$	$9.1093837015 \times 10^{-33}\,\mathrm{g}$
σ_T	Thomson cross-section	$6.6524587321 \times 10^{-29}\,\mathrm{m^2}$	$6.6524587321 \times 10^{-25}\,\mathrm{cm^2}$
G	Gravitational constant	$6.67430 \times 10^{-11}\,\mathrm{m^3\,kg^{-1}\,s^{-2}}$	$6.67430 \times 10^{-8}\,\mathrm{cm^3\,g^{-1}\,s^{-2}}$

Table A.1: Physical Constants used in this work, the SI units are updated to the latest prescription of the Bureau International des Poids et Mesures. The Gaussian units are computed from them.

B | Lorentz Transformations

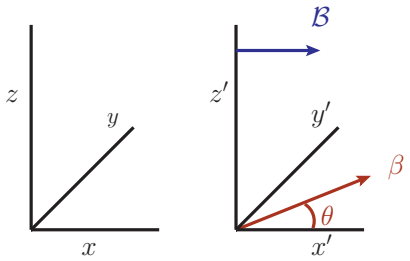

Figure B.1: The reference frame with primed axis is moving at velocity $\mathcal{B}$ with respect to the observer frame, in direction parallel to its x-axis.

Here we derive the transformations of Lorentz factor (energy) and angles of a particle (photon) in a reference frame that is moving at velocity $\mathcal{B} = v_{\text{frame}}/c$ with respect to the observer frame. Consider a particle with four-momentum $p = (\gamma mc, \gamma m\boldsymbol{v})$ in the observer frame, moving with velocity β at an angle $\theta = \arccos(\mu)$ with respect to the x-axis (such that its x-component of the momentum can be written as $p_x = \gamma m v_x = \gamma m \beta c \mu$). Let us consider a second reference frame moving with velocity $\mathcal{B}$ and Lorentz factor Γ in direction parallel to the x-axis of the observer frame, as shown in Figure B.1. The first component of the four-momentum, p_0, transforms in the frame with velocity $\mathcal{B}$, as (simplifying mc)

$$\gamma' = \Gamma\gamma(1 - \mathcal{B}\beta\mu), \tag{B.1}$$

the second component of the four-momentum, p_x, transforms as (simplifying mc)

$$\gamma'\beta'\mu' = \Gamma\gamma(\beta\mu - \mathcal{B}). \tag{B.2}$$

If the particle is ultrarelativistic ($\beta \to 1$) the ratio of Eq. B.2 to Eq. B.1 returns the transformation of the cosine of the angle,

$$\beta' = \frac{\mu - \mathcal{B}}{1 - \mathcal{B}\mu}. \tag{B.3}$$

If we consider a photon in place of the particle, we shall substitute in the previous formulas $\beta \to 1$ and the

Lorentz factor with the dimensionless photon energy $\gamma \to \epsilon = h\nu/(m_e c^2)$, obtaining the transformations

$$\begin{aligned} \epsilon' &= \Gamma\epsilon(1 - \mathcal{B}\mu), \\ \mu' &= \frac{\mu - \mathcal{B}}{1 - \mathcal{B}\mu}, \end{aligned} \tag{B.4}$$

and the reverse transformations (from the frame comoving with $\mathcal{B}$ to the observer frame) reads

$$\begin{aligned} \epsilon &= \Gamma\epsilon'(1 + \mathcal{B}\mu'), \\ \mu &= \frac{\mu' + \mathcal{B}}{1 + \mathcal{B}\mu'}. \end{aligned} \tag{B.5}$$

Bibliography

J. E. Keeler. The Importance of Astrophysical Research and the Relation of Astrophysics to Other Physical Sciences. *The Astrophysical Journal*, 6:271, Oct 1897. doi: 10.1086/140401.

J. Fraunhofer. Kurzer Bericht von den Resultaten neuerer Versuche über die Gesetze des Lichtes, und die Theorie derselben. *Annalen der Physik*, 74(8):337–378, Jan 1823. doi: 10.1002/andp.18230740802.

V. F. Hess. Über Beobachtungen der durchdringenden Strahlung bei sieben Freiballonfahrten. *Phys. Z.*, 13:1084–1091, 1912.

E. O. Lawrence et al. Initial Performance of the 60-Inch Cyclotron of the William H. Crocker Radiation Laboratory, University of California. *Physical Review*, 56(1):124–124, Jul 1939. doi: 10.1103/PhysRev.56.124.

C. D. Anderson. The Positive Electron. *Physical Review*, 43(6):491–494, Mar 1933. doi: 10.1103/PhysRev.43.491.

S. H. Neddermeyer and C. D. Anderson. Cosmic-Ray Particles of Intermediate Mass. *Physical Review*, 54(1):88–89, Jul 1938. doi: 10.1103/PhysRev.54.88.2.

M. Spurio. *Probes of Multimessenger Astrophysics*. Springer International Publishing, second edition, 2018. doi: 10.1007/978-3-319-96854-4.

A. M. Hillas. The Origin of Ultra-High-Energy Cosmic Rays. *Annual review of astronomy and astrophysics*, 22:425–444, Jan 1984. doi: 10.1146/annurev.aa.22.090184.002233.

M. Ackermann et al. Detection of the Characteristic Pion-Decay Signature in Supernova Remnants. *Science*, 339(6121):807–811, Feb 2013. doi: 10.1126/science.1231160.

IceCube Collaboration. Evidence for High-Energy Extraterrestrial Neutrinos at the IceCube Detector. *Science*, 342(6161):1242856, Nov 2013. doi: 10.1126/science.1242856.

D. Maurin et al. A database of charged cosmic rays. *Astronomy and Astrophysics*, 569:A32, Sep 2014. doi: 10.1051/0004-6361/201321344.

M. Amenomori et al. The All-Particle Spectrum of Primary Cosmic Rays in the Wide Energy Range from 10^{14} to 10^{17} eV Observed with the Tibet-III Air-Shower Array. *The Astrophysical Journal*, 678 (2):1165–1179, May 2008. doi: 10.1086/529514.

W. D. Apel et al. The spectrum of high-energy cosmic rays measured with KASCADE-Grande. *Astroparticle Physics*, 36(1):183–194, Aug 2012. doi: 10.1016/j.astropartphys.2012.05.023.

F. Fenu et al. The cosmic ray energy spectrum measured using the Pierre Auger Observatory. In 35th International Cosmic Ray Conference (2017), page 486. Available at https://pos.sissa.it/301.

A. A. Abdo et al. Fermi Large Area Telescope Observations of Markarian 421: The Missing Piece of its Spectral Energy Distribution. *The Astrophysical Journal*, 736(2):131, Aug 2011a. doi: 10.1088/0004-637X/736/2/131.

A. A. Abdo et al. Insights into the High-energy γ-ray Emission of Markarian 501 from Extensive Multifrequency Observations in the Fermi Era. *The Astrophysical Journal*, 727(2):129, Feb 2011b. doi: 10.1088/0004-637X/727/2/129.

T. K. Gaisser et al. *Cosmic Rays and Particle Physics*. Cambridge University Press, second edition, 2016. doi: 10.1017/CBO9781139192194.

J. F. Carlson and J. R. Oppenheimer. On Multiplicative Showers. *Physical Review*, 51:220–231, February 1937. doi: 10.1103/PhysRev.51.220.

B. Rossi and K. Greisen. Cosmic-Ray Theory. *Reviews of Modern Physics*, 13:240–309, October 1941. doi: 10.1103/RevModPhys.13.240.

NASA. U.S. Standard Atmosphere, 1976. Technical report, U.S. Government Printing Office, Washington, D.C., 1976. Available at https://ntrs.nasa.gov/archive/nasa/casi.ntrs.nasa.gov/19770009539.pdf.

W. Heitler. *Quantum Theory of Radiation*. Oxford University Press, Oxford, 1944.

J. Matthews. A Heitler model of extensive air showers. *Astroparticle Physics*, 22:387–397, January 2005. doi: 10.1016/j.astropartphys.2004.09.003.

W. R. Leo. *Techniques for Nuclear and Particle Physics Experiments*. Springer-Verlag Berlin Heidelberg, second revised edition, 1994. doi: 10.1007/978-3-642-57920-2.

K. Greisen. The Extensive Air Showers. *Prog. Cosmic Ray Physics*, 3:1–141, 1956.

F. Nerling et al. Universality of electron distributions in high-energy air showers – Description of Cherenkov light production. *Astroparticle Physics*, 24:421–437, January 2006. doi: 10.1016/j.astropartphys.2005.09.002.

P. Lipari. Concepts of "age" and "universality" in cosmic ray showers. *Physical Review D*, 79(6):063001, March 2009. doi: 10.1103/PhysRevD.79.063001.

M. de Naurois and D. Mazin. Ground-based detectors in very-high-energy gamma-ray astronomy. *Comptes Rendus Physique*, 16:610–627, August 2015. doi: 10.1016/j.crhy.2015.08.011.

D. Heck et al. *CORSIKA: a Monte Carlo code to simulate extensive air showers.* Forschungszentrum Karlsruhe GmbH, Karlsruhe (Germany), February 1998.

S. Braibant, G. Giacomelli, and M. Spurio. *Particles and Fundamental Interactions*. Springer Netherlands, first edition, 2012. doi: 10.1007/978-94-007-2464-8.

A. M. Hillas. Differences between Gamma-Ray and Hadronic Showers. *Space Science Reviews*, 75:17–30, January 1996. doi: 10.1007/BF00195021.

P. A. Čerenkov. Visible Radiation Produced by Electrons Moving in a Medium with Velocities Exceeding that of Light. *Physical Review*, 52:378–379, August 1937. doi: 10.1103/PhysRev.52.378.

F. I. Boley. Atmospheric Čerenkov Radiation from Cosmic-Ray Air Showers. *Reviews of Modern Physics*, 36:792–808, July 1964. doi: 10.1103/RevModPhys.36.792.

J. D. Jackson. *Classical electrodynamics*. Wiley, New York, NY, 3rd ed. edition, 1999. ISBN 9780471309321.

K. Greisen. Cosmic Ray Showers. *Annual Review of Nuclear and Particle Science*, 10:63–108, 1960. doi: 10.1146/annurev.ns.10.120160.000431.

M. Tanabashi et al. Review of Particle Physics. *Physical Review D*, 98(3):030001, August 2018. doi: 10.1103/PhysRevD.98.030001.

R. M. Wagner. *Measurement of Very High Energy Gamma-Ray Emission from Four Blazars Using the MAGIC Telescope and a Comparative Blazar Study*. PhD thesis, Technische Universität München, 2006. Available at https://publications.mpp.mpg.de/2006/MPP-2006-245/FullText.pdf.

P. K. F. Grieder. *Extensive Air Showers*. Springer-Verlag Berlin Heidelberg, 2010. doi: https://doi.org/10.1007/978-3-540-76941-5.

W. Galbraith and J. V. Jelley. Light Pulses from the Night Sky associated with Cosmic Rays. *Nature*, 171:349–350, February 1953. doi: 10.1038/171349a0.

A. E. Chudakov et al. Cerenkov radiation produced by extensive air showers of cosmic ray. In Zhdanov (1960), pages 50–57.

G. Cocconi. An air shower telescope and the detection of 10^{12} eV photon sources. In Zhdanov (1960), pages 309–311.

A. E. Chudakov et al. On the high energy photons from local sources. In Daniels et al. (1964), pages 199–204.

T. C. Weekes et al. A Search for Discrete Sources of Cosmic Gamma Rays of Energy $10^{11} - 10^{12}$ eV. *Astrophysical Journal*, 174:165, May 1972. doi: 10.1086/151479.

G. G. Fazio et al. Detection of High-Energy Gamma Rays from the Crab Nebula. *Astrophysical Journal*, 175:L117, August 1972. doi: 10.1086/180998.

B. M. Vladimirsky et al. High-Energy Gamma-Ray Outburst in the Direction of the X-Ray Source CYG X-3. In Chasson (1973), pages 199–204.

K. E. Turver and T. C. Weekes. Gamma-rays above 100 GeV. *Philosophical Transactions of the Royal Society of London Series A*, 301:615–628, June 1981. doi: 10.1098/rsta.1981.0140.

A. M. Hillas. Cerenkov light images of EAS produced by primary gamma. In Jones et al. (1985), pages 445–448.

T. C. Weekes et al. Observation of TeV gamma rays from the Crab nebula using the atmospheric Cerenkov imaging technique. *Astrophysical Journal*, 342:379–395, July 1989. doi: 10.1086/167599.

G. H. Rieke. a Search for Cosmic Sources of Gamma Rays with Energies Between 10^{11} and 10^{14} ev. *SAO Special Report*, 301, June 1969.

M. De Naurois. *Very High Energy astronomy from H.E.S.S. to CTA. Opening of a new astro- nomical window on the non-thermal Universe.* Habilitation thesis, Université Pierre et Marie Curie - Paris VI, 2012. Available at https://tel.archives-ouvertes.fr/tel-00687872/en.

A. M. Hillas. Evolution of ground-based gamma-ray astronomy from the early days to the Cherenkov Telescope Arrays. *Astroparticle Physics*, 43:19–43, March 2013. doi: 10.1016/j.astropartphys.2012.06.002.

G. Pühlhofer et al. The technical performance of the HEGRA system of imaging air Cherenkov telescopes. *Astroparticle Physics*, 20:267–291, Dec 2003. doi: 10.1016/j.astropartphys.2003.06.001.

C. Baixeras et al. Commissioning and first tests of the MAGIC telescope. *Nuclear Instruments and Methods in Physics Research A*, 518:188–192, February 2004. doi: 10.1016/j.nima.2003.10.057.

R. Mirzoyan. First time detection of a GRB at sub-TeV energies; MAGIC detects the GRB 190114C. *The Astronomer's Telegram*, 12390:1, Jan 2019.

J. Aleksić et al. Performance of the MAGIC stereo system obtained with Crab Nebula data. *Astroparticle Physics*, 35:435–448, February 2012a. doi: 10.1016/j.astropartphys.2011.11.007.

J. Aleksić et al. The major upgrade of the MAGIC telescopes, Part I: The hardware improvements and the commissioning of the system. *Astroparticle Physics*, 72:61–75, January 2016a. doi: 10.1016/j.astropartphys.2015.04.004.

J. Aleksić et al. The major upgrade of the MAGIC telescopes, Part II: A performance study using observations of the Crab Nebula. *Astroparticle Physics*, 72:76–94, January 2016b. doi: 10.1016/j.astropartphys.2015.02.005.

G. Giavitto. *Observing the VHE Gamma-Ray Sky with the MAGIC Telescopes: the Blazar B3 2247+381 and the Crab Pulsar*. PhD thesis, Universitat Autònoma de Barcelona, 2012. Available at https://inspirehep.net/record/1424356.

R. López-Coto. *Very-high-energy gamma-ray observations of pulsar wind nebulae and cataclysmic variable stars with MAGIC and development of trigger systems for IACTs*. PhD thesis, Universitat Autònoma de Barcelona, 2015. Available at https://www.mpi-hd.mpg.de/personalhomes/rlopez/Theses/PhD_thesis.pdf.

D. Bastieri et al. The Mirrors for the MAGIC Telescopes. In Sripathi Acharya et al. (2005), page 283.

D. Bastieri et al. The reflecting surface of the MAGIC-II Telescope. In Caballero et al. (2008), pages 1547–1550.

A. Biland et al. The Active Mirror Control of the MAGIC Telescopes. In Caballero et al. (2008), pages 1353–1356.

J. Sitarek et al. Analysis techniques and performance of the Domino Ring Sampler version 4 based readout for the MAGIC telescopes. *Nuclear Instruments and Methods in Physics Research A*, 723:109–120, September 2013. doi: 10.1016/j.nima.2013.05.014.

M. Bitossi et al. Ultra-Fast Sampling and Data Acquisition Using the DRS4 Waveform Digitizer. *IEEE Transactions on Nuclear Science*, 63:2309–2316, August 2016. doi: 10.1109/TNS.2016.2578963.

C. Fruck et al. A novel LIDAR-based Atmospheric Calibration Method for Improving the Data Analysis of MAGIC. In Saa (2014), page 1054. Available at https://inspirehep.net/record/1285998.

R. Zanin. *Observation of the Crab pulsar wind nebula and microquasar candidates with MAGIC*. PhD thesis, Universitat Autònoma de Barcelona, 2011. Available at https://magicold.mpp.mpg.de/publications/theses/RZanin1.pdf.

A. Berti et al. Search for High Energy emission from GRBs with MAGIC. In Andreja Gomboc, editor, *New Frontiers in Black Hole Astrophysics*, volume 324 of *IAU Symposium*, pages 70–73, Jan 2017. doi: 10.1017/S1743921317001442.

D. Tescaro et al. The MAGIC telescopes DAQ software and the on-the-fly online analysis client. In Saa (2014), page 0122. Available at https://inspirehep.net/record/1257342.

I. Oya et al. Data Quality Check and On-Site Analysis of the MAGIC Telescope. *Astrophysics and Space Science Proceedings*, 14:519, Jan 2010. doi: 10.1007/978-3-642-11250-8_156.

R. Mirzoyan and E. Lorenz. Measurement of the night sky light background at La Palma. Technical report, MPI-PhE/94-35, MPI Munich, 1994. Available at https://magicold.mpp.mpg.de/publications/articles/LONS.ps.gz.

M. L. Ahnen et al. Performance of the MAGIC telescopes under moonlight. *Astroparticle Physics*, 94: 29–41, September 2017a. doi: 10.1016/j.astropartphys.2017.08.001.

V. P. Fomin et al. New methods of atmospheric Cherenkov imaging for gamma-ray astronomy. I. The false source method. *Astroparticle Physics*, 2:137–150, May 1994. doi: 10.1016/0927-6505(94)90036-1.

M. L. Ahnen et al. Limits on the flux of tau neutrinos from 1 PeV to 3 EeV with the MAGIC telescopes. *Astroparticle Physics*, 102:77–88, November 2018. doi: 10.1016/j.astropartphys.2018.05.002.

V. A. Acciari et al. Constraining very-high-energy and optical emission from FRB 121102 with the MAGIC telescopes. *Monthly Notices of the Royal Astronomical Society*, 481:2479–2486, December 2018a. doi: 10.1093/mnras/sty2422.

R. Zanin et al. MARS, the MAGIC analysis and reconstruction software. In Saa (2014), page 773. Available at https://inspirehep.net/record/1412925.

R. Brun and F. Rademakers. ROOT — An object oriented data analysis framework. *Nuclear Instruments and Methods in Physics Research A*, 389:81–86, February 1997. doi: 10.1016/S0168-9002(97)00048-X.

J. L. Contreras et al. Data model issues in the Cherenkov Telescope Array project. In 34th International Cosmic Ray Conference (2015), page 960. Available at https://pos.sissa.it/236.

P. Majumdar et al. Monte Carlo simulation for the MAGIC telescope. In Sripathi Acharya et al. (2005), page 203.

R. Mirzoyan. On the calibration accuracy of light sensors in atmospheric Cherenkov fluorescence and neutrino experiment. In Potgieter et al. (1997), pages 265–268.

W. Hofmann et al. Comparison of techniques to reconstruct VHE gamma-ray showers from multiple stereoscopic Cherenkov images. *Astroparticle Physics*, 12:135–143, November 1999. doi: 10.1016/S0927-6505(99)00084-5.

J. Albert et al. Implementation of the Random Forest method for the Imaging Atmospheric Cherenkov Telescope MAGIC. *Nuclear Instruments and Methods in Physics Research A*, 588:424–432, April 2008a. doi: 10.1016/j.nima.2007.11.068.

C. Gini. Measurement of inequality of incomes. *The Economic Journal*, 31(121):124–126, 1921. ISSN 00130133, 14680297. doi: DOI:10.2307/2223319. URL http://www.jstor.org/stable/2223319.

R. W. Lessard et al. A new analysis method for reconstructing the arrival direction of TeV gamma rays using a single imaging atmospheric Cherenkov telescope. *Astroparticle Physics*, 15:1–18, March 2001. doi: 10.1016/S0927-6505(00)00133-X.

J. Aleksić et al. Search for an extended VHE γ-ray emission from Mrk 421 and Mrk 501 with the MAGIC Telescope. *Astronomy and Astrophysics*, 524:A77, December 2010a. doi: 10.1051/0004-6361/201014747.

I. R. King. The Profile of a Star Image. *Publications of the Astronomical Society of the Pacific*, 83:199, April 1971. doi: 10.1086/129100.

I. Vovk et al. Spatial likelihood analysis for MAGIC telescope data. From instrument response modelling to spectral extraction. *Astronomy and Astrophysics*, 619:A7, November 2018. doi: 10.1051/0004-6361/201833139.

D. Berge et al. Background modelling in very-high-energy γ-ray astronomy. *Astronomy and Astrophysics*, 466:1219–1229, May 2007. doi: 10.1051/0004-6361:20066674.

F. Aharonian et al. Evidence for TeV gamma ray emission from Cassiopeia A. *Astronomy and Astrophysics*, 370:112–120, April 2001. doi: 10.1051/0004-6361:20010243.

T.-P. Li and Y.-Q. Ma. Analysis methods for results in gamma-ray astronomy. *The Astrophysical Journal*, 272:317–324, September 1983. doi: 10.1086/161295.

F. Piron et al. Temporal and spectral gamma-ray properties of Mkn 421 above 250 GeV from CAT observations between 1996 and 2000. *Astronomy and Astrophysics*, 374:895–906, August 2001. doi: 10.1051/0004-6361:20010798.

J. Albert et al. Unfolding of differential energy spectra in the MAGIC experiment. *Nuclear Instruments and Methods in Physics Research A*, 583:494–506, December 2007. doi: 10.1016/j.nima.2007.09.048.

A. N. Tikhonov and V. Y. Arsenin. *Solutions of ill-posed problems*. V. H. Winston & Sons, 1977.

M. Bertero. Linear inverse and ill-posed problems. volume 75 of *Advances in Electronics and Electron Physics*, pages 1 – 120. Academic Press, 1989. doi: https://doi.org/10.1016/S0065-2539(08)60946-4.

M. Schmelling. The method of reduced cross-entropy a general approach to unfold probability distributions. *Nuclear Instruments and Methods in Physics Research A*, 340:400–412, February 1994. doi: 10.1016/0168-9002(94)90119-8.

W. A. Rolke et al. Limits and confidence intervals in the presence of nuisance parameters. *Nuclear Instruments and Methods in Physics Research A*, 551:493–503, October 2005. doi: 10.1016/j.nima.2005.05.068.

D. C. Wells et al. FITS - a Flexible Image Transport System. *Astronomy and Astrophysics Supplement Series*, 44:363, June 1981.

C. Deil et al. Open high-level data formats and software for gamma-ray astronomy. In *6th International Symposium on High Energy Gamma-Ray Astronomy*, volume 1792 of *American Institute of Physics Conference Series*, page 070006, January 2017a. doi: 10.1063/1.4969003.

C. Deil et al. Gammapy - A prototype for the CTA science tools. In 35th International Cosmic Ray Conference (2017). Available at https://pos.sissa.it/301/766/pdf.

A. Weiser and S. E. Zarantonello. A note on piecewise linear and multilinear table interpolation in many dimensions. *Mathematics of Computation*, 50(181):189–196, 1988.

N. Gehrels. Use of νF_ν spectral energy distributions for multiwavelength astronomy. *Nuovo Cimento B Serie*, 112B:11–15, Jan 1997.

B. S. Acharya et al. Introducing the CTA concept. *Astroparticle Physics*, 43:3–18, March 2013. doi: 10.1016/j.astropartphys.2013.01.007.

CTA Consortium. *Science with the Cherenkov Telescope Array*. World Scientific Publishing Co. Pte. Ltd., 2019. doi: 10.1142/10986.

H. Abdalla et al. The H.E.S.S. Galactic plane survey. *Astronomy and Astrophysics*, 612:A1, Apr 2018a. doi: 10.1051/0004-6361/201732098.

G. Dubus et al. Surveys with the Cherenkov Telescope Array. *Astroparticle Physics*, 43:317–330, March 2013. doi: 10.1016/j.astropartphys.2012.05.020.

C. Nigro et al. Towards open and reproducible multi-instrument analysis in gamma-ray astronomy. *Astronomy and Astrophysics*, 625:A10, May 2019. doi: 10.1051/0004-6361/201834938.

H.E.S.S. Collaboration. H.E.S.S. first public test data release. *arXiv e-prints*, art. arXiv:1810.04516, Oct 2018.

J. Knödlseder et al. GammaLib and ctools. A software framework for the analysis of astronomical gamma-ray data. *Astronomy and Astrophysics*, 593:A1, Aug 2016. doi: 10.1051/0004-6361/201628822.

F. Aharonian et al. The Crab Nebula and Pulsar between 500 GeV and 80 TeV: Observations with the HEGRA Stereoscopic Air Cerenkov Telescopes. *The Astrophysical Journal*, 614:897–913, October 2004. doi: 10.1086/423931.

F. Aharonian et al. Observations of the Crab nebula with HESS. *Astronomy and Astrophysics*, 457: 899–915, October 2006. doi: 10.1051/0004-6361:20065351.

J. Albert et al. VHE γ-Ray Observation of the Crab Nebula and its Pulsar with the MAGIC Telescope. *The Astrophysical Journal*, 674:1037–1055, February 2008b. doi: 10.1086/525270.

J. Aleksić et al. Performance of the MAGIC stereo system obtained with Crab Nebula data. *Astroparticle Physics*, 35:435–448, Feb 2012b. doi: 10.1016/j.astropartphys.2011.11.007.

W. B. Atwood et al. The Large Area Telescope on the Fermi Gamma-Ray Space Telescope Mission. *The Astrophysical Journal*, 697:1071–1102, Jun 2009. doi: 10.1088/0004-637X/697/2/1071.

M. Ajello et al. 3FHL: The Third Catalog of Hard Fermi-LAT Sources. *The Astrophysical Journal Supplement Series*, 232:18, October 2017. doi: 10.3847/1538-4365/aa8221.

J. Holder et al. The first VERITAS telescope. *Astroparticle Physics*, 25:391–401, July 2006. doi: 10.1016/j.astropartphys.2006.04.002.

J. S. Perkins et al. VERITAS Telescope 1 Relocation: Details and Improvements. In *Proceedings, 2nd Fermi Symposium, Washington, USA, 2-5 November 2009*, December 2009.

D. B. Kieda et al. The Gamma Ray Detection sensitivity of the upgraded VERITAS Observatory. In Saa (2014), page 700. Available at https://inspirehep.net/record/1318537.

H. Anderhub et al. Design and operation of FACT - the first G-APD Cherenkov telescope. *Journal of Instrumentation*, 8:P06008, Jun 2013. doi: 10.1088/1748-0221/8/06/P06008.

M. Nöthe et al. Towards Robotic Operation with the First G-APD Cherenkov Telescope. *arXiv e-prints*, art. arXiv:1806.01542, Jun 2018.

J. Aleksić et al. Measurement of the Crab Nebula spectrum over three decades in energy with the MAGIC telescopes. *Journal of High Energy Astrophysics*, 5:30–38, March 2015. doi: 10.1016/j.jheap.2015.01.002.

H. E. S. S. Collaboration and LAT Collaboration. Gamma-ray blazar spectra with H.E.S.S. II mono analysis: The case of PKS 2155-304 and PG 1553+113. *Astronomy and Astrophysics*, 600:A89, Apr 2017. doi: 10.1051/0004-6361/201629427.

M. Meyer et al. The Crab Nebula as a standard candle in very high-energy astrophysics. *Astronomy and Astrophysics*, 523:A2, Nov 2010. doi: 10.1051/0004-6361/201014108.

H. Dickinson and J. Conrad. Handling systematic uncertainties and combined source analyses for Atmospheric Cherenkov Telescopes. *Astroparticle Physics*, 41:17–30, January 2013. doi: 10.1016/j.astropartphys.2012.10.004.

H. Dembinski et al. Data-driven model of the cosmic-ray flux and mass composition from 10 GeV to 10^{11} GeV. In 35th International Cosmic Ray Conference (2017), page 533. Available at https://pos.sissa.it/301.

C. Nigro et al. The joint-crab bundle, 2018. URL https://zenodo.org/record/2381863. doi: 10.5281/zenodo.2381863, https://zenodo.org/record/2381863.

P. Freeman et al. Sherpa: a mission-independent data analysis application. In J.-L. Starck and F. D. Murtagh, editors, *Astronomical Data Analysis*, volume 4477 of *Proc. SPIE*, pages 76–87, November 2001. doi: 10.1117/12.447161.

V. Zabalza. Naima: a Python package for inference of particle distribution properties from nonthermal spectra. In 34th International Cosmic Ray Conference (2015), page 922. Available at https://pos.sissa.it/236.

E. Prandini et al. Study of hadron and gamma-ray acceptance of the MAGIC telescopes: towards an improved background estimation. In 34th International Cosmic Ray Conference (2015), page 721. Available at https://pos.sissa.it/236.

D. L. Meier. *Black Hole Astrophysics: The Engine Paradigm*. 2012.

I. Kant. *Allgemeine Naturgeschichte und Theorie des Himmels (Universal Natural History and Theory of the Heavens)*. Petersen, 1755. Available in German at http://www.deutschestextarchiv.de/book/show/kant_naturgeschichte_1755.

C. Messier. Catalogue des Nébuleuses et des Amas d'Étoiles (Catalog of Nebulae and Star Clusters). Technical report, Jan 1781.

J. L. E. Dreyer. A New General Catalogue of Nebulæ and Clusters of Stars, being the Catalogue of the late Sir John F. W. Herschel, Bart, revised, corrected, and enlarged. *Memoirs of the Royal Astronomical Society*, 49:1, Jan 1888.

E. A. Fath. The spectra of some spiral nebulae and globular star clusters. *Publications of the Astronomical Society of the Pacific*, 21:138, jun 1909. doi: 10.1086/121907. URL https://doi.org/10.1086%2F121907.

W. W. Campbell and G. F. Paddock. The Spectrum and Radial Velocity of the Spiral Nebula N. G. C. 4151. *Publications of the Astronomical Society of the Pacific*, 30:68, Feb 1918. doi: 10.1086/122694.

V. M. Slipher. The spectrum and velocity of the nebula N.G.C. 1068 (M 77). *Lowell Observatory Bulletin*, 3:59–62, Jan 1917.

H. D. Curtis. Descriptions of 762 Nebulae and Clusters Photographed with the Crossley Reflector. *Publications of Lick Observatory*, 13:9–42, 1918.

E. P. Hubble. NGC 6822, a remote stellar system. *The Astrophysical Journal*, 62:409–433, Dec 1925. doi: 10.1086/142943.

C. K. Seyfert. Nuclear Emission in Spiral Nebulae. *The Astrophysical Journal*, 97:28, Jan 1943. doi: 10.1086/144488.

É. Ya. Khachikyan and D. W. Weedman. A spectroscopic study of luminous galactic nuclei. *Astrophysics*, 7(3):231–240, Jul 1971. ISSN 1573-8191. doi: 10.1007/BF01001021. URL https://doi.org/10.1007/BF01001021.

H. Netzer. *The Physics and Evolution of Active Galactic Nuclei*. Cambridge University Press, 2013. doi: 10.1017/CBO9781139109291.

A. C. S. Readhead et al. A jet in the nucleus of NGC6251. *Nature*, 272:131–134, Mar 1978. doi: 10.1038/272131a0.

R. D. Blandford and M. J. Rees. A "twin-exhaust" model for double radio sources. *Monthly Notices of the Royal Astronomical Society*, 169:395–415, Dec 1974. doi: 10.1093/mnras/169.3.395.

A. S. Bennett. The revised 3C catalogue of radio sources. *Memoirs of the Royal Astronomical Society*, 68:163, Jan 1962.

B. L. Fanaroff and J. M. Riley. The morphology of extragalactic radio sources of high and low luminosity. *Monthly Notices of the Royal Astronomical Society*, 167:31P–36P, May 1974. doi: 10.1093/mnras/167.1.31P.

D. E. Osterbrock et al. The optical spectra of 3C 227 and other broad-line radio galaxies. *The Astrophysical Journal*, 206:898–909, Jun 1976. doi: 10.1086/154454.

C. Hazard. The method of lunar occultations and its application to a survey of the radio sources 3C 212. *Monthly Notices of the Royal Astronomical Society*, 124:343, Jan 1962. doi: 10.1093/mnras/124.4.343.

M. Schmidt. 3C 273 : A Star-Like Object with Large Red-Shift. *Nature*, 197:1040, Mar 1963. doi: 10.1038/1971040a0.

J. B. Oke. Absolute Energy Distribution in the Optical Spectrum of 3C 273. *Nature*, 197:1040–1041, Mar 1963. doi: 10.1038/1971040b0.

E. P. Hubble. Extragalactic nebulae. *The Astrophysical Journal*, 64:321–369, Dec 1926. doi: 10.1086/143018.

I. Robinson et al., editors. *Quasi-stellar sources and gravitational collapse*, 1965.

J. B. Hutchings et al. The Twin-Nucleus Merging Galaxy Markarian 266 (NGC 5256). *Astronomical Journal*, 96:1227, Oct 1988. doi: 10.1086/114876.

J. B. Hutchings and S. G. Neff. Optical Imaging of the Low-Redshift Superluminous QSO 1821+643. *Astronomical Journal*, 101:2001, Jun 1991. doi: 10.1086/115824.

R. D. Blandford and A. Königl. Relativistic jets as compact radio sources. *The Astrophysical Journal*, 232:34–48, Aug 1979. doi: 10.1086/157262.

M. J. Rees. Appearance of Relativistically Expanding Radio Sources. *Nature*, 211:468–470, Jul 1966. doi: 10.1038/211468a0.

M. H. Cohen et al. The Small-Scale Structure of Radio Galaxies and Quasi-Stellar Sources at 3.8 Centimeters. *The Astrophysical Journal*, 170:207, Dec 1971. doi: 10.1086/151204.

J. L. Schmitt. BL Lac identified as a Radio Source. *Nature*, 218:663, May 1968. doi: 10.1038/218663a0.

X. Rodrigues et al. Neutrinos and Ultra-high-energy Cosmic-ray Nuclei from Blazars. *The Astrophysical Journal*, 854:54, Feb 2018. doi: 10.3847/1538-4357/aaa7ee.

G. Fossati et al. A unifying view of the spectral energy distributions of blazars. *Monthly Notices of the Royal Astronomical Society*, 299:433–448, Sep 1998. doi: 10.1046/j.1365-8711.1998.01828.x.

G. Ghisellini et al. A theoretical unifying scheme for gamma-ray bright blazars. *Monthly Notices of the Royal Astronomical Society*, 301:451–468, Dec 1998. doi: 10.1046/j.1365-8711.1998.02032.x.

G. Ghisellini et al. The Fermi blazar sequence. *Monthly Notices of the Royal Astronomical Society*, 469: 255–266, Jul 2017. doi: 10.1093/mnras/stx806.

M. Ackermann et al. The Third Catalog of Active Galactic Nuclei Detected by the Fermi Large Area Telescope. *The Astrophysical Journal*, 810:14, Sep 2015. doi: 10.1088/0004-637X/810/1/14.

P. Padovani et al. Active galactic nuclei: what's in a name? *Astronomy and Astrophysics Review*, 25:2, Aug 2017. doi: 10.1007/s00159-017-0102-9.

R. R. J. Antonucci and J. S. Miller. Spectropolarimetry and the nature of NGC 1068. *The Astrophysical Journal*, 297:621–632, Oct 1985. doi: 10.1086/163559.

I. N. Evans et al. HST Imaging of the Inner 3 Arcseconds of NGC 1068 in the Light of [O iii] lambda 5007. *The Astrophysical Journal*, 369:L27, Mar 1991. doi: 10.1086/185951.

W. Jaffe et al. A large nuclear accretion disk in the active galaxy NGC4261. *Nature*, 364:213–215, Jul 1993. doi: 10.1038/364213a0.

G. A. Shields. Thermal continuum from accretion disks in quasars. *Nature*, 272:706–708, Apr 1978. doi: 10.1038/272706a0.

M. Elvis. A Structure for Quasars. *The Astrophysical Journal*, 545:63–76, Dec 2000. doi: 10.1086/317778.

B. Groves. The Narrow-line Region: Current Models and Future Questions. In L. C. Ho and J. W. Wang, editors, *The Central Engine of Active Galactic Nuclei*, volume 373 of *Astronomical Society of the Pacific Conference Series*, page 511, Oct 2007.

R. Blandford et al. Relativistic Jets in Active Galactic Nuclei. *arXiv e-prints*, art. arXiv:1812.06025, Dec 2018.

R. D. Blandford and R. L. Znajek. Electromagnetic extraction of energy from Kerr black holes. *Monthly Notices of the Royal Astronomical Society*, 179:433–456, May 1977. doi: 10.1093/mnras/179.3.433.

C. Zier and P. L. Biermann. Binary black holes and tori in AGN. II. Can stellar winds constitute a dusty torus? *Astronomy and Astrophysics*, 396:91–108, Dec 2002. doi: 10.1051/0004-6361:20021339.

C. M. Urry and P. Padovani. Unified Schemes for Radio-Loud Active Galactic Nuclei. *Publications of the Astronomical Society of the Pacific*, 107:803, Sep 1995. doi: 10.1086/133630.

H. Netzer. Revisiting the Unified Model of Active Galactic Nuclei. *Annual Review of Astronomy and Astrophysics*, 53:365–408, Aug 2015. doi: 10.1146/annurev-astro-082214-122302.

E. Fermi. On the Origin of the Cosmic Radiation. *Physical Review*, 75:1169–1174, Apr 1949. doi: 10.1103/PhysRev.75.1169.

W. F. Swann. Hoffmann Stösse and the Origin of Cosmic-Ray Ionization. *Physical Review*, 44:1025–1027, Dec 1933. doi: 10.1103/PhysRev.44.1025.

A. R. Bell. The acceleration of cosmic rays in shock fronts - I. *Monthly Notices of the Royal Astronomical Society*, 182:147–156, Jan 1978. doi: 10.1093/mnras/182.2.147.

L. D. Landau and E. M. Lifshitz. *Fluid mechanics*. 1959.

K. Schwarzschild. Über das Gravitationsfeld eines Massenpunktes nach der Einsteinschen Theorie (On the Gravitational Field of a Mass Point According to Einstein's Theory). *Sitzungsberichte der Königlich Preußischen Akademie der Wissenschaften (Berlin*, pages 189–196, Jan 1916.

L. Bergström and A. Goobar. *Cosmology and Particle Astrophysics*. 2004. doi: 10.1007/3-540-37719-0.

R. P. Kerr. Gravitational Field of a Spinning Mass as an Example of Algebraically Special Metrics. *Physics Review Letters*, 11:237–238, Sep 1963. doi: 10.1103/PhysRevLett.11.237.

R. H. Boyer and R. W. Lindquist. Maximal Analytic Extension of the Kerr Metric. *Journal of Mathematical Physics*, 8:265–281, Feb 1967. doi: 10.1063/1.1705193.

S. N. Zhang et al. Black Hole Spin in X-Ray Binaries: Observational Consequences. *The Astrophysical Journal*, 482:L155–L158, Jun 1997. doi: 10.1086/310705.

F. M. Rieger. Nonthermal Processes in Black Hole-Jet Magnetospheres. *International Journal of Modern Physics D*, 20:1547–1596, Jan 2011. doi: 10.1142/S0218271811019712.

A. S. Eddington. On the radiative equilibrium of the stars. *Monthly Notices of the Royal Astronomical Society*, 77:596–612, Jun 1917. doi: 10.1093/mnras/77.8.596.

N. I. Shakura and R. A. Sunyaev. Black holes in binary systems. Observational appearance. *Astronomy and Astrophysics*, 500:33–51, Jun 1973.

R. Narayan and I. Yi. Advection-dominated Accretion: A Self-similar Solution. *The Astrophysical Journal*, 428:L13, Jun 1994. doi: 10.1086/187381.

R. Narayan and I. Yi. Advection-dominated Accretion: Underfed Black Holes and Neutron Stars. *The Astrophysical Journal*, 452:710, Oct 1995. doi: 10.1086/176343.

R. Narayan et al. Advection-dominated accretion around black holes. In M. A. Abramowicz, G. Björnsson, and J. E. Pringle, editors, *Theory of Black Hole Accretion Disks*, pages 148–182, Jan 1998.

T. Oliphant. NumPy: A guide to NumPy. USA: Trelgol Publishing, 2006. URL http://www.numpy.org/. http://www.numpy.org/.

Astropy Collaboration. Astropy: A community Python package for astronomy. *Astronomy and Astrophysics*, 558:A33, October 2013. doi: 10.1051/0004-6361/201322068.

C. D. Dermer and G. Menon. *High Energy Radiation from Black Holes: Gamma Rays, Cosmic Rays, and Neutrinos*. 2009.

C. D. Dermer et al. Gamma-Ray Studies of Blazars: Synchro-Compton Analysis of Flat Spectrum Radio Quasars. *The Astrophysical Journal*, 692:32–46, Feb 2009. doi: 10.1088/0004-637X/692/1/32.

J. D. Finke. External Compton Scattering in Blazar Jets and the Location of the Gamma-Ray Emitting Region. *The Astrophysical Journal*, 830:94, Oct 2016. doi: 10.3847/0004-637X/830/2/94.

George B. Rybicki and Alan P. Lightman. *Radiative Processes in Astrophysics*. Wiley-VCH, 1986.

A. Crusius and R. Schlickeiser. Synchrotron radiation in random magnetic fields. *Astronomy and Astrophysics*, 164:L16–L18, Aug 1986.

F. A. Aharonian. Angular, spectral, and time distributions of highest energy protons and associated secondary gamma rays and neutrinos propagating through extragalactic magnetic and radiation fields. *Physical Review D*, 82(4):043002, August 2010. doi: 10.1103/PhysRevD.82.043002.

S. P. Reynolds. Theoretical Studies of Compact Radio Sources - Part Two - Inverse-Compton Radiation from Anisotropic Photon and Electron Distributions - General Results and Spectra from Relativistic Flows. *The Astrophysical Journal*, 256:38, May 1982. doi: 10.1086/159882.

F. C. Jones. Calculated Spectrum of Inverse-Compton-Scattered Photons. *Physical Review*, 167(5): 1159–1169, Mar 1968. doi: 10.1103/PhysRev.167.1159.

J. D. Finke et al. Synchrotron Self-Compton Analysis of TeV X-Ray-Selected BL Lacertae Objects. *The Astrophysical Journal*, 686(1):181–194, Oct 2008. doi: 10.1086/590900.

C. D. Dermer and R. Schlickeiser. Model for the High-Energy Emission from Blazars. *The Astrophysical Journal*, 416:458, Oct 1993. doi: 10.1086/173251.

M. Georganopoulos et al. The Beaming Pattern and Spectrum of Radiation from Inverse Compton Scattering in Blazars. *The Astrophysical Journal*, 561(1):111–117, Nov 2001. doi: 10.1086/323225.

M. Boettcher and C. D. Dermer. Reverberation mapping of the central regions of active galactic nuclei using high-energy γ-ray observations. *Astronomy and Astrophysics*, 302:37, Oct 1995.

B. M. Peterson and A. Wandel. Keplerian Motion of Broad-Line Region Gas as Evidence for Supermassive Black Holes in Active Galactic Nuclei. *The Astrophysical Journal*, 521(2):L95–L98, Aug 1999. doi: 10.1086/312190.

B. M. Peterson et al. Reverberation Mapping of the Seyfert 1 Galaxy NGC 7469. *The Astrophysical Journal*, 795(2):149, Nov 2014. doi: 10.1088/0004-637X/795/2/149.

M. Nenkova et al. AGN Dusty Tori. II. Observational Implications of Clumpiness. *The Astrophysical Journal*, 685(1):160–180, Sep 2008. doi: 10.1086/590483.

E. Dwek and F. Krennrich. The extragalactic background light and the gamma-ray opacity of the universe. *Astroparticle Physics*, 43:112–133, Mar 2013. doi: 10.1016/j.astropartphys.2012.09.003.

A. Franceschini, G. Rodighiero, and M. Vaccari. Extragalactic optical-infrared background radiation, its time evolution and the cosmic photon-photon opacity. *Astronomy and Astrophysics*, 487(3):837–852, Sep 2008. doi: 10.1051/0004-6361:200809691.

A. Domínguez et al. Extragalactic background light inferred from AEGIS galaxy-SED-type fractions. *Monthly Notices of the Royal Astronomical Society*, 410:2556–2578, Feb 2011. doi: 10.1111/j.1365-2966.2010.17631.x.

K. Mannheim and P. L. Biermann. Photomeson production in active galactic nuclei. *Astronomy and Astrophysics*, 221:211–220, Sep 1989.

J. G. Kirk and A. Mastichiadis. X-ray flares from runaway pair production in active galactic nuclei. *Nature*, 360(6400):135–137, Nov 1992. doi: 10.1038/360135a0.

A. Mastichiadis and J. G. Kirk. Self-consistent particle acceleration in active galactic nuclei. *Astronomy and Astrophysics*, 295:613, March 1995.

IceCube Collaboration et al. Multimessenger observations of a flaring blazar coincident with high-energy neutrino IceCube-170922A. *Science*, 361(6398):eaat1378, Jul 2018. doi: 10.1126/science.aat1378.

IceCube Collaboration. Neutrino emission from the direction of the blazar TXS 0506+056 prior to the IceCube-170922A alert. *Science*, 361(6398):147–151, Jul 2018. doi: 10.1126/science.aat2890.

S. Ansoldi et al. The Blazar TXS 0506+056 Associated with a High-energy Neutrino: Insights into Extragalactic Jets and Cosmic-Ray Acceleration. *The Astrophysical Journal*, 863(1):L10, Aug 2018a. doi: 10.3847/2041-8213/aad083.

M. Cerruti et al. Leptohadronic single-zone models for the electromagnetic and neutrino emission of TXS 0506+056. *Monthly Notices of the Royal Astronomical Society*, 483(1):L12–L16, Feb 2019. doi: 10.1093/mnrasl/sly210.

S. Gao et al. Modelling the coincident observation of a high-energy neutrino and a bright blazar flare. *Nature Astronomy*, 3:88–92, Jan 2019. doi: 10.1038/s41550-018-0610-1.

A. Keivani et al. A Multimessenger Picture of the Flaring Blazar TXS 0506+056: Implications for High-energy Neutrino Emission and Cosmic-Ray Acceleration. *The Astrophysical Journal*, 864(1):84, Sep 2018. doi: 10.3847/1538-4357/aad59a.

R. Liu et al. Hadronuclear interpretation of a high-energy neutrino event coincident with a blazar flare. *Physical Review D*, 99(6):063008, Mar 2019. doi: 10.1103/PhysRevD.99.063008.

W. Bednarek and R. J. Protheroe. Gamma-rays from interactions of stars with active galactic nucleus jets. *Monthly Notices of the Royal Astronomical Society*, 287(3):L9–L13, May 1997. doi: 10.1093/mnras/287.3.L9.

M. V. Barkov. Gamma-ray Flares from Red Giant/Jet Interactions in Active Galactic Nuclei. *The Astrophysical Journal*, 724(2):1517–1523, Dec 2010. doi: 10.1088/0004-637X/724/2/1517.

K. Mannheim and P. L. Biermann. Gamma-ray flaring of 3C 279 : a proton-initiated cascade in the jet ? *Astronomy and Astrophysics*, 253:L21–L24, Jan 1992.

A. Mücke and R. J. Protheroe. A proton synchrotron blazar model for flaring in Markarian 501. *Astroparticle Physics*, 15(1):121–136, Mar 2001. doi: 10.1016/S0927-6505(00)00141-9.

W. Bednarek and R. J. Protheroe. Gamma-ray and neutrino flares produced by protons accelerated on an accretion disc surface in active galactic nuclei. *Monthly Notices of the Royal Astronomical Society*, 302(2):373–380, Jan 1999. doi: 10.1046/j.1365-8711.1999.02132.x.

A. M. Atoyan and C. D. Dermer. Neutral Beams from Blazar Jets. *The Astrophysical Journal*, 586(1):79–96, Mar 2003. doi: 10.1086/346261.

F. A. Aharonian. TeV gamma rays from BL Lac objects due to synchrotron radiation of extremely high energy protons. *New Astronomy*, 5(7):377–395, Nov 2000. doi: 10.1016/S1384-1076(00)00039-7.

A. Mücke et al. BL Lac objects in the synchrotron proton blazar model. *Astroparticle Physics*, 18(6):593–613, Mar 2003. doi: 10.1016/S0927-6505(02)00185-8.

V. A. Acciari et al. Detection of persistent VHE gamma-ray emission from PKS 1510-089 by the MAGIC telescopes during low states between 2012 and 2017. *Astronomy and Astrophysics*, 619:A159, Nov 2018b. doi: 10.1051/0004-6361/201833618.

J. Aleksić et al. MAGIC Discovery of Very High Energy Emission from the FSRQ PKS 1222+21. *The Astrophysical Journal Letters*, 730:L8, March 2011. doi: 10.1088/2041-8205/730/1/L8.

A. Abramowski et al. H.E.S.S. discovery of VHE γ-rays from the quasar PKS 1510-089. *Astronomy and Astrophysics*, 554:A107, Jun 2013. doi: 10.1051/0004-6361/201321135.

M. L. Ahnen et al. Very High Energy γ-Rays from the Universe's Middle Age: Detection of the z = 0.940 Blazar PKS 1441+25 with MAGIC. *The Astrophysical Journal Letters*, 815:L23, December 2015. doi: 10.1088/2041-8205/815/2/L23.

M. L. Ahnen et al. Detection of very high energy gamma-ray emission from the gravitationally lensed blazar QSO B0218+357 with the MAGIC telescopes. *Astronomy and Astrophysics*, 595:A98, November 2016a. doi: 10.1051/0004-6361/201629461.

M. Cerruti et al. H.E.S.S. discovery of very-high-energy emission from the blazar PKS 0736+017: on the location of the γ-ray emitting region in FSRQs. *International Cosmic Ray Conference*, 35:627, January 2017.

R. Mirzoyan. Detection of very-high-energy gamma-ray emission from the FSRQ Ton 0599 with the MAGIC telescopes. *The Astronomer's Telegram*, 11061:1, Dec 2017.

R. C. Hartman et al. The Third EGRET Catalog of High-Energy Gamma-Ray Sources. *The Astrophysical Journal Supplement Series*, 123:79–202, Jul 1999. doi: 10.1086/313231.

F. Verrecchia et al. An updated list of AGILE bright γ-ray sources and their variability in pointing mode. *Astronomy and Astrophysics*, 558:A137, October 2013. doi: 10.1051/0004-6361/201321452.

A. A. Abdo et al. Fermi Large Area Telescope and Multi-wavelength Observations of the Flaring Activity of PKS 1510-089 between 2008 September and 2009 June. *The Astrophysical Journal*, 721:1425–1447, Oct 2010. doi: 10.1088/0004-637X/721/2/1425.

F. D'Ammando et al. AGILE detection of extreme γ-ray activity from the blazar PKS 1510-089 during March 2009. Multifrequency analysis. *Astronomy and Astrophysics*, 529:A145, May 2011. doi: 10.1051/0004-6361/201016128.

A. P. Marscher et al. Probing the Inner Jet of the Quasar PKS 1510-089 with Multi-Waveband Monitoring During Strong Gamma-Ray Activity. *The Astrophysical Journal*, 710:L126–L131, Feb 2010. doi: 10.1088/2041-8205/710/2/L126.

M. Orienti et al. Radio and γ-ray follow-up of the exceptionally high-activity state of PKS 1510-089 in 2011. *Monthly Notices of the Royal Astronomical Society*, 428:2418–2429, Jan 2013. doi: 10.1093/mnras/sts201.

S. Saito et al. Very Rapid High-amplitude Gamma-Ray Variability in Luminous Blazar PKS 1510-089 Studied with Fermi-LAT. *The Astroparticle Journal*, 766:L11, Mar 2013. doi: 10.1088/2041-8205/766/1/L11.

F. Lucarelli et al. AGILE detection of increasing gamma-ray emission from the FSRQ PKS1510-089. *The Astronomer's Telegram*, 3934:1, Feb 2012.

M. L. Ahnen et al. Multiwavelength observations of a VHE gamma-ray flare from PKS 1510-089 in 2015. *Astronomy and Astrophysics*, 603:A29, Jul 2017b. doi: 10.1051/0004-6361/201629960.

M. Zacharias et al. The exceptional VHE gamma-ray outburst of PKS 1510-089 in May 2016. 35th International Cosmic Ray Conference (2017), art. 655. Available at https://pos.sissa.it/301.

J. R. Mattox et al. The Likelihood Analysis of EGRET Data. *The Astrophysical Journal*, 461:396, Apr 1996. doi: 10.1086/177068.

F. Acero et al. Fermi Large Area Telescope Third Source Catalog. *The Astrophysical Journal Supplement*, 218(2):23, Jun 2015. doi: 10.1088/0067-0049/218/2/23.

F. Acero et al. Development of the Model of Galactic Interstellar Emission for Standard Point-source Analysis of Fermi Large Area Telescope Data. *The Astrophysical Journal Supplement Series*, 223:26, Apr 2016. doi: 10.3847/0067-0049/223/2/26.

M. Ackermann et al. Resolving the Extragalactic γ -Ray Background above 50 GeV with the Fermi Large Area Telescope. *Physical Review Letters*, 116:151105, Apr 2016. doi: 10.1103/PhysRevLett.116.151105.

J. Aleksić et al. MAGIC gamma-ray and multi-frequency observations of flat spectrum radio quasar PKS 1510-089 in early 2012. *Astronomy and Astrophysics*, 569:A46, Sep 2014a. doi: 10.1051/0004-6361/201423484.

D. N. Burrows et al. The Swift X-Ray Telescope. In K. A. Flanagan and Oswald H. W. Siegmund, editors, *X-Ray and Gamma-Ray Instrumentation for Astronomy XIII*, volume 5165 of *Society of Photo-Optical Instrumentation Engineers (SPIE) Conference Series*, pages 201–216, Feb 2004. doi: 10.1117/12.504868.

V. Fallah Ramazani et al. Empirical multi-wavelength prediction method for very high energy gamma-ray emitting BL Lacertae objects. *Astronomy and Astrophysics*, 608:A68, Dec 2017. doi: 10.1051/0004-6361/201730505.

J. Kataoka et al. Multiwavelength Observations of the Powerful Gamma-Ray Quasar PKS 1510-089: Clues on the Jet Composition. *The Astrophysical Journal*, 672:787–799, Jan 2008. doi: 10.1086/523093.

T. S. Poole et al. Photometric calibration of the Swift ultraviolet/optical telescope. *Monthly Notices of the Royal Astronomical Society*, 383:627–645, Jan 2008. doi: 10.1111/j.1365-2966.2007.12563.x.

C. M. Raiteri et al. Another look at the BL Lacertae flux and spectral variability. Observations by GASP-WEBT, XMM-Newton, and Swift in 2008-2009. *Astronomy and Astrophysics*, 524:A43, Dec 2010. doi: 10.1051/0004-6361/201015191.

I. Agudo et al. Mapcat: Monitoring AGN with Polarimetry at the Calar Alto Telescopes. In *International Journal of Modern Physics Conference Series*, volume 8 of *International Journal of Modern Physics Conference Series*, pages 299–302, Jan 2012. doi: 10.1142/S2010194512004746.

S. G. Jorstad et al. Flaring Behavior of the Quasar 3C 454.3 Across the Electromagnetic Spectrum. *The Astrophysical Journal*, 715:362–384, May 2010. doi: 10.1088/0004-637X/715/1/362.

E. Bonning et al. SMARTS Optical and Infrared Monitoring of 12 Gamma-Ray Bright Blazars. *The Astrophysical Journal*, 756:13, Sep 2012. doi: 10.1088/0004-637X/756/1/13.

R. M. Zerbi et al. The REM telescope: detecting the near infra-red counterparts of Gamma-Ray Bursts and the prompt behavior of their optical continuum. *Astronomische Nachrichten*, 322:275–285, Dec 2001. doi: 10.1002/1521-3994(200112)322:5/6<275::AID-ASNA275>3.0.CO;2-N.

I. Agudo et al. POLAMI: Polarimetric Monitoring of AGN at Millimetre Wavelengths - I. The programme, calibration and calibrator data products. *Monthly Notices of the Royal Astronomical Society*, 474:1427–1435, Feb 2018a. doi: 10.1093/mnras/stx2435.

C. Thum et al. POLAMI: Polarimetric Monitoring of Active Galactic Nuclei at Millimetre Wavelengths - II. Widespread circular polarization. *Monthly Notices of the Royal Astronomical Society*, 473:2506–2520, Jan 2018. doi: 10.1093/mnras/stx2436.

I. Agudo et al. POLAMI: Polarimetric Monitoring of Active Galactic Nuclei at Millimetre Wavelengths - III. Characterization of total flux density and polarization variability of relativistic jets. *Monthly Notices of the Royal Astronomical Society*, 473:1850–1867, Jan 2018b. doi: 10.1093/mnras/stx2437.

V. Ramakrishnan et al. Locating the γ-ray emission site in Fermi/LAT blazars - II. Multifrequency correlations. *Monthly Notices of the Royal Astronomical Society*, 456:171–180, Feb 2016. doi: 10.1093/mnras/stv2653.

H. Teraesranta et al. Fifteen years monitoring of extragalactic radio sources at 22, 37 and 87 GHz. *Astronomy and Astrophysics Supplement Series*, 132:305–331, Nov 1998. doi: 10.1051/aas:1998297.

J. L. Richards et al. Blazars in the Fermi Era: The OVRO 40 m Telescope Monitoring Program. *The Astrophysical Journal Supplement Series*, 194:29, Jun 2011. doi: 10.1088/0067-0049/194/2/29.

K. Oh et al. The 105-Month Swift-BAT All-sky Hard X-Ray Survey. *The Astrophysical Journal Supplement*, 235(1):4, Mar 2018. doi: 10.3847/1538-4365/aaa7fd.

J. G. Kirk et al. Particle acceleration and synchrotron emission in blazar jets. *Astronomy and Astrophysics*, 333:452–458, May 1998.

M. Chiaberge and G. Ghisellini. Rapid variability in the synchrotron self-Compton model for blazars. *Monthly Notices of the Royal Astronomical Society*, 306(3):551–560, Jul 1999. doi: 10.1046/j.1365-8711.1999.02538.x.

Y. Liu et al. The Jet Power, Radio Loudness, and Black Hole Mass in Radio-loud Active Galactic Nuclei. *The Astrophysical Journal*, 637(2):669–681, Feb 2006. doi: 10.1086/498639.

A. Barnacka et al. PKS 1510-089: a rare example of a flat spectrum radio quasar with a very high-energy emission. *Astronomy and Astrophysics*, 567:A113, Jul 2014. doi: 10.1051/0004-6361/201322205.

W. J. Potter and G. Cotter. Synchrotron and inverse-Compton emission from blazar jets - I. A uniform conical jet model. *Monthly Notices of the Royal Astronomical Society*, 423(1):756–765, Jun 2012. doi: 10.1111/j.1365-2966.2012.20918.x.

G. Ghisellini and F. Tavecchio. Canonical high-power blazars. *Monthly Notices of the Royal Astronomical Society*, 397(2):985–1002, Aug 2009. doi: 10.1111/j.1365-2966.2009.15007.x.

A. M. Tanner et al. A Study of Quasar Absorption-Line Systems With IRAS. *Astronomical Journal*, 112:62, Jul 1996. doi: 10.1086/117988.

L. Costamante et al. On the origin of gamma-rays in Fermi blazars: beyondthe broad-line region. *Monthly Notices of the Royal Astronomical Society*, 477(4):4749–4767, Jul 2018. doi: 10.1093/mnras/sty887.

M. Meyer et al. Characterizing the Gamma-Ray Variability of the Brightest Flat Spectrum Radio Quasars Observed with the Fermi LAT. *The Astrophysical Journal*, 877(1):39, May 2019. doi: 10.3847/1538-4357/ab1651.

S. Ansoldi et al. Gamma-ray flaring activity of NGC1275 in 2016-2017 measured by MAGIC. *Astronomy and Astrophysics*, 617:A91, Sep 2018b. doi: 10.1051/0004-6361/201832895.

F. Aharonian et al. Is the giant radio galaxy M 87 a TeV gamma-ray emitter? *Astronomy and Astrophysics*, 403:L1–L5, May 2003. doi: 10.1051/0004-6361:20030372.

F. Aharonian et al. Discovery of Very High Energy γ-Ray Emission from Centaurus a with H.E.S.S. *The Astrophysical Journal*, 695(1):L40–L44, Apr 2009. doi: 10.1088/0004-637X/695/1/L40.

J. Aleksić et al. Detection of Very High Energy γ-ray Emission from the Perseus Cluster Head-Tail Galaxy IC 310 by the MAGIC Telescopes. *The Astrophysical Journal*, 723(2):L207–L212, Nov 2010b. doi: 10.1088/2041-8205/723/2/L207.

J. Aleksić et al. Detection of very-high energy γ-ray emission from NGC 1275 by the MAGIC telescopes. *Astronomy and Astrophysics*, 539:L2, Mar 2012c. doi: 10.1051/0004-6361/201118668.

H. Abdalla et al. H.E.S.S. discovery of very high energy γ-ray emission from PKS 0625-354. *Monthly Notices of the Royal Astronomical Society*, 476(3):4187–4198, May 2018b. doi: 10.1093/mnras/sty439.

R. Mukherjee. VERITAS discovery of VHE emission from the FRI radio galaxy 3C 264. *The Astronomer's Telegram*, 11436:1, Mar 2018.

J. Aleksić et al. Contemporaneous observations of the radio galaxy NGC 1275 from radio to very high energy γ-rays. *Astronomy and Astrophysics*, 564:A5, April 2014b. doi: 10.1051/0004-6361/201322951.

J.-P. Lenain et al. A synchrotron self-Compton scenario for the very high energy γ-ray emission of the radiogalaxy M 87. Unifying the TeV emission of blazars and other AGNs? *Astronomy and Astrophysics*, 478:111–120, January 2008. doi: 10.1051/0004-6361:20077995.

J. Aleksić et al. Black hole lightning due to particle acceleration at subhorizon scales. *Science*, 346: 1080–1084, November 2014c. doi: 10.1126/science.1256183.

V. A. Acciari et al. Radio Imaging of the Very-High-Energy γ-Ray Emission Region in the Central Engine of a Radio Galaxy. *Science*, 325(5939):444, Jul 2009. doi: 10.1126/science.1175406.

A. Donea and P. L. Biermann. The Structure of Accretion Flow at the Base of Jets in AGN. *Publications of the Astronomical Society of Australia*, 19(1):125–128, Jan 2002. doi: 10.1071/AS01078.

T. Hovatta et al. Doppler factors, Lorentz factors and viewing angles for quasars, BL Lacertae objects and radio galaxies. *Astronomy and Astrophysics*, 494(2):527–537, Feb 2009. doi: 10.1051/0004-6361: 200811150.

R. Lynds. Improved Photographs of the NGC 1275 Phenomenon. *The Astrophysical Journal*, 159:L151–L154, Mar 1970. doi: 10.1086/180500.

K. Asada et al. The Expanding Radio Lobe of 3C 84 Revealed by VSOP Observations. *Publications of the Astronomical Society of Japan*, 58:261–270, Apr 2006. doi: 10.1093/pasj/58.2.261.

A. W. Strong and G. F. Bignami. Gamma-ray observations toward NGC 1275 and the origin of the emissionin the infrared, X-rays, and gamma-rays. *The Astrophysical Journal*, 274:549–557, Nov 1983. doi: 10.1086/161469.

A. A. Abdo et al. Fermi Discovery of Gamma-ray Emission from NGC 1275. *The Astrophysical Journal*, 699(1):31–39, Jul 2009. doi: 10.1088/0004-637X/699/1/31.

J. Kataoka et al. γ-ray Spectral Evolution of NGC 1275 Observed with Fermi Large Area Telescope. *The Astrophysical Journal*, 715(1):554–560, May 2010. doi: 10.1088/0004-637X/715/1/554.

A. M. Brown and J. Adams. High-energy γ-ray properties of the Fanaroff-Riley type I radio galaxy NGC 1275. *Monthly Notices of the Royal Astronomical Society*, 413(4):2785–2790, Jun 2011. doi: 10.1111/j.1365-2966.2011.18351.x.

M. L. Ahnen et al. Deep observation of the NGC 1275 region with MAGIC: search of diffuse γ-ray emission from cosmic rays in the Perseus cluster. *Astronomy and Astrophysics*, 589:A33, May 2016b. doi: 10.1051/0004-6361/201527846.

V. A. Acciari et al. Constraining dark matter lifetime with a deep gamma-ray survey of the Perseus galaxy cluster with MAGIC. *Physics of the Dark Universe*, 22:38–47, Dec 2018c. doi: 10.1016/j.dark.2018.08.002.

E. E. Falco et al. The Updated Zwicky Catalog (UZC). *Publications of the Astronomical Society of the Pacific*, 111(758):438–452, Apr 1999. doi: 10.1086/316343.

M. Wood et al. Fermipy: An open-source Python package for analysis of Fermi-LAT Data. In 35th International Cosmic Ray Conference (2017), page 824. Available at https://pos.sissa.it/301.

V. A. Acciari et al. Measurement of the Extragalactic Background Light using MAGIC and Fermi-LAT gamma-ray observations of blazars up to z = 1. *Monthly Notices of the Royal Astronomical Society*, page 910, Apr 2019. doi: 10.1093/mnras/stz943.

M. Fiorucci et al. VRI Photometry of Stars in the Fields of 16 Blazars. *Publications of the Astronomical Society of the Pacific*, 110(744):105–110, Feb 1998. doi: 10.1086/316127.

E. F. Schlafly et al. Measuring Reddening with Sloan Digital Sky Survey Stellar Spectra and Recalibrating SFD. *The Astrophysical Journal*, 737(2):103, Aug 2011. doi: 10.1088/0004-637X/737/2/103.

R. J. Wilman et al. The nature of the molecular gas system in the core of NGC 1275. *Monthly Notices of the Royal Astronomical Society*, 359:755–764, May 2005. doi: 10.1111/j.1365-2966.2005.08956.x.

J. Scharwächter et al. Kinematics and excitation of the molecular hydrogen accretion disc in NGC 1275. *Monthly Notices of the Royal Astronomical Society*, 429:2315–2332, March 2013. doi: 10.1093/mnras/sts502.

F. Tavecchio and G. Ghisellini. On the spine-layer scenario for the very high-energy emission of NGC 1275. *Monthly Notices of the Royal Astronomical Society*, 443:1224–1230, September 2014. doi: 10.1093/mnras/stu1196.

M. Zacharias and R. Schlickeiser. A new ordering parameter of spectral energy distributions from synchrotron self-Compton emitting blazars. *Monthly Notices of the Royal Astronomical Society*, 420(1):84–102, Feb 2012. doi: 10.1111/j.1365-2966.2011.20004.x.

G. Ghisellini et al. General physical properties of bright Fermi blazars. *Monthly Notices of the Royal Astronomical Society*, 402(1):497–518, Feb 2010. doi: 10.1111/j.1365-2966.2009.15898.x.

A. Neronov and F. A. Aharonian. Production of TeV Gamma Radiation in the Vicinity of the Supermassive Black Hole in the Giant Radio Galaxy M87. *The Astrophysical Journal*, 671(1):85–96, Dec 2007. doi: 10.1086/522199.

A. Levinson and F. Rieger. Variable TeV Emission as a Manifestation of Jet Formation in M87? *The Astrophysical Journal*, 730(2):123, Apr 2011. doi: 10.1088/0004-637X/730/2/123.

K. Hirotani and H. Pu. Energetic Gamma Radiation from Rapidly Rotating Black Holes. *The Astrophysical Journal*, 818(1):50, Feb 2016. doi: 10.3847/0004-637X/818/1/50.

P. Goldreich and W. H. Julian. Pulsar Electrodynamics. *The Astrophysical Journal*, 157:869, Aug 1969. doi: 10.1086/150119.

K. Hirotani. Very High-Energy Emission from the Direct Vicinity of Rapidly Rotating Black Holes. *Galaxies*, 6(4):122, Nov 2018. doi: 10.3390/galaxies6040122.

K. Hirotani et al. Lepton Acceleration in the Vicinity of the Event Horizon: Very High Energy Emissions from Supermassive Black Holes. *The Astrophysical Journal*, 845(1):77, Aug 2017. doi: 10.3847/1538-4357/aa7895.

K. Hirotani et al. Accretion in a Kerr Black Hole Magnetosphere: Energy and Angular Momentum Transport between the Magnetic Field and the Matter. *The Astrophysical Journal*, 386:455, Feb 1992. doi: 10.1086/171031.

S Hirose et al. Magnetically Driven Accretion Flows in the Kerr Metric. II. Structure of the Magnetic Field. *The Astrophysical Journal*, 606(2):1083–1097, May 2004. doi: 10.1086/383184.

G. Ghisellini et al. The power of relativistic jets is larger than the luminosity of their accretion disks. *Nature*, 515(7527):376–378, Nov 2014. doi: 10.1038/nature13856.

35th International Cosmic Ray Conference, editor. *Proceedings, 35th International Cosmic Ray Conference (ICRC 2017): Bexco, Busan, Korea, July 12-20, 2017*, 2017. Proceedings of Science. Available at https://pos.sissa.it/301.

G. B. Zhdanov, editor. *Proceedings from the 6th International Cosmic Ray Conference, held in Moscow, Russia*, volume 2, Extensive Air Showers and Cascades Process, 1960.

R. R. Daniels et al., editors. *Proceedings from the 8th International Cosmic Ray Conference, Jaipur, India*, volume 4, Extensive Air Showers, 1964. Commercial Printing Press, Ltd., Bombay, India.

R. L. Chasson, editor. *Proceedings of the 13th International Conference on Cosmic Rays, held in Denver, Colorado*, volume 1 (OG Sessions), 1973. University of Denver, Colorado Associated University Press, Boulder, CO.

F. C. Jones et al., editors. *Proceedings of the 19th International Cosmic Ray Conference, La Jolla, California, USA*, volume 3, 1985. NASA Conference Publication No. 2376, Goddard Space Flight Center, Greenbelt, MD.

P. Sripathi Acharya et al., editors. *Proceedings of the 29th International Cosmic Ray Conference. August 3-10, 2005, Pune, India*, volume 5, 2005. Mumbai: Tata Institute of Fundamental Research.

R. Caballero et al., editors. *Proceedings of the 30th International Cosmic Ray Conference. July 3-11, 2007, Mérida, Yucatán, Mexico*, volume 3, 2008. Universidad Nacional Autónoma de México, Mexico City, Mexico.

A. Saa, editor. *Proceedings, 33rd International Cosmic Ray Conference (ICRC2013): Rio de Janeiro, Brazil, July 2-9, 2013*, 2014. Braz. J. Phys., 44(5):415–608. Available at https://inspirehep.net/record/1318537.

34th International Cosmic Ray Conference, editor. *Proceedings, 34th International Cosmic Ray Conference (ICRC2015): The Hague, The Netherlands, July 30-August 6, 2015*, 2015. Proceedings of Science. Available at https://pos.sissa.it/236.

M. S. Potgieter et al., editors. *Proceedings of the 25th International Conference on Cosmic Rays, 28 Jul - 8 Aug 1997, Durban, South Africa*, volume 1-8, 1997. Durban Singapore: Durban Univ., World Scientific, 1997.

Abbreviations

3C Third Cambridge Catalogue of Radio Sources

3CR Revised Third Cambridge Catalogue of Radio Sources

3FGL Fermi Large Area Telescope Third Source Catalog

3LAC Third Catalog of Active Galactic Nuclei Detected by the Fermi Large Area Telescope

ADAF Advection Dominated Accreton Flow

ADC analogue to digital converter

AGILE Astrorivelatore Gamma ad Immagini LEggero

AGN Active Galactic Nucleus

Swift-BAT Swift Burst Alert Telescope

BH Black Hole

BL Lac BL Lacertae object

BLR Broad Line Region

BLRG Broad Line Radio Galaxy

CARMA Combined Array for Research in Millimeter-Wave Astronomy

CC Central Control

CCD Charge-Coupled Device

CGS Centimeter Gram Second

CH Counting House

CoG Center of Gravity

CORSIKA COsmic Ray SImulations for KAscade

CR Cosmic Ray

CTA Cherenkov Telescope Array

C.U. Crab Units

DAQ DAta Acquisition

Dec Declination

DL0 Data Level 0

DL1 Data Level 1

DL2 Data Level 2

DL3 Data Level 3

DL4 Data Level 4

DL5 Data Level 5

DOI Data Object Identifier

DRS4 Domino Ring Sampler version 4

DT Discriminator Threshold

EAS Extensive Air Shower

EBL Extragalactic Background Light

EC External Compton

EGRET Energetic Gamma Ray Experiment Telescope

EM Electromagnetic

ERF Electron Rest Frame

FACT First G-APD Cherenkov Telescope

***Fermi*-LAT** *Fermi* Large Area Telescope

FITS Flexible Image Transport System

FoV Field of View

FSRQ Flat Spectrum Radio Quasar

GADF Gamma Astro Data Format

GCN Gamma-ray Coordinates Network

GRB Gamma Ray Burst

GTI Good Time Inetrvals

HDU Header Data Unit

HE High Energy, $100\,\mathrm{MeV} < E_\gamma < 100\,\mathrm{GeV}$

HEGRA High Energy Gamma Ray Array

H.E.S.S. High Energy Stereoscopic System

HV high voltage

IACT Imaging Atmospheric Cherenkov Telescope

IR Infrared

IRAM Institut de Radioastronomie Millimétrique

IRF Instrument Response Function

ISCO Innermost Stable Circular Orbit

KVA Kunglinga Vetenskaps Akademien

L0 Level 0 Trigger

L1 Level 1 Trigger

L3 Level 3 Trigger

LED Light Emitting Diode

LIDAR LIght Detection And Ranging

LP log parabola

LST Large Size Telescope

LUT Look Up Table

M1 MAGIC-I

M2 MAGIC-II

MAGIC Major Atmospheric Imaging Gamma-ray Cherenkov

MAPCAT Monitoring AGN with Polarimetry at the Calar Alto 2.2m Telescope

MARS MAGIC Analysis and Reconstruction Software

MC Monte Carlo (simulation process)

MJD Modified Julian Date

MST Medium Size Telescope

NASA National Aeronautics and Space Administration

NGC New General Catalogue

NLR Narrow Line Region

NLRG Narrow Line Radio Galaxy

NN Next Neighbour

NSB Night Sky Background

OO Object Oriented

ORM Observatorio del Roque de los Muchachos

OVRO Owens Valley

PDF Probability Density Function

PMT photomultiplier tube

POLAMI Polarimetric Monitoring of AGN at Millimitre Wavelengths

PSF Point Spread Function

QSR Quasi-Stellar Radio Source

RA Right Ascension

REM Rapid Eye Mount

RF Random Forest

RG Radio Galaxy

RIAF Radiatively Inefficient Accreton Flow

RMS Root Mean Square

RoI Region of Interest

SED Spectral Energy Distribution

SI International System of Units

SiPM silicon photo-multipliers

SMARTS Small and Moderate Aperture Research Telescope System

SSA Synchrotron Self Absorption

SSC Synchrotron Self Compton

SST Small Size Telescope

TS Test Statistic

UV Ultraviolet

Swift-UVOT Swift Ultra Violet Optical Telescope

VERITAS Very Energetic Radiation Imaging Telescope Array System

VHE Very High Energy, $100\,\mathrm{GeV} < E_\gamma < 100\,\mathrm{TeV}$

VLBI Very Large Baseline Interferometry

Swift-XRT Swift X-Ray Telescope

List of Figures

List of Tables

Acknowledgements

I would like to express my gratitude to:

- Prof. Elisa Bernardini for allowing me to start my scientific career and supervising this thesis;
- Dr. Gernot Maier and Prof. Alberto Franceschini for taking the effort of refereeing this thesis;
- all the (present and past) members of the MAGIC group in DESY Zeuthen: Konstancja, Wriju, Dariusz and Giovanna;
- Julian Sitarek and Abelardo Moralejo, as I looked at them as my mentors in these three years;
- Tarek Hassan for his essential contribution to my Ph.D., involving me in the most fruitful and interesting projects, constantly encouraging and advising me;
- Xavier Rodrigues for patiently helping me with the blazar modelling;
- all the people who have read and provided comments on this thesis (in order of chapters): Rolf Bühler, Roberta Zanin, Konstancja Satalecka, Orel Gueta, Iftach Sade, Abelardo Moralejo, Xavier Rodriguez, Julian Sitarek, Tarek Hassan, Federica Bradascio, Josefa Becerra González, Simon Bonnefoy, Simone Garrappa, Moritz Hütten. A special thank to Alicia Fattorini for translating the abstract in German. I apologize for any error left.

I would like to express my affection to:

- my father Rocco and my mother Lucia for all the the sacrifices they endured;
- my brother Diego for staying home and supporting the household;
- Carmine for his friendship;
- Valerio and Gianmarco for I consider them my brothers;
- the second family I found in Wedding: Michele e Nicole, Matteo e Antonella;
- Simon for his good spirit;
- Federica and Simone for their patience with me.

Erklärung

Ich erkläre, dass ich die vorliegende Dissertation selbständig und nur unter Verwendung der von mir gemäß § 7 Abs. 3 der Promotionsordnung der Mathematisch-Naturwissenschaftlichen Fakultät, veröffentlicht im Amtlichen Mitteilungsblatt der Humboldt-Universität zu Berlin Nr. 42/2018 am 11/07/2018, angegebenen Hilfsmittel angefertigt habe.

Berlin, den 29/05/2019

Cosimo Nigro

Publication List

- *Towards open and reproducible multi-instrument analysis in gamma-ray astronomy*, C.Nigro et al., May 2019, Astronomy & Astrophysics, Volume 625, id.A10, 8 pp.
- *Detection of persistent VHE gamma-ray emission from PKS 1510-089 by the MAGIC telescopes during low states between 2012 and 2017*, MAGIC Collaboration (corresponding author), November 2018, Astronomy & Astrophysics, Volume 619, id.A159, 11 pp.
- *Gamma-ray flaring activity of NGC1275 in 2016-2017 measured by MAGIC*, MAGIC Collaboration (corresponding author), September 2018, Astronomy & Astrophysics, Volume 617, id.A91, 9 pp.